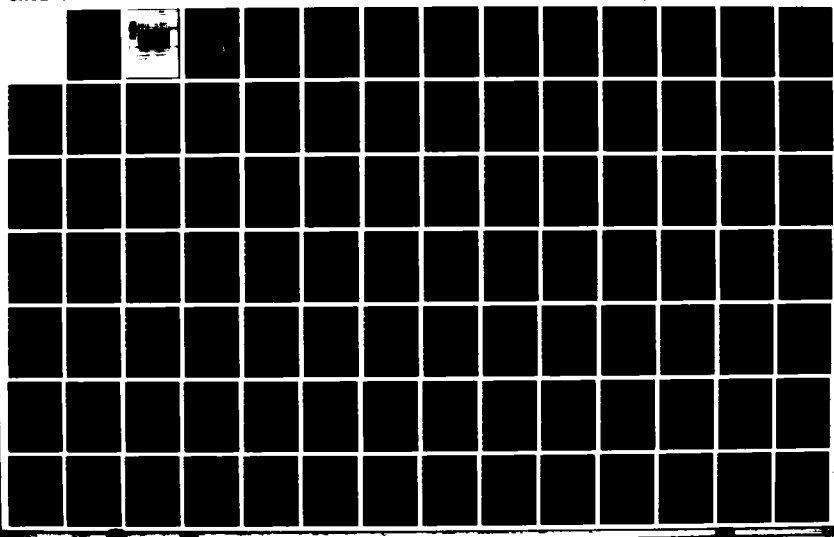


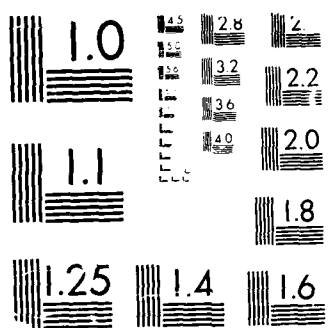
AD-A192 997

EXPERIMENTAL STUDY OF UNSTEADY SEPARATING TURBULENT
BOUNDARY LAYERS(U) VIRGINIA POLYTECHNIC INST AND STATE
UNIV BLACKSBURG DEPT OF A. N K AGARWAL ET AL. FEB 88
UNCLASSIFIED AFOSR-TR-88-0271 AFOSR-84-0134

1/2

F/G 28/4 NL





MICROCOPY RESOLUTION TEST CHART

© 1972 STANAGEN CORP.

Final Technical Report

to

The Air Force Office of
Scientific Research Grant 84-0134

**EXPERIMENTAL STUDY OF UNSTEADY SEPARATING
TURBULENT BOUNDARY LAYERS**

by

N.K. Agarwal and R.L. Simpson

February 1988



**VIRGINIA
POLYTECHNIC
INSTITUTE**

DISTRIBUTION STATEMENT A

(2)

Final Technical Report

to

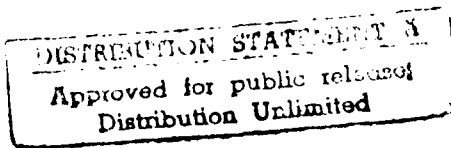
The Air Force Office of
Scientific Research Grant 84-0134

**EXPERIMENTAL STUDY OF UNSTEADY SEPARATING
TURBULENT BOUNDARY LAYERS**

by

N.K. Agarwal and R.L. Simpson

February 1988



Department of Aerospace and Ocean Engineering
Virginia Polytechnic Institute and State University
Blacksburg, Virginia 24061

EXPERIMENTAL STUDY OF UNSTEADY SEPARATING TURBULENT BOUNDARY LAYERS

Accession For	
NTIS CRA&I	<input checked="" type="checkbox"/>
DTIC TAB	<input type="checkbox"/>
Unpublished	<input type="checkbox"/>
Justification	
By	
Distribution	
Av. Intensity Copies	
Dist	Avail. Non-For Selling
A-1	



February 1988

N.K. Agarwal and R.L. Simpson
Virginia Polytechnic Institute and State University
Aerospace and Ocean Engineering
Blacksburg, Virginia 24061

UNCLASSIFIED

SECURITY CLASSIFICATION OF THIS PAGE

REPORT DOCUMENTATION PAGE

Form Approved
OMB No. 0704-0188

1a. REPORT SECURITY CLASSIFICATION Unclassified		1b. RESTRICTIVE MARKINGS Unclassified	
2a. SECURITY CLASSIFICATION AUTHORITY		3. DISTRIBUTION/AVAILABILITY OF REPORT Unclassified-Unlimited Approved for public release, distribution unlimited	
2b. DECLASSIFICATION/DOWNGRADING SCHEDULE			
4. PERFORMING ORGANIZATION REPORT NUMBER(S)		5. MONITORING ORGANIZATION REPORT NUMBER(S) AFOSR TR- 88-0271	
6a. NAME OF PERFORMING ORGANIZATION Aerospace and Ocean Engrg. Dept Virginia Polytechnic Inst. & S.U.	6b. OFFICE SYMBOL (If applicable)	7a. NAME OF MONITORING ORGANIZATION AFOSR - Aerospace Sciences	
6c ADDRESS (City, State, and ZIP Code) Blacksburg, Virginia 24061	7b. ADDRESS (City, State, and ZIP Code) Building 410 Bolling AFB, DC 20332		
8a. NAME OF FUNDING/SPONSORING ORGANIZATION AFOSR-Aerospace Sciences	8b. OFFICE SYMBOL (If applicable) AJA	9. PROCUREMENT INSTRUMENT IDENTIFICATION NUMBER AFOSR 84-0134	
8c ADDRESS (City, State, and ZIP Code) Building 410 Bolling AFB, DC 20332	10. SOURCE OF FUNDING NUMBERS		
	PROGRAM ELEMENT NO. 61102F	PROJECT NO. 216-7	TASK NO. A2
11. TITLE (Include Security Classification) Experimental Study of Unsteady Separating Turbulent Boundary Layers			
12. PERSONAL AUTHOR(S) N.K. Agarwal and R.L. Simpson			
13a. TYPE OF REPORT Final Technical	13b. TIME COVERED FROM 7/1/84 TO 12/31/84	14. DATE OF REPORT (Year, Month, Day) February 1988	15. PAGE COUNT 175
16. SUPPLEMENTARY NOTATION			
17. COSATI CODES		18. SUBJECT TERMS (Continue on reverse if necessary and identify by block number) Unsteady flows, laser anemometry, turbulence, separation <	
FIELD	GROUP	SUB-GROUP	
19. ABSTRACT (Continue on reverse if necessary and identify by block number)			
<p>A detailed experimental study of two large amplitude unsteady freestream flows and a third unsteady flow produced by an oscillating roof damper is reported. Detailed ensemble-averaged velocity and turbulence measurements were made using hot-wire and laser anemometers. While the primary function of this report is to present and document these data, some discussion of the results and a number of data plots are presented. The reduced data are available on computer diskettes.</p> <p>Upstream of detachment at the phases with no flow reversal, the flows are quasi-steady. For the large amplitude flows, at low velocity phases some flow reversal occurs upstream of detachment, which was not observed in the moderate amplitude flow studied by Simpson et al. (1983).</p> <p>After the beginning of detachment, large amplitude and phase variations develop through each flow. Huge backflow velocities, as large as free-stream, were measured. Mean backflow velocities close to the wall are described by the steady flow law of the backflow (Simpson,</p>			
20. DISTRIBUTION/AVAILABILITY OF ABSTRACT <input checked="" type="checkbox"/> UNCLASSIFIED/UNLIMITED <input checked="" type="checkbox"/> SAME AS RPT. <input type="checkbox"/> DTIC USERS		21. ABSTRACT SECURITY CLASSIFICATION Unclassified/Unlimited	
22a. NAME OF RESPONSIBLE INDIVIDUAL J M MICHAEL AFL		22b. TELEPHONE (Include Area Code) 4936	22c. OFFICE SYMBOL / /

19. ABSTRACT (continued)

1983) and appear to behave in a quasi-steady manner. Hysteresis in relationships between flow parameters has been observed.

New information on Reynolds shearing stress and the phase lag of turbulence structure with the ensemble-averaged velocity has been obtained. Low and negative values of the shear correlation coefficients during phases with flow reversal have been measured. This is a non-quasi-steady effect which the current turbulence models can not account for.

TABLE OF CONTENTS

REPORT DOCUMENTATION PAGE - ABSTRACT	i
TABLE OF CONTENTS	iii
LIST OF FIGURES	iv
NOMENCLATURE	x
1. INTRODUCTION	1
2. EXPERIMENTAL EQUIPMENT	2
2.1 Basic Wind Tunnel	2
2.2 Programmable-Rotating-Blade Damper	4
2.3 Boundary Layer Control System	5
2.4 Hot-Wire Anemometer	6
2.5 Laser Anemometer	6
2.6 Data Reduction	9
3. DESCRIPTION OF TEST FLOWS	11
4. EXPERIMENTAL RESULTS	13
5. SUMMARY OF RESULTS	20
6. PERSONNEL	22
7. INTERACTIONS	22
REFERENCES	23
FIGURES	25
APPENDIX A - TABLES	144
APPENDIX B - Data Organization	162

List of Figures

FIGURE 1	Sideview of the Test Section	25
FIGURE 2	Schematic of the Wind Tunnel and Rotating Damper ..	26
FIGURE 3	Modifications to the Wind Tunnel for $k = 1.03$ flow with 'roof damper'	27
FIGURE 4	Free-Stream Mean Velocity	28
FIGURES 5a-5c	Ratio of Free-Stream Harmonics Amplitude to Mean Velocity	29
FIGURES 6a-6c	Mean Pressure Gradient Distribution Along the Tunnel Centerline and Limits of Unsteady Pressure Gradient	31
FIGURES 7a-7c	Phase Angles of First Harmonic	33
FIGURES 8a-8b	Ensemble-Averaged Free-Stream Velocity Along the Tunnel Length, $k = 0.61$ Flow	35
FIGURES 9a-9b	Ensemble-Averaged Free-Stream Velocity Along the Tunnel Length, $k = 1.33$ Flow	37
FIGURES 10a-10b	Ensemble-Averaged Free-Stream Velocity Along the Tunnel Length, $k = 1.03$ Flow with "Roof Damper"	39
FIGURES 11a-11f	Free-Stream Velocity and Pressure Gradient, $k = 0.61$ Flow	41
FIGURES 12a-12f	Free-Stream Velocity and Pressure Gradient, $k = 1.33$ Flow	44
FIGURES 13a-13b	Free-Stream Velocity and Pressure Gradient, $k = 1.03$ Flow with "Roof Damper"	47
FIGURES 14a-14b	Ensemble-Averaged Velocity Profiles, \hat{U}/U_e , $k = 0.61$ Flow	50

FIGURES 15a-15b	Ensemble-Averaged Velocity Profiles, \hat{U}/\hat{U}_e , $k = 1.33$ Flow 52
FIGURES 16	Ensemble-Averaged Velocity Profiles, \hat{U}/\hat{U}_e at $X = 1.63$ m, $k = 1.03$ Flow with "Roof Damper" 54
FIGURES 17	Streamwise Turbulence Intensity Profiles, $\sqrt{\hat{u}^2/\hat{U}_e}$ at $X = 0.53$ m, $k = 1.33$ Flow 55
FIGURES 18	Normal-to-the-Wall Turbulence Intensity Profiles, $\sqrt{\hat{V}^2/\hat{U}_e}$ at $X = 0.53$ m, $k = 1.33$ Flow 56
FIGURES 19a-19b	Ensemble-Averaged Law-of-the-Wall Velocity Profiles U^+ vs. $\log_{10} y^+$, $X = 0.53$ m, $k = 1.33$ Flow 57
FIGURE 20	Correlation Between C_f Obtained from Semi-Log Region and C_f Obtained from Ludwieg-Tillmann Equation, $k = 1.33$ Flow 59
FIGURES 21a-21g	Variation of Displacement Thickness δ^* , Momentum Thickness $\hat{\theta}$, Shape Factor \hat{H} and Reynolds Number Re_{θ}^* with Phase Angle, $k = 0.61$ Flow 60
FIGURES 22a-22g	Variation of Displacement Thickness δ^* , Momentum Thickness $\hat{\theta}$, Shape Factor \hat{H} and Reynolds Number Re_{θ}^* with Phase Angle, $k = 1.33$ Flow 63
FIGURES 23a-23e	Variation of Displacement Thickness δ^* , Momentum Thickness $\hat{\theta}$, Shape Factor \hat{H} and Reynolds Number Re_{θ}^* with Phase Angle, $k = 1.03$ Flow with "Roof Damper" 67
FIGURES 24a-24b	Variation of \hat{Y}_{pu} vs. X , $k = 0.61$ Flow 69
FIGURES 25a-25b	Variation of \hat{Y}_{pu} vs. X , $k = 1.33$ Flow 70
FIGURES 26a-26b	Variation of \hat{Y}_{pu} vs. X , $k = 1.03$ Flow with "Roof

	Damper"	71
FIGURES 27a-27b	Variation of Acceleration Parameter \hat{k} with Phase Angle, $k = 0.61$ Flow	72
FIGURES 28a-28c	Variation of Acceleration Parameter \hat{k} with Phase Angle, $k = 1.33$ Flow	73
FIGURE 29	Variation of Acceleration Parameter, \hat{k} with Phase Angle at $X = 1.63$ m, $k = 1.03$ Flow with "Roof Damper"	75
FIGURE 30	Ensemble-Averaged Shear-Stress Correlation Coefficient Profile at $wt = 30^\circ$, $X = 0.53$ m, $k = 1.33$ Flow	76
FIGURE 31	Variation of Phase Angle of First Harmonic of Velocity, $k = 0.61$ Flow	77
FIGURE 32	Variation of Phase Angle of First Harmonic of Velocity, $k = 1.33$ Flow	78
FIGURE 33	Variation of Phase Angle of First Harmonic of Velocity, $k = 1.03$ Flow with "Roof Damper"	79
FIGURES 34a-34c	Ensemble-Averaged Velocity Profiles, at $X = 2.95$ m, $k = 0.61$ Flow	80
FIGURES 35a-35b	Ensemble-Averaged Velocity Profiles, at $X = 3.51$ m, $k = 0.61$ Flow	83
FIGURES 36a-36b	Ensemble-Averaged Velocity Profiles, at $X = 4.27$ m, $k = 0.61$ Flow	85
FIGURES 37a-37b	Ensemble-Averaged Velocity Profiles, at $X = 2.95$ m, $k = 1.33$ Flow	87
FIGURES 38a-38b	Ensemble-Averaged Velocity Profiles, at $X = 3.51$ m, $k = 1.33$ Flow	89

FIGURES 39a-39b	Ensemble-Averaged Velocity Profiles, at $X = 4.27 \text{ m}$, $k = 1.33$ Flow	91
FIGURES 40a-40b	Ensemble-Averaged Velocity Profiles, at $X = 3.01 \text{ m}$, $k = 1.03$ with "Roof Damper"	93
FIGURES 41a-41b	Ensemble-Averaged Velocity Profiles, at $X = 3.28 \text{ m}$ with "Roof Damper"	95
FIGURES 42a-42b	Ensemble-Averaged Velocity Profiles, at $X = 3.59 \text{ m}$ with "Roof Damper"	97
FIGURES 43a-43b	Ensemble-Averaged Velocity Profiles, at $X = 4.12 \text{ m}$ with "Roof Damper"	99
FIGURE 44	Ensemble-Averaged Law-of-the-Wall Velocity Profiles, \hat{U}^+ vs. $\log_{10} y^+$ at $X = 2.95 \text{ m}$, $k = 0.61$ Flow	101
FIGURE 45	Ensemble-Averaged Law-of-the-Wall Velocity Profiles, \hat{U}^+ vs. $\log_{10} y^+$ at $X = 2.95 \text{ m}$, $k = 1.33$ Flow	102
FIGURE 46	Correlation Between C_f Obtained from Semi-Log Region and C_f Obtained from Ludwieg-Tillmann Equation at $X = 3.01 \text{ m}$, $k = 1.03$ Flow with "Roof Damper"	103
FIGURES 47a-47b	Ensemble-Averaged Reynolds Shearing Stress, $-\hat{u}\hat{v}/\hat{U}_e^2$ Profiles, $X = 4.27 \text{ m}$, $k = 0.61$ Flow	104
FIGURES 48a-48b	Ensemble-Averaged Reynolds Shearing Stress, $-\hat{u}\hat{v}/\hat{U}_e^2$ Profiles, $X = 4.27$, $k = 1.33$ Flow	106
FIGURES 49a-49b	Ensemble-Averaged Shear Stress Correlation Coefficient Profiles at $X = 4.27 \text{ m}$, $k = 1.33$ Flow ..	108
FIGURES 50a-50d	Ensemble-Averaged Reynolds Shearing Stress, $-\hat{u}\hat{v}/\hat{U}_e^2$	

Profiles, at $X = 3.59$ m, $k = 1.03$ Flow with "Roof Damper"	110
FIGURES 51a-51b Streamwise Turbulence Intensity, \hat{u}^2/\hat{U}_e^2	
Profiles at $X = 4.27$ m, $k = 0.61$ Flow	114
FIGURES 52a-52b Streamwise Turbulence Intensity, \hat{u}^2/\hat{U}_e^2	
Profiles at $X = 4.27$ m, $k = 1.33$ Flow	116
FIGURES 53a-53d Streamwise Turbulence Intensity, \hat{u}^2/\hat{U}_e^2	
Profiles at $X = 3.59$ m, $k = 1.03$ Flow with "Roof Damper"	118
FIGURES 54a-54b Normal-to-Wall Turbulence Intensity, \hat{v}^2/\hat{U}_e^2 ,	
Profiles at $X = 4.27$ m, $k = 0.61$ Flow	122
FIGURES 55a-55b Normal-to-Wall Turbulence Intensity, \hat{v}^2/\hat{U}_e^2 ,	
Profiles at $X = 4.27$ m, $k = 1.33$ Flow	124
FIGURES 56a-56d Normal-to-Wall Turbulence Intensity, \hat{v}^2/\hat{U}_e^2 ,	
Profiles at $X = 3.59$ m, $k = 1.03$ Flow with "Roof Damper"	126
FIGURE 57 Normalized Backflow Velocity at $X = 3.59$ m, $k = 1.03$ Flow with "Roof Damper"	130
FIGURE 58 Variation of Phase Angle of First Harmonics at $X = 4.27$ m, $k = 1.33$ Flow	131
FIGURE 59 Variation of Phase Angle of First Harmonics at $X = 2.95$ m, $k = 0.61$ Flow	132
FIGURE 60 Variation of Phase Angle of First Harmonics at $X = 2.95$ m, $k = 1.33$ Flow	132
FIGURES 61a-61c $ \hat{U}_N /\hat{U}_e$ vs. $\hat{\gamma}_{pu\ min}$, $k = 0.61$ Flow	133
FIGURES 62a-62c $ \hat{U}_N /\hat{U}_e$ vs. $\hat{\gamma}_{pu\ min}$, $k = 1.33$ Flow	134
FIGURES 63a-63b $ \hat{U}_N /\hat{U}_e$ vs. $\hat{\gamma}_{pu\ min}$, $k = 1.03$ Flow with	

	"Roof Damper"	136
FIGURES 64a-64c	$-\hat{u}\hat{v}_{\max} / \hat{U}_e^2$ vs. $\frac{1}{H}$, $k = 1.03$ Flow with "Roof Damper"	137
FIGURE 65	$\frac{ \hat{U}_N }{\hat{U}_e}$ vs. $\frac{-\hat{u}\hat{v}}{\sqrt{\hat{u}^2} \sqrt{\hat{v}^2}}$ at $X = 4.27$ m, $k = 1.33$ Flow ...	139
FIGURES 66a-66c	$-\hat{u}\hat{v}_{\max} / \sqrt{\hat{u}^2} \sqrt{\hat{v}^2}$ vs. $\frac{1}{H}$, $k = 1.03$ Flow with "Roof Damper"	140
FIGURES 67a-67c	$ \hat{U}_N / \hat{U}_e$ vs. $\frac{1}{H}$	142

NOMENCLATURE

C	length of converging-diverging portion of test section, 4.9 m
C_p	pressure coefficient, $2(P-P_i)/\rho \bar{U}_{ei}^2$
$\hat{C}_f/2$	$= \hat{\tau}_w/\rho \bar{U}_e^2$, local skin-friction coefficient
f	frequency, Hz
F	$= \bar{f} + \tilde{f} + f$, instantaneous signal
\hat{F}	$= \bar{f} + \tilde{f}$, ensemble-average of F for a specific phase
\hat{H}	shape factor $= \hat{\delta^*}/\hat{\theta}$
k	thermal conductivity
\hat{k}	$= \omega C/2\bar{U}_{ie}$, reduced frequency
\hat{N}	distance from the wall to the minimum velocity in the ensemble-averaged velocity profile backflow
P	pressure
\hat{Re}_θ	$= \hat{U}_e \hat{\theta}/v$, momentum thickness Reynolds number
T	period of imposed oscillation
t	time
\bar{U}	time-averaged velocity
\hat{U}	Periodic velocity
\hat{U}, \hat{v}	ensemble-averaged velocities in x, y directions, respectively
u, v	turbulent fluctuations in x, y directions, respectively
$\hat{-uv}$	ensemble-averaged Reynolds shear stress
$\hat{u^2}, \hat{v^2}$	ensemble-averaged mean square values of u and v
\hat{U}_τ	$= (\hat{\tau}_w/\rho)^{1/2}$, shear velocity
\hat{U}^+	$= \hat{U}/\hat{U}_\tau$
\hat{U}_N	maximum backflow velocity
\bar{U}_{ei}	mean test section entrance velocity

\tilde{U}_{ne} amplitude of n^{th} harmonic
 x, y, z streamwise, normal, and spanwise coordinates
 y^+ a Reynolds number = yU_{τ}/ν

Greek Symbols

$\hat{\delta}$ y where $\hat{J} = 0.99 \hat{U}_e$
 $\hat{\delta}^*$ displacement thickness
 κ von Karman constant, 0.41
 $\hat{\theta}$ momentum thickness
 ϕ_{ne} phase angle of n^{th} harmonic of velocity
 ν kinematic viscosity
 $\hat{\gamma}_{pu}$ ensemble-averaged forward flow fraction at 1 mm from the wall
 $\hat{\gamma}_{pu_{\min}}$ $\hat{\gamma}_{pu}$ at a distance \hat{N} from the wall
 γ_{ie} phase angle of first harmonic pressure gradient
 ρ density
 $\hat{\tau}_w$ shearing stress
 ω $2\pi f$

Subscripts

e freestream or condition outside shear flow
n harmonic number, e.g., 1, 2, etc.
w denotes wall value
min,max minimum and maximum value

1. INTRODUCTION

Unsteady turbulent boundary layers are of considerable interest because of unsteady aerodynamic phenomena associated with blades in compressors and turbines, helicopter rotors in translating motion, high pressure recovery diffusers and aeroelastic flutter and support of aerofoils. They are particularly important during high loading conditions when separation may be present during a portion of the oscillation cycle. Under such conditions significant interaction between the thick turbulent shear layer and the inviscid flow occurs. Thus experimental information on the structure of separating unsteady turbulent shear layers is necessary for the proper understanding and calculation of the physical behavior of these practical flows.

Simpson, Shivaprasad and Chew (1983a) and Simpson and Shivaprasad (1983b) have reported the measurements showing the effect of frequency on moderate amplitude (amplitude to mean velocity ratio of 0.33) sinusoidal unsteadiness of the free-stream velocity on a separating boundary layer at reduced frequencies $k = \omega C / 2\bar{U}_{ei}$ of 0.61 and 0.90, where \bar{U}_{ei} is the test section entrance time-averaged free-stream velocity, $C = 4.9$ m, length of the converging-diverging test section shown in Figure 1, and $\omega = 2\pi f$, where f is 0.596 Hz, the frequency of flow oscillation.

In this report measurements are presented for two large amplitude (amplitude to mean velocity ratio of 0.8) gust flows produced by an in-stream rotating blade damper at $k = 0.61$ and 1.33 and an oscillating flow with $k = 1.03$ produced with a test section "roof damper". Detailed ensemble-averaged velocity and turbulence measurements were made using hot-wire and laser anemometers. While the primary function of this report is to present and document these data, some discussion of the results and a number

of data plots are presented. The reduced data are available on computer diskettes.

Agarwal and Simpson (1986, 1987a,b) have reported some results for the two large amplitude flows. These large amplitude flows show some unique features not observed in moderate amplitude flows, viz., during strongly decelerating and minimum free-stream velocity phases, backflow occurs in the diffuser section and even near the wall in the converging section. This appears to be due to the strong oscillating pressure gradient that opposes the slow-near-wall flow to produce backflow. In the absence of flow reversal, as in the moderate amplitude flows studied earlier, the flow is quasi-steady. It is clear from earlier results of Simpson *et al.* (1983) and those for these flows that substantial hysteresis of the turbulence structure occurs for unsteady separating flows and the oscillation waveform and amplitude strongly affect the detached flow behavior. New information on Reynolds' shear stress and phase lag of the turbulence structure with respect to the ensemble-averaged velocity profile structure has been obtained and is discussed briefly here. More detailed discussions will be contained in journal publications (Agarwal and Simpson, 1988a,b).

2. EXPERIMENTAL EQUIPMENT

2.1 Basic Wind-Tunnel

Figure 1 is a side view schematic of the 8 m long, 0.91 m wide test section of the wind tunnel. The test wall is constructed from 18 mm thick fin-form plywood, reinforced every 28 cm with 7.6 x 3.8 x 0.6 cm cross-section steel channel. This reinforcement was necessary since Acharya and Reynolds (1975) found that test wall amplitudes as small as 0.025 mm produced up to 10% error in \tilde{U} measurements near the wall. However, some

test-wall oscillation was still present, which was removed by supporting the test wall directly under the point of measurements, on columns attached to concrete floor. The side walls of the wind tunnel are made of float glass to prevent laser signal dispersion, while the upper wall is made of plexiglass.

The mainstream flow of the blown, open-circuit wind tunnel is introduced into the test section after passing through a filter, blower, a fixed-setting damper, the in-stream rotating-blade damper discussed in section 2.2 below, a section of honeycomb to remove the mean swirl of the flow, seven screens to remove much of the turbulence intensity, and finally through a two-dimensional 4:1 contraction-ratio nozzle to further reduce the longitudinal turbulence intensity while accelerating the flow to the test speed (see Figure 2).

The inviscid core flow was uniform within 0.05% in the spanwise direction and within 1% in the vertical direction. The test wall boundary layer was tripped by the blunt leading edge of the plywood floor, the height of the step from the wind-tunnel contraction to the test wall being 0.63 cm.

To obtain additional information on how oscillating pressure gradient affects the detached flow structure an unsteady flow generated with a damper in the roof of the test section and with $k = 1.03$ was also studied.

In this flow case the first 8 foot section remained unchanged from the arrangement used for all other flows. The roof of the second or diverging section was made from a fine screen for producing an easily-controlled pressure gradient. A set of 12 rotating blade dampers mounted above this section (called "roof damper") controlled the phase and amplitude of the part of the main flow diverted through the roof. A perforated plate at the test section exit, as used by Saripalli and Simpson (1980), was used to

increase the test section back pressure. A wooden piece 0.38 m long was placed over the roof to delay detachment. This arrangement is schematically shown in Figure 3. This flow will be referred to as $k = 1.03$ flow with "roof damper". For this flow the in-stream rotating damper, used for the large amplitude flows was kept fully open and stationary.

2.2 Programmable-Rotating-Blade Damper

Investigators of experimentally-produced unsteady flows normally have little control over the waveform of the flow unsteadiness. Although the waveform may consist principally of a given frequency, substantial contributions normally come from higher harmonics. The in-stream rotating-blade-damper system used by Simpson, Shivaprasad and Chew (1983) and Simpson and Shivaprasad (1983) and described in detail by Simpson, Sallas and Nasburg (1978) was also used here for the two large amplitude ($k = 0.61$ and 1.33) gust flows. In this system, the angular velocity of the rotating blades in the in-stream damper in the flow downstream of the blower is varied during a cycle so as to produce the desired waveform shape, amplitude and frequency of the flow entering the test section. In the current experiments, the 0.596 Hz and 0.954 Hz flow oscillations had a velocity amplitude of about ~ 0.8 of the mean velocity.

The 0.954 Hz flow oscillation produced with the "roof damper" had a velocity amplitude of ~ 0.12 of the mean velocity. In this case, the in-stream damper in the flow downstream of the blower was not used.

The electronics were the same in all experiments. All events during an oscillation cycle were synchronized with respect to a "reference" square wave voltage signal at the oscillation frequency generated by the quartz clock in the control electronics. A 'clock' square-wave voltage signal with

a frequency 96 times the reference signal is also generated to aid data acquisition. Data were acquired at the beginning of each of 96 bins of a cycle. Reference signal was also recorded to ensure the phase repeatability of the acquired data.

The variation in the period of each flow cycle and the 'jitter' follows a Gaussian distribution and Simpson et al. (1983) estimated that jitter has no affect on ensemble-averaged velocity values and only an effect on low turbulence level fluctuation measurements.

2.3 Boundary Layer Control System

The active boundary-layer control system, which is described in some detail by Saripalli and Simpson (1980), was installed on the non-test walls of the test section to inhibit undesirable flow three-dimensionality and to prevent separation. Because the static pressure in the test section is time varying in these unsteady experiments, no passive boundary layer control can be used that depends on a steady test section pressure higher than the pressure outside the tunnel. Highly two-dimensional wall jets of high-velocity air were introduced at the beginning of each of the three sections of the tunnel. At the later two streamwise locations the incoming boundary layer was partially removed by a highly two-dimensional suction system.

To examine the two-dimensionality of the mean boundary layer flow, smoke was introduced in the tunnel and a sheet of laser light produced by a cylindrical lens was used to illuminate the smoke. Upstream of separation, negligible spanwise diffusion of the smoke was observed, indicating no gross flow three-dimensionality. Wall jets and suction boundary-layer controls were adjusted to produce a nearly two-dimensional flow pattern for all the three flows.

2.4 Hot-Wire Anemometer

Miller (1976) type integrated circuit hot-wire anemometers and linearizers, as modified by Simpson, Heizer and Nasburg (1979) were used for the present experiments. The frequency response was flat up to 7.5 kHz for an overheat ratio of 0.7. This moderately high overheat ratio was used for two reasons. First as shown by Wood (1975) the range of flat frequency response is improved with a higher overheat ratio. Secondly to minimize the affect of air-temperature oscillation on the hot wire behavior. A standard TSI model 1243-T.2 cross-wire probe was used for measurements. The closest to the wall that this probe could safely make measurements was about 0.035 inch.

The traversing mechanism used for the boundary layer velocity measurements was mounted on the supporting frame for the upper wall except for the $k = 1.03$ flow with the "roof damper". In that case the hot wire support was mounted on the bottom wall and the hot-wire stem was fed through a hole in the test wall for measurements beyond 2.25 m. A cathetometer was used to accurately locate the probe sensor from the wall with an uncertainty of about ± 0.002 inches. The detailed streamwise free-stream velocity distributions were obtained using a model TSI 1218-T1.5 model probe mounted on a mobile cart that was easily positioned along the flow. Hot-wire calibrations were made using a TSI model 1125 calibrator. A standard TSI model 1015C correlator was used to obtain difference of signals from two wires of the cross-wire probe.

2.5 Laser Anemometer

The laser anemometer (LDA) used in these experiments is described in some detail by Simpson and Chew (1979). It is a two-velocity-component

(U,V) directionally sensitive fringe-type system that has been by Simpson et al. (1983) and Simpson and Shivaprasad (1983). The unshifted and 21.505 MHz Bragg-cell shifted beams lie in a horizontal plane and measure the streamwise velocity with vertical fringes. The unshifted and -15.158 MHz Bragg cell shifted beams lie in a vertical plane and measure $(-V \cos 4.4^\circ + W \sin 4.4^\circ)$ with almost horizontal fringes. The 21.505 MHz and -15.158 MHz beams form a third fringe pattern that measures $(U - V \cos 4.4^\circ + W \sin 4.4^\circ)$ around 36.663 MHz. Since

$$\hat{u}^2 \text{ and } (\hat{-v} \cos 4.4^\circ + \hat{w} \sin 4.4^\circ)^2$$

were measured independently and uw was presumed very small, the Reynolds shearing stress $\hat{-uv}$ resulted from this measurement. To increase the signal-to-noise ratio during \hat{U} and \hat{V} measurements, vertical and horizontal beams were switched off, respectively, and the central beam was blocked during $(U - V \cos 4.4^\circ + W \sin 4.4^\circ)/\sqrt{2}$ measurements. Signal processing was by fast-sweep-rate sampling spectrum analysis, as described by Simpson and Barr (1975).

Difficulties with seeding a highly turbulent flow are well known since such flows are characterized by intense mixing. This problem is even more aggravated with a high amplitude unsteady flow; to have the required smoke concentration at each phase the volumetric flow rate needs to vary with the velocity. The smoke is generated by six adjustable Laskin nozzles, each of which blows compressed air through 4 orifices 1 mm in diameter into dioctal phthalate (DOP). The DOP is atomized by the shearing action of the compressed air jets and produces a mean particle diameter of about 1 μm . Here 0.057 cubic meters per minute of smoke at a concentration of about 4.8×10^{-3} kg per cubic meter of blown air was used. The smoke was distributed along the tunnel width just upstream of the test section by 33 evenly spaced

holes in a cylindrical manifold, which is supplied with the smoke into both its ends. This constant volumetric flow rate resulted in a low smoke concentration and consequently, low data rate during the accelerating velocity phases of the cycle and at higher velocity phases away from the wall, where velocities are higher.

A special solenoid-controlled butterfly valve which provides a variation in the volumetric flow rate was designed and connected between the smoke supply and one end of the smoke manifold. A signal from a pressure transducer mounted flush with the tunnel wall in the upstream wind tunnel honeycomb section was used to activate the solenoid. An electronic circuit provided a time delay between the transducer signal and activation of the solenoid to account for the time that the flow takes to travel from the honeycomb to the point of measurement. The valve was open during accelerating phases of the cycle and closed during the decelerating phases. Trials for various combinations of time delays, the time for which the valve was open, and the smoke flowrate from the other end of the manifold were not very successful in producing a more uniform data rate during all phases of the cycle. However, the data rate was improved by recirculating the used smoke in the wind-tunnel room in addition to that obtained from the smoke system.

The minimum data rate required is 59S^{-1} and 95S^{-1} for $f = 0.596$ and 0.954 Hz flows respectively. But since new signals are not spaced equally in time, a higher data rate is necessary. With a good SNR (above 15-20 dB) a data rate of 400 new signals per second for most of the oscillation cycles was obtained.

2.6 Data Reduction

The velocity at any instant can be written as

$$U(t) = \bar{U} + \tilde{U} + u = \hat{U} + u$$

where \bar{U} is the time-averaged velocity \tilde{U} is the periodic velocity contribution and u is the fluctuation contribution.

\bar{U} is simple time averaged of the velocity value, \hat{U} for each phase angle is obtained by ensemble-averaging the velocity measurements for that phase over many cycles. Ensemble-averaged mean square turbulence quantities were obtained by subtracting the smoothed ensembled-averaged velocity for a cycle from the raw data and averaging the square over many cycles. Mean and turbulence quantities were averaged over four adjacent bins of the cycle to produce 15° averages for each of 24 bins.

Results were obtained by averaging over 200 oscillation cycles. However, for laser anemometer measurements at some phases of the oscillation cycle number of data were less than 200, as data carried over from the previous bins were discarded during data processing. Furthermore, at each phase of the cycle data points falling beyond three standard deviation were discarded. This amounted to no more than 1-2% rejection of data.

Close to the wall and up to distances where intermittent backflow exists at any phase of the oscillation cycle, laser anemometer measurements were made. Cross-wire anemometer measurements were also made nearly at the same axial location. To increase the range of validity of X-wire data, in the detached flow region, the X-wire probe was inclined 10° to the test wall, i.e., mounted parallel to the top wall for $k = 0.61$ and 1.33 flows. In data reduction, mean and turbulence quantities were converted back into the laboratory coordinate system.

Due to the fact that the laser measurements beyond 240 mm from wall were not possible (restricted by movement of the table on which laser and optics were mounted) composite profiles of mean velocity and turbulence quantities were obtained by merging the data files obtained by these two methods. In addition to providing data beyond 240 mm from the test wall, cross-wire measurements also gave some region of overlap with LDA data. Only valid X-wire anemometer data were retained and the following criteria were used to check the validity:

(a) A Gaussian velocity probability distribution is approximately valid, so that there should be no flow reversal (Simpson, 1976) and the data are valid if

$$\sqrt{\frac{u^2}{\bar{u}}} < 0.3 \quad (1)$$

(b) The magnitude of the flow incidence angle to the cross-wire bisector is less than or equal to 30° then the data are considered valid, i.e.,

$$\theta = \tan^{-1} \left| \frac{\hat{v}}{\hat{u}} \right| \leq 30^\circ \quad (2)$$

By the above criteria the cross-wire data cease to be valid as the backflow region is approached. Valid data show good agreement with laser measurements at locations where both measurements are available.

Estimated uncertainties for the hot wire are $\Delta \hat{u} = \pm 3.2\%$, $\Delta \hat{v}^2 = \pm 10\%$, $\Delta(-\hat{u}\hat{v}) = \pm 20\%$ and for the laser anemometer are $\Delta \hat{u}$ and $\Delta \hat{v} = \pm 0.25$ m/s, $\Delta \hat{u}^2$ and $\Delta \hat{v}^2 = \pm 4\%$ of the maximum profile value, $\Delta(-\hat{u}\hat{v}) = \pm 20\%$ and $\Delta \hat{Y}_{pu} = \pm 0.02$ for all phases. For the phases where the total number of data samples was much less than 200 (after discarding the sample carried over from the previous bins) the uncertainties were higher and the LDA data were discarded.

3. DESCRIPTION OF TEST FLOWS

The ensembled-averaged free-stream velocity \bar{U}_e outside the boundary layer can be expressed in terms of its Fourier components \tilde{U}_{ne} as

$$\hat{\bar{U}}_e = \bar{U}_e \left\{ 1 + \sum_{n=1}^{\infty} \left[\frac{\tilde{U}_{ne}}{\bar{U}_e} \cos(\omega nt - \phi_{ne}) \right] \right\} \quad (3)$$

Figures 4 and 5 show the mean free-stream velocity and amplitude of higher harmonics for all the three flows. Upstream of 2.8 m the first

harmonic ratio $\frac{\bar{U}_{1e}}{\bar{U}_e}$ is ~ 0.8 for $k = 0.61$ and 1.33 flows and about 0.12 for

$k = 1.03$ flow with "roof damper". Second harmonic amplitude to mean ratios are 8-10%, 15-20% and 6-7% whereas third harmonic amplitude to mean ratios are 4-6%, 3-7% and 3-4% of the mean velocity, respectively.

Using these streamwise distributions the free-stream streamwise pressure gradient can be calculated from the unsteady Bernoulli equation and the mean and first harmonics and is given by

$$\frac{1}{\rho} \frac{d\bar{P}}{dx} = - [\bar{U}_e \bar{U}'_e + \frac{1}{2} \bar{U}_{1e} \bar{U}'_{1e}] + [(\bar{U}_e \bar{U}'_{1e} + \bar{U}_{1e} \bar{U}'_e)^2 + \bar{U}_{1e}^2 (\bar{U}_e \phi'_{1e} - \omega)^2]^{1/2} \cos(\omega t - \phi_{1e} - 180^\circ - \gamma_{1e}),$$

where

$$\gamma_{1e} = \arctan \frac{\bar{U}_{1e} (\bar{U}_e \phi'_{1e} - \omega)}{\bar{U}_e \bar{U}'_{1e} + \bar{U}_{1e} \bar{U}'_e}. \quad (4)$$

Here prime denotes streamwise derivatives. These derivatives are evaluated at a given streamwise location by differentiating the least square curve fit of a quadratic model of the five data points nearest to that location.

Figures 6a-6c show the non-dimensional mean, maximum and minimum pressure gradients $\frac{dC_p}{dx}$ along the centerline of the test wall. Here $C_p = 2(P - P_i)/\rho \bar{U}_{ei}^2$ where i denotes the nominal mean free-stream entrance

condition. Unlike the moderate amplitude flows of Simpson et al. (1983a,b) in the diverging section a small favorable pressure gradient exists during the high velocity phases for all the three flows.

Figures 7a-7c show the phase angle of the first harmonics of the free-stream velocity ϕ_{1e} and the pressure gradient $\gamma_{1e} + \phi_{1e} + 180$ and show that the first harmonic pressure gradient strongly lags the local free-stream velocity in the converging section of the tunnel upstream of 2 m. The lag is considerably lower in the diverging section. After detachment the oscillating pressure gradient only slightly lags (or leads) the velocity oscillation with the onset of pressure gradient relaxation, as also observed by Simpson et al. (1983a,b) in moderate amplitude unsteady flows.

Free-stream velocity distribution along the tunnel length (Figures 8-10) show a disturbance travelling downstream. The changes in free stream velocities are confirmed by X-wire and normal wire measurements. Although the effect with high frequency flows ($k = 1.33$ and $k = 1.03$ with "roof damper") is quite pronounced, a weaker affect is evident with $k = 0.61$ flow. This disturbance has a phase shift of about $\pi/3$ for $X = 0.61$ m to $X = 4.27$ m for $k = 1.33$ flow. For $k = 1.03$ flow with "roof damper", this effect is seen only beyond 3 m with a phase shift of about $\pi/4$ from $X = 3.30$ m to $X = 4.37$ m. This effect was not observed in moderate amplitude flows of Simpson et al.

Study of the velocity and pressure gradient oscillations shows that upstream of the throat where the maximum velocity increases as the tunnel area decreases there are some phases where an adverse pressure gradient exists as shown in Figures 11-13 for all the three flows. In the diverging section of the tunnel, where large backflow exists, an adverse pressure gradient is present for most of the phases of the cycle and higher harmonics

of the pressure gradient are produced that subject the boundary layer to several pressure gradient oscillations per cycle of the velocity. For $k = 1.33$ flow, higher harmonics of the pressure gradient are produced upstream of detachment also.

4. EXPERIMENTAL RESULTS

Ensemble-averaged velocity profiles were obtained using cross-wire and laser anemometers. In regions where both the laser and cross-wire anemometer produce valid data, the results agreed within the experimental uncertainties.

Ensemble-averaged velocity data for various phases at $X = 0.53$ m and 1.45 m for large amplitude flows and at $X = 1.63$ m for $k = 1.03$ flow with "roof damper" are shown in Figures 14 to 16. For the $k = 1.03$ flow with "roof damper" at all the phases and at the high free-stream velocity phases, i.e., $45^\circ \leq \omega_t \leq 315^\circ$, of the $k = 0.61$ and 1.33 flow the shape of the velocity profiles are essentially the same as observed by Simpson et al. (1983a,b) for the steady and moderate amplitude flow and are similar to that for low Reynolds number attached turbulent boundary layers. A semi-logarithmic region is clearly evident.

$\overline{\hat{u}^2}/U_e$ and $\overline{\hat{v}^2}/U_e$ collapse on top of another for these high velocity and accelerating phases, as shown in Figures 17-18. Figures 19a and 19b give law-of-the-wall plots for these phases. The mean wall shear stress values were obtained by adopting Coles and Hirst (1969) method which requires that for a given \hat{U}_τ , $\hat{U}^+ = 16.23$ at $y^+ = 100$. The logarithmic law-of-the-wall equation

$$\hat{U}^+ = \frac{1}{\kappa} \ln y^+ + 5.0 \quad (5)$$

where κ is 0.41, is also shown in Figures 19a-19b by a solid line. Skin friction coefficient values obtained by this method are presented in tables 1-3 (Appendix A). As can be expected for these flows with adverse pressure gradients, the skin friction decreases in the streamwise direction until the reattachment process begins. The skin friction coefficient was also calculated using the Ludwieg-Tillmann (1950) relation (which is valid for the phases with the attached flow),

$$\hat{C}_f = 0.246 \times 10^{-0.678\hat{H}} \times \hat{Re}_{\theta}^{-0.268} \quad (6)$$

The skin friction coefficients obtained by these two methods show good agreement, within the experimental uncertainties, as shown in Figure 20. Variation of $\hat{\delta}^*$, $\hat{\theta}$, \hat{H} and \hat{Re}_{θ} for all the three flows before detachment are shown in Figures 21a-21d, 22a-22d and 23a.

At low velocity phases for the $k = 0.61$ and 1.33 flows close to the wall intermittent backflow exists upstream of the throat as shown in Figures 24-25 with the fraction of time that there is downstream flow $\hat{\gamma}_{pu}$ less than unity. These values were obtained from direct LDA measurements and also from the LDA, \hat{U} and \hat{u}^2 data using the Gaussian probability distribution (Simpson 1976)

$$\hat{\gamma}_{pu} = \frac{1}{2} [1 + \text{erf}\left(\frac{\hat{U}}{(2\hat{u}^2)^{1/2}}\right)] . \quad (7)$$

In two moderate amplitude flows studied by Simpson *et al.* (1983a,b) this intermittent backflow upstream of detachment was not observed. Ensemble-averaged velocity profiles at these phases, i.e., $315^\circ \leq \omega_t \leq 45^\circ$ (as shown in Figures 14 and 15 for 15° , 30° , 345° and 360°) are quite different. These velocity profiles at the low velocity phases where the flow is accelerating, i.e., $\omega_t \leq 45^\circ$ are very similar to the strongly-accelerated

sink flow studied by Simpson and Wallace (1975). The unsteady flow acceleration parameter

$$\hat{K} = \frac{\nu}{\hat{U}_e^3} \left[\frac{\partial \hat{U}_e}{\partial t} + \hat{U}_e \frac{\partial \hat{U}_e}{\partial x} \right] \quad (8)$$

has large values at these phases as shown in Figures 27-28 (but not for $k = 1.03$ flow as shown in Figure 29).

Simpson and Wallace (1975) observed that for a steady flow with $K > 3.6 \times 10^{-6}$ at low momentum Reynolds numbers, relaminarization of an initially turbulent boundary layer could occur. For the $k = 0.61$ flow, $\hat{K} > 3.6 \times 10^{-6}$ over 20° of the cycle during rapid acceleration from the minimum velocity phases. For the same phases in the $k = 1.33$ flow, \hat{K} is over 10 times greater. In both these flows nearly zero correlation coefficients $-\hat{u}\hat{v}/\hat{u}\hat{v}$ were observed at these phases (Figure 30). These large \hat{K} values are sufficient to produce laminar-like ensemble-averaged profiles during a short portion of the cycle, but are not imposed long enough to produce true relaminarization. Velocity profiles at the locations (Figures 14 and 15) for $\omega t = 345^\circ$ and 360° , when the flow is highly decelerating and similar to typically high adverse pressure gradient flows (Simpson 1981a).

Upstream of detachment the ensemble-averaged velocity profiles exhibit a negligible phase angle variation through the boundary layer for all three flows (Figures 31-33). Simpson *et al.* (1983b) showed that the phase angle variation of the ensemble-averaged oscillation is zero within a semi-logarithmic region. The ensemble-averaged turbulence profiles for the phases without flow reversal are similar to those for the comparable steady flow and \tilde{u}^2 and \tilde{v}^2 are in phase with \tilde{U} . Near detachment, outer region results for the ensemble-averaged velocity profiles at the phases without flow reversal follow the universal velocity defect law proposed by Schofield

(1980). Ensemble-averaged velocity profiles in the detaching and reattaching parts of the flows are presented in Figures 34-43. Velocity profiles for the "detaching" phases are presented as $\frac{\hat{U}}{U_e}$ vs $\frac{y}{\delta}$, whereas for the reattaching phases absolute velocities are presented (this is because of absence of the core for these low velocity phases). For $k = 1.03$ flow with "roof damper" all the velocity profiles (except at $X = 4.12$ m) are presented as $\frac{\hat{U}}{U_e}$ vs $\frac{y}{\delta}$. Also for this flow, as evident from Figures 40-43, velocity profiles almost collapse over one another except at the phases where the velocity profile shows rapid changes because of the travelling wave.

For the $k = 0.61$ and 1.33 flows, backflow velocities are very large and for the $k = 1.33$ flow at some phases are even larger in magnitude than the free-stream velocity. Figures 34, 37 and 40 show distinct semi-logarithmic velocity profiles for the part of the cycle as soon as there is no mean backflow. Figures 44 and 45 give law-of-the-wall plots for these phases for the $k = 0.61$ and 1.33 flows. Values of wall shear stress deduced from the attached flow logarithmic "law of the wall" velocity profiles are in good agreement with obtained using Ludwieg and Tillmann equation as shown in Figures 46 and are also within experimental uncertainty of the measured Reynolds shear stresses in the semi-log region. This reattachment of the flow is apparently due to the increasing rate of strain $\frac{\partial \hat{U}}{\partial y}$, the outer region shear stress for the thinning shear layer, and the convection of the upstream flow. Note that the semi-log region velocities remain almost independent of time for $105^\circ < \omega t < 165^\circ$.

During larger backflows, significant turbulence production occurs near the wall and all the Reynolds-averaged momentum equation terms

$$\hat{\frac{\partial U}{\partial t}} + \hat{U} \hat{\frac{\partial U}{\partial x}} + \hat{V} \hat{\frac{\partial U}{\partial y}} = - \frac{1}{\rho} \hat{\frac{\partial P}{\partial x}} + \hat{\frac{\partial (-uv)}{\partial y}} \quad (9)$$

are important. Figures 47-50 show that decreasing Reynolds shearing stress and correlation coefficients of -0.5 or so are produced near the wall during these larger backflow phases. Typically large correlation coefficients of 0.5 are in the outer region where most of the turbulence energy production and the maximum shearing stress occur. During the reattaching or "washout" of detached flow phases, the backflow velocities decrease and the near wall shearing stresses and correlation coefficients increase toward attached flow values. Figures 51-56 show ensemble-averaged $\hat{\frac{u^2}{U_e^2}}$ and $\hat{\frac{v^2}{U_e^2}}$ profiles at some locations in detached flow.

As suggested by Simpson et al. (1981) the near wall backflow is dominated by viscous affects because the Reynolds shearing stress is relatively unimportant and the mean flow can be considered to be uncoupled for the turbulence. A velocity profile model of the type $\hat{\frac{U}{U_N}} = f(y/N)$ fits the flow structure. For the $k = 0.61$ and 1.33 flows a semi-logarithmic overlap region described by

$$\hat{\frac{U}{|U_N|}} = -0.3 \ln \left| \frac{y}{N} \right| + B \quad (10)$$

seem to exist for $0.02 < y/N < 0.15$, where B is a constant. For the $k = 1.03$ flow with "roof damper" this semi-logarithmic region also exist (as shown in Figure 57) but backflow thicknesses are very large (> 25 cm) and it appears there is some additional length scale which influences the outer part of the backflow. We are continuing to investigate this behavior.

Ensemble-averaged velocities in the backflow lead the free-stream velocity by a large amount. Similar to the moderate amplitude flows, (Simpson et al., 1983), the phase angle of first harmonic does not vary

appreciably with y in the nearest wall region. Far downstream where the ensemble-averaged velocity is always negative, ϕ_1 , and \tilde{U}_1/\tilde{U}_e are nearly independent of y for $y < \hat{N}$. Thus it appears that the ensemble-averaged flow near the wall behaves like a quasi-steady flow when normalized on \tilde{U}_N and \hat{N} .

Figures 31-33 show that the ensemble-averaged velocity in the backflow has a progressively greater phase lead as one proceeds downstream. This phase lead with respect to the local freestream is higher for the $k = 0.61$ flow compared to the $k = 1.33$ flow and is even higher for the $k = 1.03$ flow with "roof damper". Upstream of detachment the Reynolds shearing stresses $-\tilde{u}\tilde{v}$ and the normal stresses \tilde{u}^2 and \tilde{v}^2 are in phase with \tilde{U} . Downstream of detachment \tilde{u}^2 and \tilde{v}^2 are substantially out of phase with $-\tilde{u}\tilde{v}$ and $-\tilde{v}\tilde{u}$ slightly lags \tilde{U}_1 (about 20°) as shown in Figures 58-60. Hysteresis in relationship in mean velocity and turbulence parameter have been observed as in the case of moderate amplitude flows studied by Simpson et al. Figures 61-63 show $|\tilde{U}_N|/\tilde{U}_e$ vs. $\hat{\gamma}_{pu\ min}$ for all the three flows. The hysteresis loops are clockwise (as in moderate amplitude flows) and are progressively greater in the downstream direction (for the larger amplitude flows, loops are not complete because of absence of core at some phases). Data are scattered at lower values of $\hat{\gamma}_{pu}$, because of the large percentage uncertainty when $\hat{\gamma}_{pu}$ is near zero. Hysteresis loops are larger for the $k = 1.33$ flow. In all the plots $|\tilde{U}_N|/\tilde{U}_e$ increases substantially during the minimum $\hat{\gamma}_{pu\ min}$ phases.

In Figures 64 and 66 data are presented for $\frac{-\tilde{u}\tilde{v}}{\tilde{U}_e^2} \max$ vs. $\frac{1}{\hat{H}}$ and $\frac{-\tilde{u}\tilde{v}}{\sqrt{\tilde{u}^2} \sqrt{\tilde{v}^2}} \max$ vs. $\frac{1}{\hat{H}}$ for the $k = 1.03$ flow with "roof damper". Data for large amplitude

flow ($k = 1.33$) are presented on another parameter cross-plot i.e., $\frac{|\hat{U}_N|}{\hat{U}_e}$

vs. $\frac{-uv}{\sqrt{u^2} \sqrt{v^2}}$ in Figure 65. Similar hysteresis loops are observed except for

the $k = 1.03$ flow with "roof damper" where double loops exist. We are continuing to investigate this phenomenon. For the $k = 1.03$ flow with "roof damper" at some phase there appears to be no hysteresis because of a nearly constant value of the shape parameter, \hat{H} .

Figure 67 presents the normalized maximum backflow velocity $|\hat{U}_N|/\hat{U}_e$ vs. $\frac{1}{\hat{H}}$ for all the three flows. The data for large amplitude flows fall between the steady separating flow line (solid line) of Simpson and Shivaprasad (1983),

$$\frac{|\hat{U}_N|}{\hat{U}_e} = 0.807 \left(1 - \frac{1}{\hat{H}}\right) - 0.577 \quad (11)$$

and that given by (dashed-line)

$$\frac{|\hat{U}_N|}{\hat{U}_e} = \frac{4}{3} \left(1 - \frac{1}{\hat{H}}\right) - 1 \quad (12)$$

which was derived (Simpson and Shivaprasad, 1983) from an approximate velocity profile based upon the assumption that ensemble-averaged profiles for phases when $\partial Y_{pu \min}/\partial t \geq 0$ are rounded near the wall and near the free-stream for a given $|\hat{U}_N|/\hat{U}_e$. As in the moderate amplitude flows, $|\hat{U}_N|/\hat{U}_e$ reaches large values with negative values of $\frac{1}{\hat{H}}$. As shown by Simpson and Shivaprasad (1983), for phases of a cycle when $\partial Y_{pu}/\partial t$ is positive different hysteresis loops occurs on these plots, indicating a different velocity profile and turbulence structure from increasingly separated phases.

5. SUMMARY OF RESULTS

It is clear from these measurements and the previous studies of Simpson et al. (1983) and Simpson and Shivaprasad (1983) in moderate amplitude flows, that the oscillation waveform and amplitude strongly influence the detached flow behavior. This is an important result since practical unsteady flows have non-sinusoidal waveforms and significantly large amplitudes. Prior to the current work no detailed velocity and turbulence measurements on large amplitude type flows had been made even though practical unsteady flows in turbomachines have non-sinusoidal waveforms and significantly large amplitudes.

During the phases that the flow is accelerating, intermittent backflow occurs only near the wall in the rapidly diverging portion of the test channel. For large amplitude flows during decelerating and minimum velocity phases, backflow occurs in the diffuser section and near the wall in the converging section as well. This behavior was not observed by Simpson et al. in moderate amplitude flows. This is an interesting result since it could be used as a possible means of increasing near wall mixing of turbulent fluid to enhance heat and mass transfer.

For all the flows studied higher harmonics of the pressure gradient are produced that subject to the boundary layer to many pressure gradient oscillations for cycle of the velocity.

Upstream of detachment the ensemble-averaged velocity profiles exhibit a negligible phase angle variation through the boundary layer and \tilde{u}^2 , \tilde{v}^2 and $-\tilde{u}\tilde{v}$ are in phase with \tilde{U} . The velocity and turbulence in the absence of flow reversal behaves in a manner as the steady flow and the flow is quasi-steady.

Downstream of detachment large amplitude and phase variations develop through the flow and there are non-quasi-steady affects on the ensemble-averaged flow structure. Backflow velocities even larger than the free-stream have been observed. Near the wall in the backflow region, the ensemble-averaged velocity leads the free-stream velocity by a large amount. The turbulence structure progressively lags the ensemble-averaged flow oscillations with $\tilde{u}\tilde{v}$ lagging \tilde{U}_1 in the backflow by about 20° , as in the moderate amplitude flows. The ensemble-averaged backflow near the wall behaves like a quasi-steady flow when normalized on \hat{U}_N and \hat{N} . Study of the ensemble-averaged backflow velocities for the $k = 1.03$ flow with "roof damper" and very large backflow thicknesses suggest that there are some other length scales for the outer part of the backflow region. We are continuing to investigate this behavior.

Low and negative values of Reynolds shearing stress and correlation coefficient during phases with flow reversal have been measured. This indicates that much of the reversed flow turbulence is left over from earlier phases when the turbulence production was large and that the adverse pressure gradients are large enough to produce significant backflow with negative shearing stress. This is a non-quasi-steady effect which the current local field turbulence models can not account for. In the detached and reattaching flow, ensemble-averaged velocity profiles and turbulence structure show the hysteresis that occur in detaching and reattaching flows, which is again a non-quasi-steady behavior.

Additional discussion of these data and their meaning will be contained in Agarwal and Simpson (1988a,b).

6. PERSONNEL

During 1984-1986, Mr. S. Ahn made single hot-wire anemometer measurements for the $k = 0.61$ flow, resulting in his M.S. degree thesis (Ahn, 1986). Dr. Y.-T. Chew, who is senior lecturer at the National University of Singapore, worked on multiple hot-wire anemometer measurement techniques during his July 1984 - February 1985 visit to VPI&SU, resulting in two papers (Chew and Simpson, 1988a,b). Dr. N.K. Agarwal joined this research group in May 1985 after completing his Ph.D. work at the University of Adelaide, Australia. In addition to this report, he is coauthor of several papers on this research: Agarwal and Simpson (1986, 1987a, 1987b, 1988a, 1988b).

7. INTERACTIONS

A number of oral presentations of these research results have been made, in most cases accompanying a written paper. Simpson (1985) and Agarwal and Simpson (1986, 1987a, 1987b) were presented at the respective conferences indicated in the references. Agarwal and Simpson (1987a) was also presented at the 1986 American Physical Society Fluid Dynamics Meeting in Columbus, Ohio.

References

1. Acharya, M. and Reynolds, W.C. 1975, "Measurements and Predictions of a Fully-Developed Turbulent Channel Flow with Imposed Controlled Oscillations," Rept. TF-8, Thermoscience Division, Dept. Mechanical Engineering, Stanford University.
2. Agarwal, N.K. and Simpson, R.L. 1986, "LDV Measurements of Large Amplitude Unsteady Separated Turbulent Boundary Layers," 3rd International Symposium of Applications of Laser Anemometry to Fluid-Mechanics, Lisbon, Portugal, July 7-9; paper 2.4.
3. Agarwal, N.K. and Simpson, R.L. 1987a, "The Structure of Large Amplitude Unsteady Separating Turbulent Boundary Layers," AIAA-87-0191, AIAA 25th Aerospace Sciences Meeting, January 12-15, Reno, Nevada.
4. Agarwal, N.K. and Simpson, R.L. 1987b, "Experimental Measurements of the Structure of a Large Amplitude Unsteady Separating Turbulent Boundary Layers," AFOSR Workshop II on Unsteady Separated Flows, July 28-30, USAFA.
5. Agarwal, N.K. and Simpson, R.L. (1988a), "Separating Turbulent Boundary Layers with Large Amplitude Unsteadiness," in preparation for submission to J. Fluid Mech.
6. Agarwal, N.K. and Simpson, R.L. (1988b), "A Separating Turbulent Boundary Layer with an Unsteady Diverging Freestream," in preparation for submission to AIAA J.
7. Ahn, S. 1986, "Unsteady Features of the Turbulent Boundary Layers," M.S. Thesis, Dept. of Aerospace and Ocean Engineering, Virginia Polytechnic Institute and State University, Blacksburg, Virginia.
8. Chew, Y.-T. and Simpson, R.L. (1988a), "The Non-real-time Explicit Data Analysis Method of Crossed Hot-wire Anemometer Measurements Including Tangential Cooling Velocity Correction," in press, J. Physics E.
9. Chew, Y.-T. and Simpson, R.L. (1988b), "An Explicit Non-real-time Data Reduction Method of Triple Sensors Hot-Wire Anemometer in Three-Dimensional Flow," in press, J. Fluids Engrg., 110, No. 2, June.
10. Coles, D. and Hirst, E.A. 1969, "Analysis of Turbulent Boundary Layers," AFOSR-IFP-Stanford Conference, Stanford University Press, Stanford, California.
11. Ludwieg, H. and Tillmann, W. 1950, "Investigation of the Wall-Shearing Stress in Turbulent Boundary Layers," NACA-TM-1285.
12. McCroskey, W.J. 1977, "Some Current Research in Unsteady Fluid Dynamics," J. of Fluids Engrg., 99, 8-39.
13. Miller, J.A. 1976, "Simple Linearized Hot-Wire Anemometer," J. of Fluids Engrg., 98, 550.
14. Saripalli and Simpson, R.L. 1980, "Investigation of Blown Boundary Layers with an Improved Wall Jet System," NASA-CR-3340.

15. Schofield, W.H. 1980, "Turbulent Boundary Layers in Strong Adverse Pressure Gradient," Australian Defense Sci. and Tech. Org. Aero. Res. Lab. Mech. Engrg. Rep. 157 (AR-002-218).
16. Simpson, R.L. 1976, "Interpreting Laser and Hot-Film Anemometer Signals in a Separating Boundary Layer," AIAA Journal, 1, 14, 124.
17. Simpson, R.L. 1983, "A Model for the Backflow Mean Velocity Profile," AIAA Journal, 21, 1, 142-143.
18. Simpson, R.L. 1985, "Two-Dimensional Turbulent Separated Flow," AGARDograph No. 287, Vol. 1.
19. Simpson, R.L. (1985), "Some Structural Features of Unsteady Separating Turbulent Shear Flows," 5th Symposium on Turbulent Shear Flows, August 7-9, Ithaca, NY (oral presentation and paper).
20. Simpson, R.L. and Barr, P.W. 1975, "Laser Doppler Velocimeter Signal Processing using Sampling Spectrum Analysis," Rev. Sci. Inst., 46, 835-837.
21. Simpson, R.L. and Chew, Y.-T. 1979, "Measurements in Highly Turbulent Flows: Steady and Unsteady Separated Turbulent Boundary Layers," Proceedings of Third International Workshop on Laser Velocimetry, 179-196, Hemisphere.
22. Simpson, R.L., Chew, Y.-T. and Shivaprasad, B.G. 1981, "The Structure of a Separating Turbulent Boundary Layer: Part 1, Mean Flow and Reynolds Stresses," J. of Fluid Mech., 113, 23.
23. Simpson, R.L., Heizer, K.W. and Nasburg, R.E. 1979, "Performance Characteristics of a Simple Linearized Hot-Wire Anemometer," J. of Fluids Engng., 101, 381.
24. Simpson, R.L., Sallas, J.J. and Nasburg, R.E. 1978, "Tailoring the Waveform of a Periodic Flow with a Programmable Damper," J. of Fluids Engng., 100, 287.
25. Simpson, R.L. and Shivaprasad, B.G. 1983, "The Structure of a Separating Turbulent Boundary Layer: Part 5. Frequency Effects on Periodic Unsteady Free Stream Flows," J. of Fluid Mech., 121, 319.
26. Simpson, R.L., Shivaprasad, B.G. and Chew, Y.-T. 1983, "The Structure of a Separating Turbulent Boundary Layer: Part 4. Effects of Periodic Free Stream Unsteadiness," J. of Fluid Mech., 127, 219.
27. Simpson, R.L. and Wallace, D.B. 1975, "Laminariscent Turbulent Boundary Layers: Experiments on Sink Flows," Project SQUID Rept. SMU-1-PU.
28. Wood, N.B. (1975), "A Method for Determination and Control of the Frequency Response of the Constant-Temperature Hot-Wire Anemometer," J. of Fluid Mech., 67, 769.

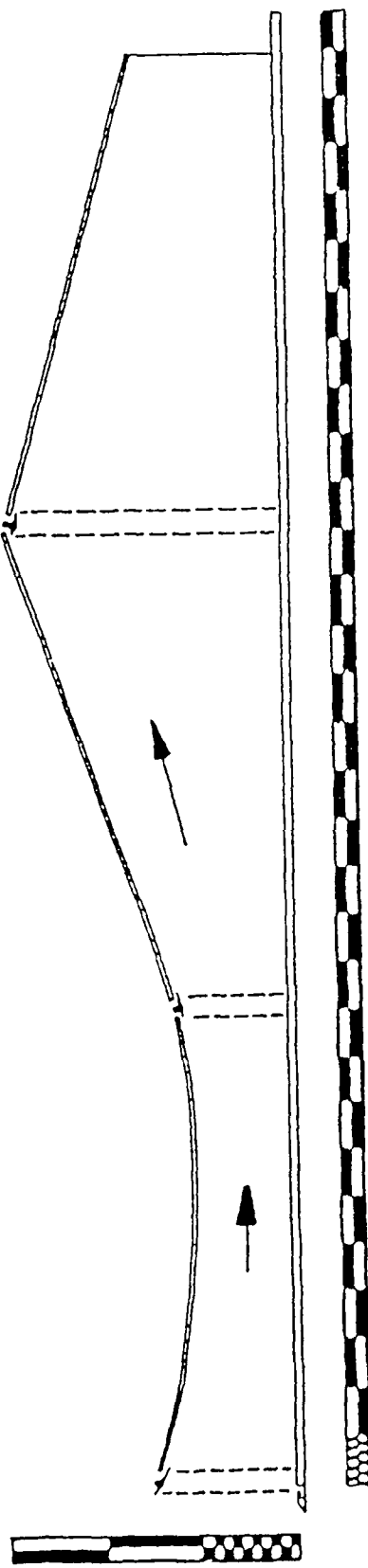


Figure 1. Sideview of the test section. Major dimension on scale is 25 mm. Note baffle plate upstream of blunt leading edge on bottom test wall and side, and upper wall jet boundary layer control.

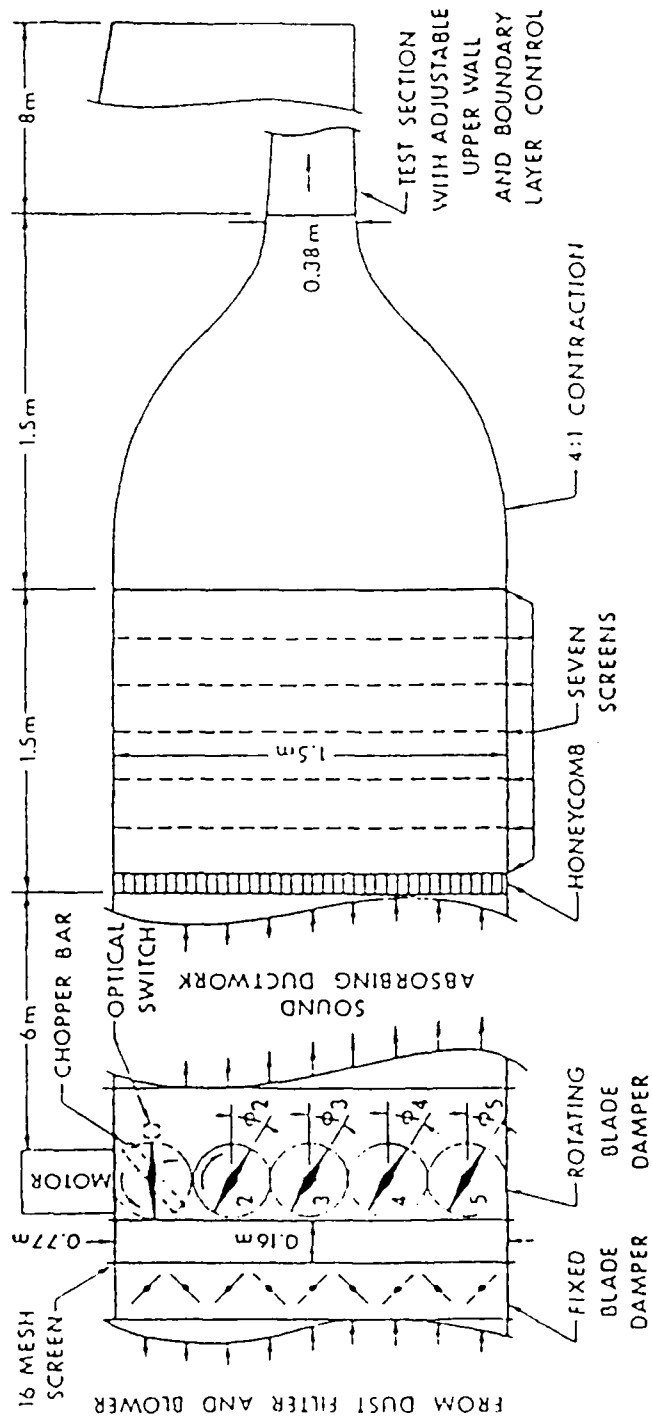


Figure 2. Schematic of the wind tunnel and rotating damper.

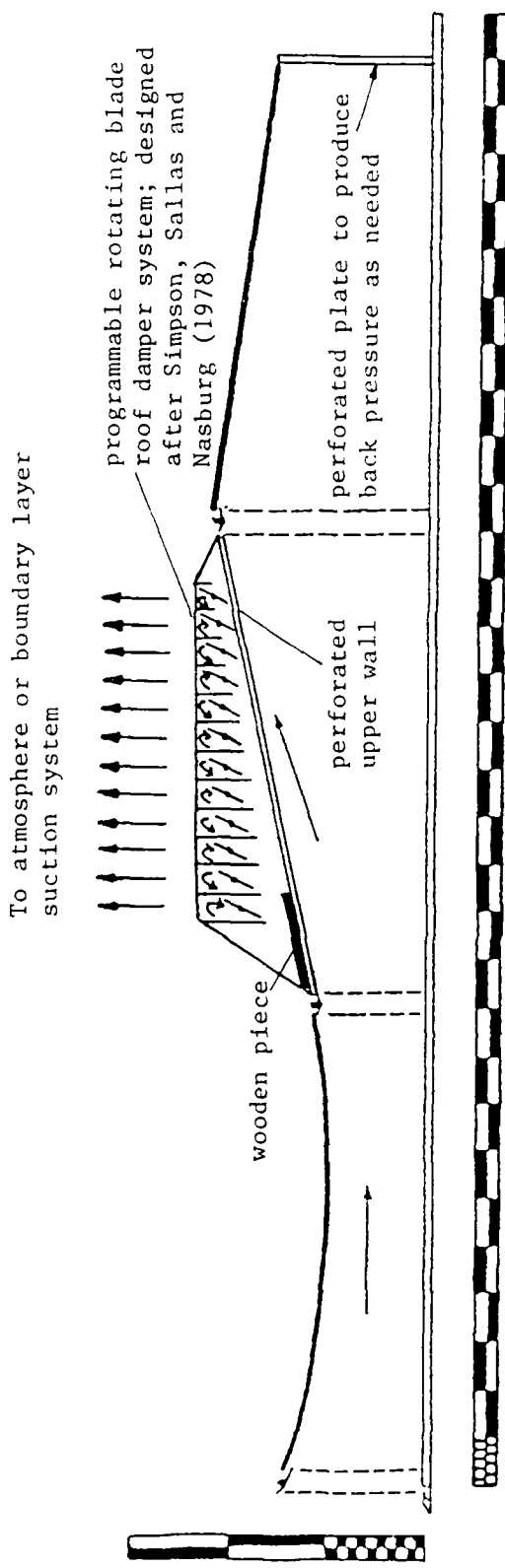


Figure 3. Modification of the wind tunnel for $k = 1.03$ flow with 'roof damper'; Note a wooden piece 0.38 m long at the start of the perforated roof and twelve damper blades.

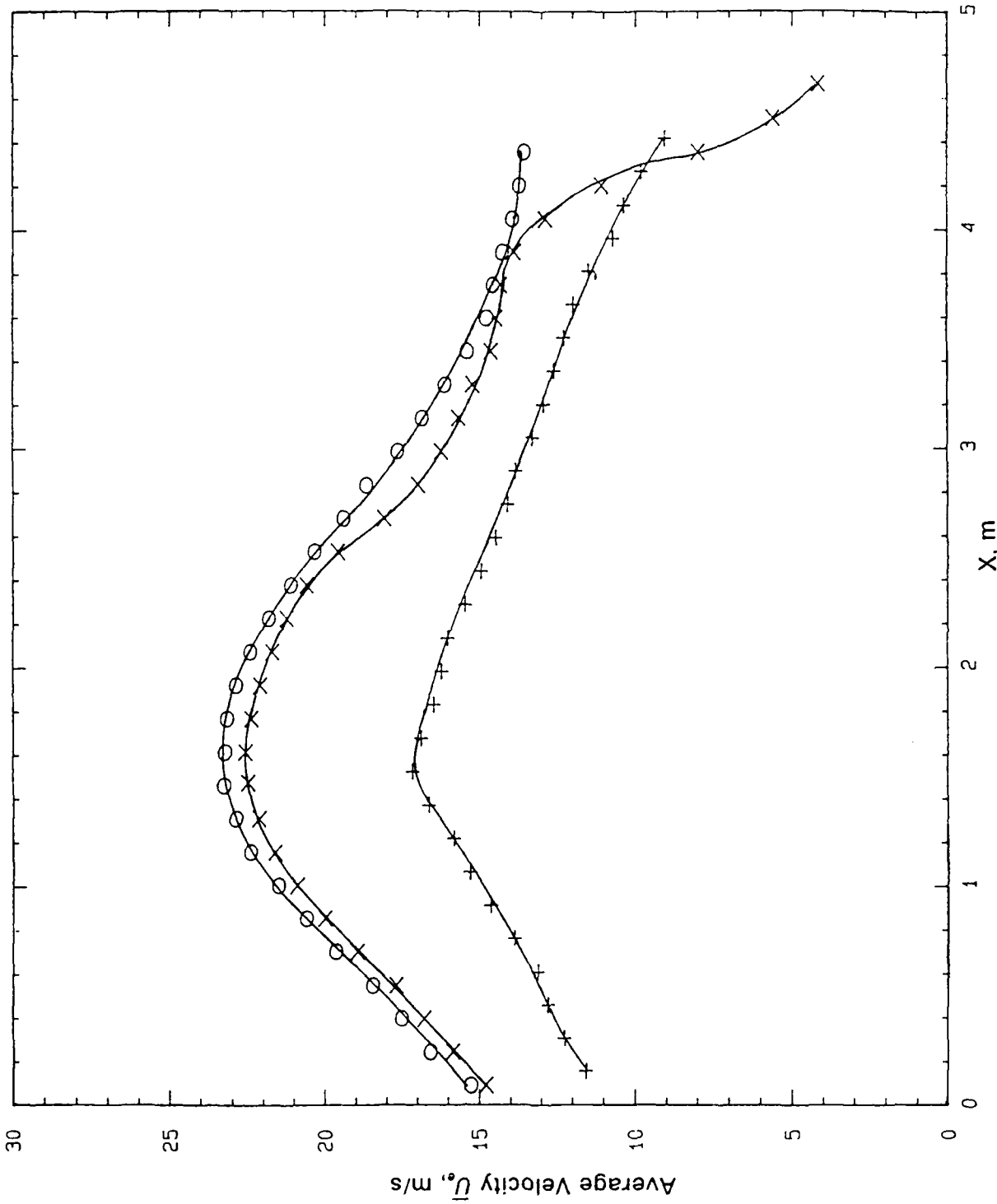


Figure 4. Free-stream mean velocity, \bar{U}_0 . O, $k = 0.61$ flow; +, $k = 1.33$ flow; X, $k = 1.03$ flow with 'roof damper'. Solid lines for visual aid only.

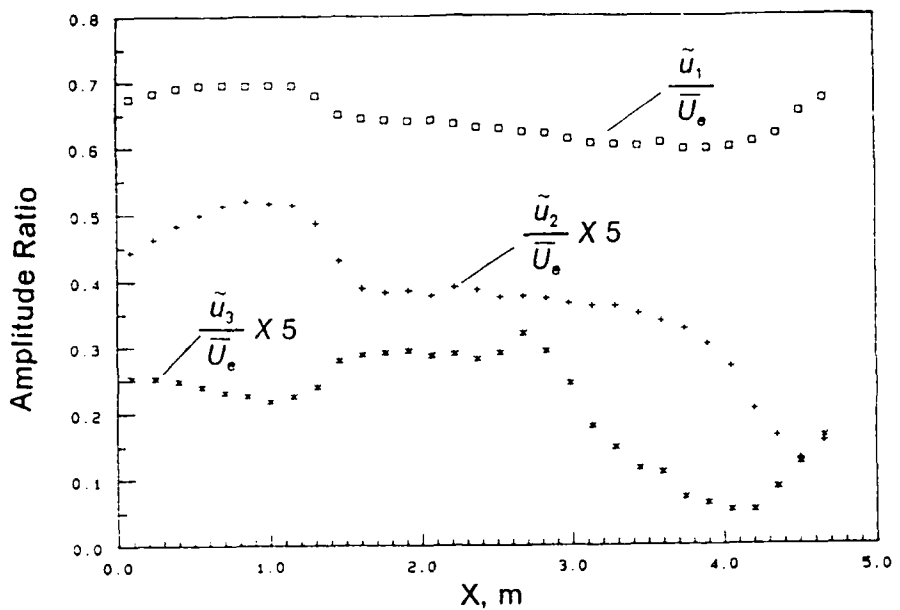


Figure 5a. Ratio of free-stream harmonics amplitude to mean velocity,
 $k=0.61$ flow.

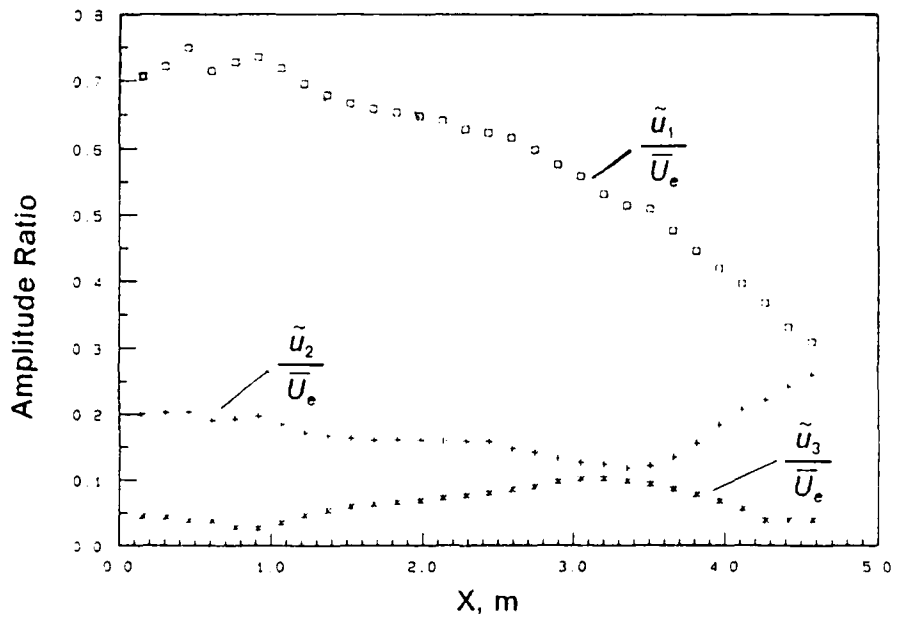


Figure 5b. Ratio of free-stream harmonics amplitude to mean velocity,
 $k=1.33$ flow.

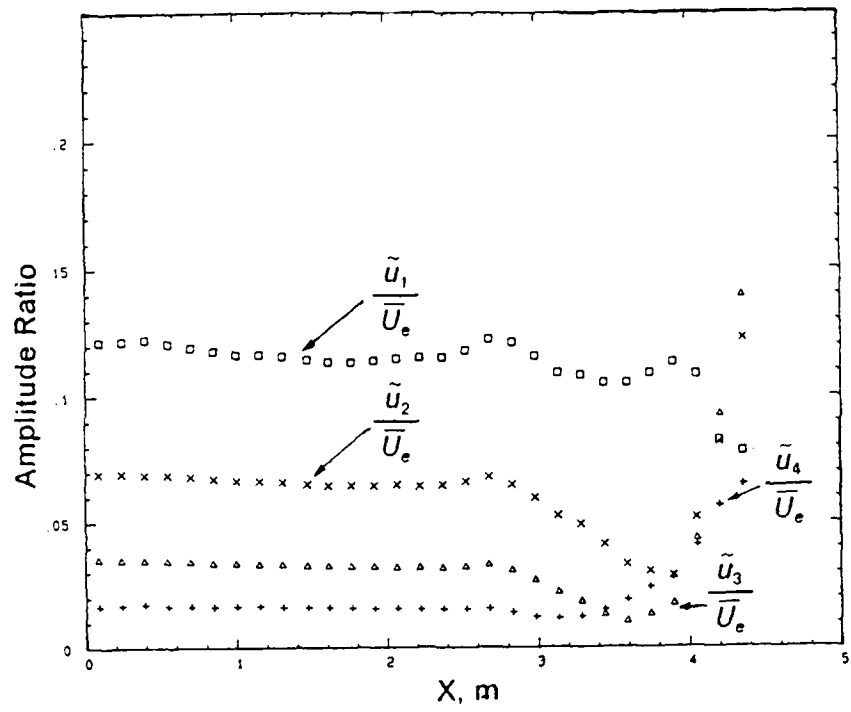


Figure 5c. Ratio of free-stream harmonics amplitude to mean velocity,
 $k = 1.03$ flow with 'roof damper'.

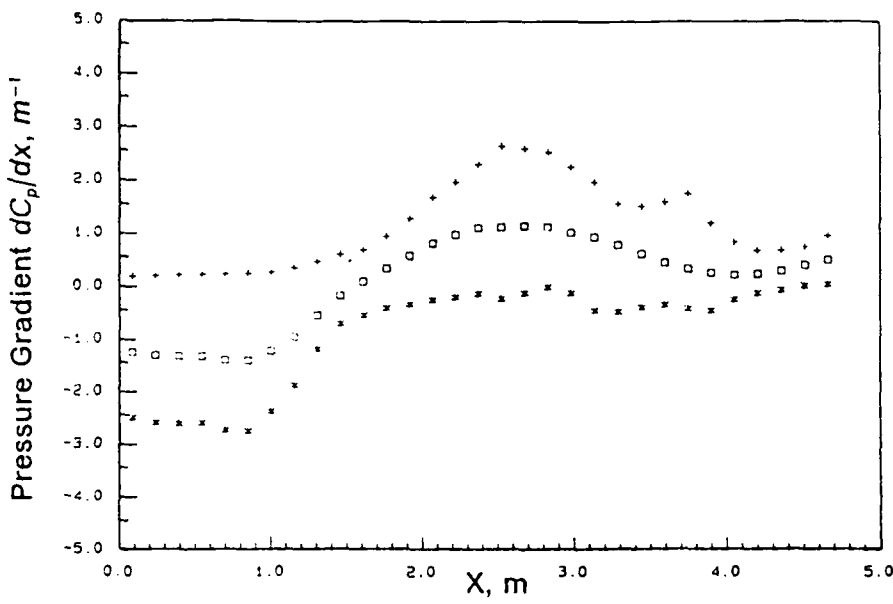


Figure 6a. Mean pressure gradient distribution along the tunnel centerline and limits of the unsteady pressure gradient, $k=0.61$ flow; $C_p = 2(P - P_i)/\rho \bar{U}_{ei}^2$. (+, maximum; \square , mean; *, minimum).

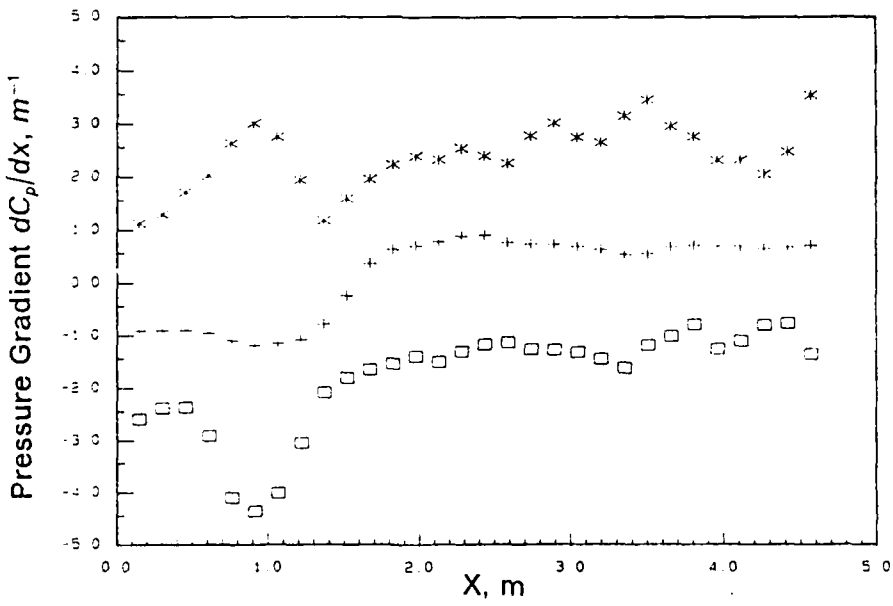


Figure 6b. Mean pressure gradient distribution along the tunnel centerline and limits of the unsteady pressure gradient, $k=1.33$ flow; $C_p = 2(P - P_i)/\rho \bar{U}_{ei}^2$. (*, maximum; +, mean; \square , minimum).

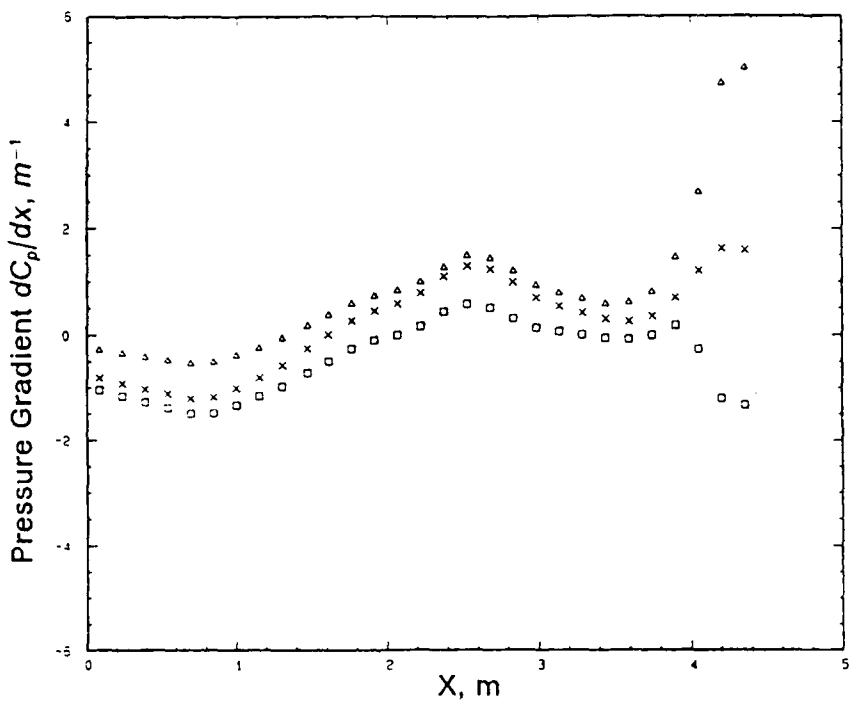


Figure 6c. Mean pressure gradient distribution along the tunnel centerline and limits of the unsteady pressure gradient, $k = 1.03$ flow with 'roof damper'; $C_p = 2(P - P_i)/\rho \bar{U}_e^2$; (Δ ,maximum; \times ,mean; \square ,minimum).

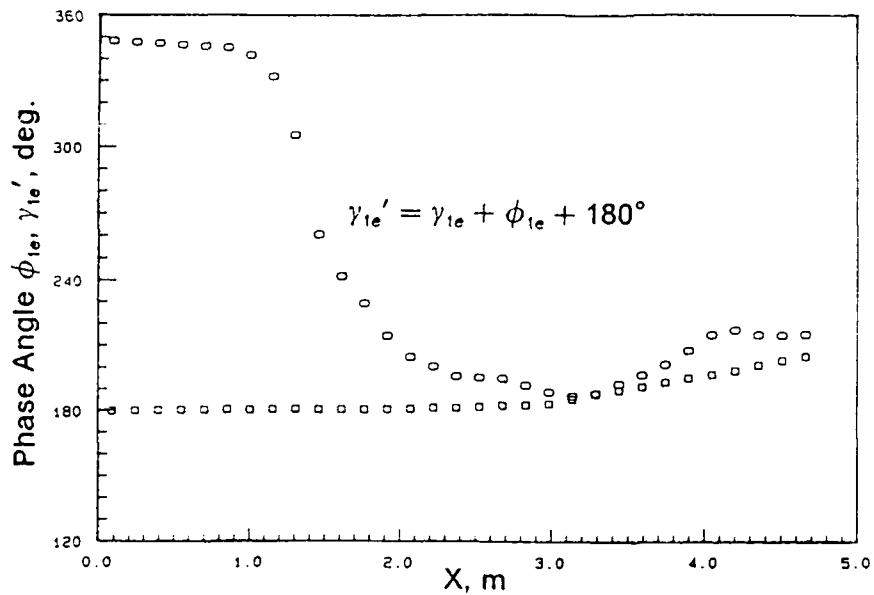


Figure 7a. Phase angles of first harmonic, $k = 0.61$ flow (\square ,free-stream velocity; \circ ,pressure gradient).

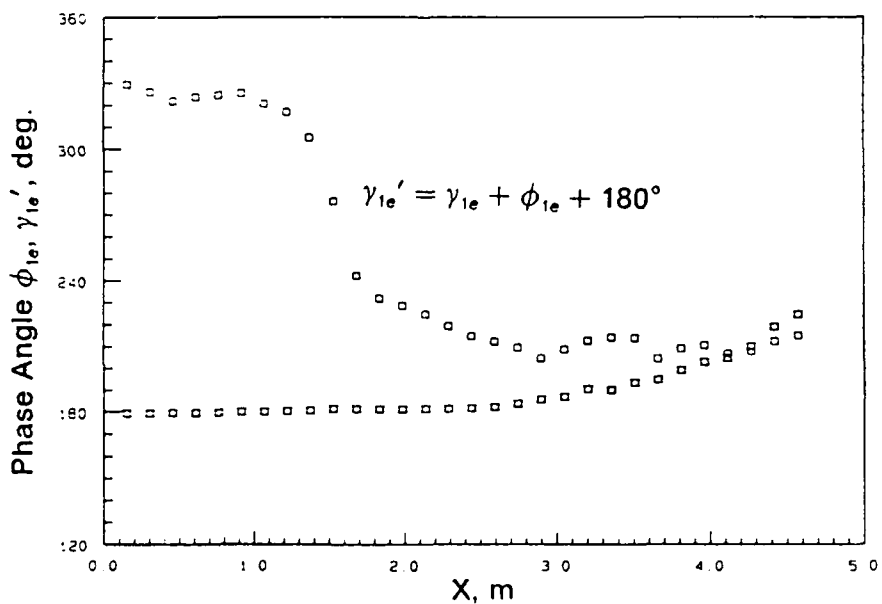


Figure 7b. Phase angles of first harmonic, $k = 1.33$ flow (\square ,free-stream velocity; \square ,pressure gradient).

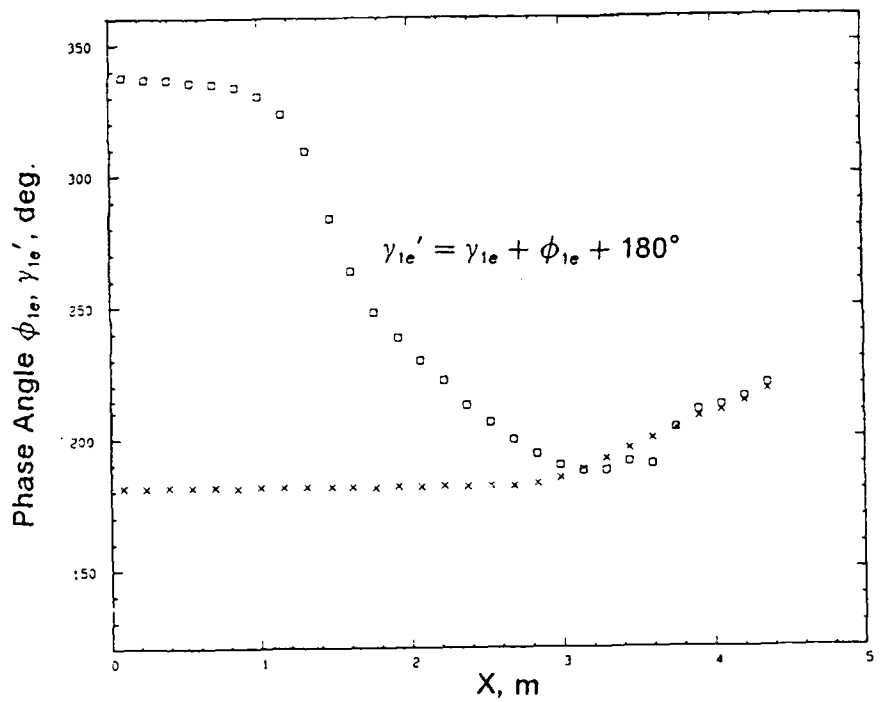


Figure 7c. Phase angles of first harmonic, $k=1.03$ flow with 'roof damper' (\times ,free-stream velocity; \square ,pressure gradient).

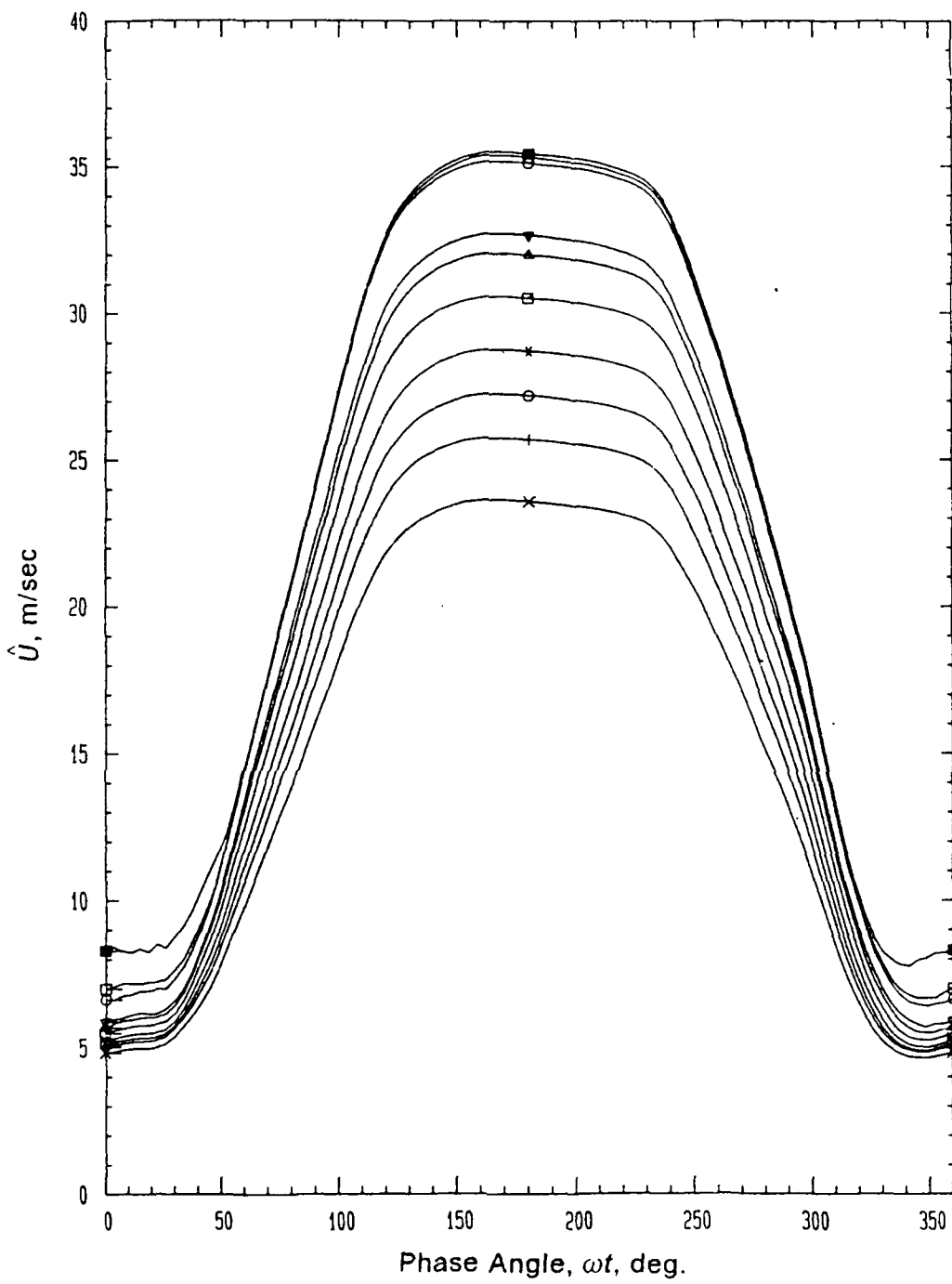


Figure 8a. Ensemble-averaged free-stream velocity along the tunnel length, $k=0.61$ flow; $0.09 \text{ m} \leq X \leq 1.46 \text{ m}$; ($\times = 0.09\text{m}$; $+$ = 0.24m ; $\circ = 0.39\text{m}$; $*$ = 0.55m ; $\square = 0.70\text{m}$; $\triangle = 0.85\text{m}$; $\nabla = 1.00\text{m}$; $\ominus = 1.16\text{m}$; $\square = 1.31\text{m}$; $\blacksquare = 1.46\text{m}$).

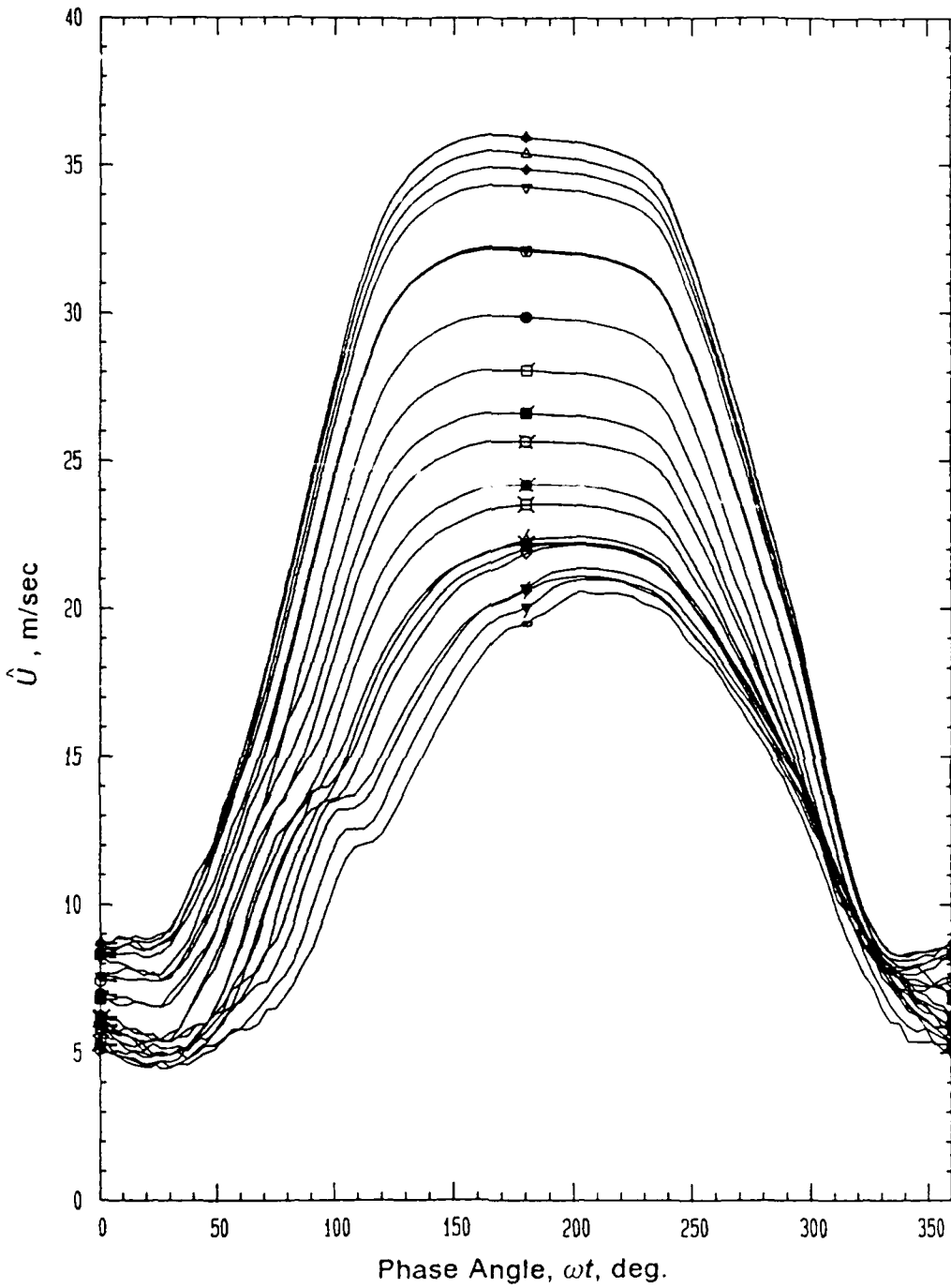


Figure 8b. Ensemble-averaged free-stream velocity along the tunnel length, $k=0.61$ flow. $1.61 \text{ m} \leq X \leq 4.66 \text{ m}$; ($\triangle = 1.61\text{m}$;
 $\blacktriangle = 1.76\text{m}$; $\diamond = 1.92\text{m}$; $\blacklozenge = 2.07\text{m}$; $\triangledown = 2.22\text{m}$; $\blacktriangledown = 2.37\text{m}$;
 $\circ = 2.53\text{m}$; $\bullet = 2.68\text{m}$; $\square = 2.83\text{m}$; $\blacksquare = 2.98\text{m}$; $\lozenge = 3.14\text{m}$.;
 $\blacksquare = 3.29\text{m}$; $\square = 3.44\text{m}$; $\blacksquare = 3.59\text{m}$; $\triangle = 3.75\text{m}$; $\blacktriangle = 3.90\text{m}$;
 $\diamond = 4.05\text{m}$; $\blacklozenge = 4.20\text{m}$; $\triangledown = 4.35\text{m}$; $\blacktriangledown = 4.51\text{m}$; $\circ = 4.66\text{m}$)

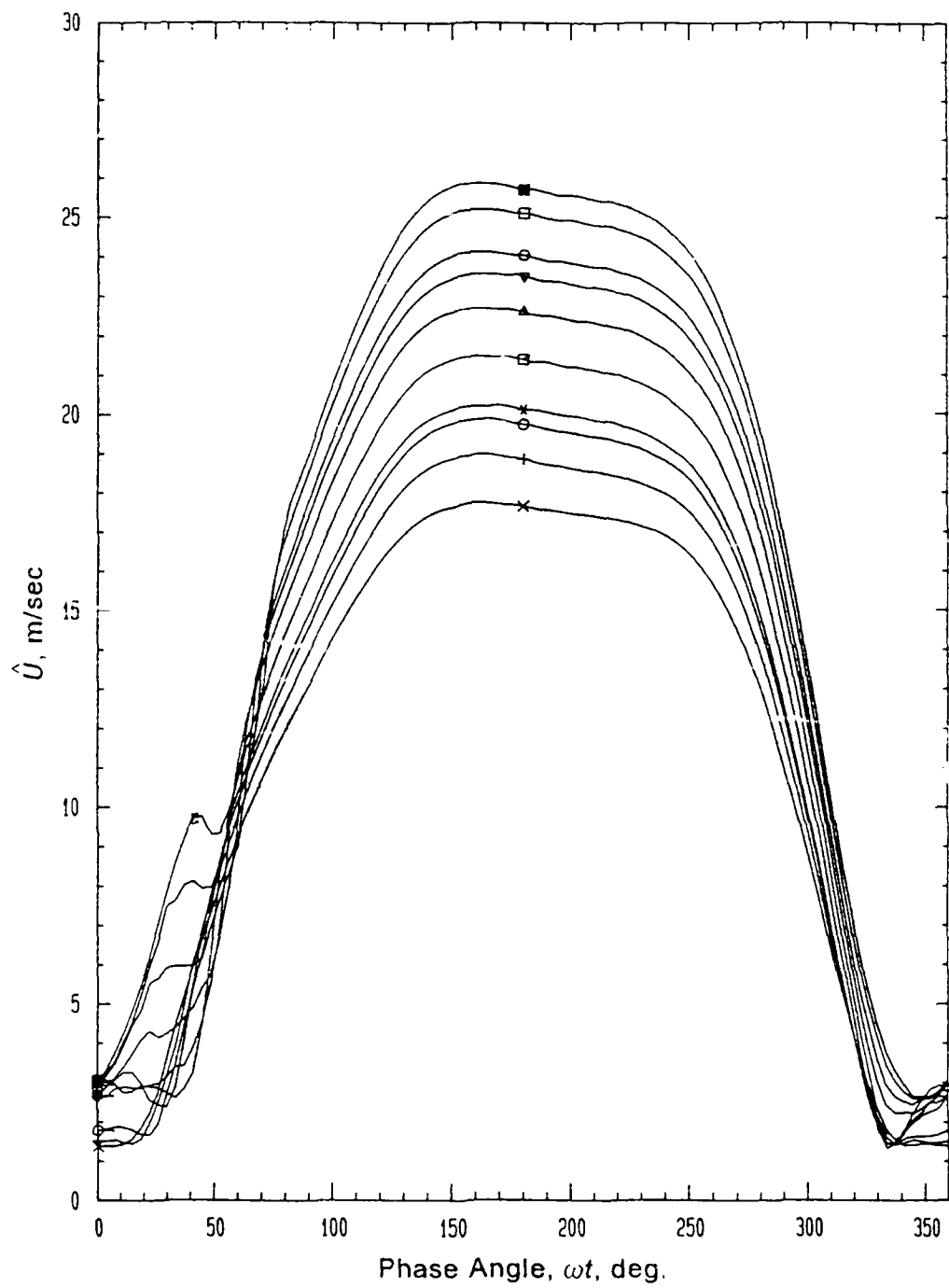


Figure 9a. Ensemble-averaged free-stream velocity along the tunnel length, $k = 1.33$ flow. $0.15 \text{ m} \leq X \leq 1.52 \text{ m}$; ($\times = 0.15\text{m}$;
 $+ = 0.30\text{m}$; $\circ = 0.46\text{m}$; $*$ = 0.61m ; $\square = 0.76\text{m}$; $\triangle = 0.91\text{m}$;
 $\nabla = 1.07\text{m}$; $\Theta = 1.22\text{m}$; $\square = 1.37\text{m}$; $\blacksquare = 1.52\text{m}$).

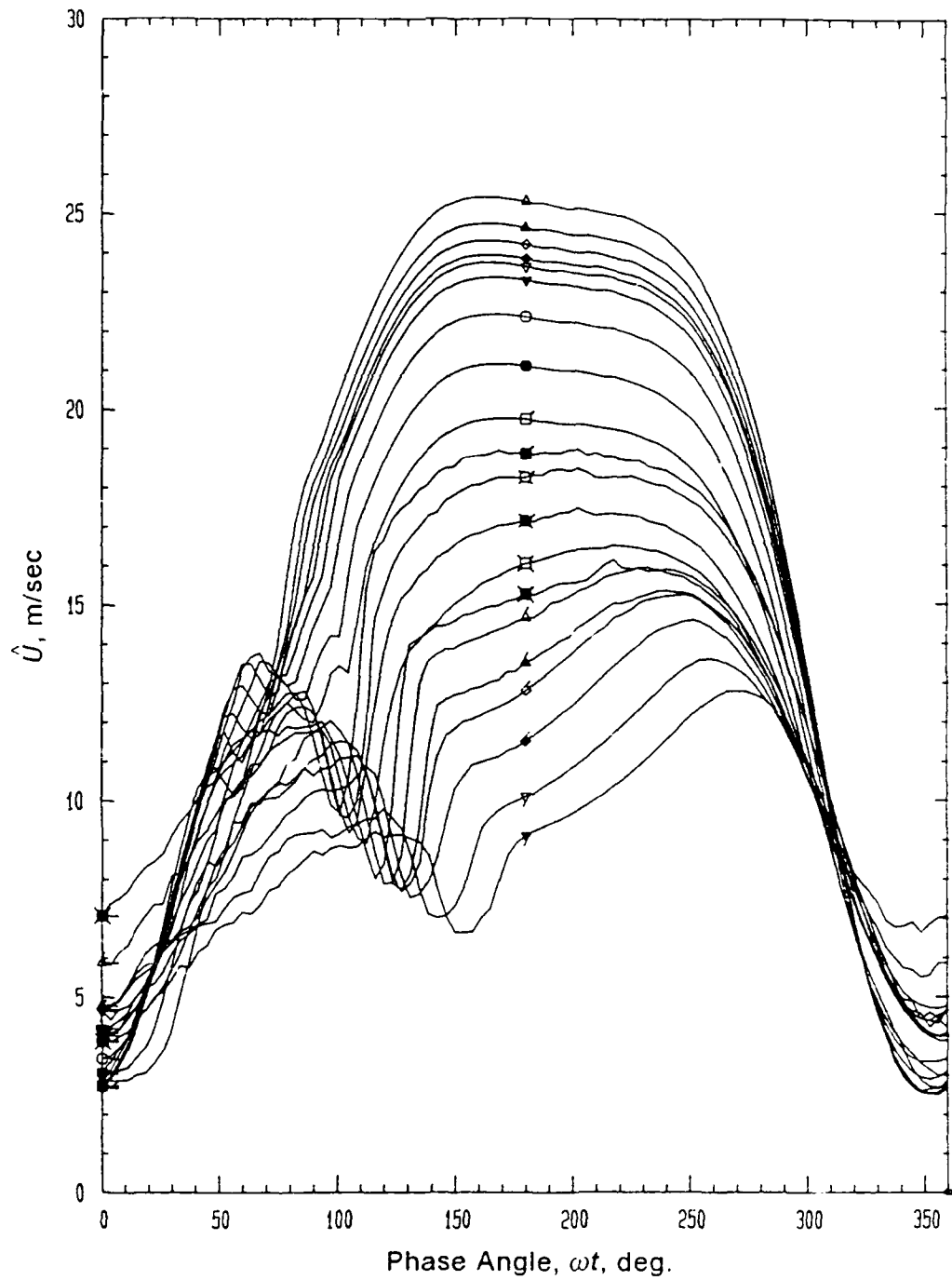


Figure 9b. Ensemble-averaged free-stream velocity along the tunnel length, $k=1.33$ flow. $1.68 \text{ m} \leq X \leq 4.57 \text{ m}$: ($\Delta = 1.68\text{m}$;
 $\blacktriangle = 1.83\text{m}$; $\diamond = 1.98\text{m}$; $\blacklozenge = 2.13\text{m}$; $\triangledown = 2.29\text{m}$; $\blacktriangledown = 2.44\text{m}$;
 $\square = 2.59\text{m}$; $\bullet = 2.74\text{m}$; $\blacksquare = 2.90\text{m}$; $\blacksquare = 3.05\text{m}$; $\boxtimes = 3.20\text{m}$.;
 $\blacksquare = 3.35\text{m}$; $\boxdot = 3.51\text{m}$; $\blacksquare = 3.66\text{m}$; $\triangle = 3.81\text{m}$; $\blacktriangle = 3.96\text{m}$;
 $\lozenge = 4.11\text{m}$; $\blacklozenge = 4.27\text{m}$; $\triangledown = 4.42\text{m}$; $\blacktriangledown = 4.57\text{m}$).

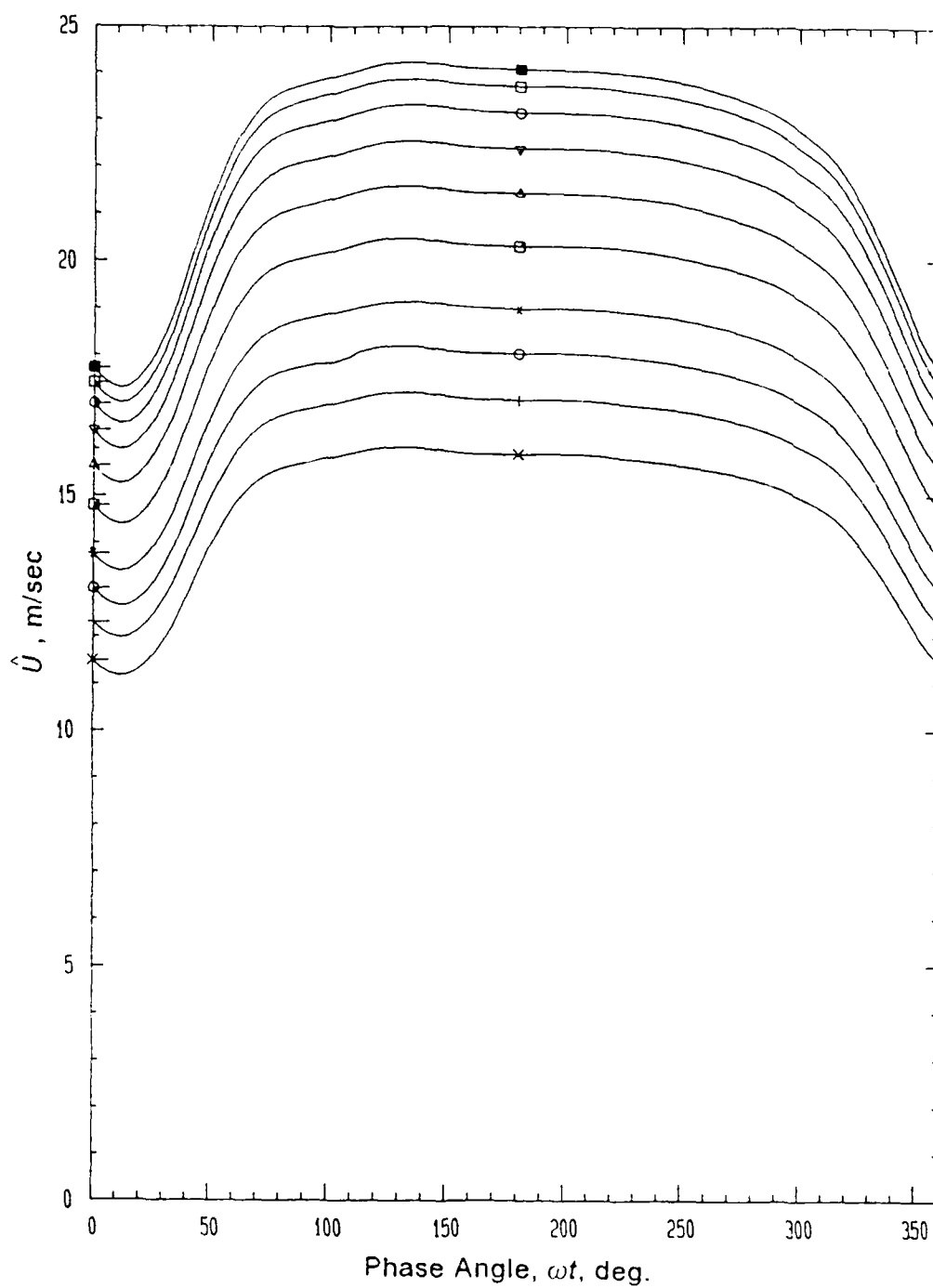


Figure 10a. Ensemble-averaged free-stream velocity along the tunnel length, $k = 1.03$ flow with 'roof damper'. $0.09 \text{ m} \leq X \leq 1.46 \text{ m}$; Legend same as in figure 8a.

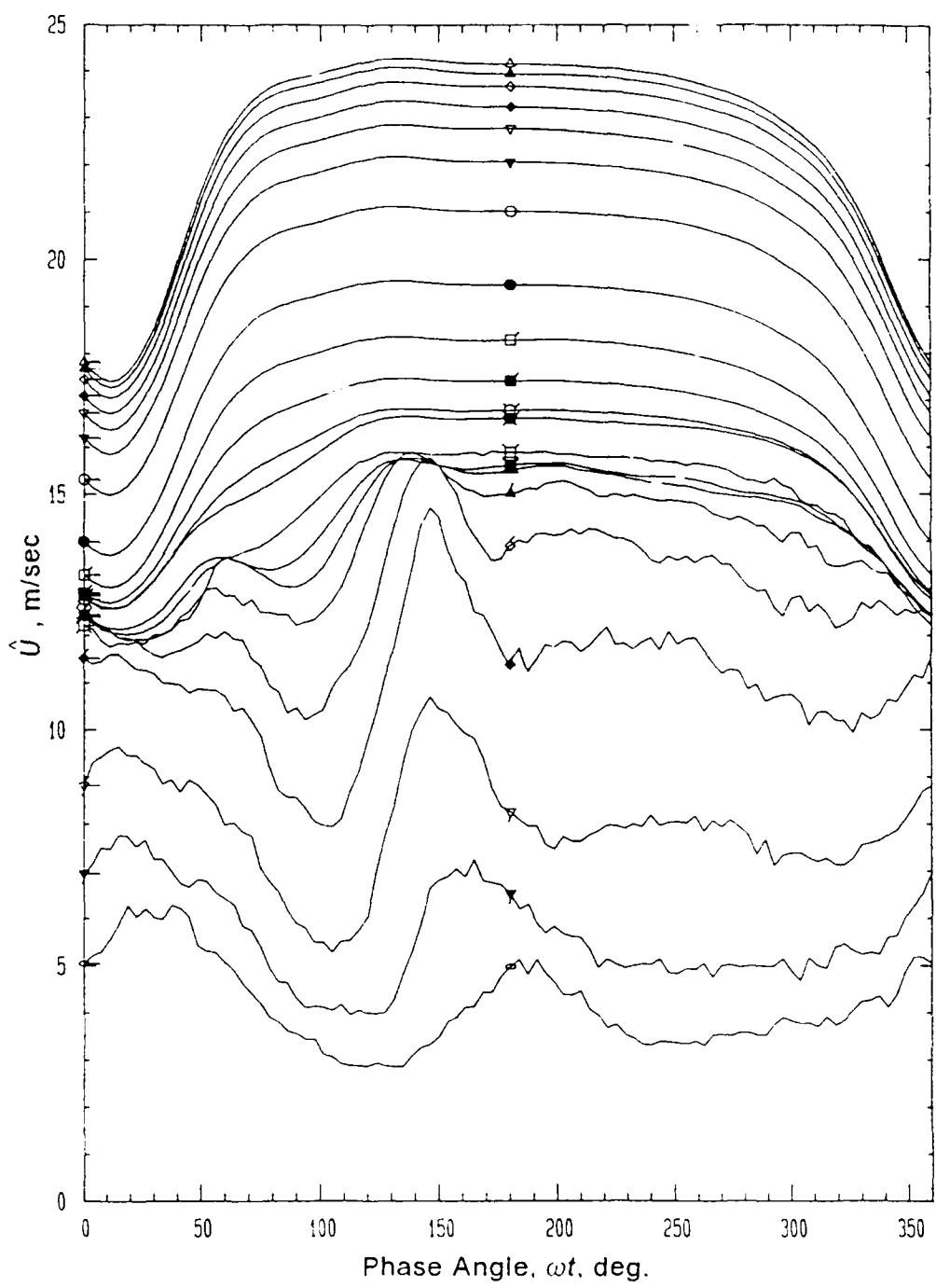


Figure 10b. Ensemble-averaged free-stream velocity along the tunnel length, $k = 1.03$ flow with 'roof damper'. $1.61\text{m} \leq X \leq 4.66\text{m}$: Legend same as in figure 8b.

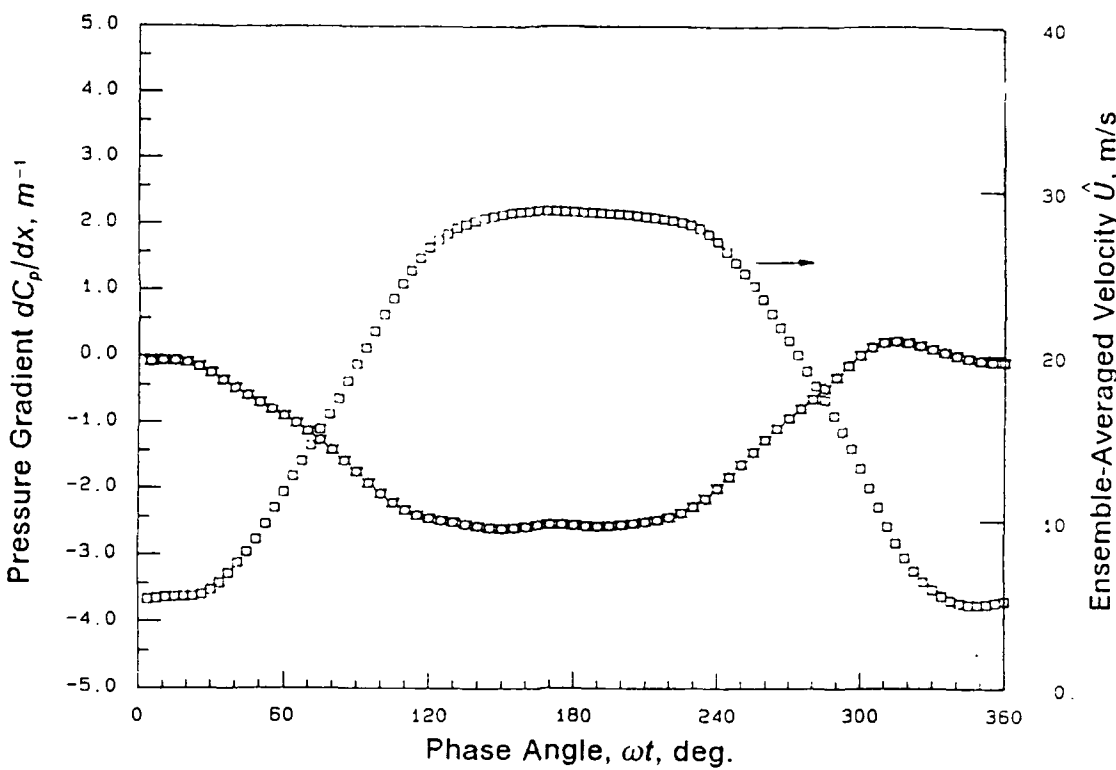


Figure 11a. Free-stream velocity and pressure gradient at $X=0.55$ m, $k=0.61$ flow. (\square ,free – stream; \diamond ,pressure gradient)

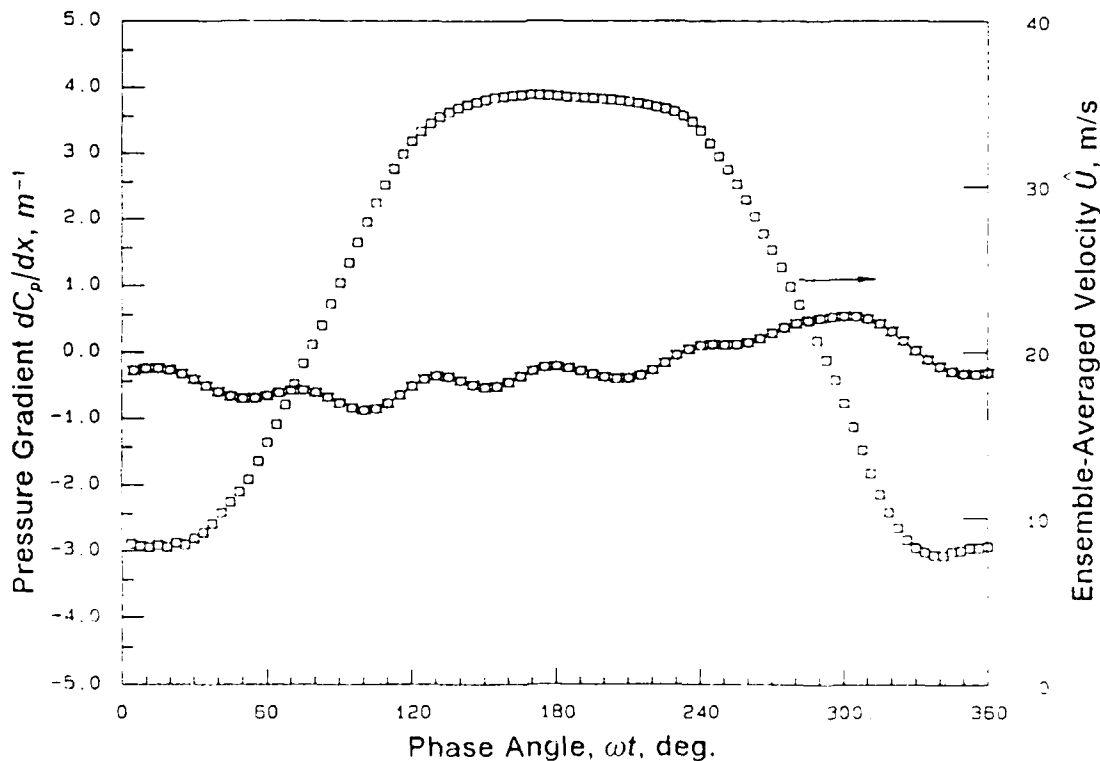


Figure 11b. Free-stream velocity and pressure gradient at $X=1.46$ m, $k=0.61$ flow.; Legend same as in figure 11a.

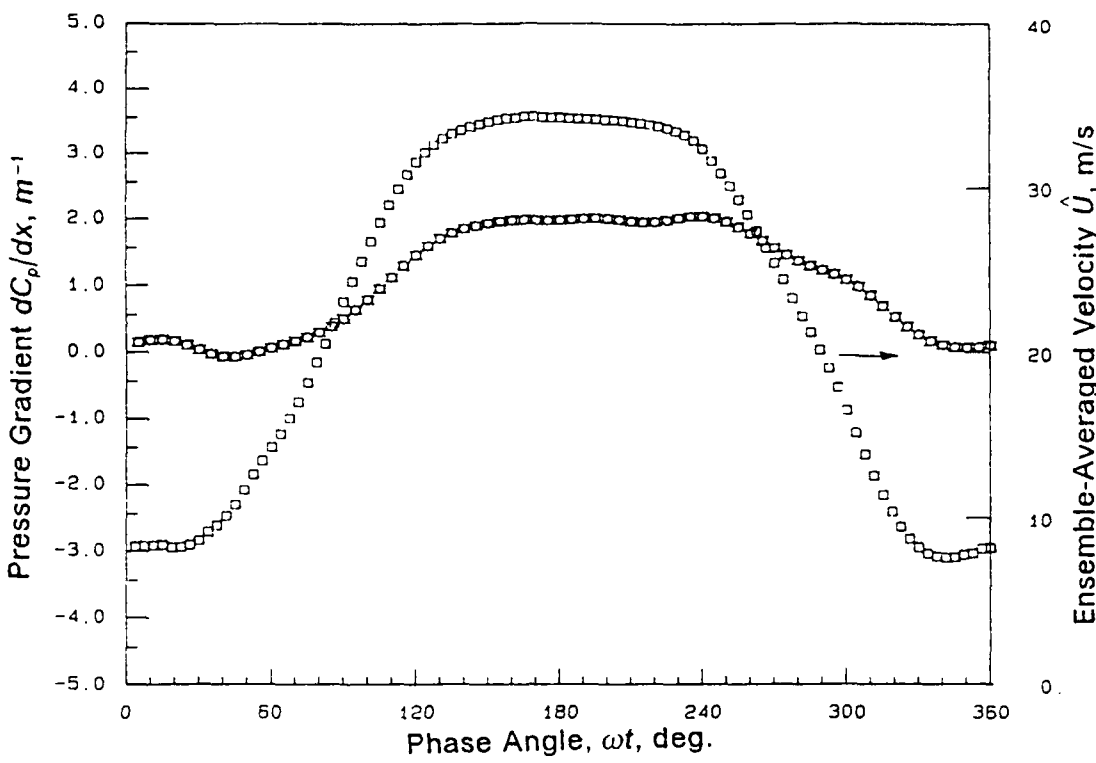


Figure 11c. Free-stream velocity and pressure gradient at $X=2.22$ m, $k=0.61$ flow.; Legend same as in figure 11a.

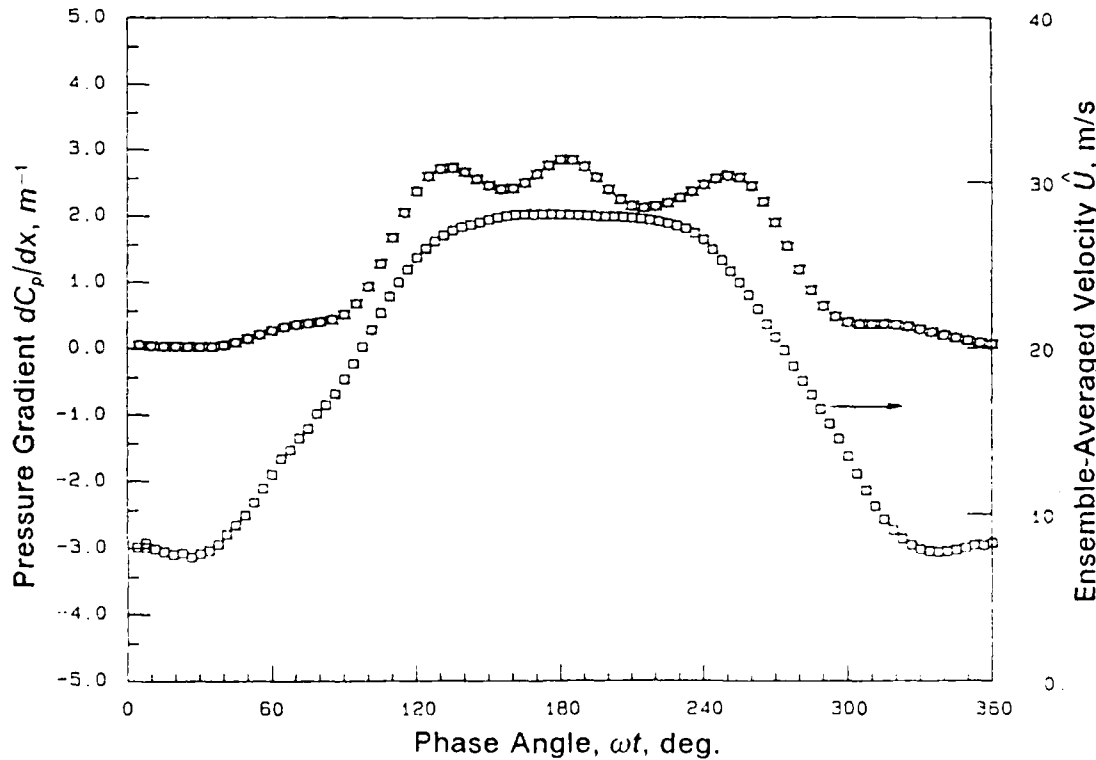


Figure 11d. Free-stream velocity and pressure gradient at $X=2.83$ m, $k=0.61$ flow; Legend same as in figure 11a.

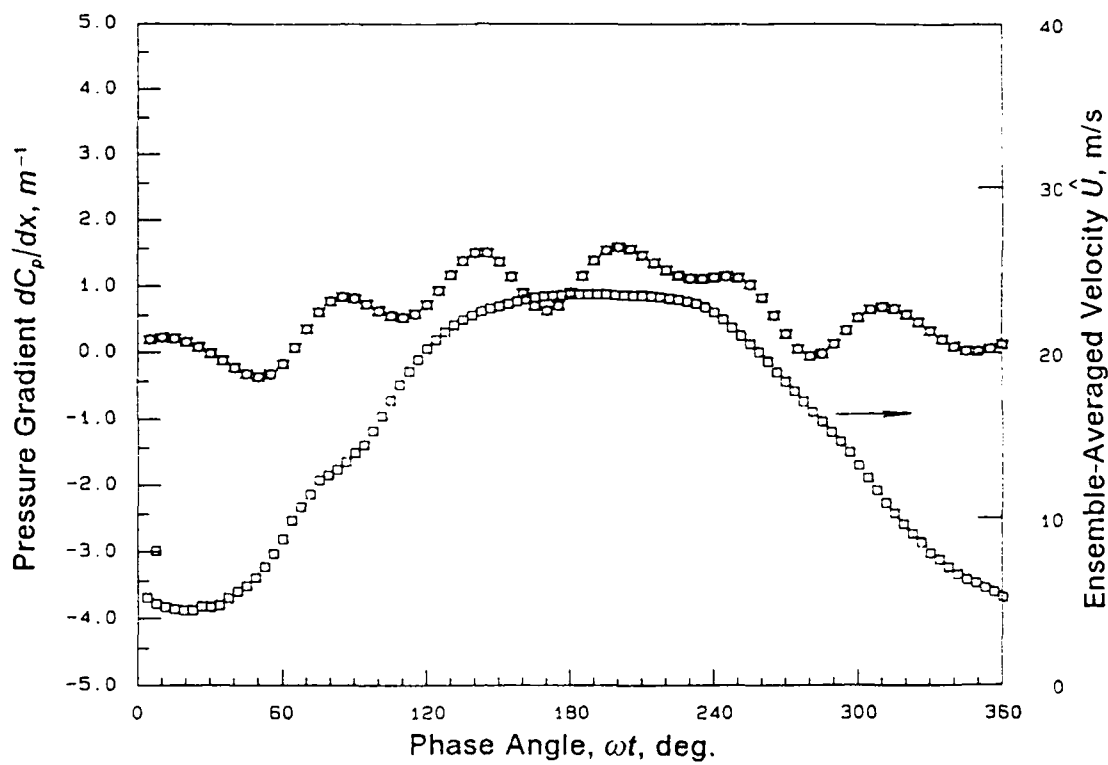


Figure 11e. Free-stream velocity and pressure gradient at $X=3.44$ m, $k=0.61$ flow; Legend same as in figure 11a.

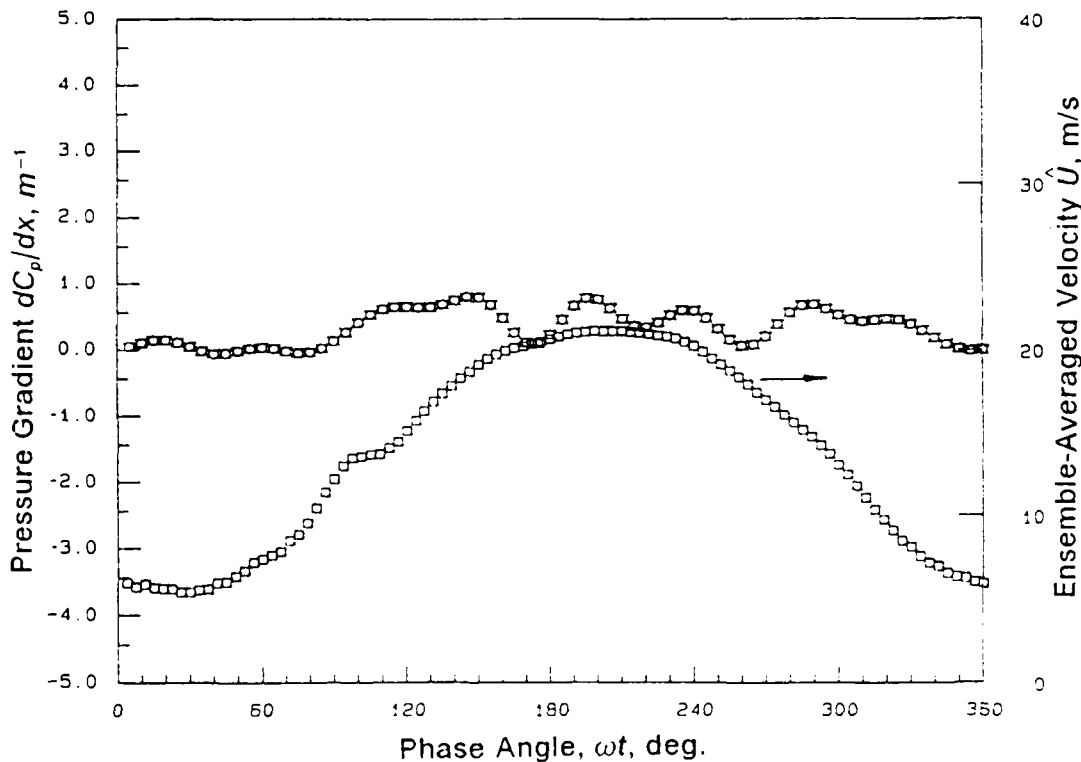


Figure 11f. Free-stream velocity and pressure gradient at $X=4.20$ m, $k=0.61$ flow; Legend same as in figure 11a.

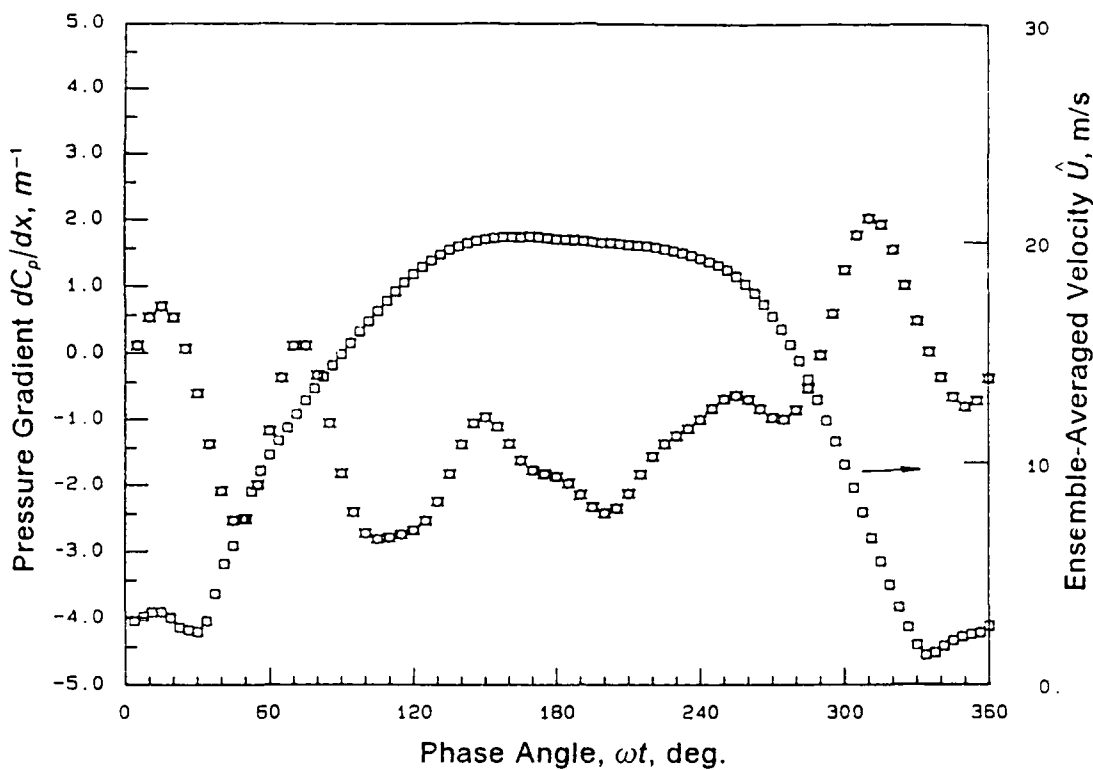


Figure 12a. Free-stream velocity and pressure gradient at $X=0.61$ m, $k=1.33$ flow; Legend same as in figure 11a.

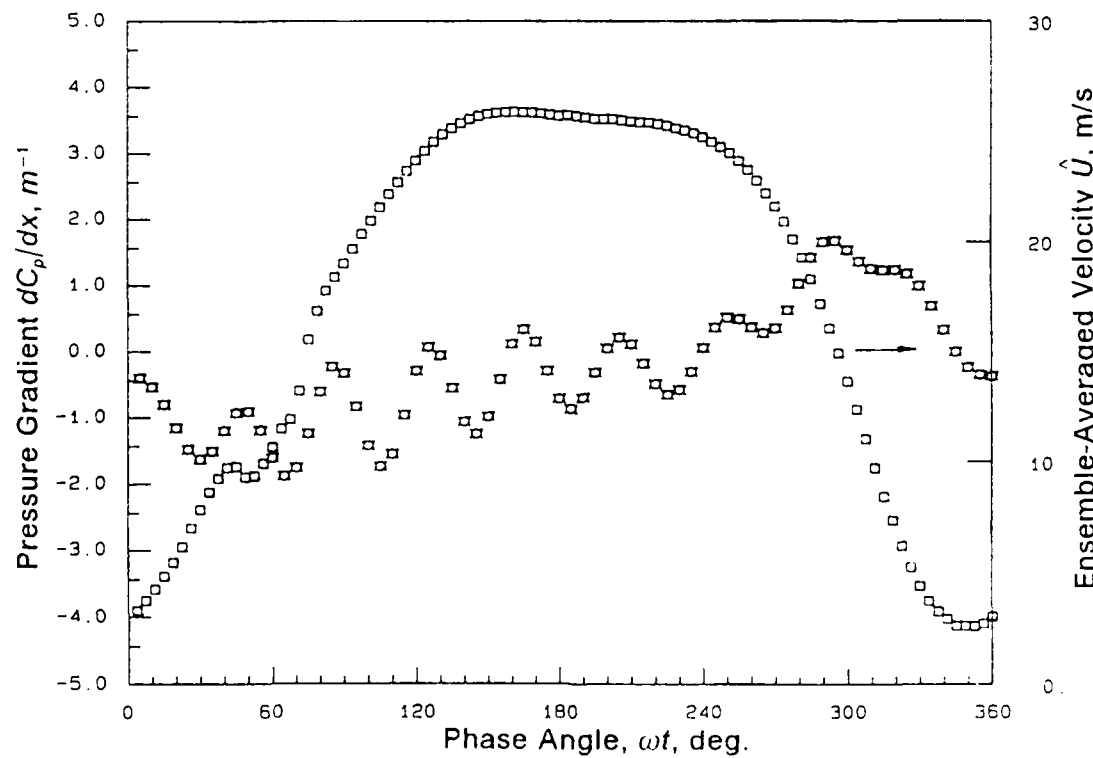


Figure 12b. Free-stream velocity and pressure gradient at $X=1.52$ m, $k=1.33$ flow; Legend same as in figure 11a.

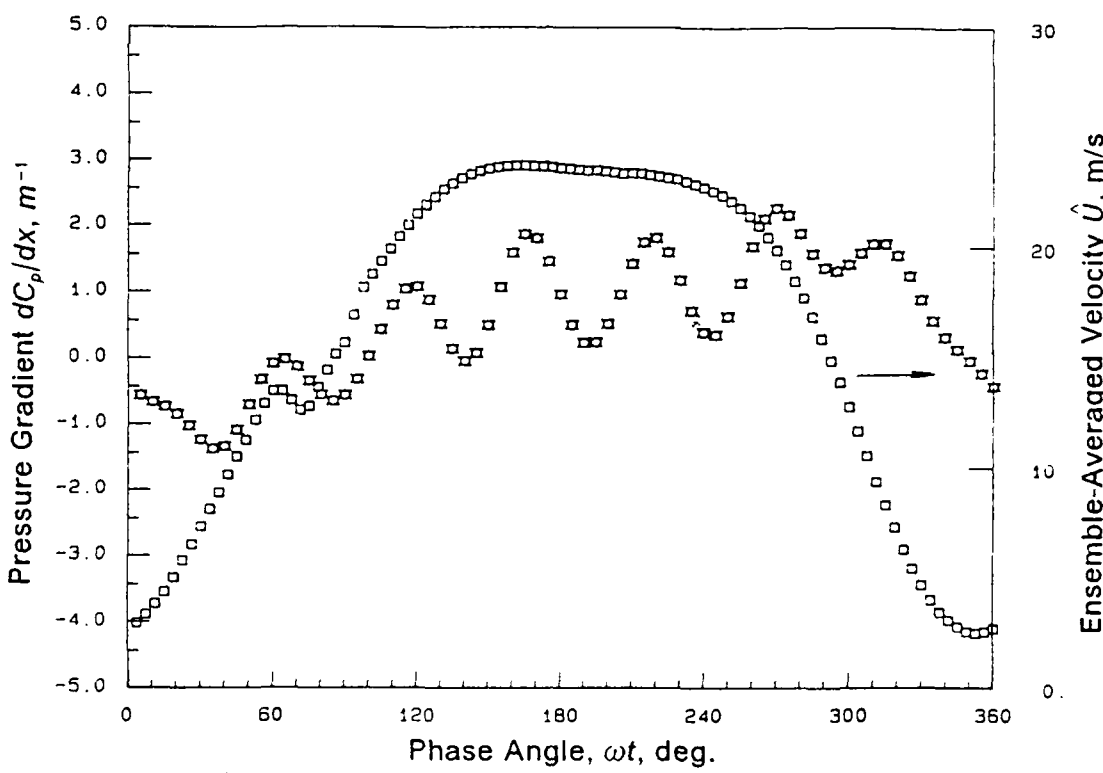


Figure 12c. Free-stream velocity and pressure gradient at $X=2.29$ m, $k=1.33$ flow; Legend same as in figure 11a.

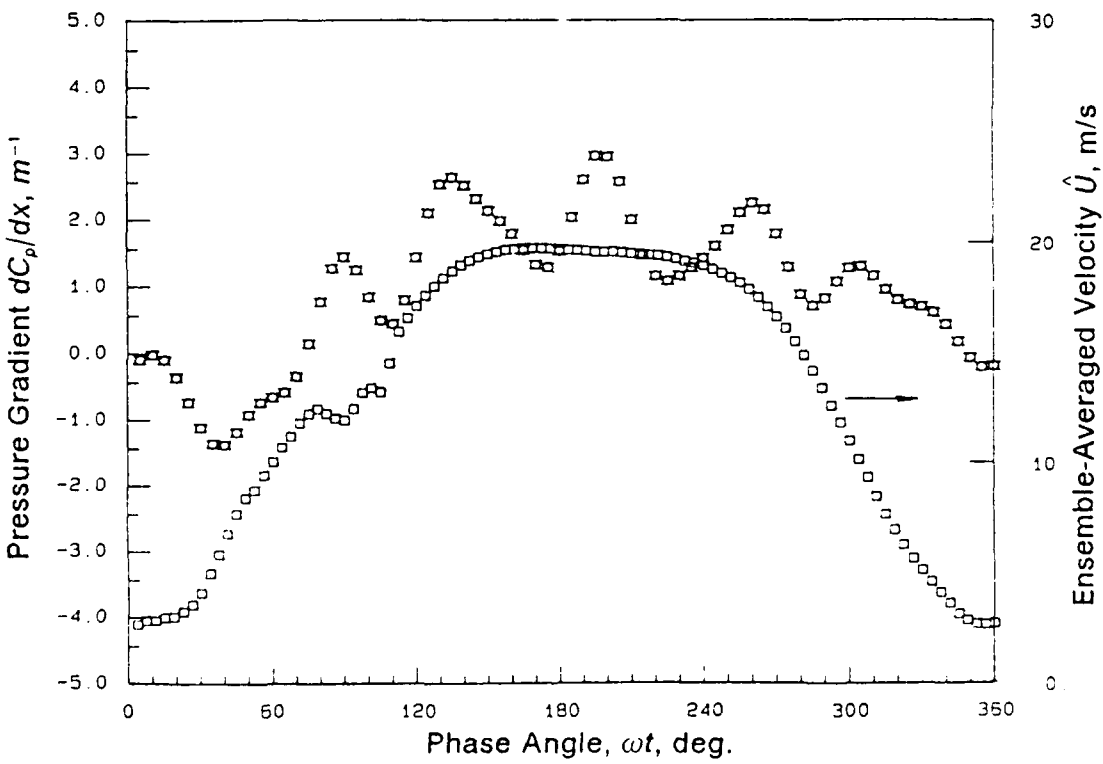


Figure 12d. Free-stream velocity and pressure gradient at $X=2.90$ m, $k=1.33$ flow; Legend same as in figure 11a.

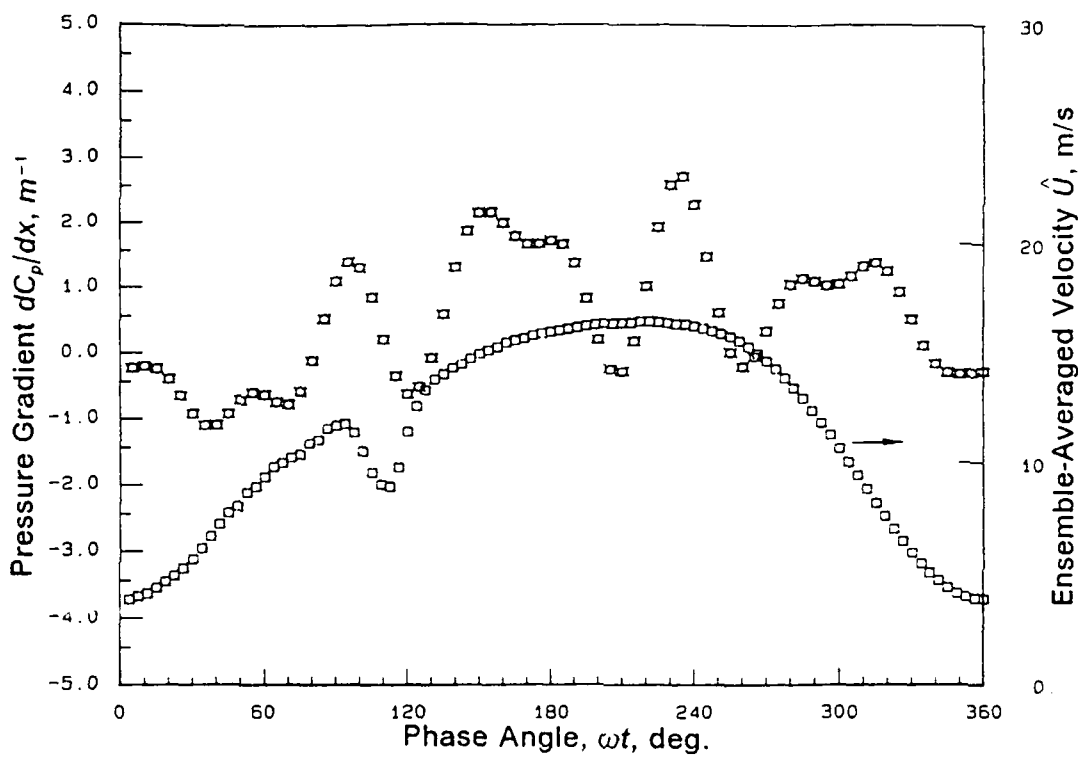


Figure 12e. Free-stream velocity and pressure gradient at $X=3.51$ m, $k=1.33$ flow; Legend same as in figure 11a.

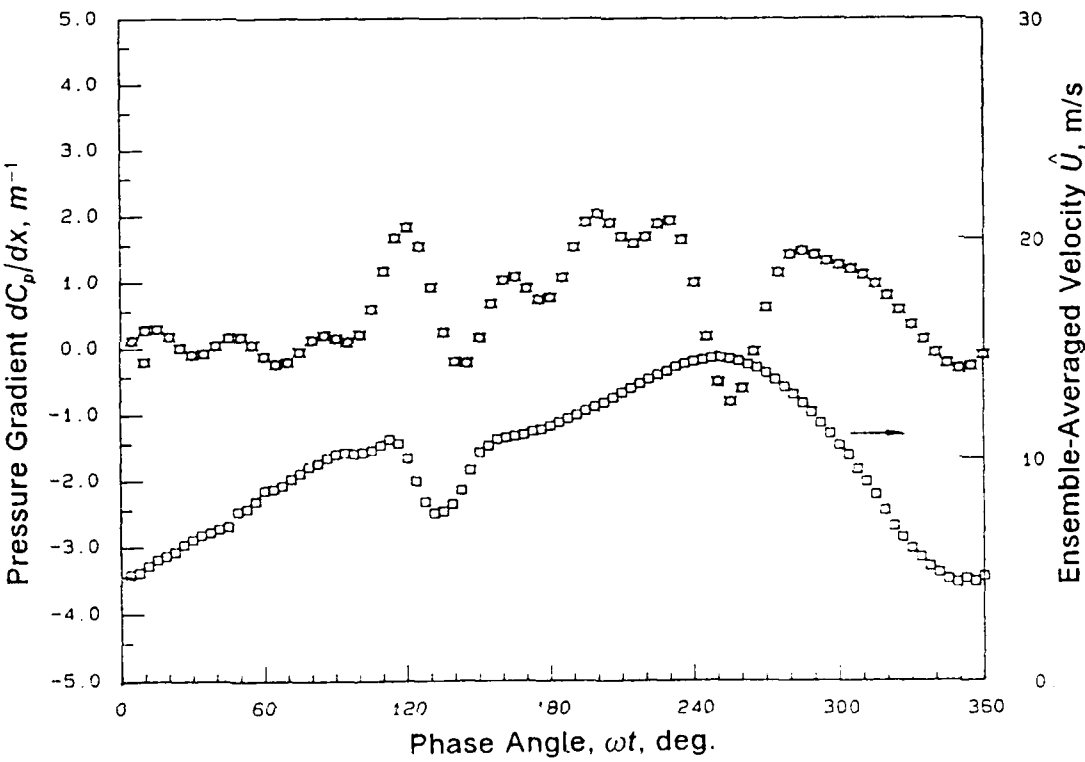


Figure 12f. Free-stream velocity and pressure gradient at $X=4.27$ m, $k=1.33$ flow; Legend same as in figure 11a.

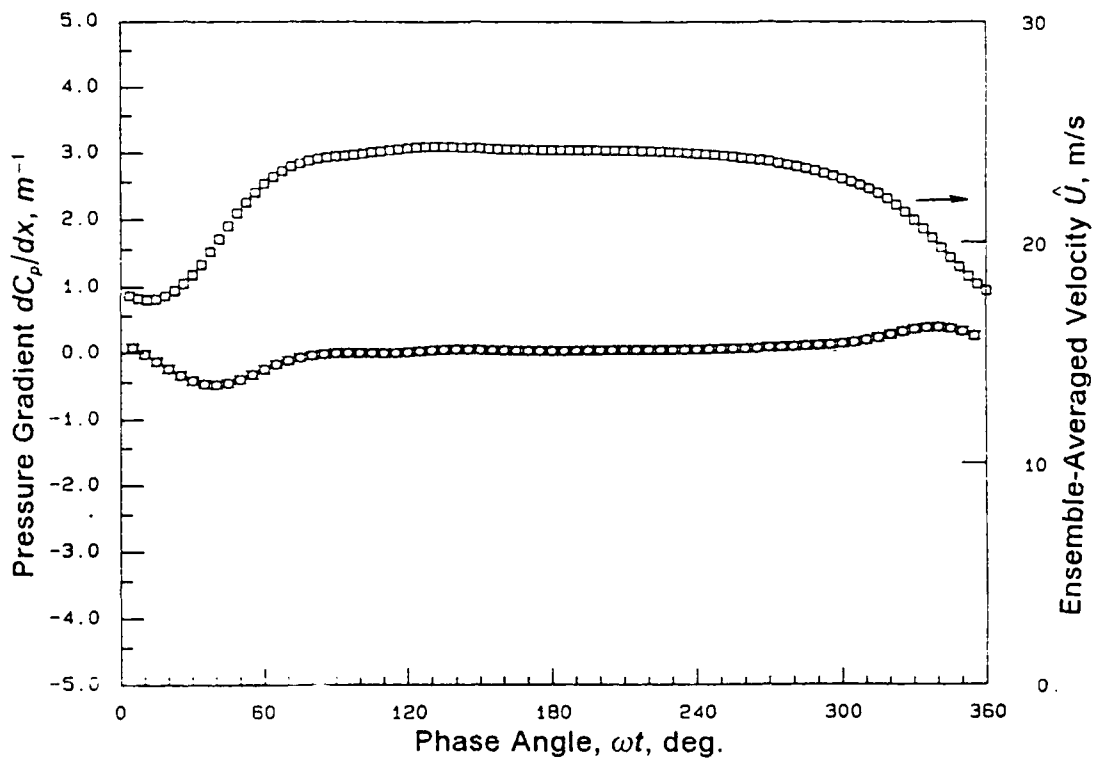


Figure 13a. Free-stream velocity and pressure gradient at $X = 1.61 \text{ m}$, $k = 1.03$ flow with 'roof damper'; Legend same as in figure 11a.

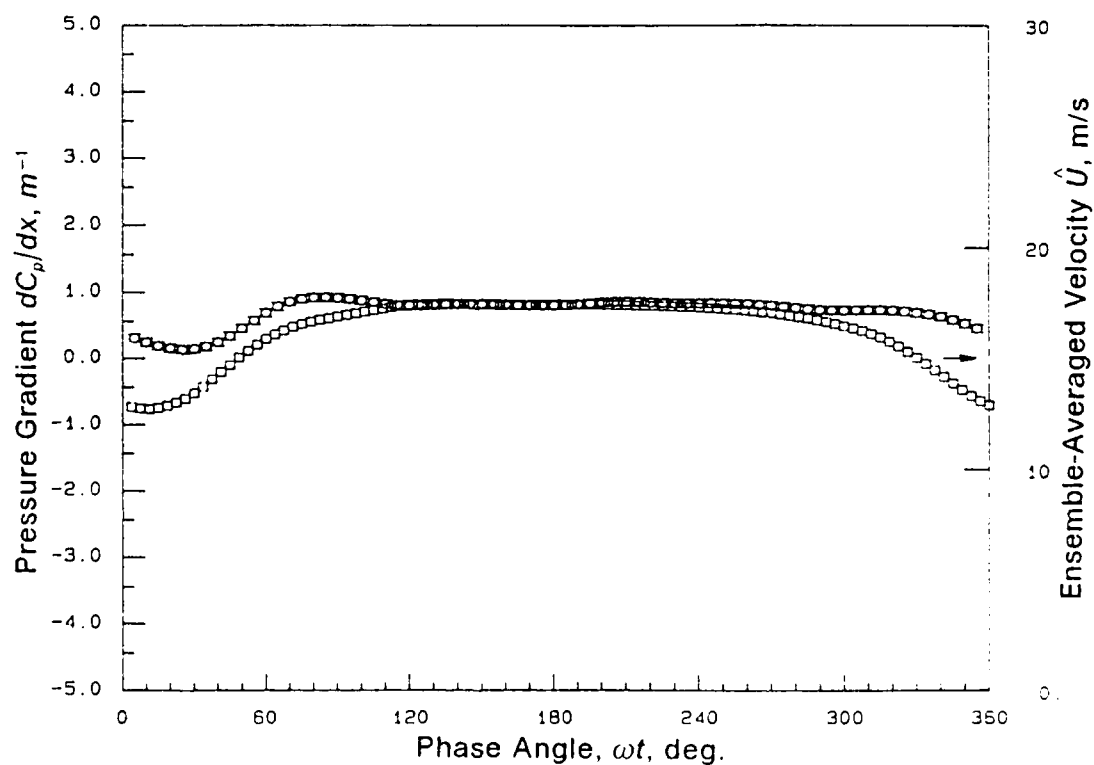


Figure 13b. Free-stream velocity and pressure gradient at $X = 2.98 \text{ m}$, $k = 1.03$ flow with 'roof damper'; Legend same as in figure 11a.

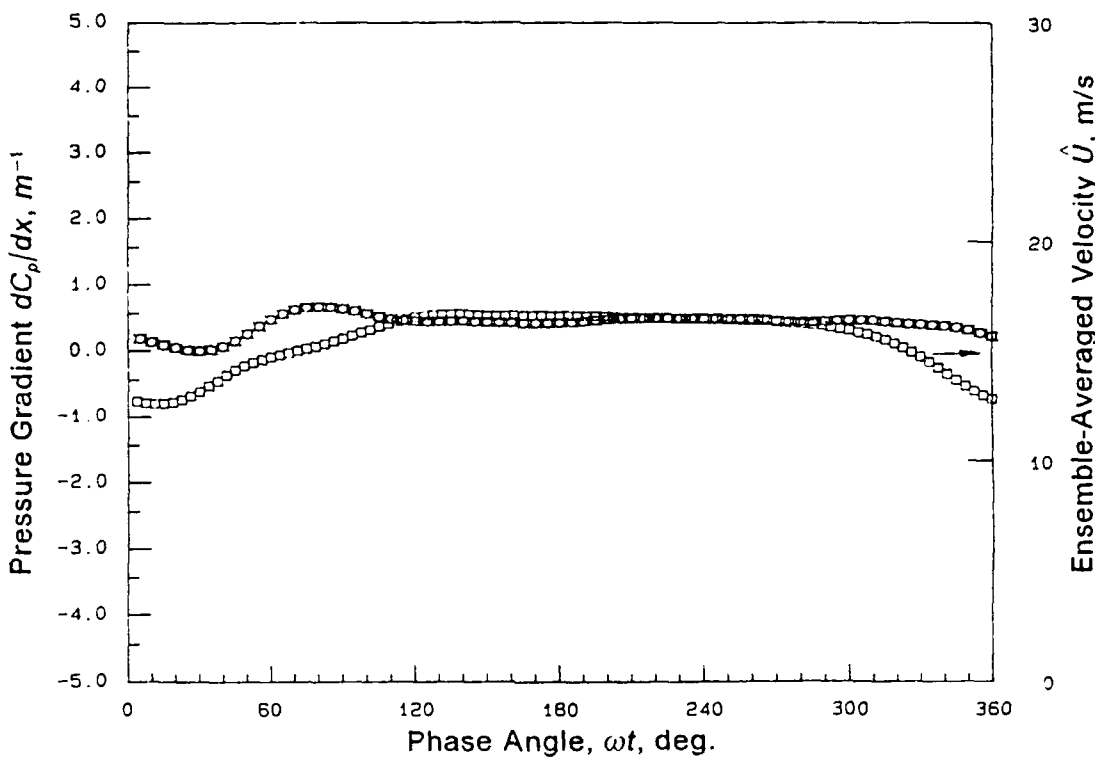


Figure 13c. Free-stream velocity and pressure gradient at $X=3.29$ m, $k=1.03$ flow with 'roof damper'; Legend same as in figure 11a.

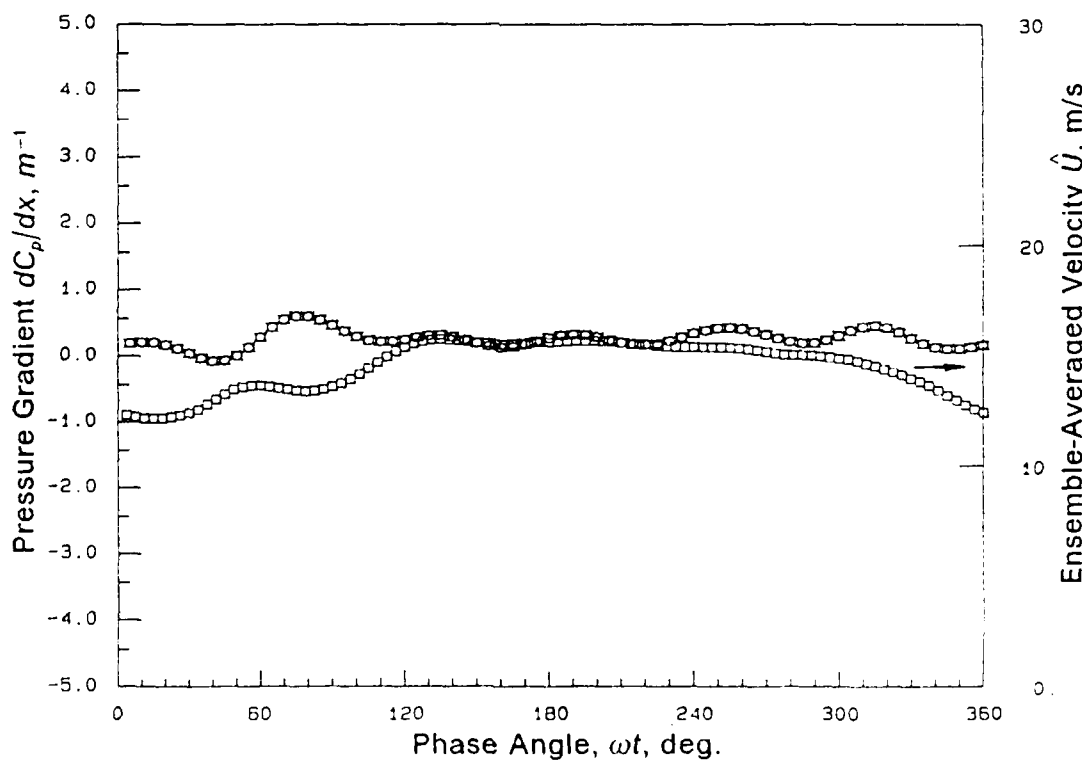


Figure 13d. Free-stream velocity and pressure gradient at $X=3.59$ m, $k=1.03$ flow with 'roof damper'; Legend same as in figure 11a.

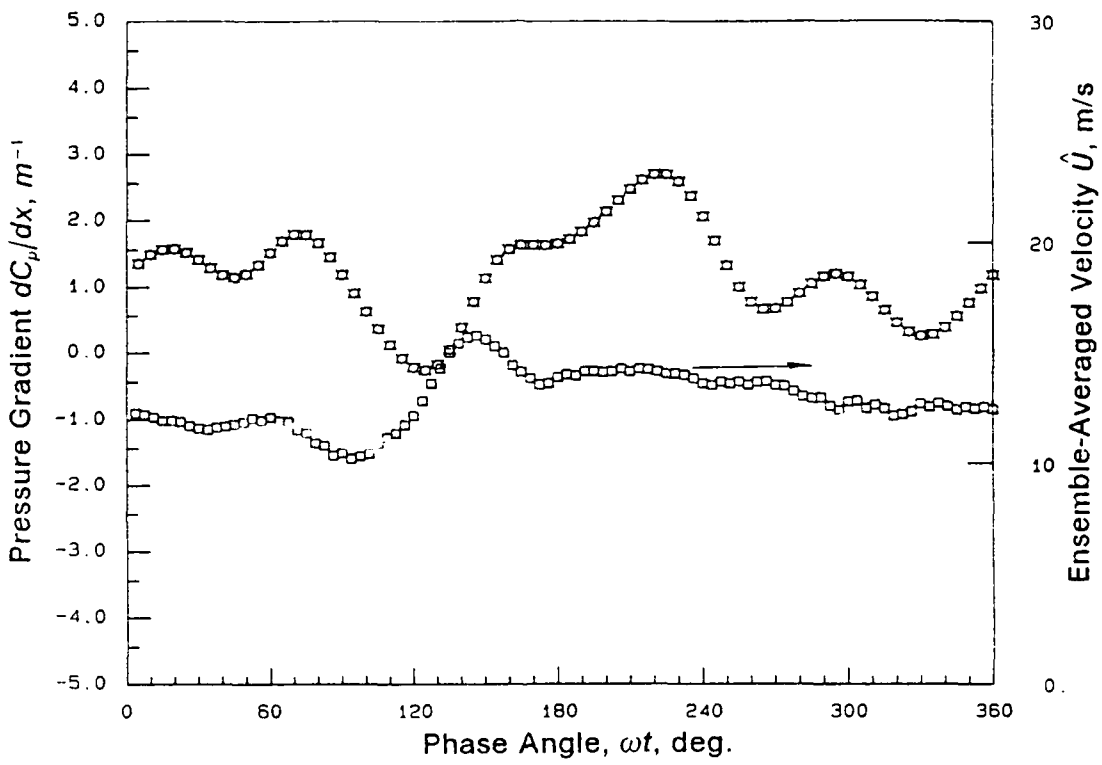


Figure 13e. Free-stream velocity and pressure gradient at $X = 4.51$ m, $k = 1.03$ flow with 'roof damper'; Legend same as in figure 11a.

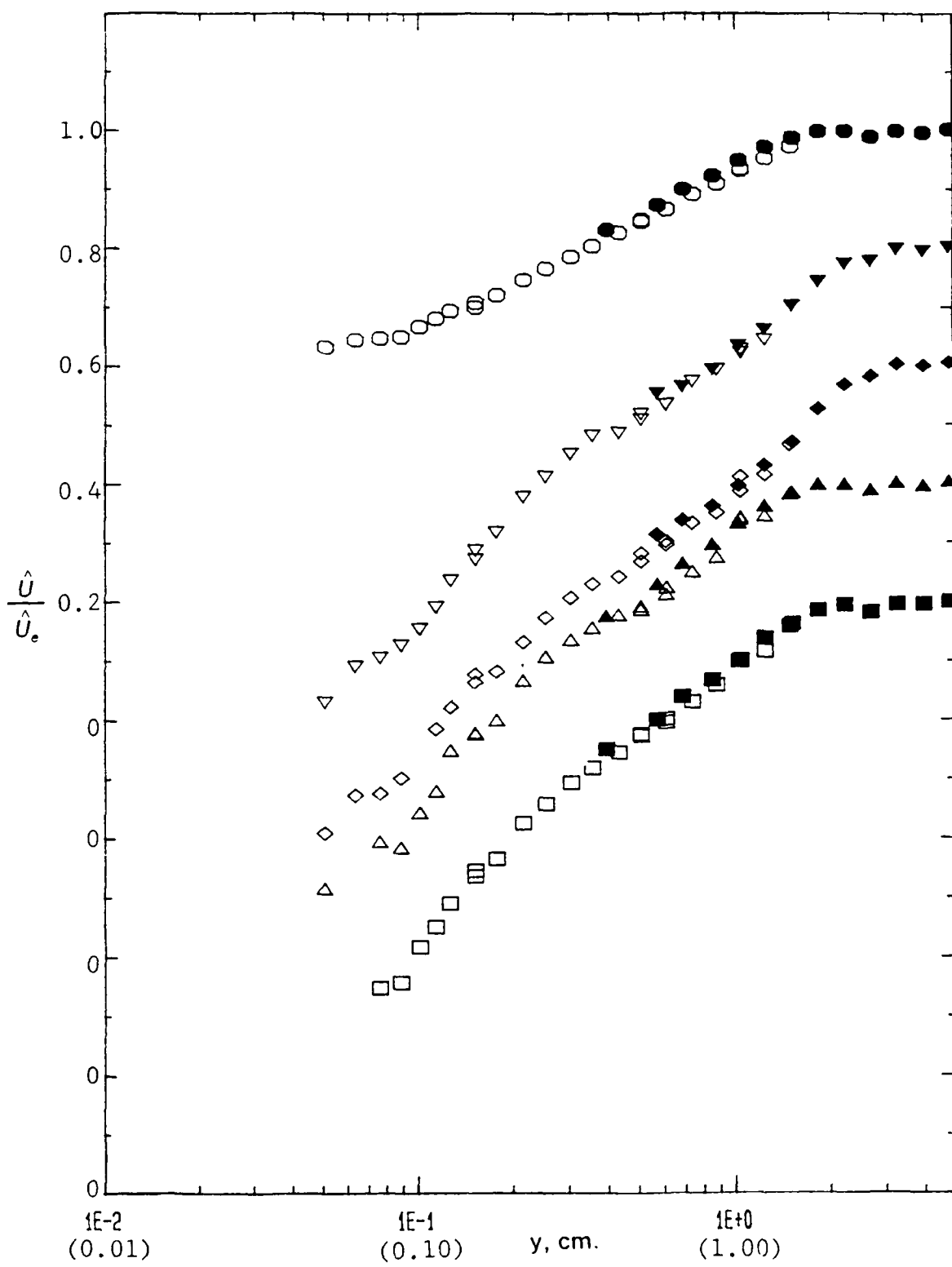


Figure 14a. Ensemble-averaged velocity profiles, \hat{U}/\hat{U}_e at $X=0.53$ m, $k=0.61$ flow: ($\square = 15^\circ$; $\triangle = 30^\circ$; $\diamond = 345^\circ$; $\nabla = 360^\circ$; $\circ = 180^\circ$); open symbols, laser anemometer; solid symbols, cross-wire measurements.

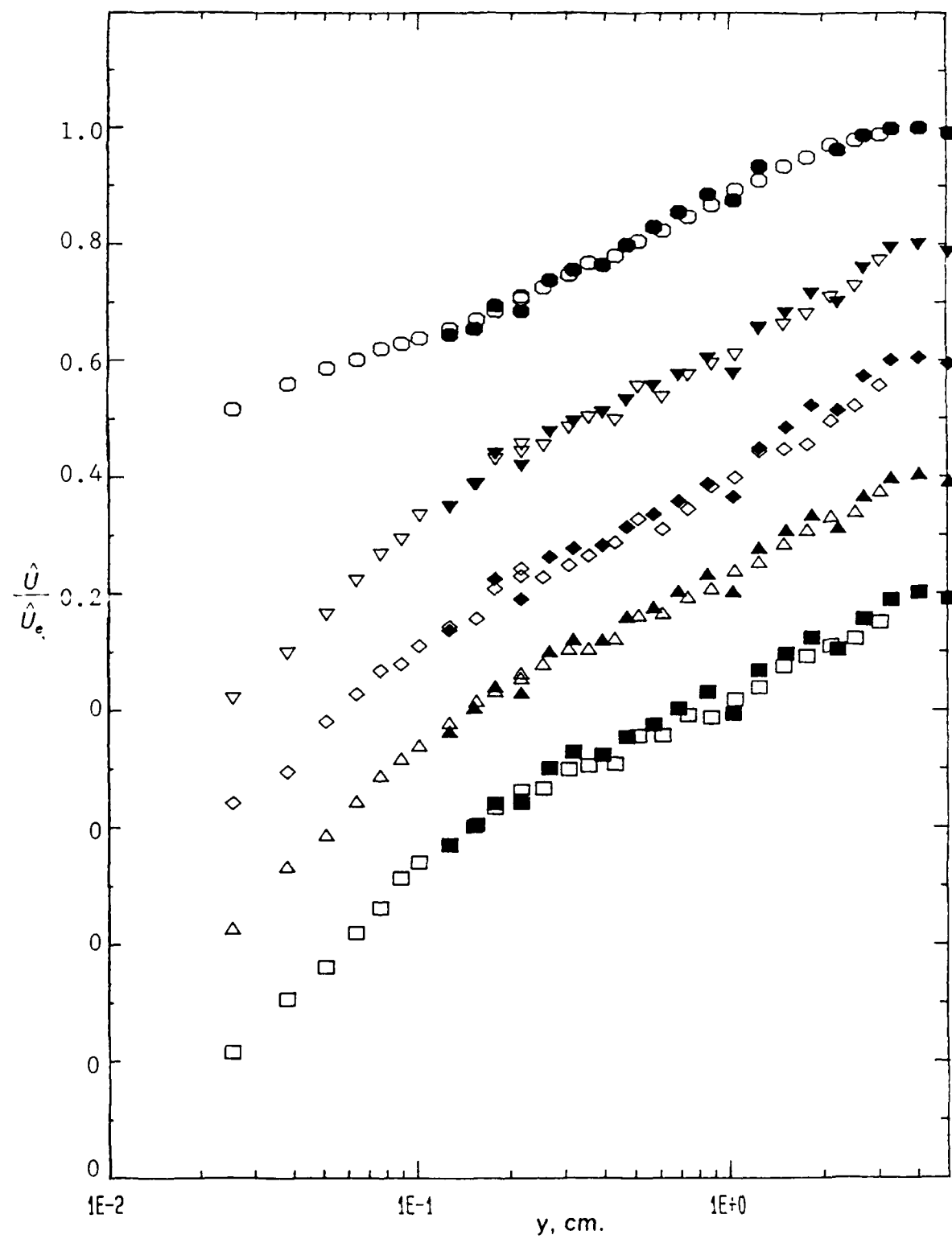


Figure 14b. Ensemble-averaged velocity profiles, \hat{U}/\hat{U}_e , at $X=1.45$ m, $k=0.61$ flow; Legend same as in figure 14a.

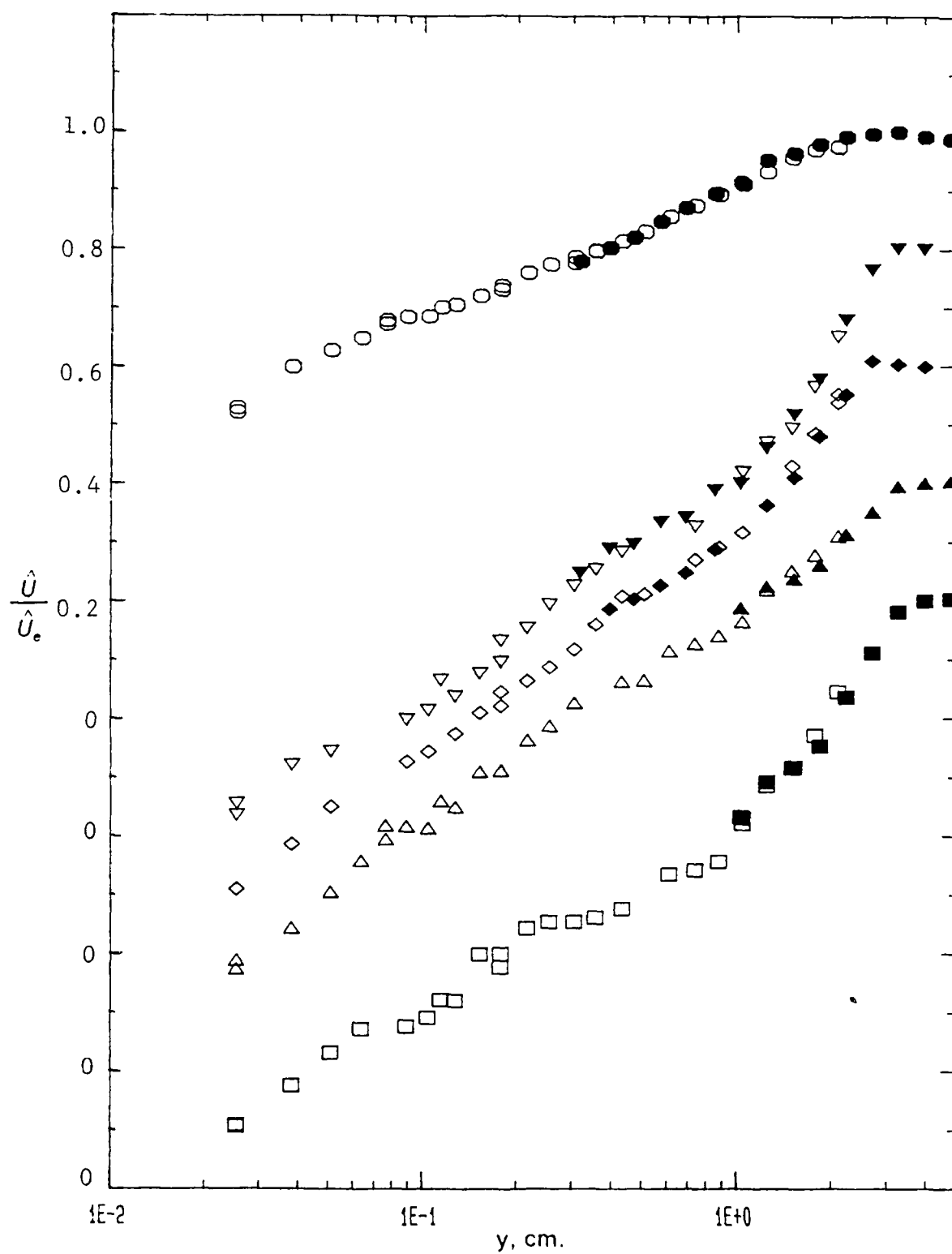


Figure 15a. Ensemble-averaged velocity profiles, \hat{U}/\hat{U}_e at $X=0.53$ m, $k=1.33$ flow; Legend same as in figure 14a.

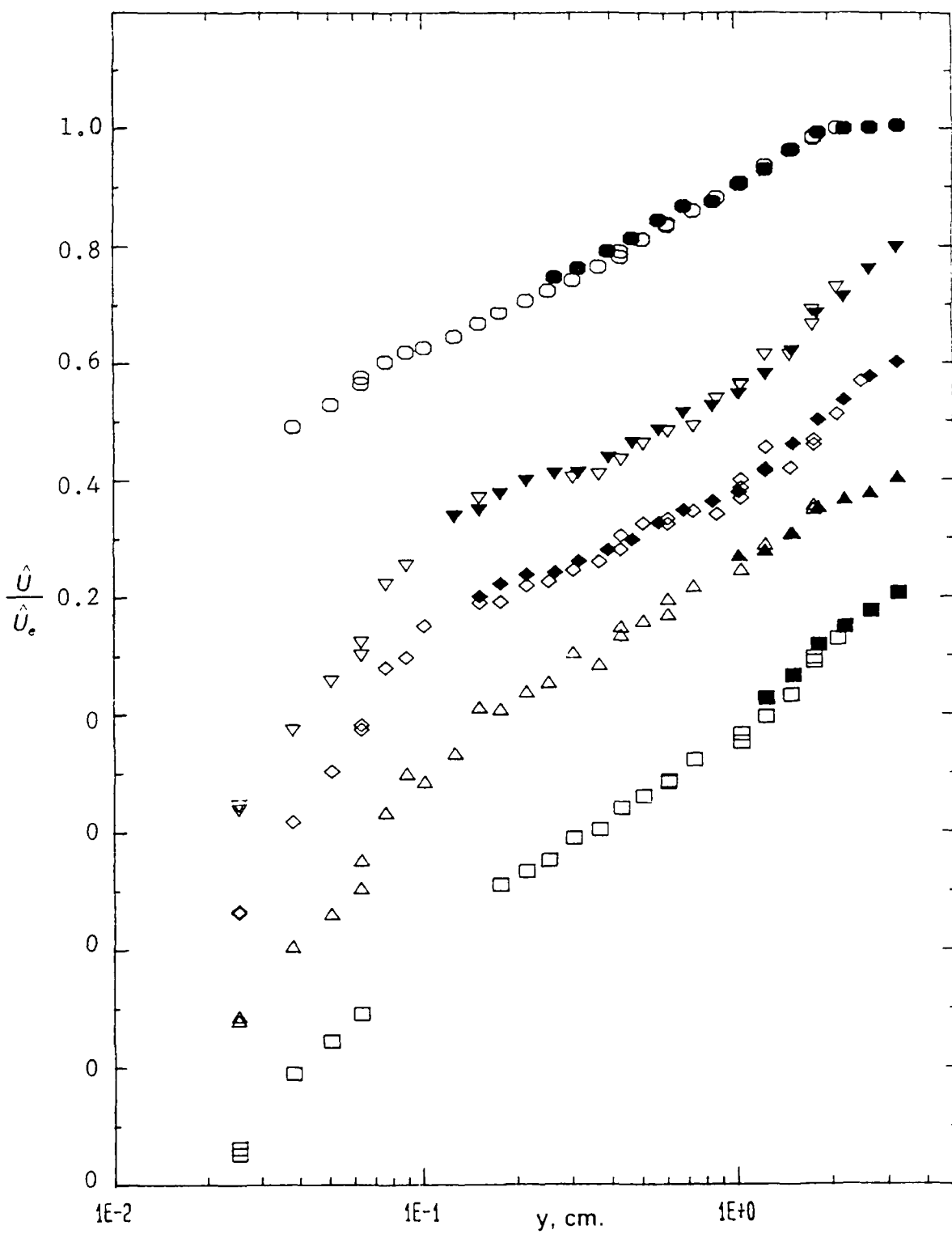


Figure 15b. Ensemble-averaged velocity profiles, \hat{U}/\hat{U}_e at $X = 1.45$ m.
 $k = 1.33$ flow; Legend same as in figure 14a.

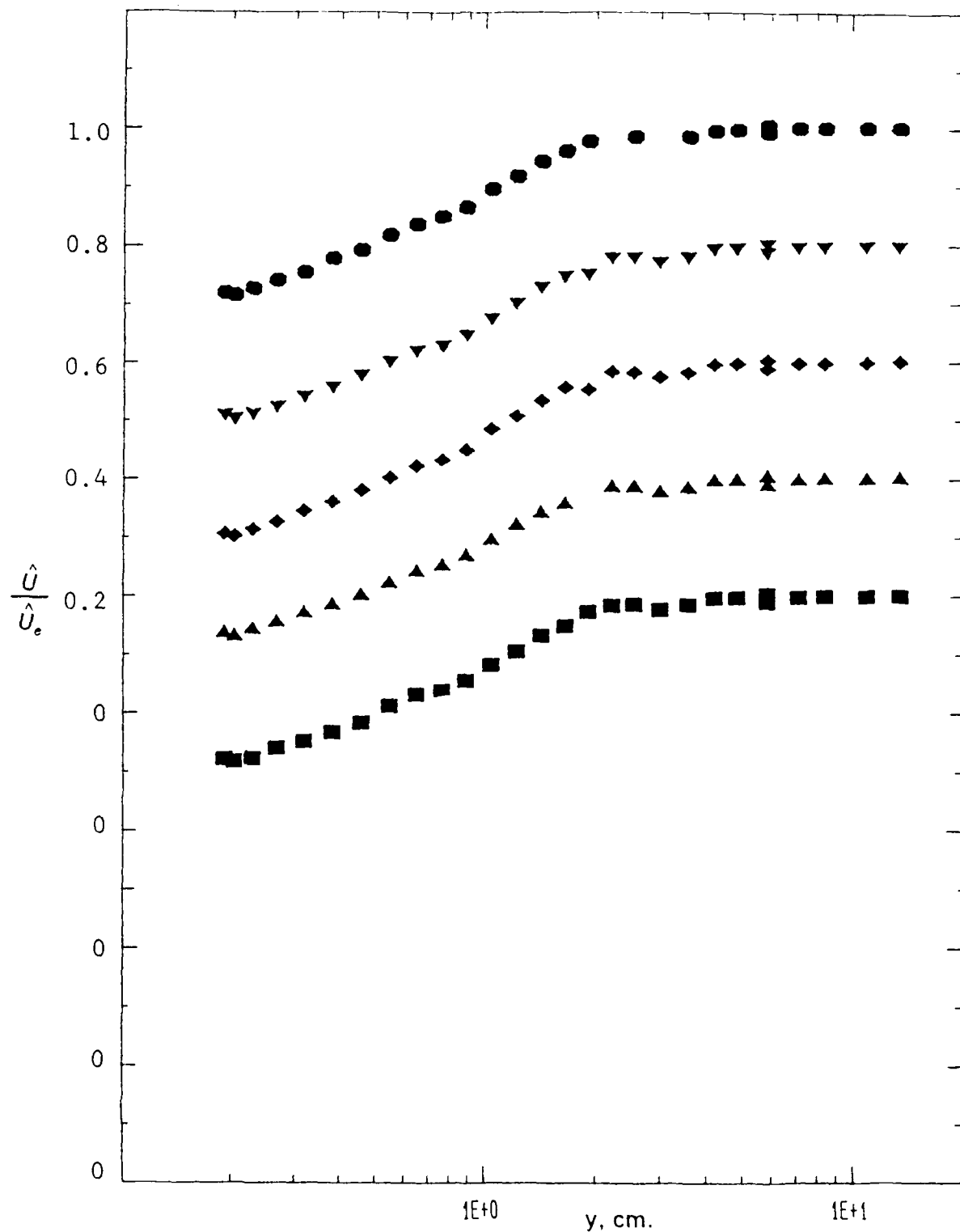


Figure 16. Ensemble-averaged velocity profiles, \hat{U}/\hat{U}_e at $X=1.63$ m, $k=1.03$ flow with 'roof damper'; ($\blacksquare = 15^\circ$; $\blacktriangle = 30^\circ$; $\blacklozenge = 345^\circ$; $\blacktriangledown = 360^\circ$; $\bullet = 180^\circ$); Cross-wire measurements.

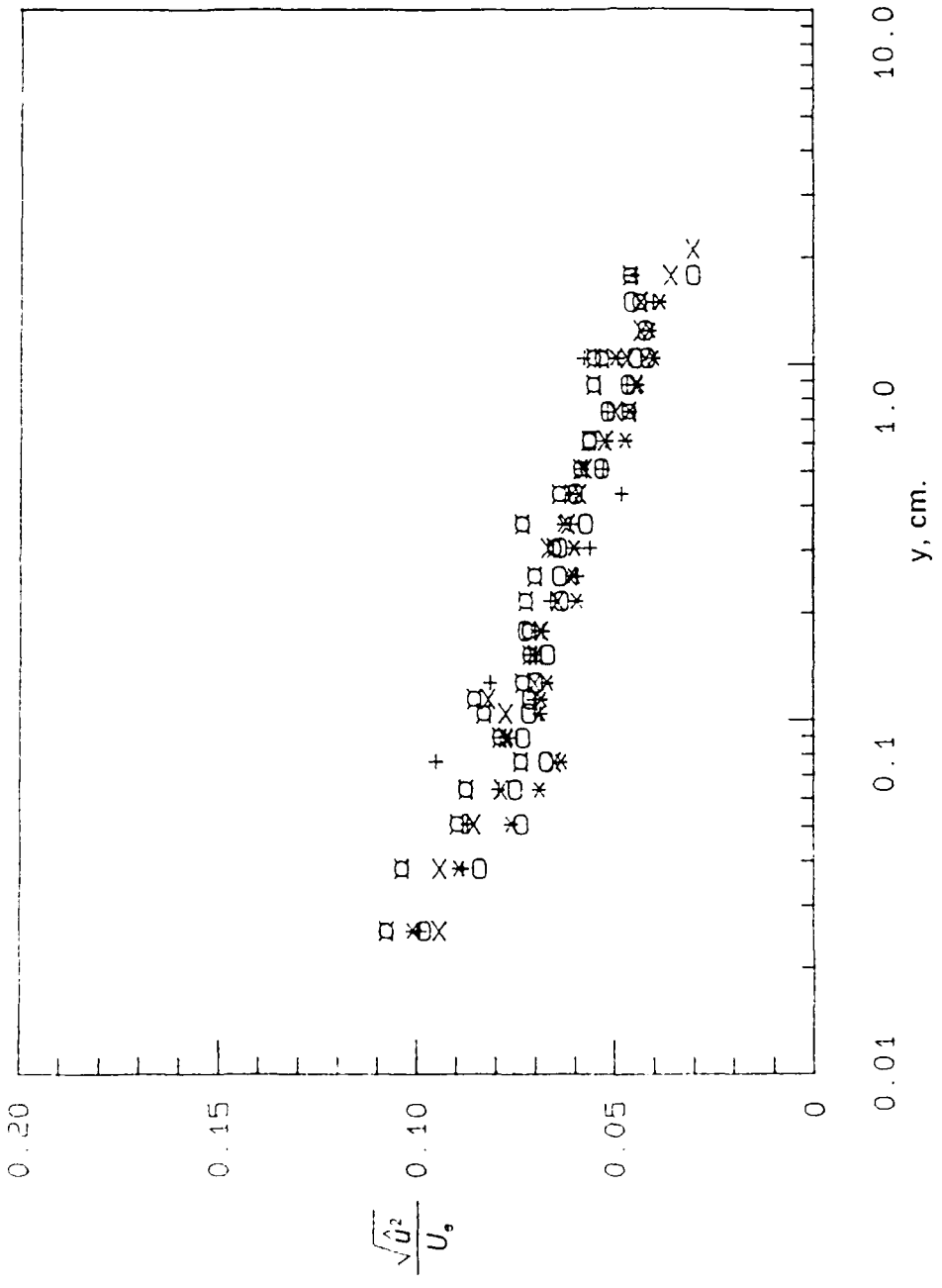


Figure 17. Streamwise turbulence intensity profiles $\sqrt{\hat{u}^2}/\hat{U}_\infty$ at $X=0.53$
 $m, k=1.33$ flow; (+ = 90° ; * = 135° ; $\circ = 180^\circ$; $\times = 225^\circ$;
 $\square = 270^\circ$)

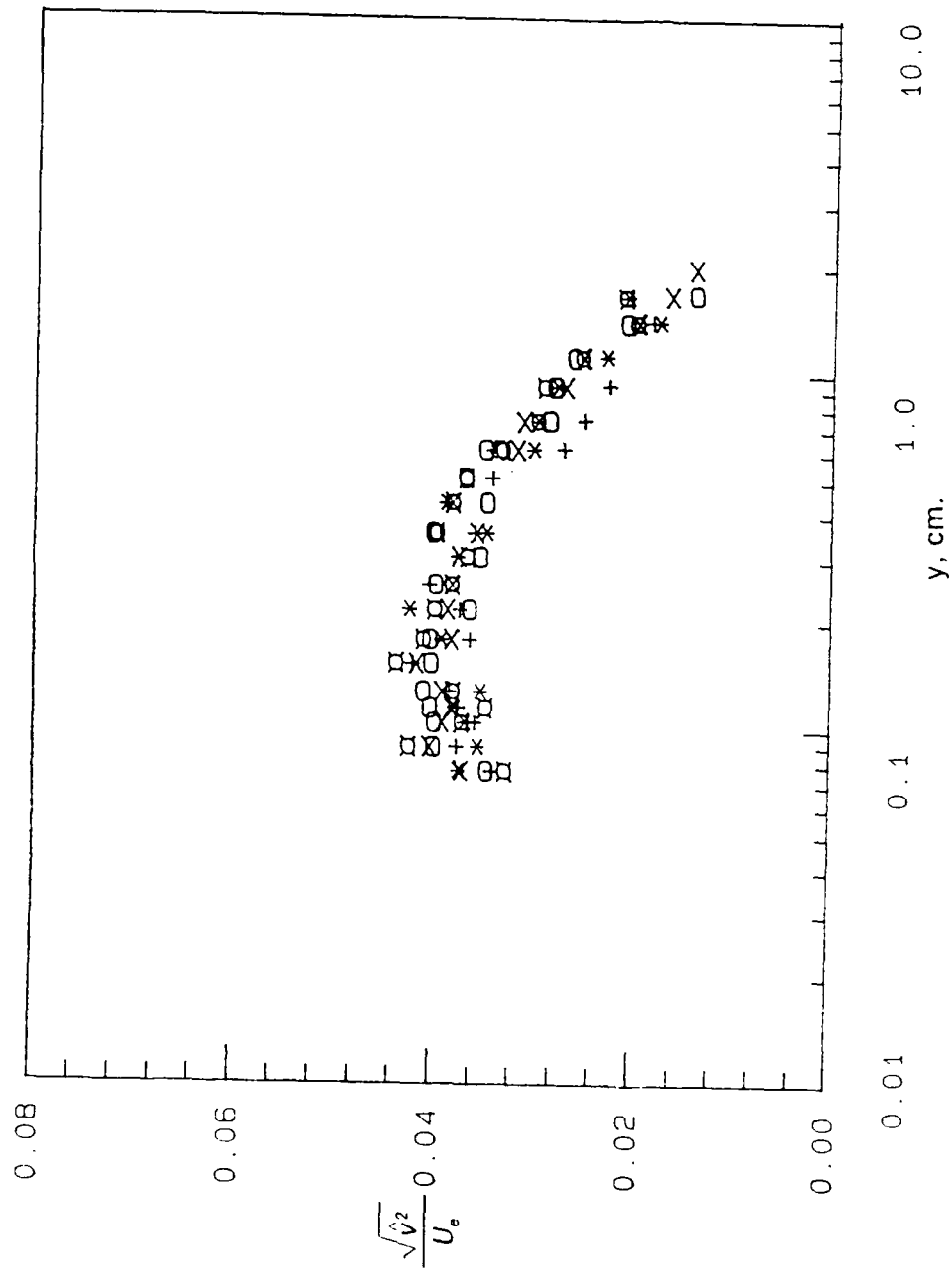


Figure 18. Normal-to-wall turbulence intensity profiles, $\sqrt{\hat{v}^2}/U_e$, at $X = 0.53 \text{ m}$, $k = 1.33$ flow; Legend same as in figure 17.

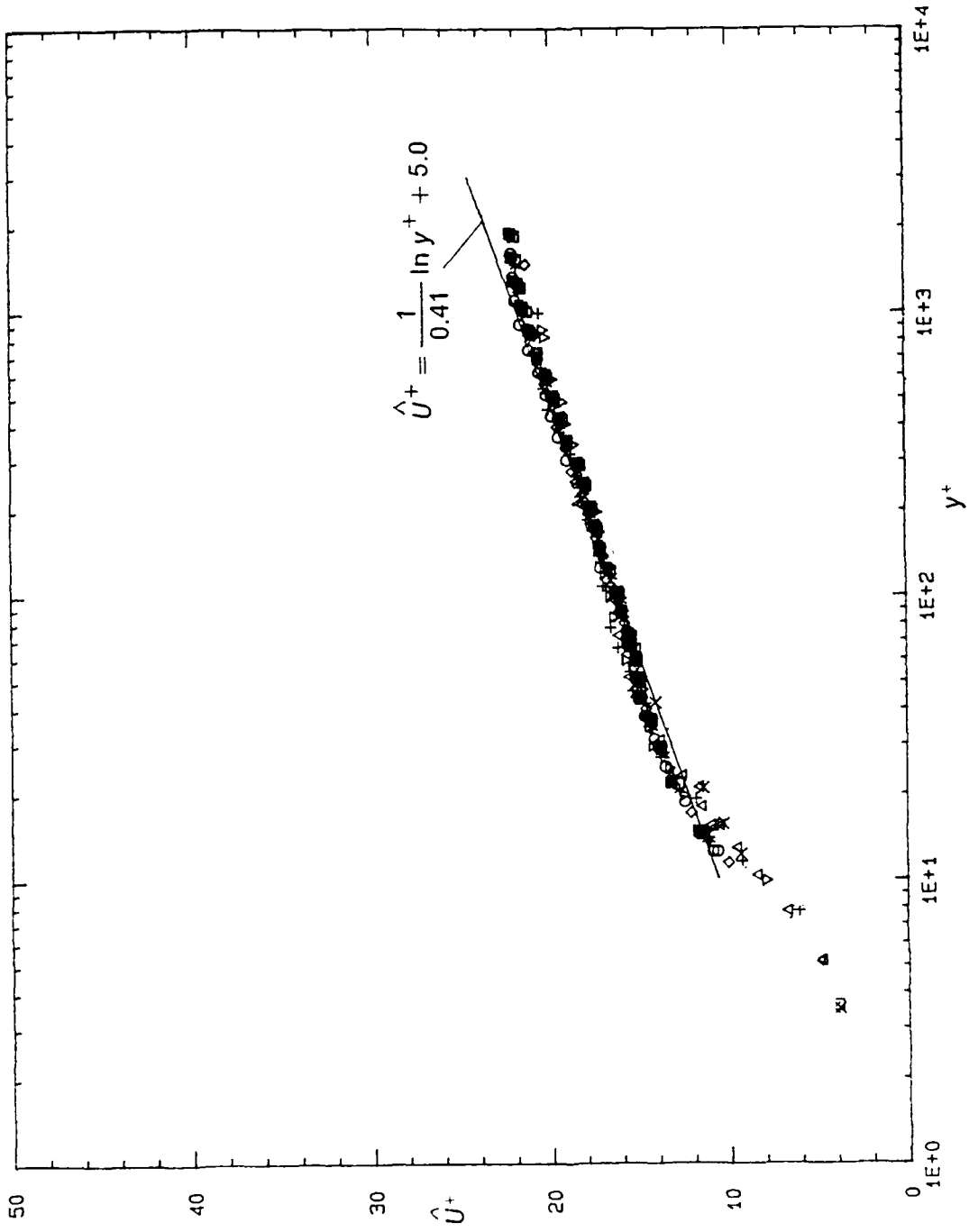


Figure 19a. Ensemble-averaged law-of-the-wall velocity profiles, \hat{U}^+ vs. $\log_{10} y^+$, $X = 0.53\text{m}$, $k = 1.33$ flow. ($\Delta = 45^\circ$; $+$ = 60° ; $\nabla = 75^\circ$; $\diamond = 90^\circ$; $\circ = 105^\circ$; $*$ = 120° ; $\square = 135^\circ$; $\triangle = 150^\circ$; $\triangledown = 165^\circ$; $\blacksquare = 180^\circ$) open symbols, laser anemometer; Solid Symbols, cross-wire measurements. Solid line given by equation 5.

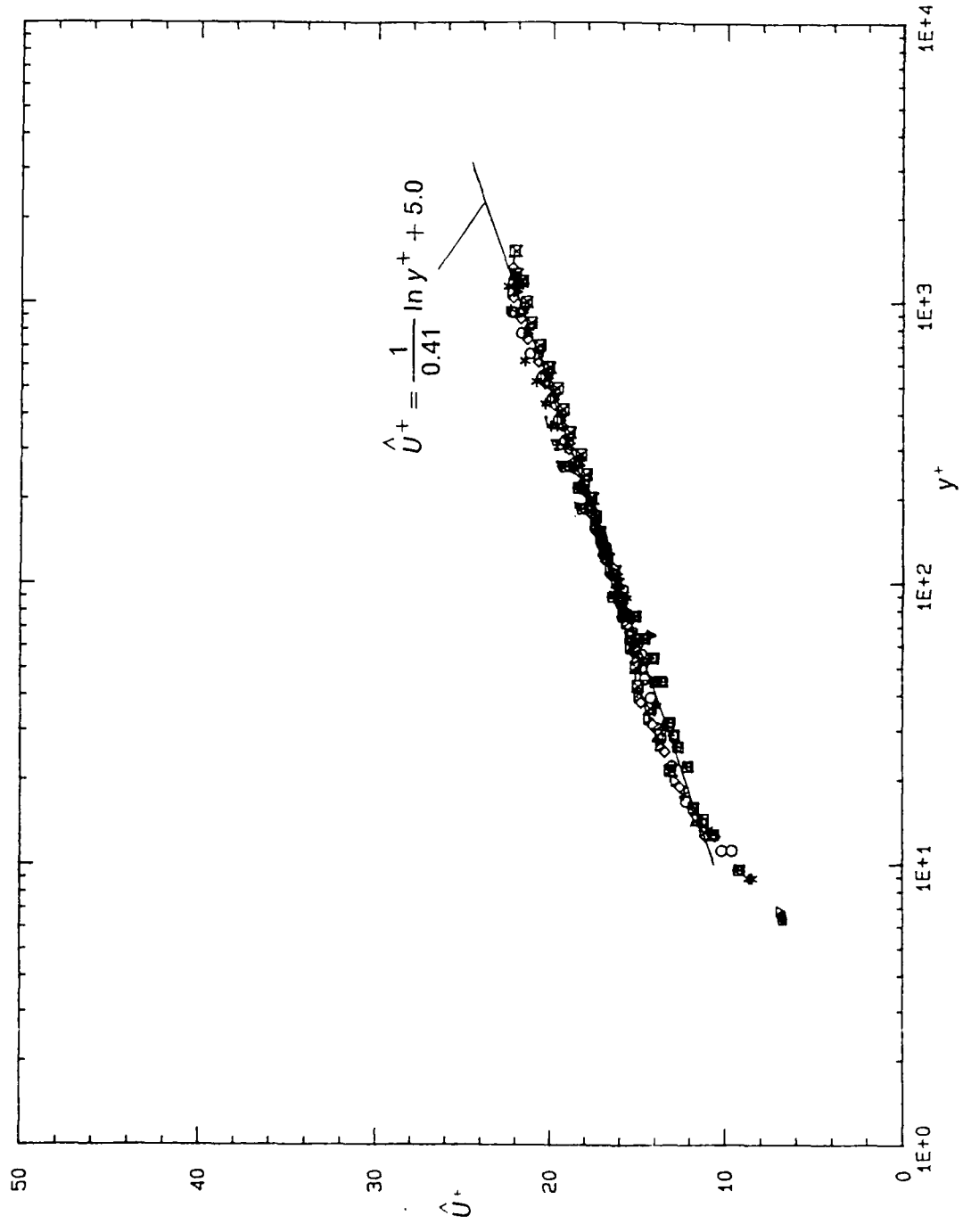


Figure 19b. Ensemble-averaged law-of-the-wall velocity profiles, $\hat{U}^+ \text{ vs. } \log_{10} y^+$, $X = 0.53\text{m}$, $k = 1.33$ flow. ($\square = 195^\circ$; $\times = 210^\circ$; $\triangle = 225^\circ$; $+$ = 240° ; $\nabla = 255^\circ$; $\diamond = 270^\circ$; $\circ = 285^\circ$; $*$ = 300° ; $\blacksquare = 315^\circ$; $\triangle = 330^\circ$) open symbols, laser anemometer; solid Symbols, cross-wire measurements. Solid line given by equation 5.

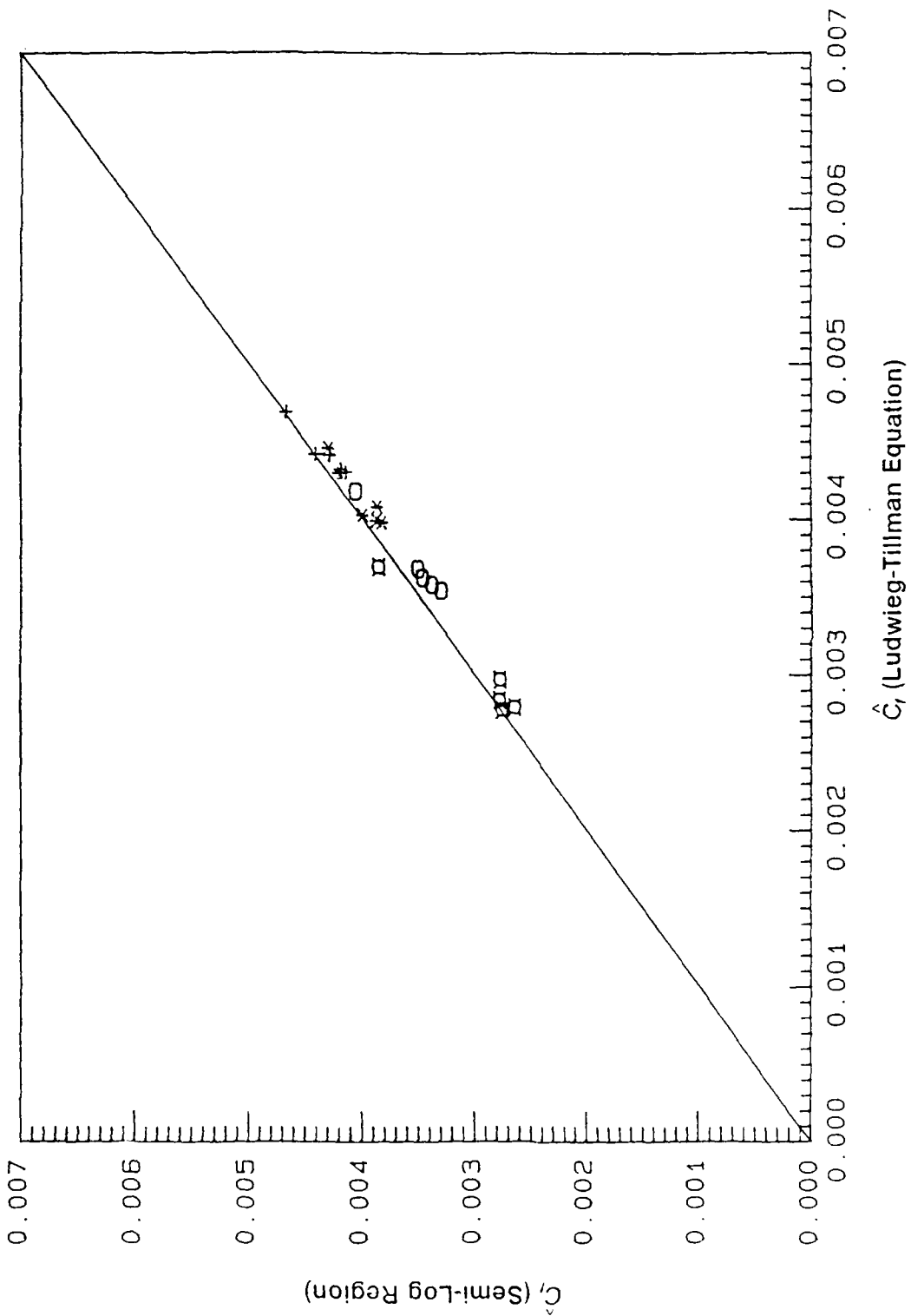


Figure 20. Correlation between \hat{C}_r obtained from Semi-Log Region and \hat{C}_r obtained from Ludwieg-Tillman equation 6; $90^\circ \leq \omega t \leq 270^\circ$; ($+$, $X = 0.53\text{ m}$, \circ , $X = 0.96\text{ m}$, \square , $X = 1.45\text{ m}$)

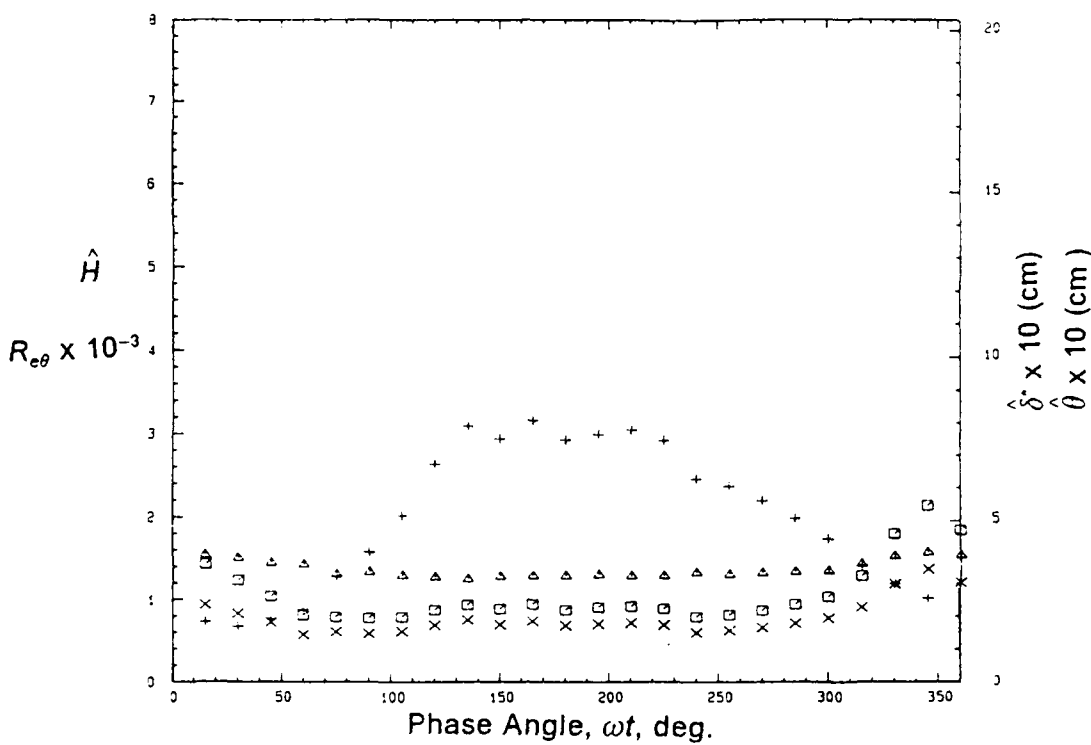


Figure 21a. Variation of displacement thickness, momentum thickness, shape factor and Reynolds number with phase angle at $X=0.53$ m, $k=0.61$ flow. ($\square = \hat{\delta}$, $\times = \hat{\theta}$, $\triangle = \hat{H}$, $+ = R_{e\theta}$)

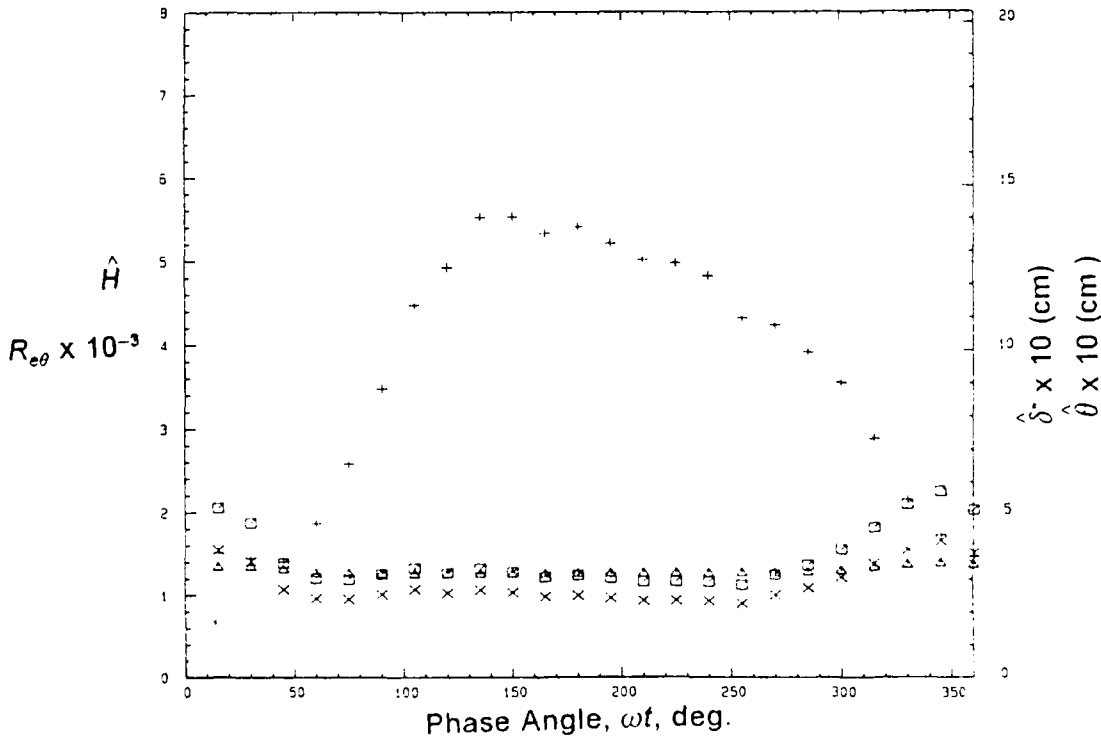


Figure 21b. Variation of displacement thickness, momentum thickness, shape factor and Reynolds number with phase angle at $X=1.45$ m, $k=0.61$ flow. Legend same as in figure 21a.

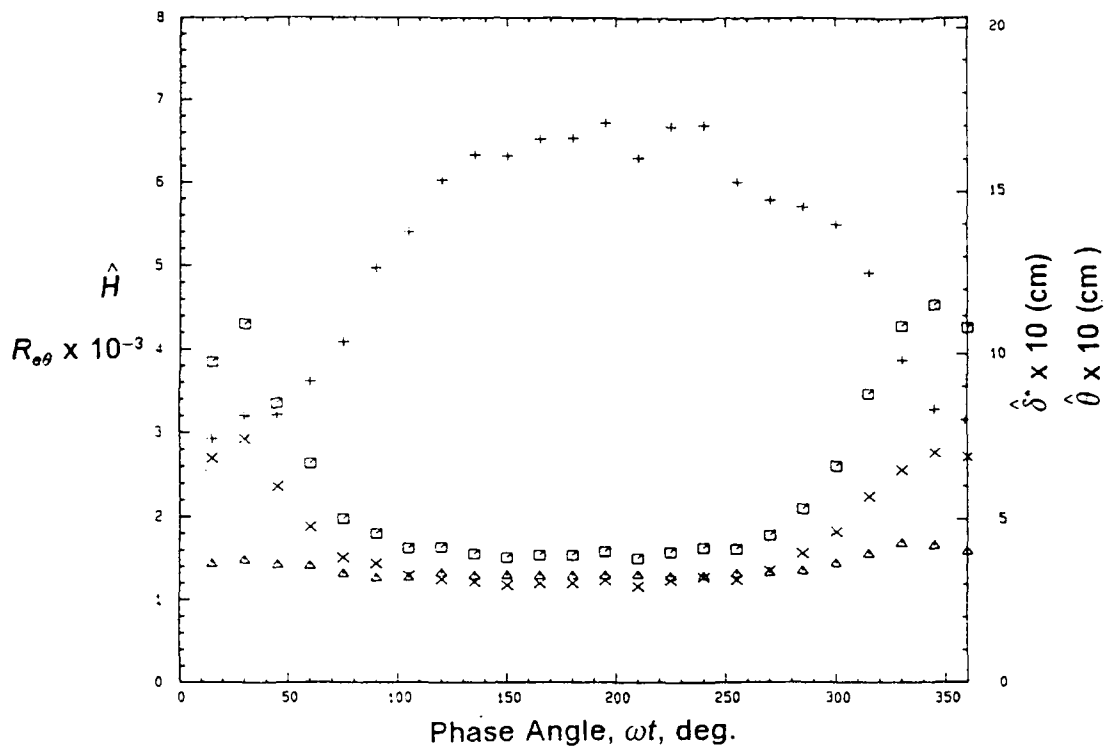


Figure 21c. Variation of displacement thickness, momentum thickness, shape factor and Reynolds number with phase angle at $X = 1.83$ m, $k = 0.61$ flow. Legend same as in figure 21a.

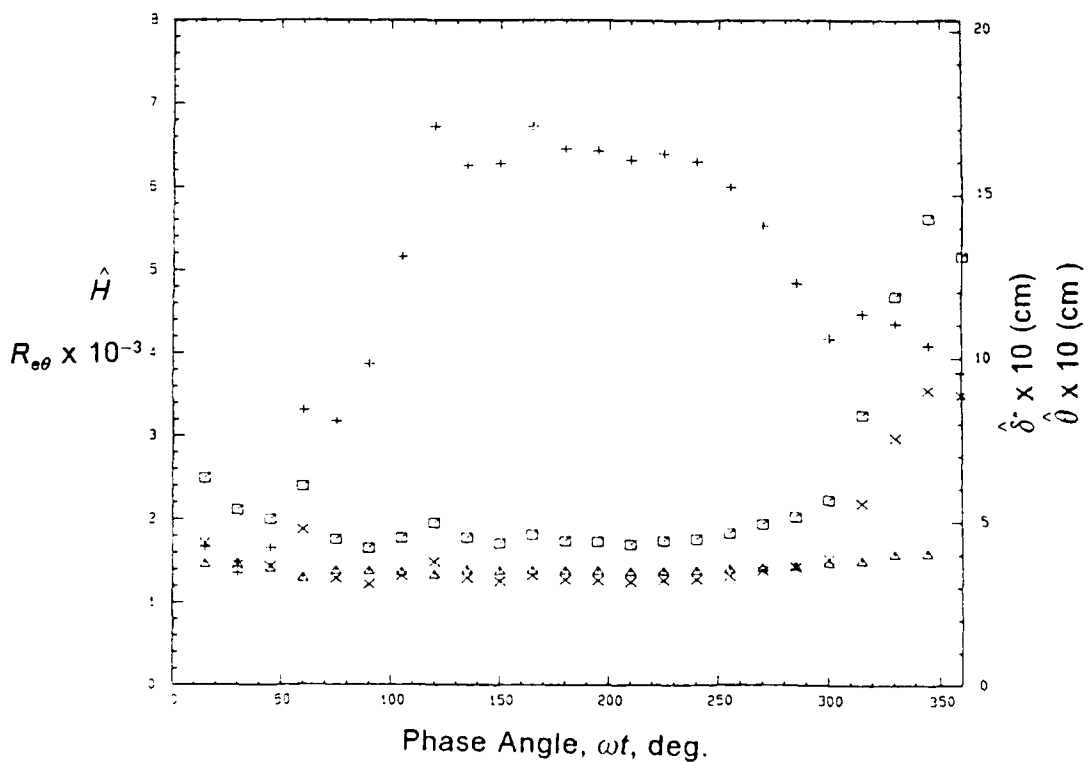


Figure 21d. Variation of displacement thickness, momentum thickness, shape factor and Reynolds number with phase angle at $X = 2.20$ m, $k = 0.61$ flow. Legend same as in figure 21a.

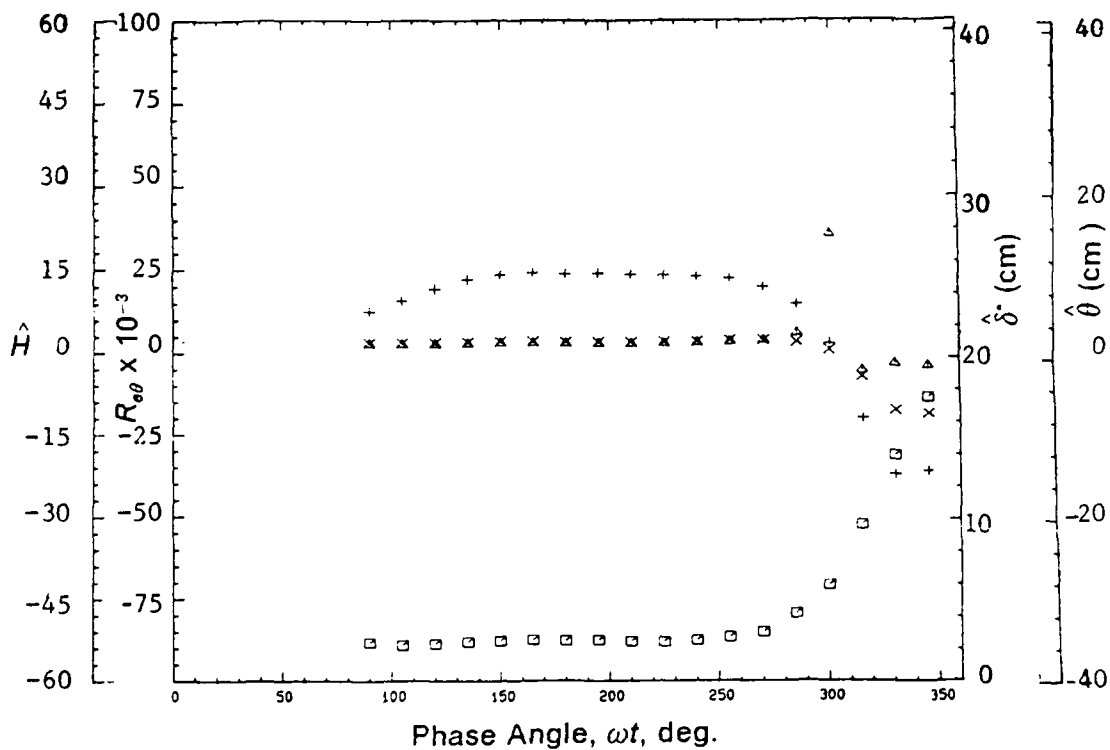


Figure 21e. Variation of displacement thickness, momentum thickness, shape factor and Reynolds number with phase angle at $X=2.95$ m, $k=0.61$ flow. Legend same as in figure 21a.

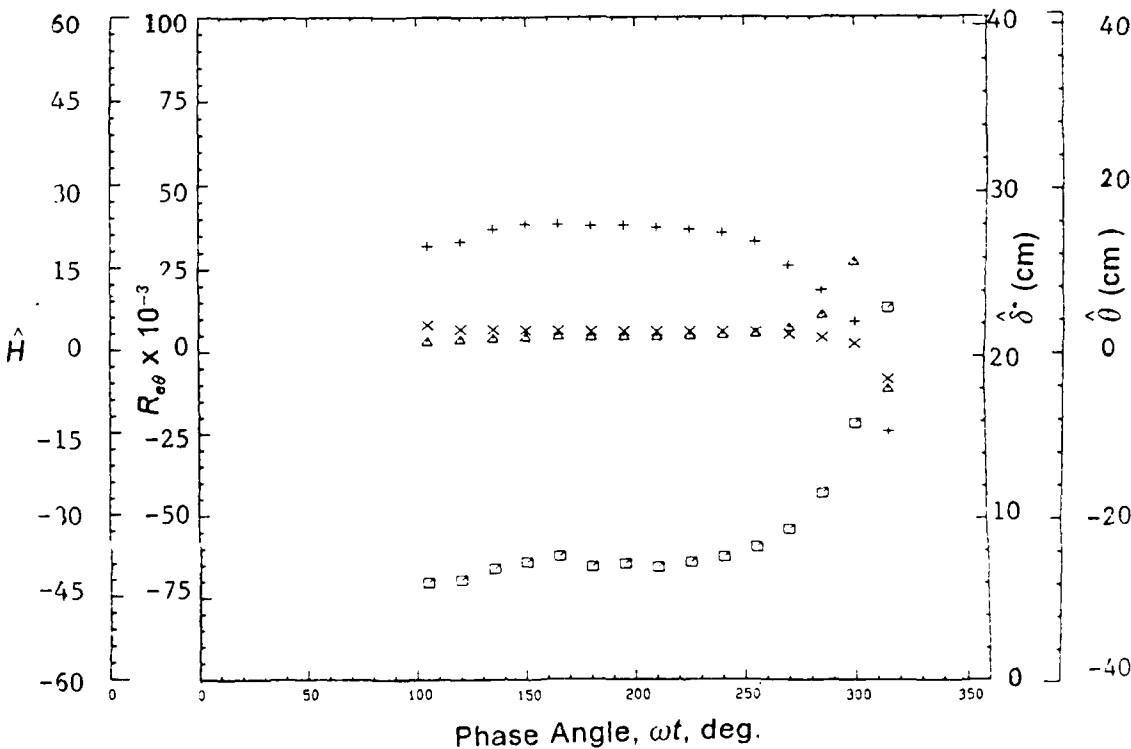


Figure 21f. Variation of displacement thickness, momentum thickness, shape factor and Reynolds number with phase angle at $X=3.51$ m, $k=0.61$ flow. Legend same as in figure 21a.

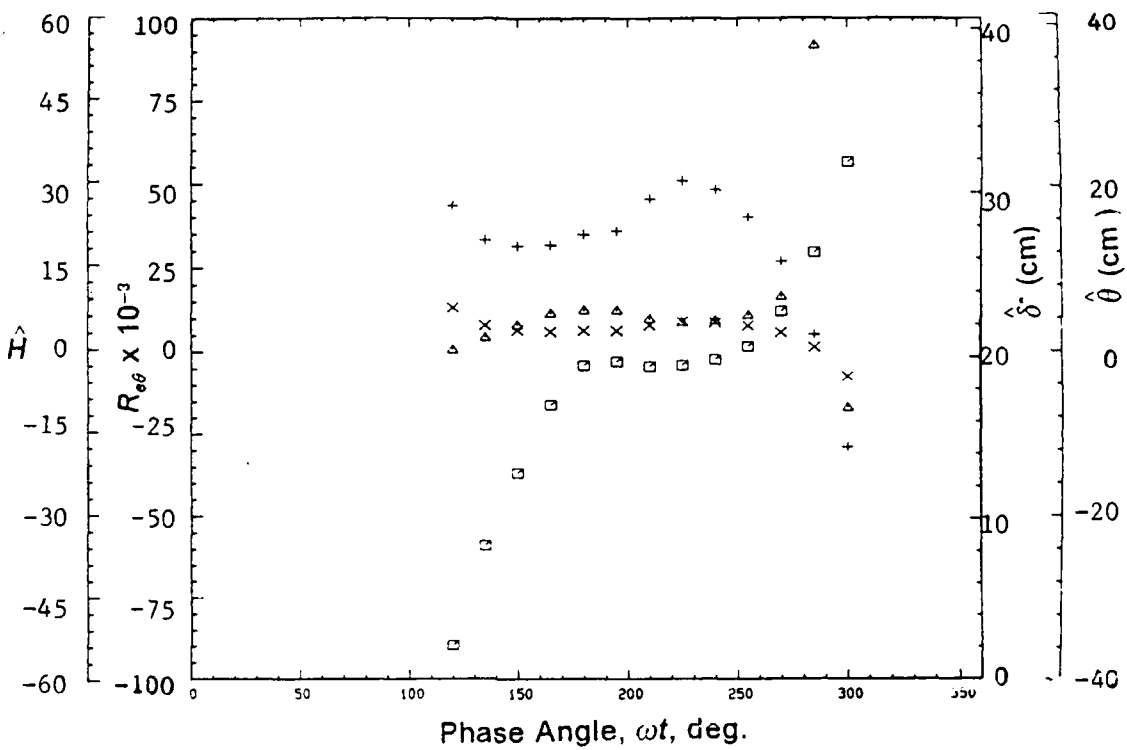


Figure 21g. Variation of displacement thickness, momentum thickness, shape factor and Reynolds number with phase angle at $X=4.27$ m, $k=0.61$ flow. Legend same as in figure 21a.

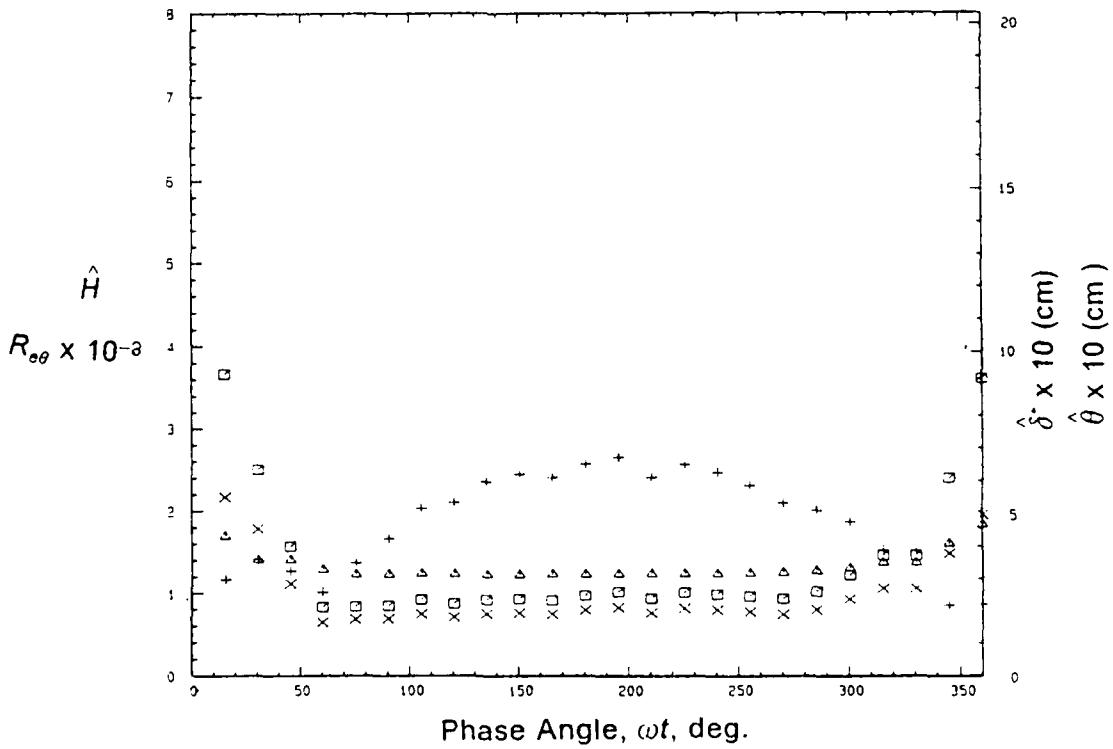


Figure 22a. Variation of displacement thickness, momentum thickness, shape factor and Reynolds number with phase angle at $X=0.53$ m, $k=1.33$ flow. Legend same as in figure 21a.

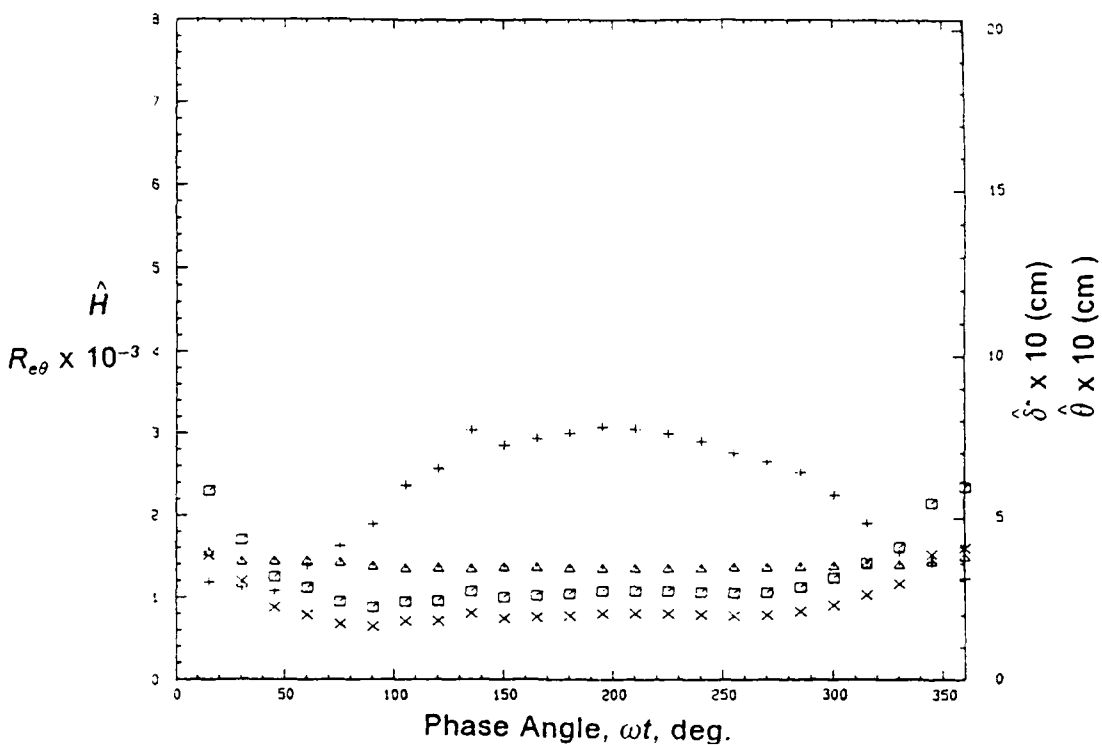


Figure 22b. Variation of displacement thickness, momentum thickness, shape factor and Reynolds number with phase angle at $X = 1.45$ m, $k = 1.33$ flow. Legend same as in figure 21a.

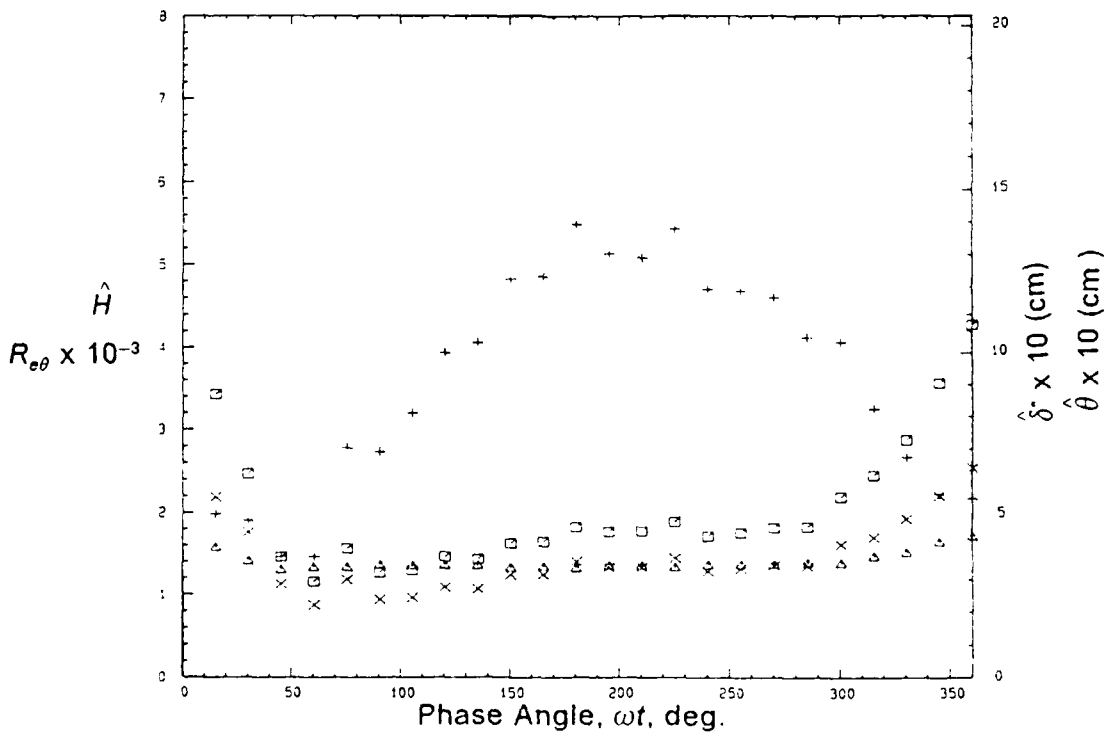


Figure 22c. Variation of displacement thickness, momentum thickness, shape factor and Reynolds number with phase angle at $X = 1.83$ m, $k = 1.33$ flow. Legend same as in figure 21a.

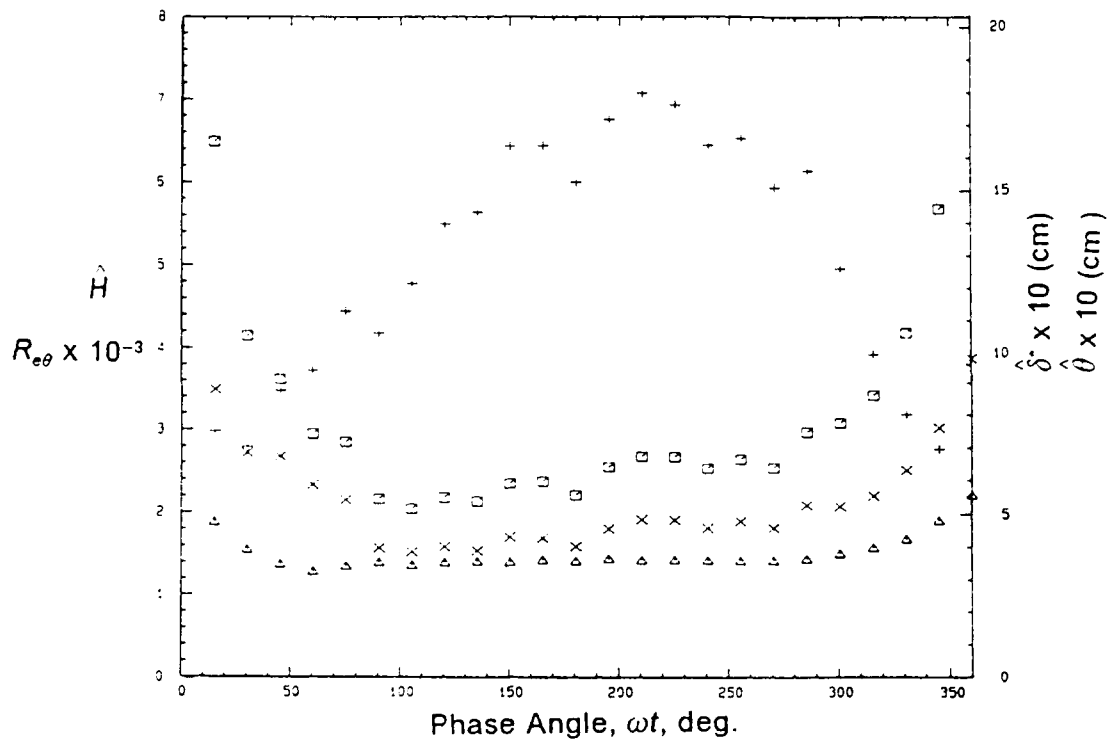


Figure 22d. Variation of displacement thickness, momentum thickness, shape factor and Reynolds number with phase angle at $X=2.20$ m, $k=1.33$ flow. Legend same as in figure 21a.

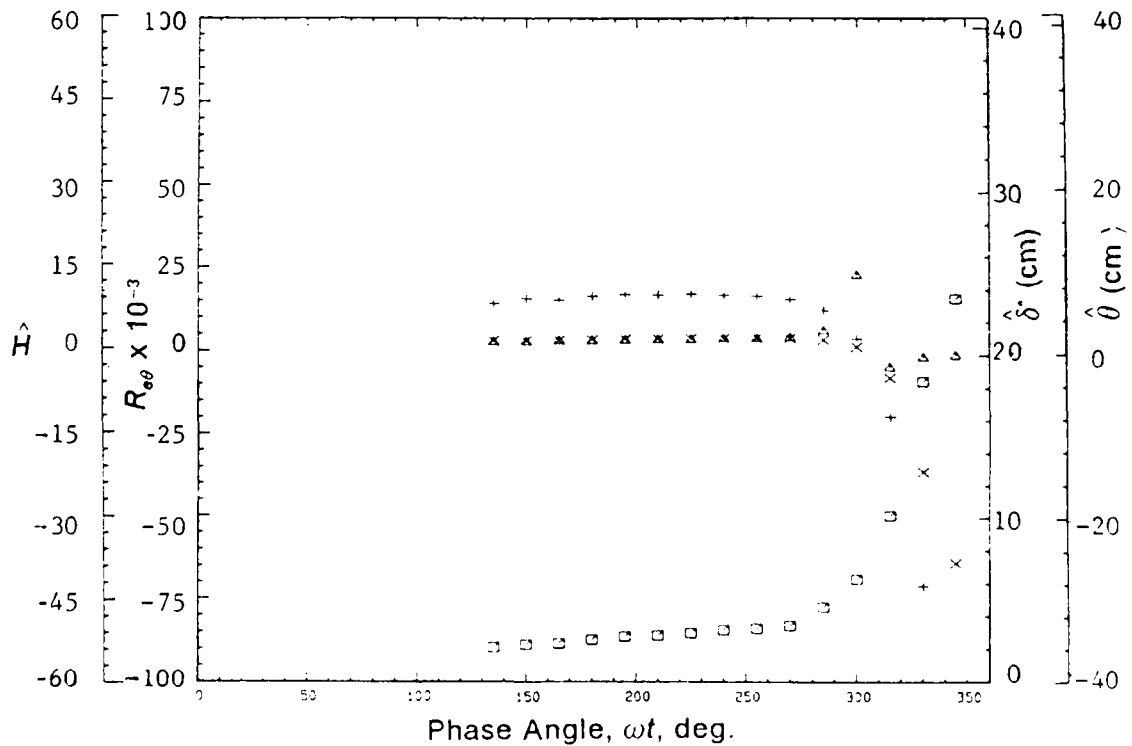


Figure 22e. Variation of displacement thickness, momentum thickness, shape factor and Reynolds number with phase angle at $X=2.95$ m, $k=1.33$ flow. Legend same as in figure 21a.

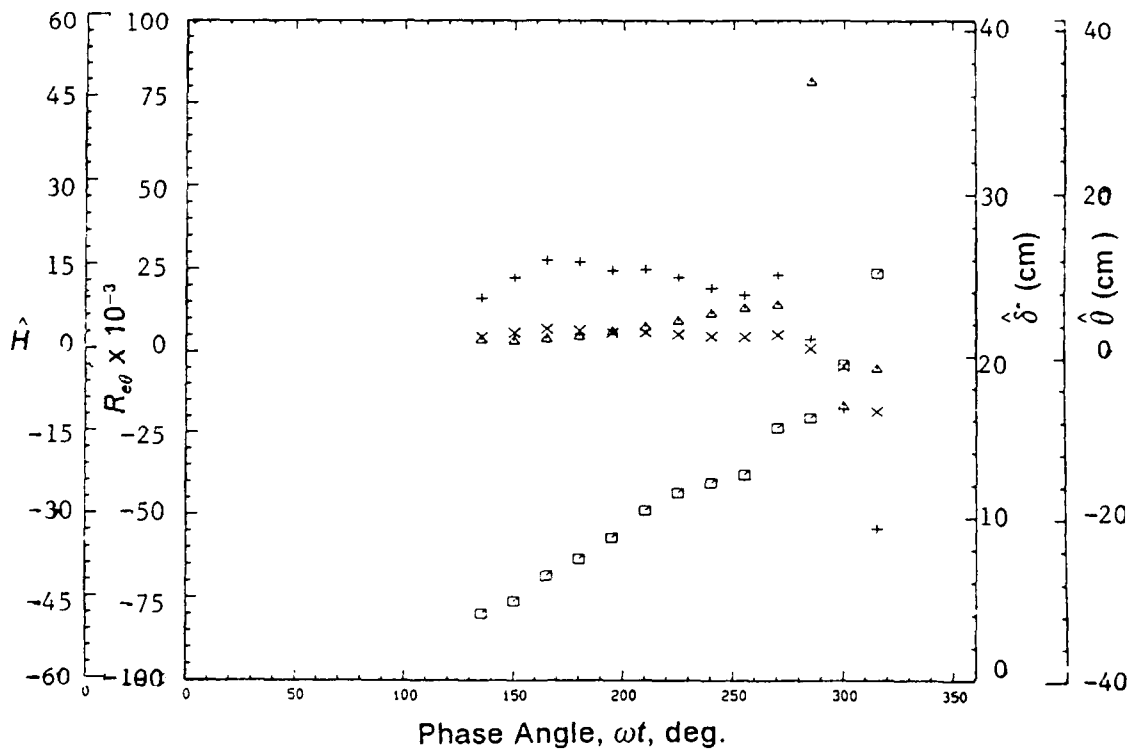


Figure 22f. Variation of displacement thickness, momentum thickness, shape factor and Reynolds number with phase angle at $X=3.51$ m, $k=1.33$ flow. Legend same as in figure 21a.

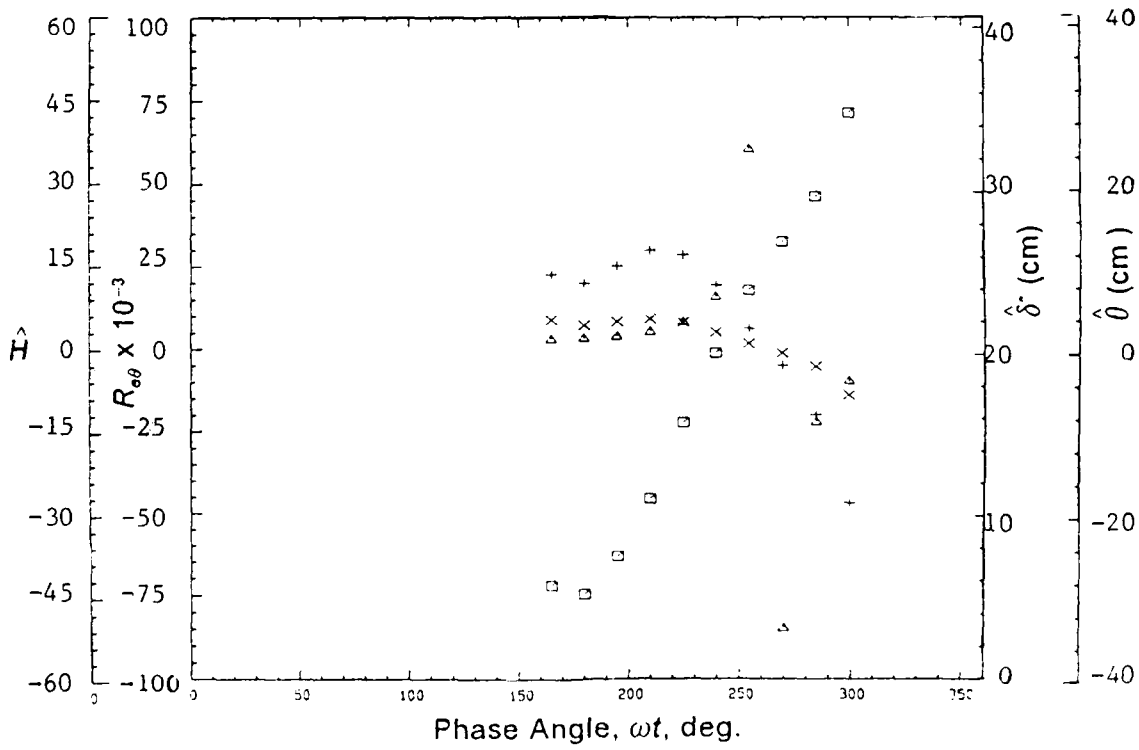


Figure 22g. Variation of displacement thickness, momentum thickness, shape factor and Reynolds number with phase angle at $X=4.27$ m, $k=1.33$ flow. Legend same as in figure 21a.

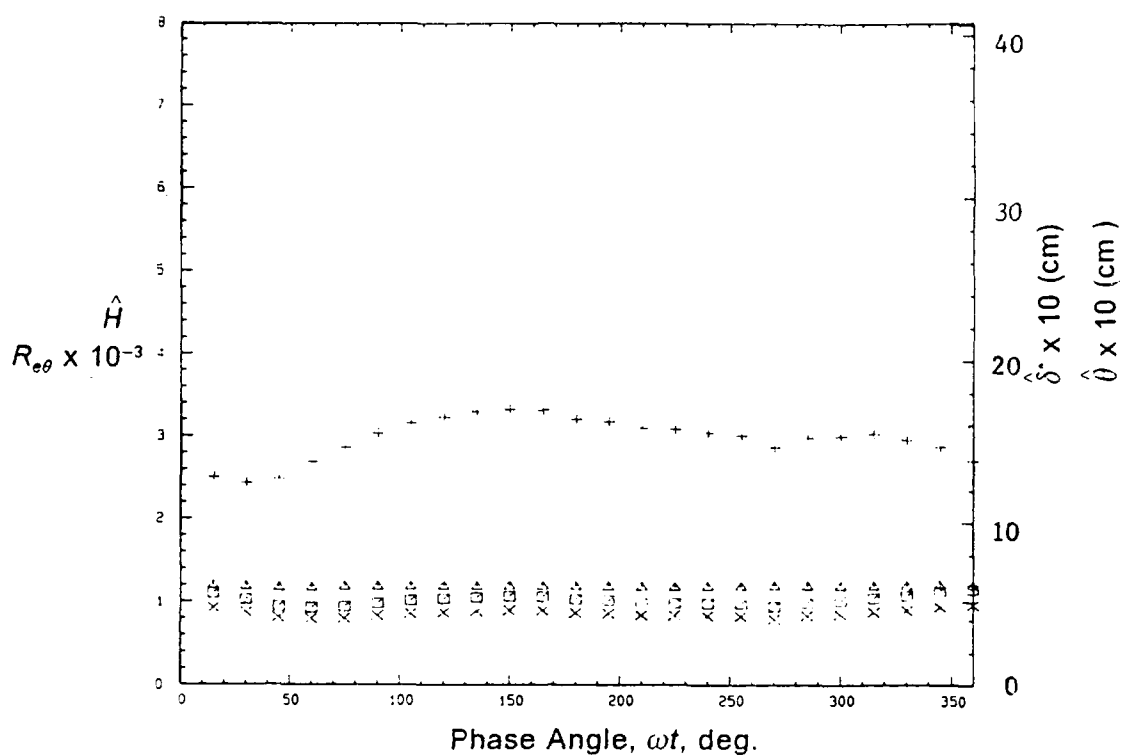


Figure 23a. Variation of displacement thickness, momentum thickness, shape factor and Reynolds number with phase angle at $X=1.63$ m, $k=1.03$ flow with 'roof damper'. Legend same as in figure 21a.

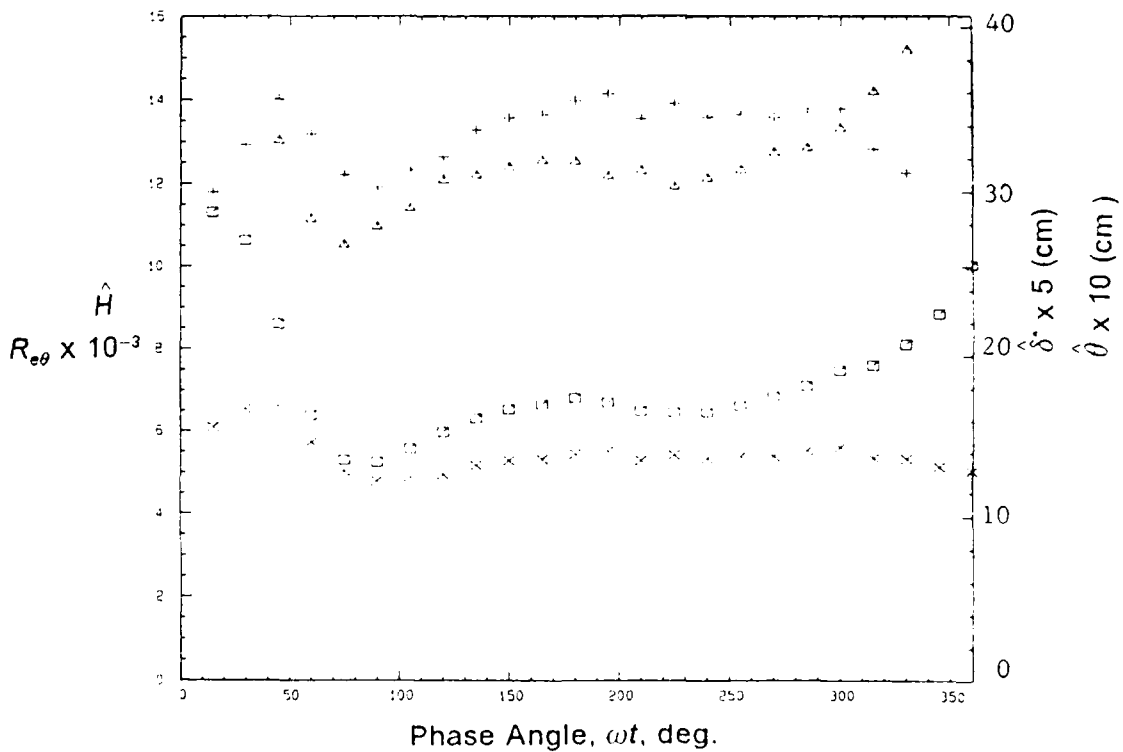


Figure 23b. Variation of displacement thickness, momentum thickness, shape factor and Reynolds number with phase angle at $X=3.01$ m, $k=1.03$ flow with 'roof damper'. Legend same as in figure 21a.

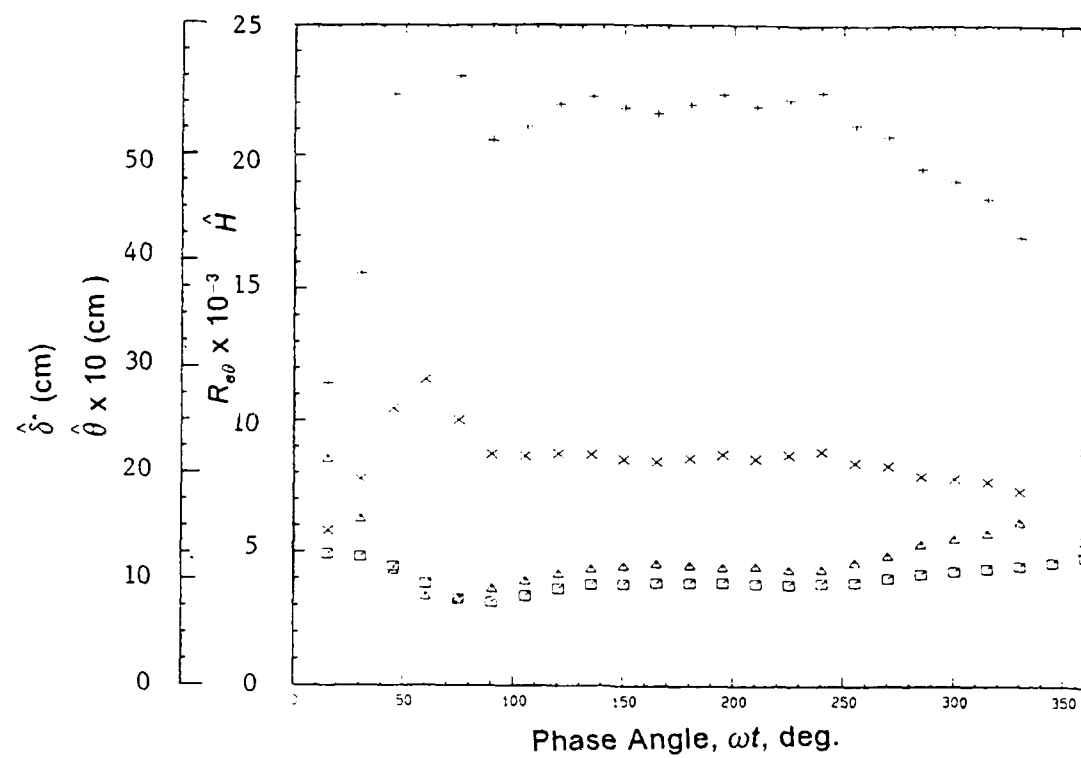


Figure 23c. Variation of displacement thickness, momentum thickness, shape factor and Reynolds number with phase angle at $X=3.28$ m, $k=1.03$ flow with 'roof damper'. Legend same as in figure 21a.

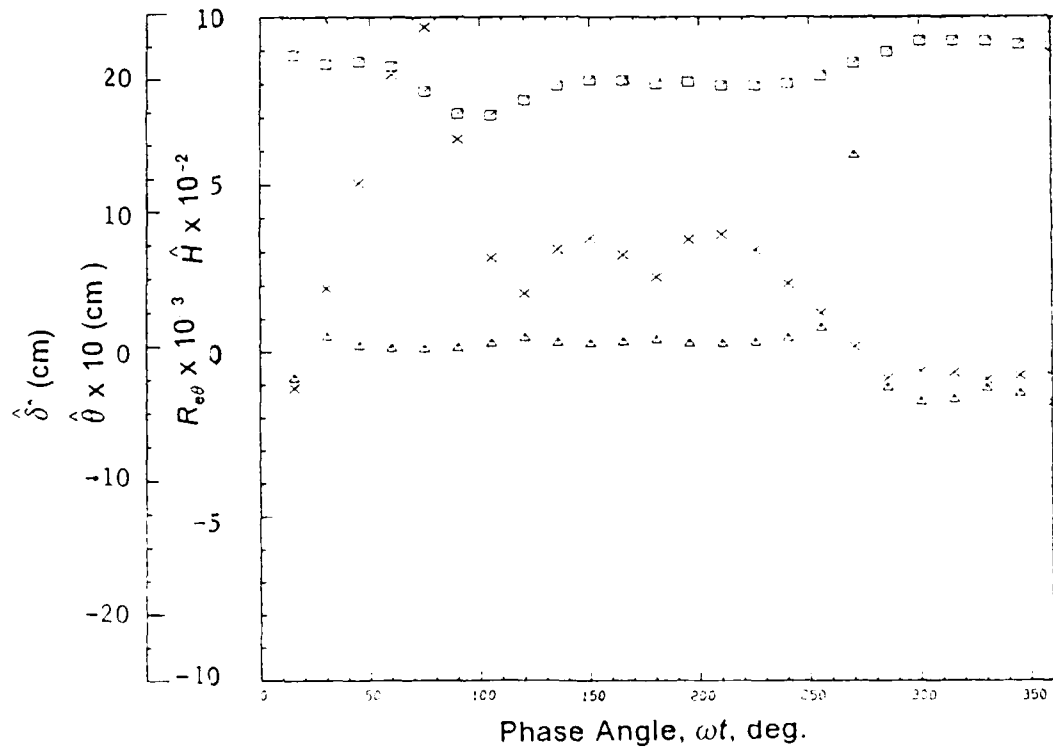


Figure 23d. Variation of displacement thickness, momentum thickness, shape factor and Reynolds number with phase angle at $X=3.58$ m, $k=1.03$ flow with 'roof damper'. Legend same as in figure 21a.

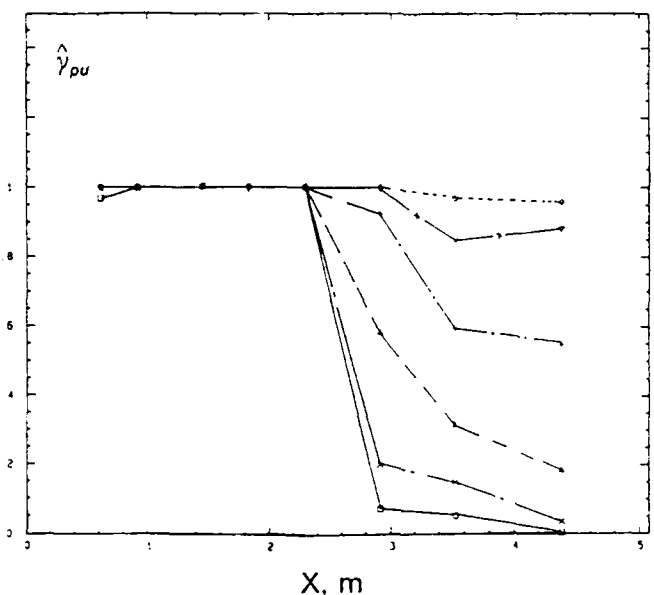


Figure 24a. Variation of $\hat{\gamma}_{pu}$ vs. X for different phases of a cycle, $k=0.61$ flow; (---) 15° ; (---) 30° ; (---) 45° ; (---) 60° ; (---x---) 75° ; (---.---) 90°).

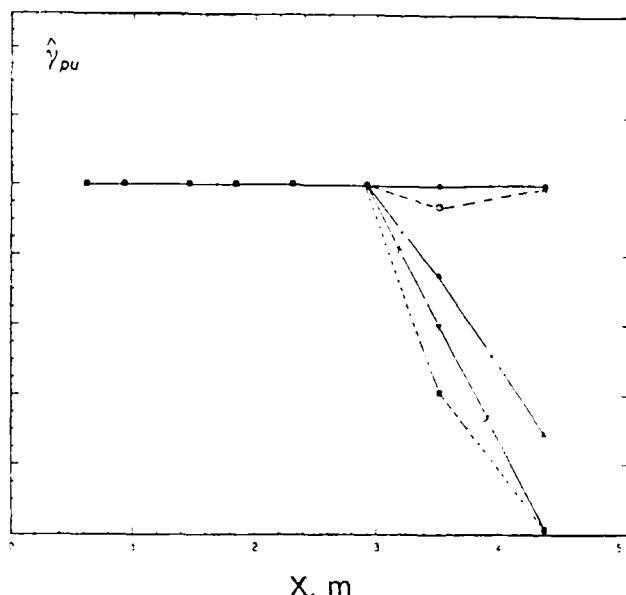


Figure 24b. Variation of $\hat{\gamma}_{pu}$ vs. X for different phases of a cycle, $k=0.61$ flow; (---) 105° ; (---) 120° ; (---) 135° ; (---) 150° ; (---x---) 165° ; (---.---) 180° .

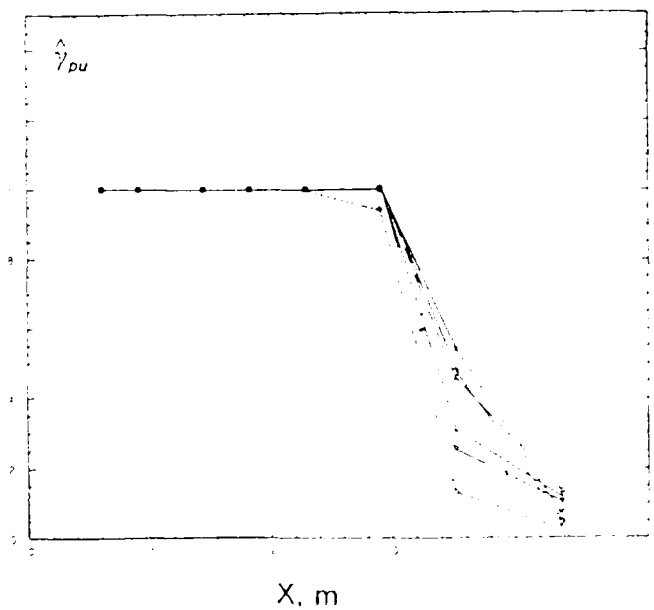


Figure 24c. Variation of $\hat{\gamma}_{pu}$ vs. X for different phases of a cycle, $k=0.61$ flow; (---) 195° ; (---) 210° ; (---) 225° ; (---) 240° ; (---x---) 255° ; (---.---) 270° .

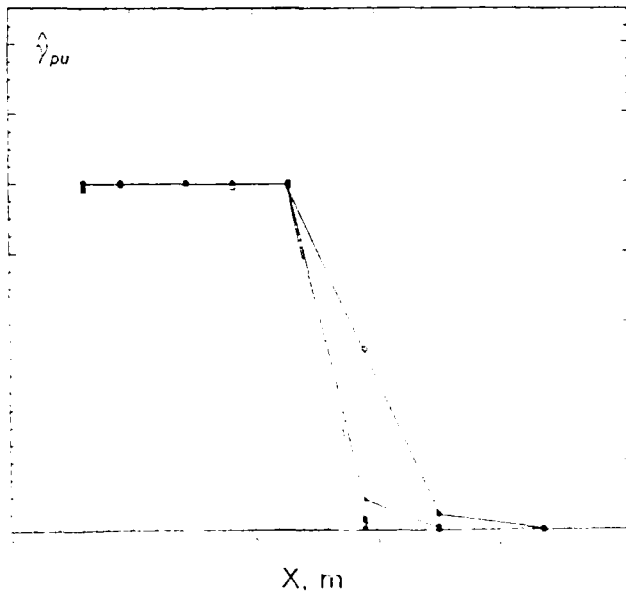


Figure 24d. Variation of $\hat{\gamma}_{pu}$ vs. X for different phases of a cycle, $k=0.61$ flow; (---) 285° ; (---) 300° ; (---) 315° ; (---) 330° ; (---x---) 345° ; (---.---) 360° .

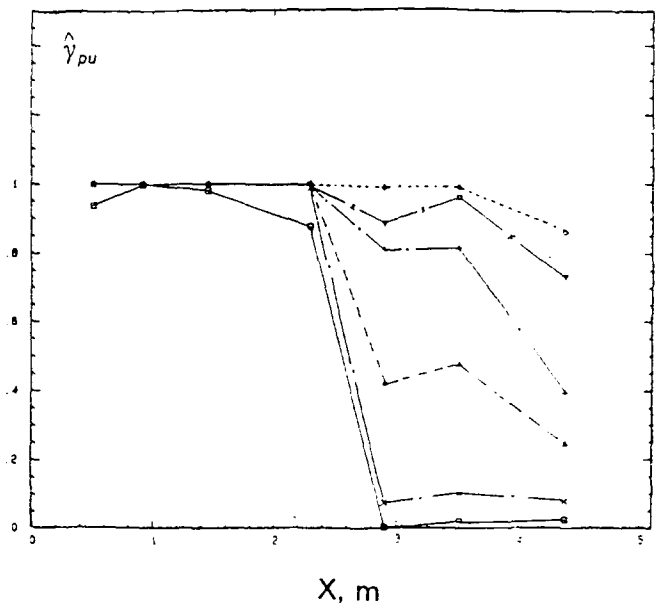


Figure 25a. Variation of $\hat{\gamma}_{pu}$ vs. X for different phases of a cycle, $k=1.33$ flow; Legend same as in figure 24a.

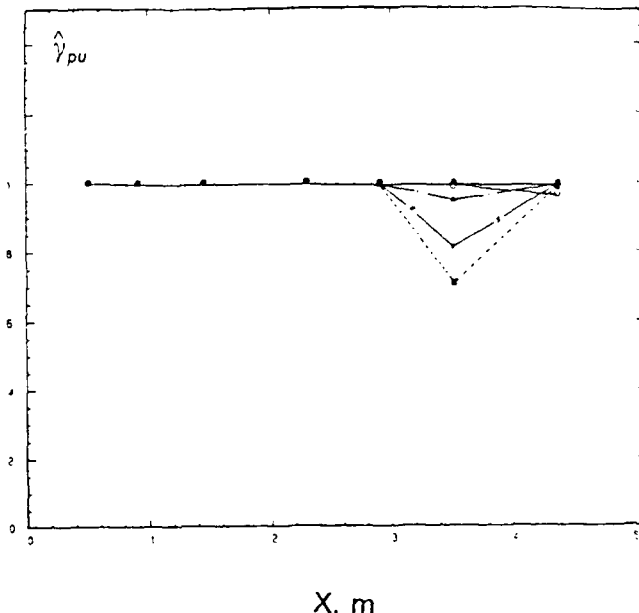


Figure 25b. Variation of $\hat{\gamma}_{pu}$ vs. X for different phases of a cycle, $k=1.33$ flow; Legend same as in figure 24b.

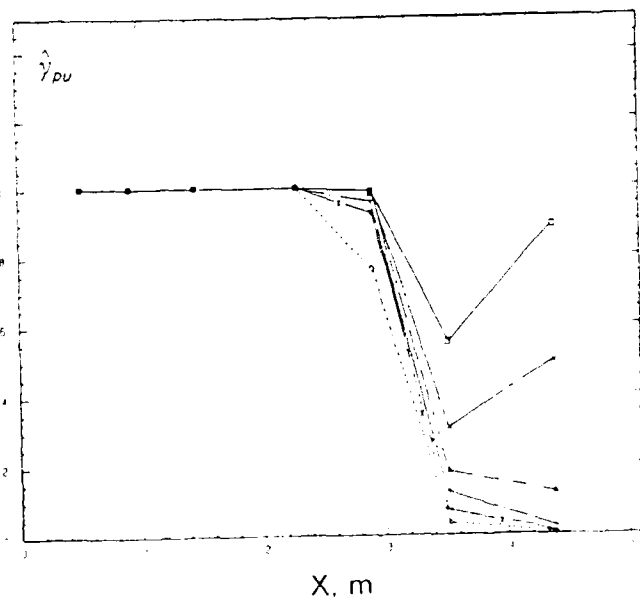


Figure 25c. Variation of $\hat{\gamma}_{tu}$ vs. X for different phases of a cycle, $k=1.33$ flow; Legend same as in figure 24c.

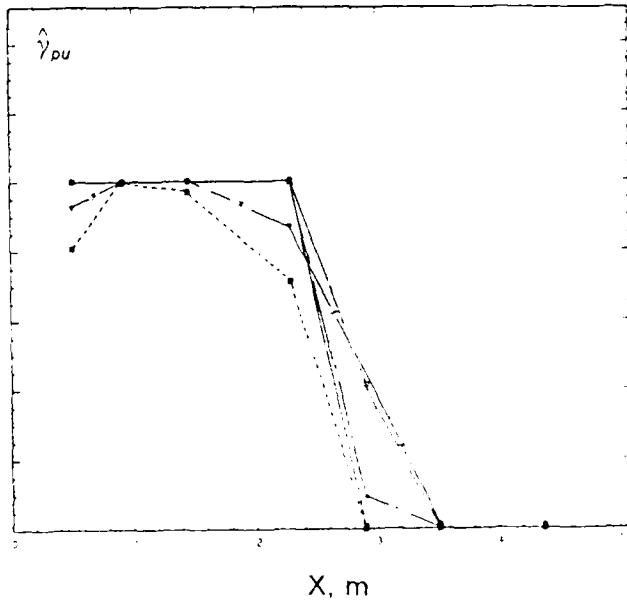


Figure 25d. Variation of $\hat{\gamma}_{tu}$ vs. X for different phases of a cycle, $k=1.33$ flow; Legend same as in figure 24d.

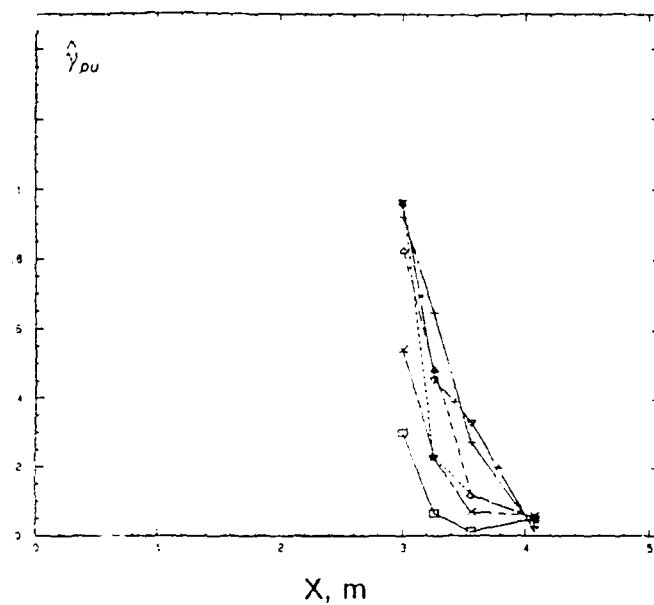


Figure 26a. Variation of $\hat{\gamma}_{pu}$ vs. X for different phases of a cycle, $k = 1.03$ flow with 'roof damper'; Legend same as in figure 24a.

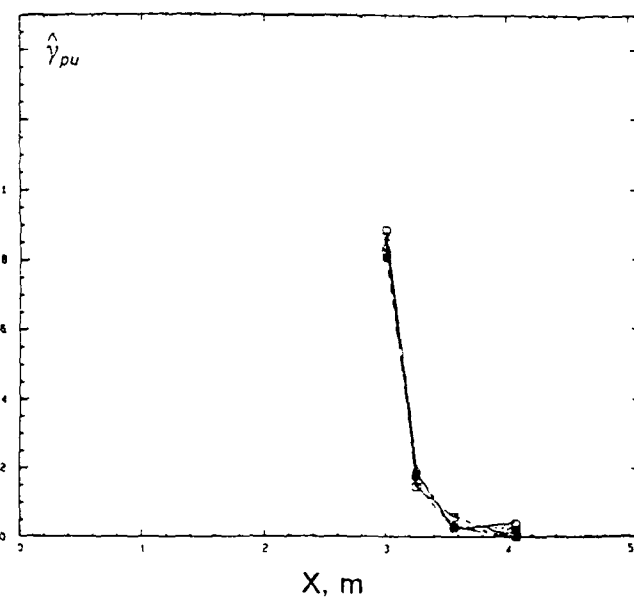


Figure 26b. Variation of $\hat{\gamma}_{pu}$ vs. X for different phases of a cycle, $k = 1.03$ flow with 'roof damper'; Legend same as in figure 24b.

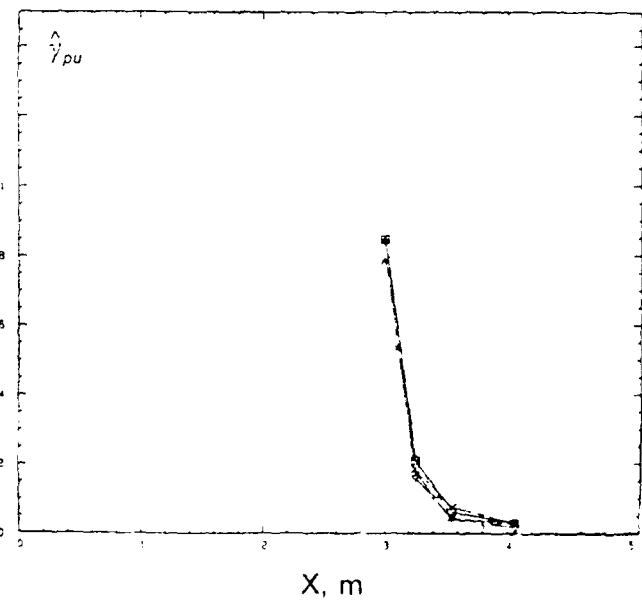


Figure 26c. Variation of $\hat{\gamma}_{pu}$ vs. X for different phases of a cycle, $k = 1.03$ flow with 'roof damper'; Legend same as in figure 24c.

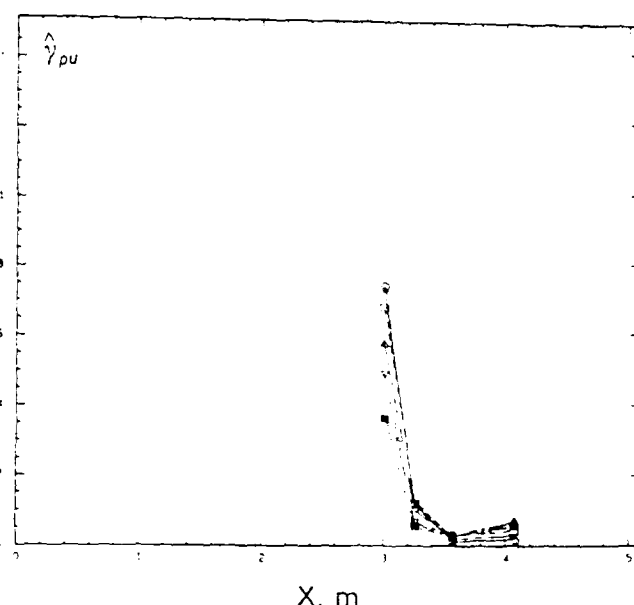


Figure 26d. Variation of $\hat{\gamma}_{pu}$ vs. X for different phases of a cycle, $k = 1.03$ flow with 'roof damper'; Legend same as in figure 24d.

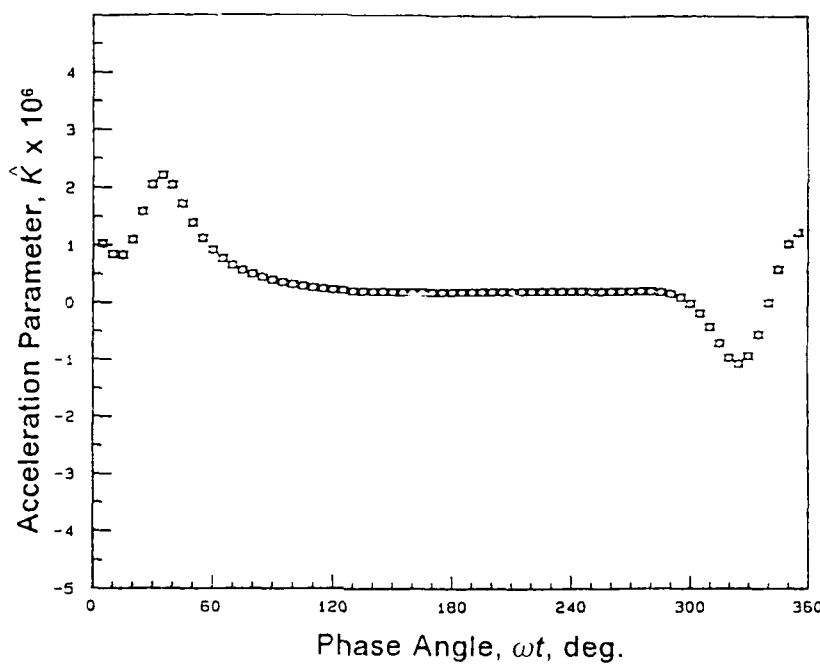


Figure 27a. Variation of acceleration parameter, \hat{K} with phase angle at $X = 0.53$ m, $k = 0.61$ flow.

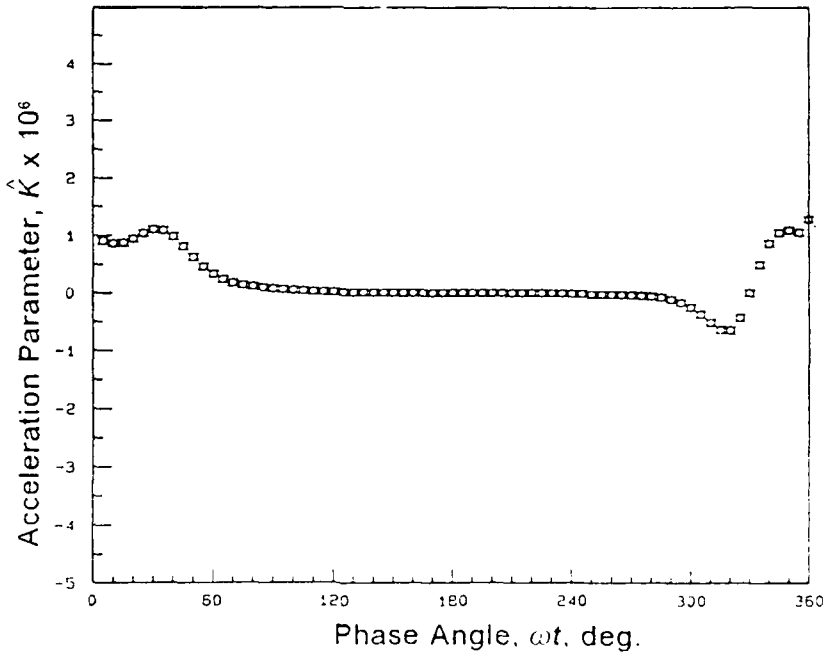


Figure 27b. Variation of acceleration parameter, \hat{K} with phase angle at $X = 1.45$ m, $k = 0.61$ flow.

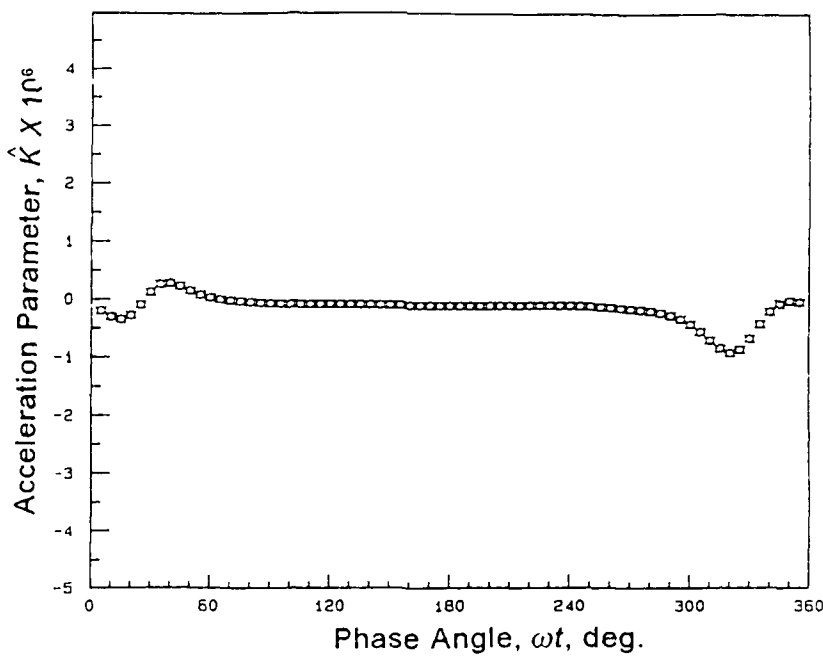


Figure 27c. Variation of acceleration parameter, \hat{K} with phase angle at $X=2.20$ m, $k=0.61$ flow.

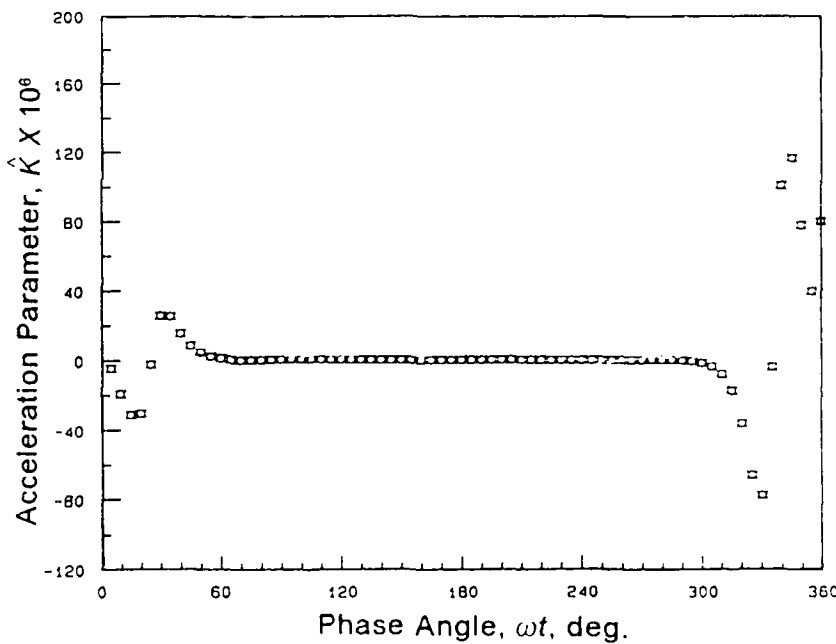


Figure 28a. Variation of acceleration parameter, \hat{K} with phase angle at $X=0.53$ m, $k=1.33$ flow.

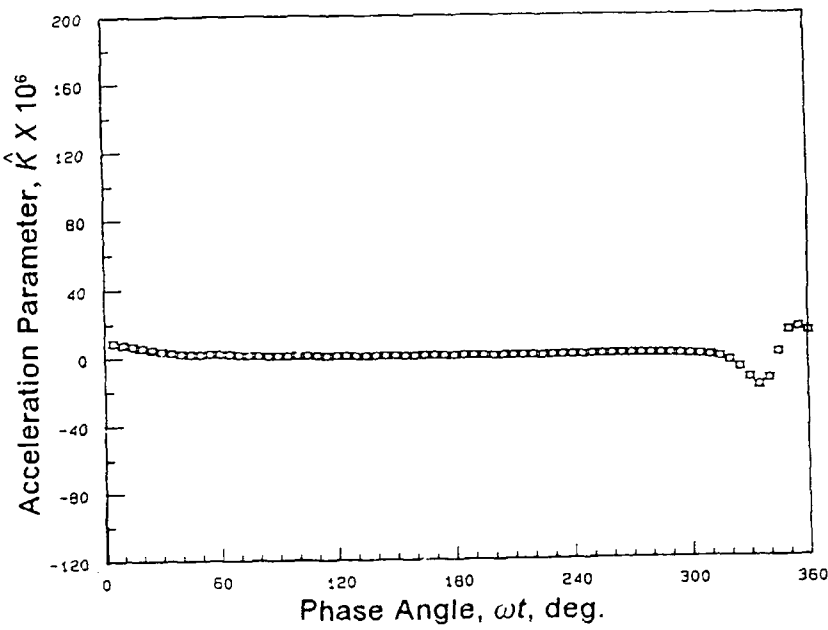


Figure 28b. Variation of acceleration parameter, \hat{K} with phase angle at $X = 1.45$ m, $k = 1.33$ flow.

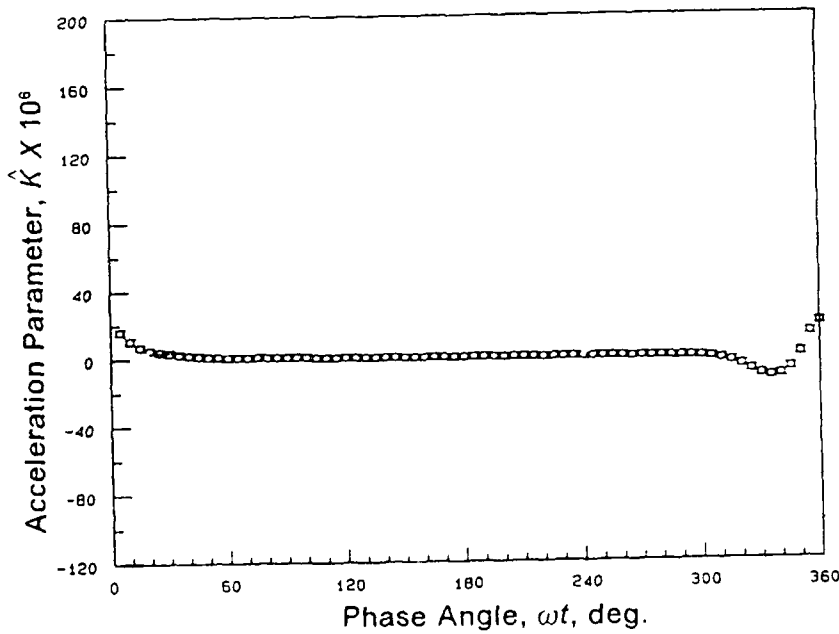


Figure 28c. Variation of acceleration parameter, \hat{K} with phase angle at $X = 2.20$ m, $k = 1.33$ flow.

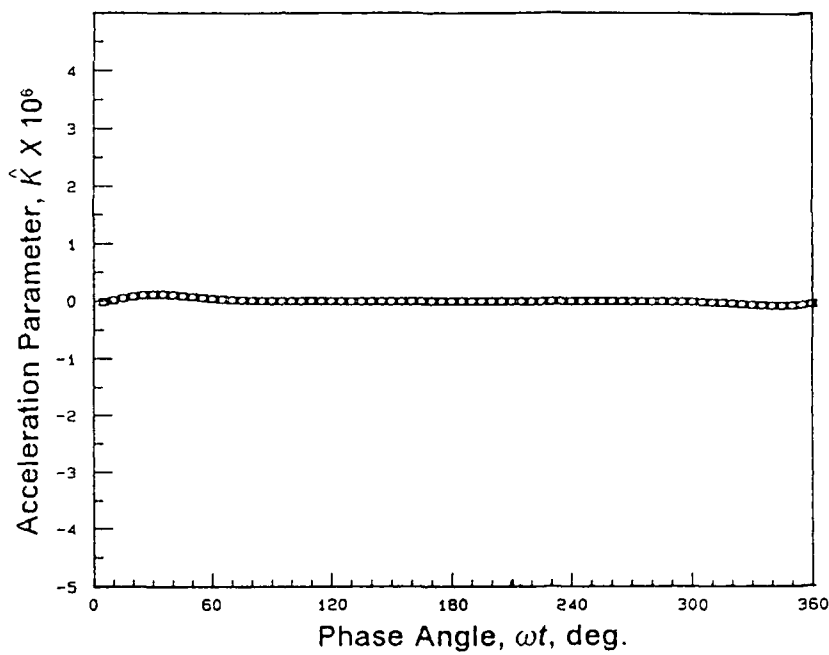


Figure 29. Variation of acceleration parameter, \hat{K} with phase angle at $X = 1.63$ m, $k = 1.03$ flow with 'roof damper'.

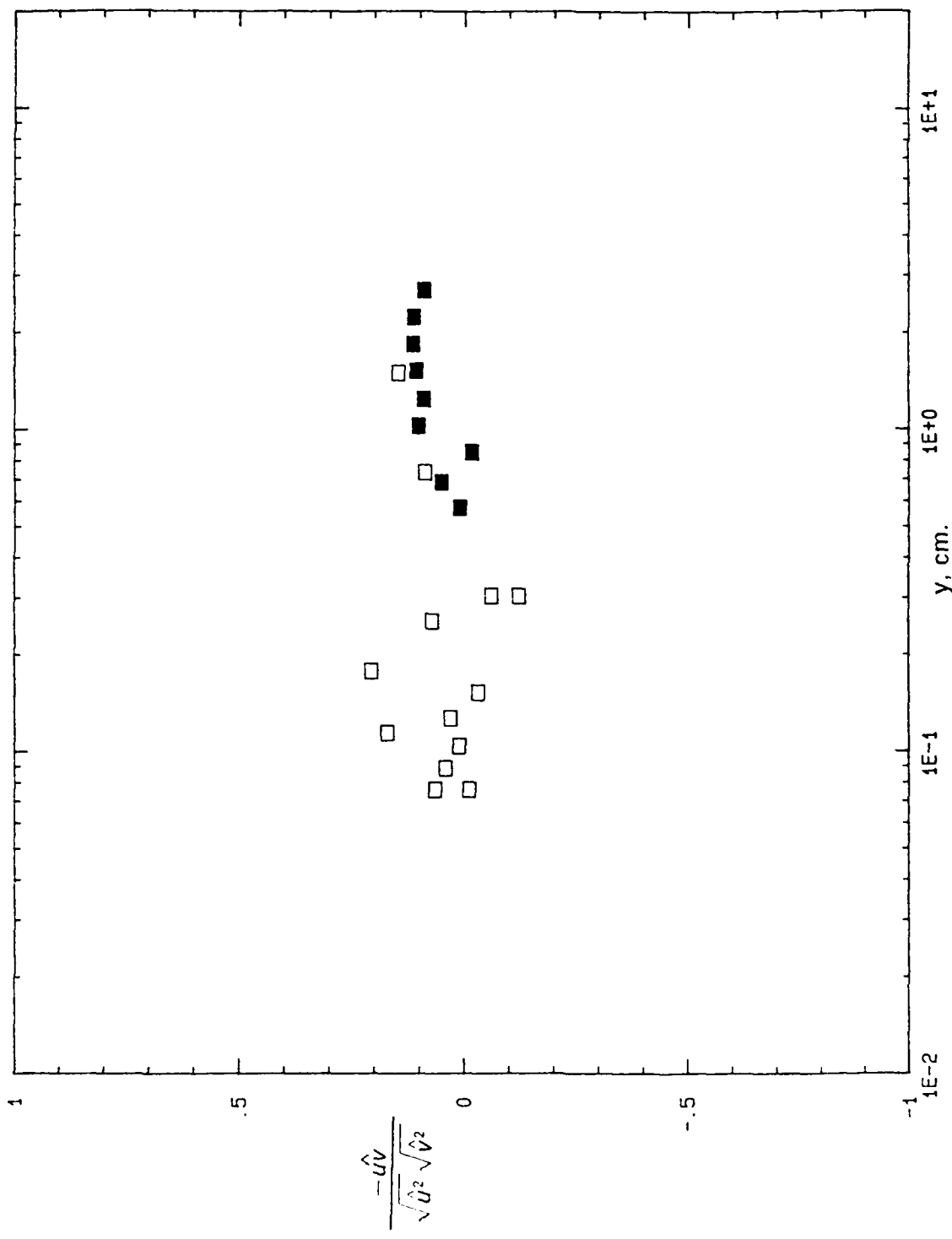


Figure 30. Ensemble-averaged shear stress correlation coefficient profile at $\omega t = 30^\circ$, $X = 0.53$ m, for $k = 1.33$ m, open symbols, laser anemometer; solid symbols, cross-wire measurements.

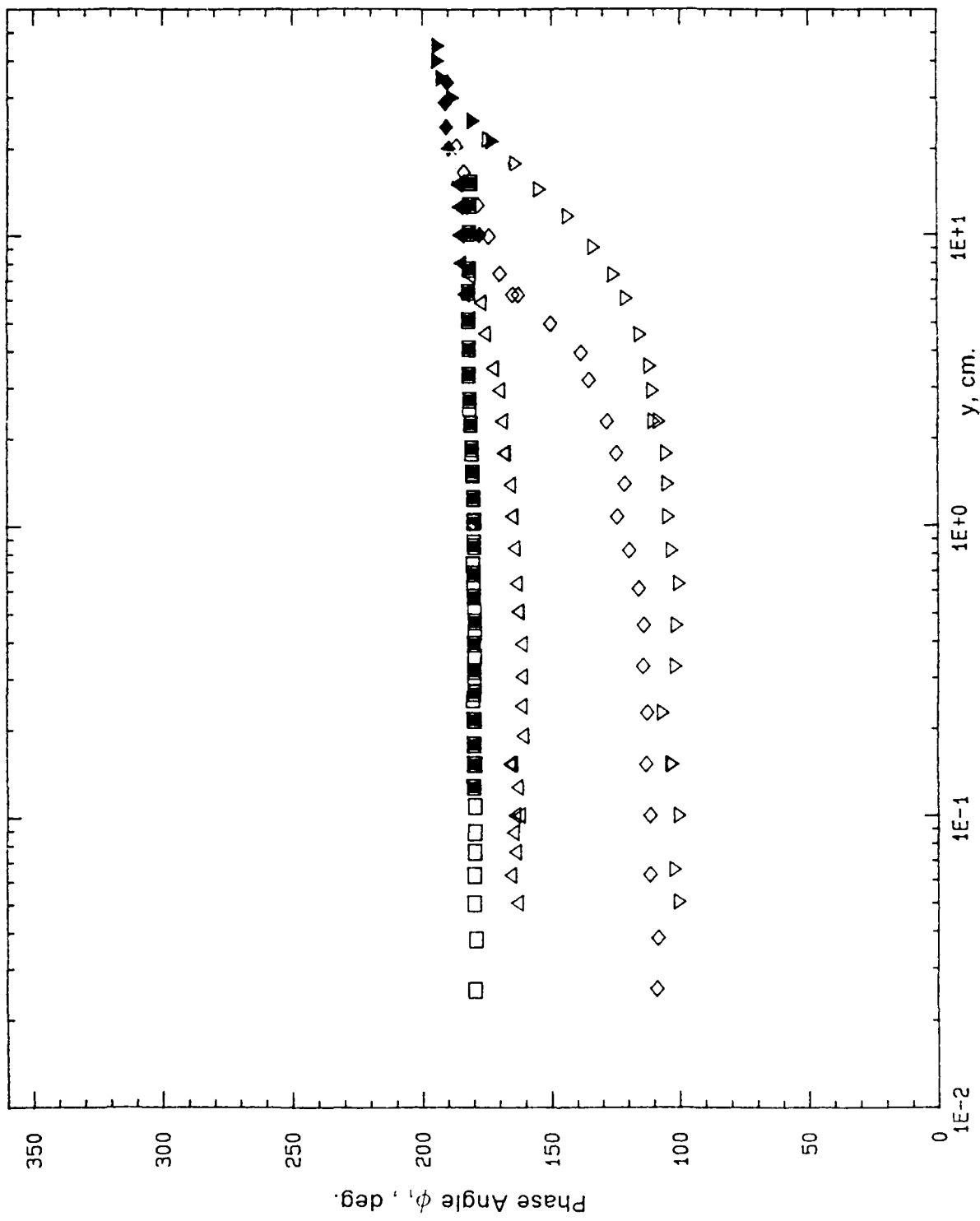


Figure 31. Variation of phase angle of first harmonic of velocity, $k = 0.61$ flow; ($\square = 2.20m$; $\triangle = 2.95m$; $\diamond = 3.51m$; $\nabla = 4.27m$); open symbols, laser anemometer; solid symbols, cross-wire measurements.

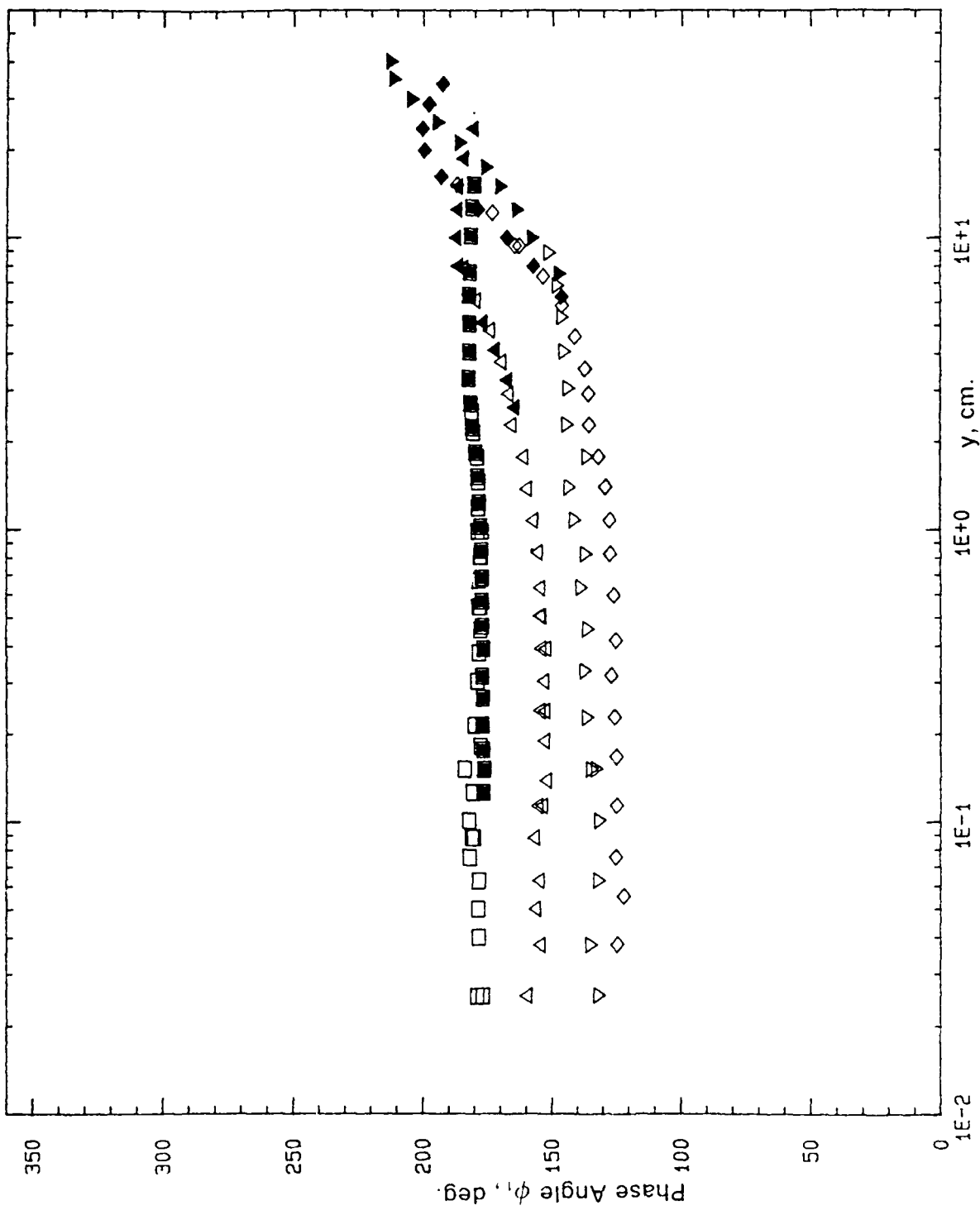


Figure 32. Variation of phase angle of first harmonic of velocity, $k = 1.33$
flow; Legend same as in figure 31.

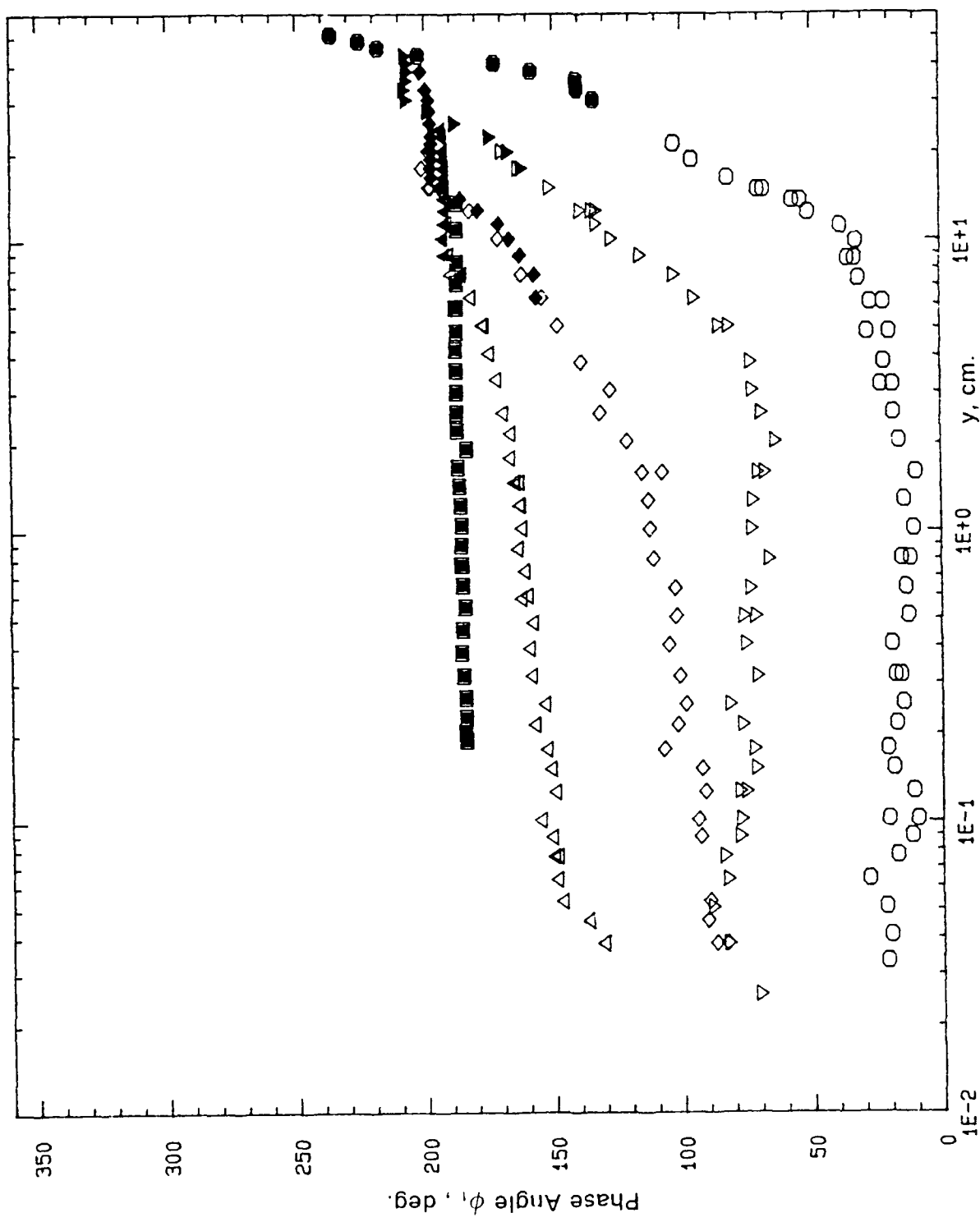


Figure 33. Variation of phase angle of first harmonic of velocity, $k = 1.03$
flow with 'roof damper'; ($\square = 1.63m$; $\triangle = 3.01m$; $\diamond = 3.28m$;
 $\nabla = 3.59m$; $\circ = 4.12m$); open symbols, laser anemometer; solid
symbols, cross-wire measurements.

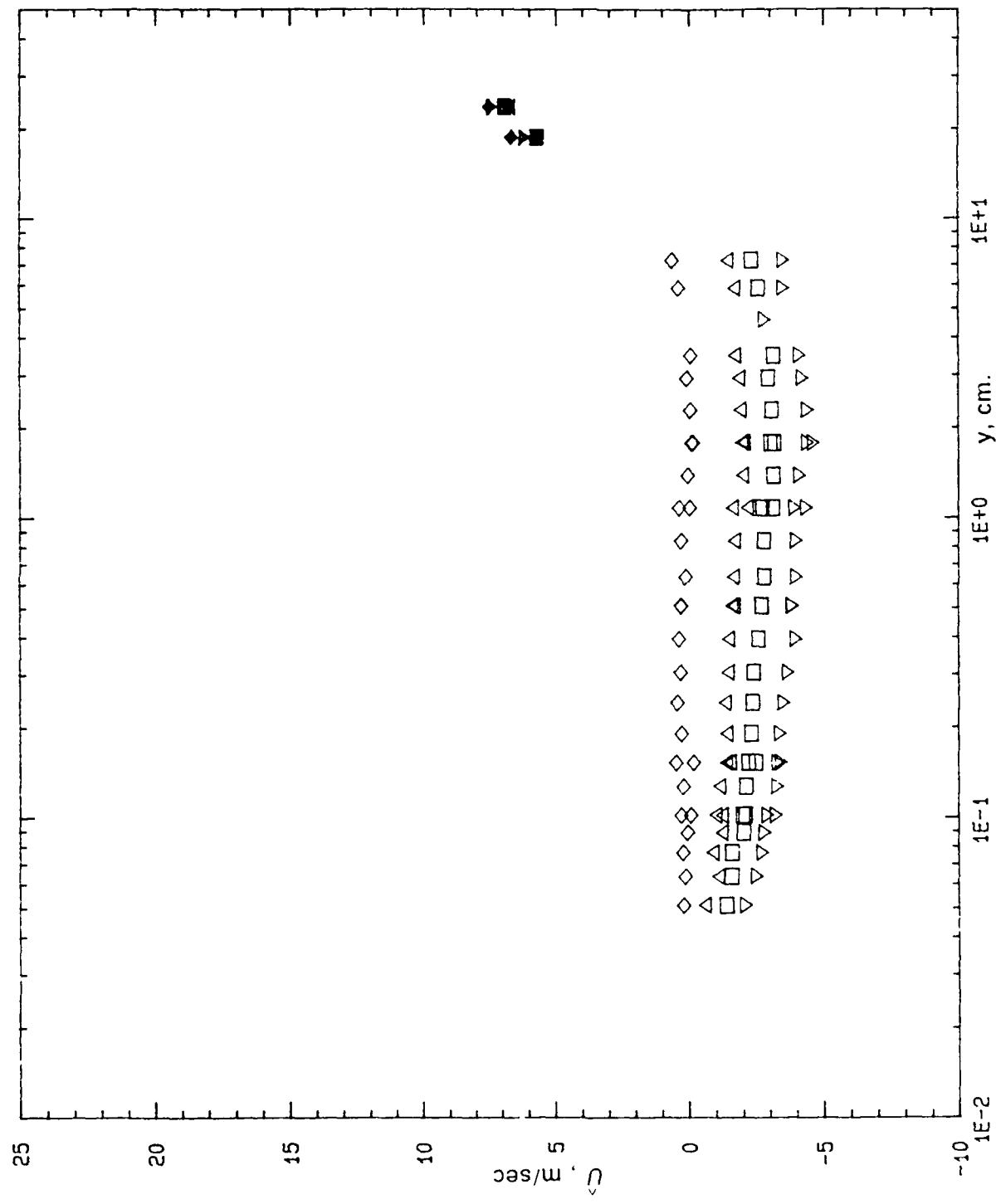


Figure 34a. Ensemble-averaged velocity profiles, \hat{U} , at $X = 2.95$ m,
 $k = 0.61$ flow for $360^\circ \leq \omega_f \leq 45^\circ$ ($\square = 15^\circ$; $\triangle = 30^\circ$; $\diamond = 45^\circ$;
 $\Delta = 360^\circ$) open symbols, laser anemometer; solid symbols,
cross-wire measurements.

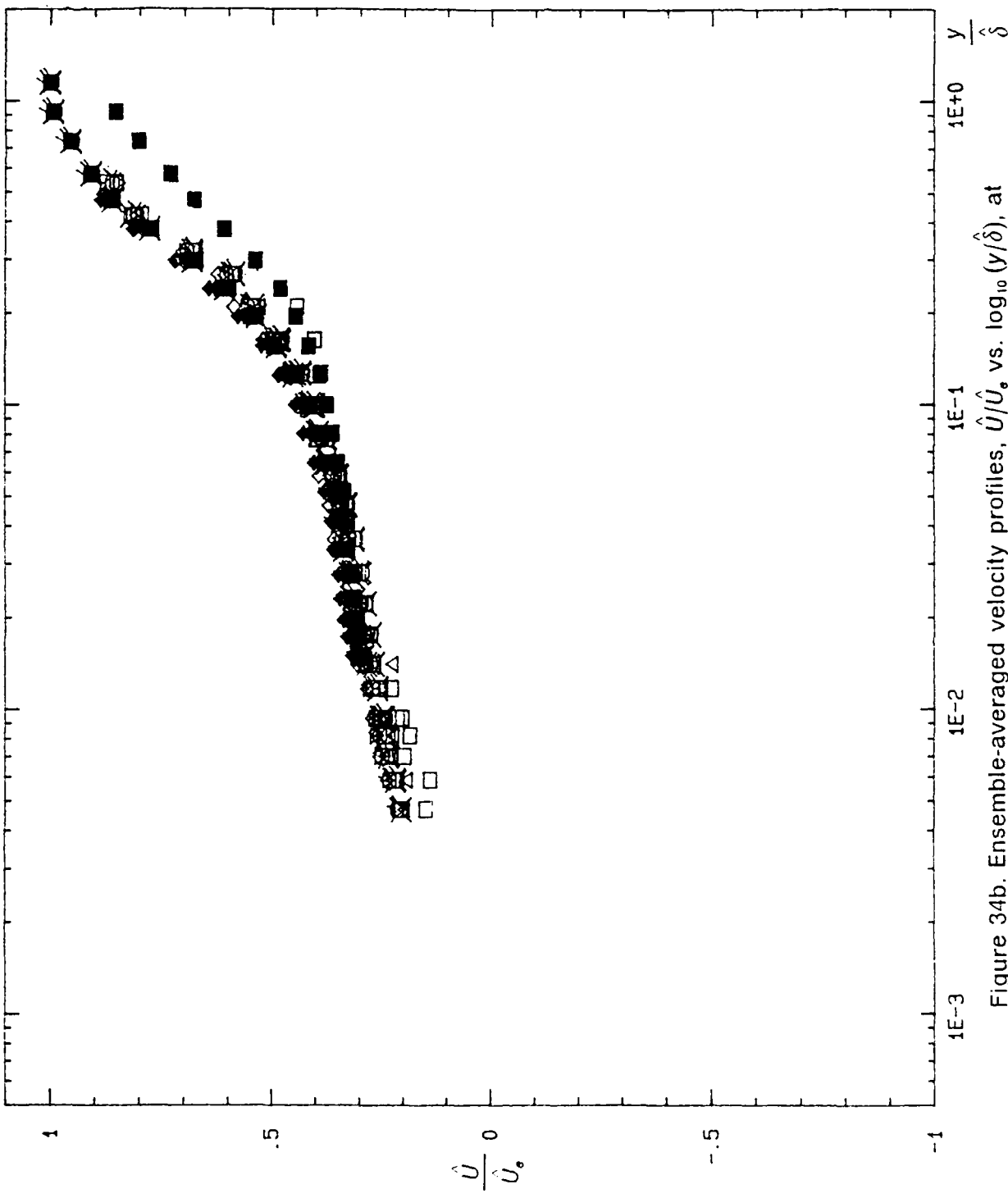


Figure 34b. Ensemble-averaged velocity profiles, \hat{U}/\hat{U}_* vs. $\log_{10}(y/\hat{\delta})$, at $X = 2.95$ m, $k = 0.61$ flow for $75^\circ \leq \omega t \leq 195^\circ$ ($\square = 75^\circ$; $\Delta = 90^\circ$; $\diamond = 105^\circ$; $\nabla = 120^\circ$; $\circ = 135^\circ$; $\square' = 150^\circ$; $\times = 165^\circ$; $\square'' = 180^\circ$; $\square''' = 195^\circ$); open symbols: laser anemometer and solid symbols: cross-wire measurements.

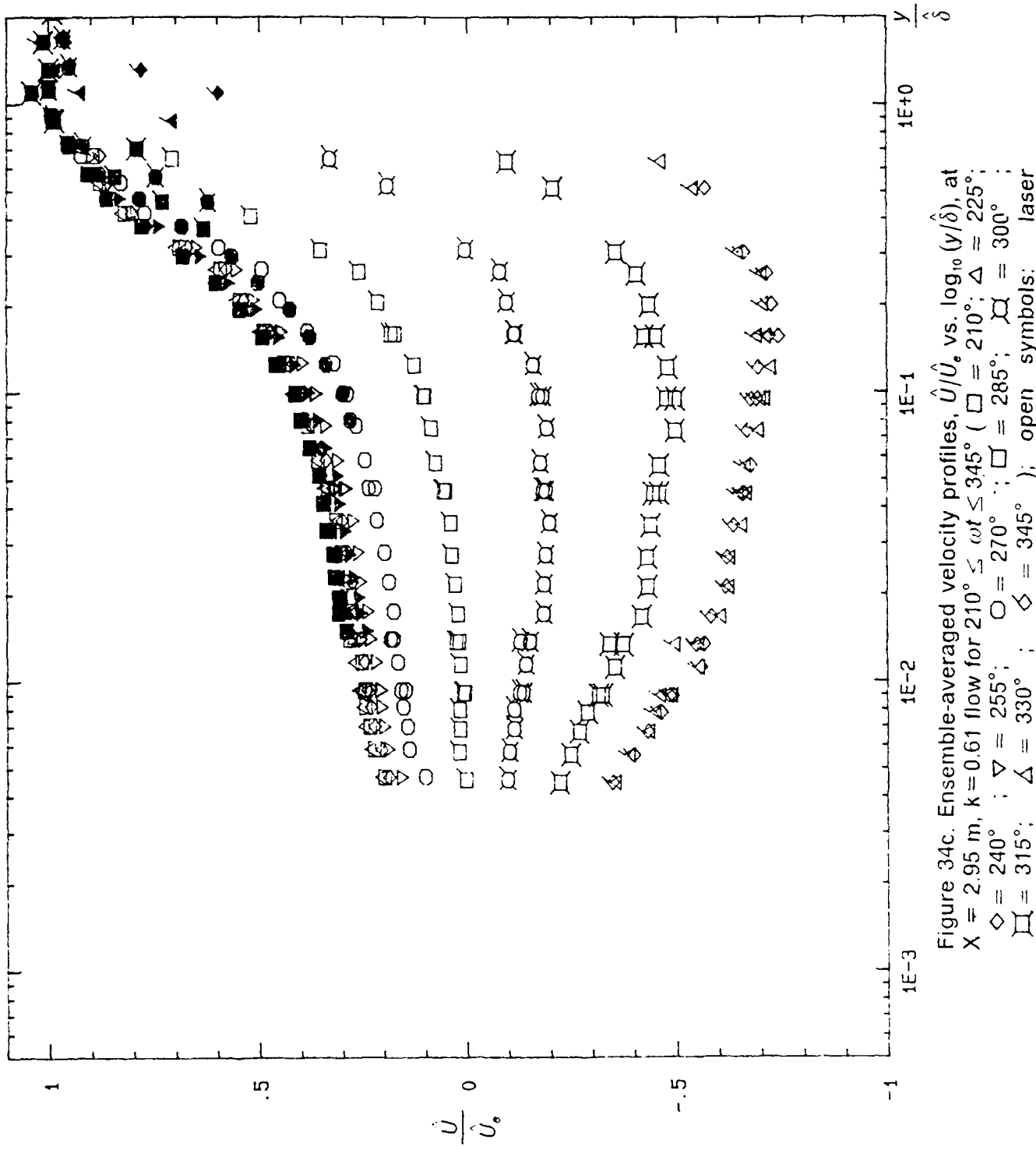


Figure 34c. Ensemble-averaged velocity profiles, \hat{U}/\hat{U}_0 , vs. $\log_{10}(y/\delta)$, at $X = 2.95$ m, $k = 0.61$ flow for $210^\circ \leq \omega_f \leq 345^\circ$ ($\square = 210^\circ$; $\Delta = 225^\circ$; $\diamond = 240^\circ$; $\nabla = 255^\circ$; $\circ = 270^\circ$; $\square = 285^\circ$; $\square = 300^\circ$; $\square = 315^\circ$; $\triangle = 330^\circ$; $\diamond = 345^\circ$); open symbols: laser anemometer and solid symbols: cross-wire measurements.

NO-R192 997

EXPERIMENTAL STUDY OF UNSTEADY SEPARATING TURBULENT
BOUNDARY LAYERS(CU) VIRGINIA POLYTECHNIC INST AND STATE
UNIV BLACKSBURG DEPT OF A. N K AGARWAL ET AL. FEB 88

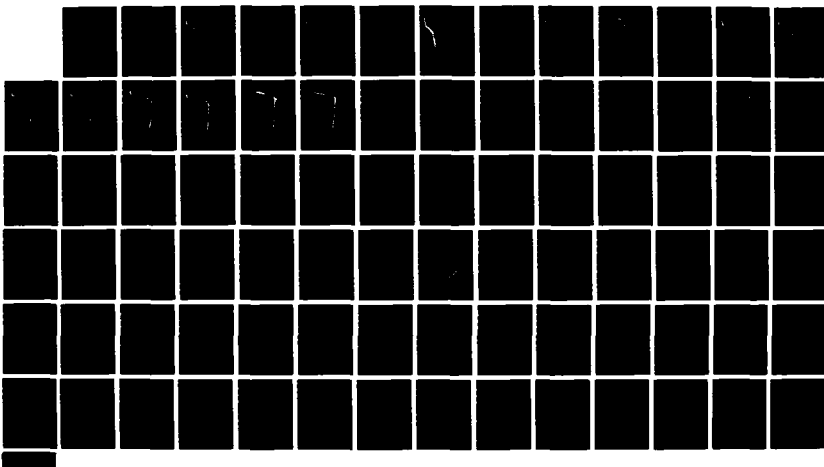
272

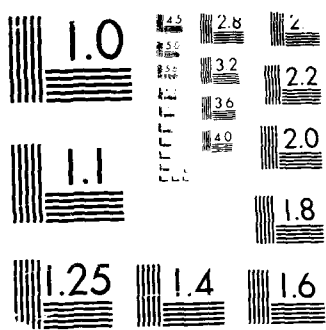
UNCLASSIFIED

AFOSR-TR-88-0271 AFOSR-84-0134

F/G 28/4

ML





MICROCOPY RESOLUTION TEST CHART
PRINTED ON 100% COTTON PAPER

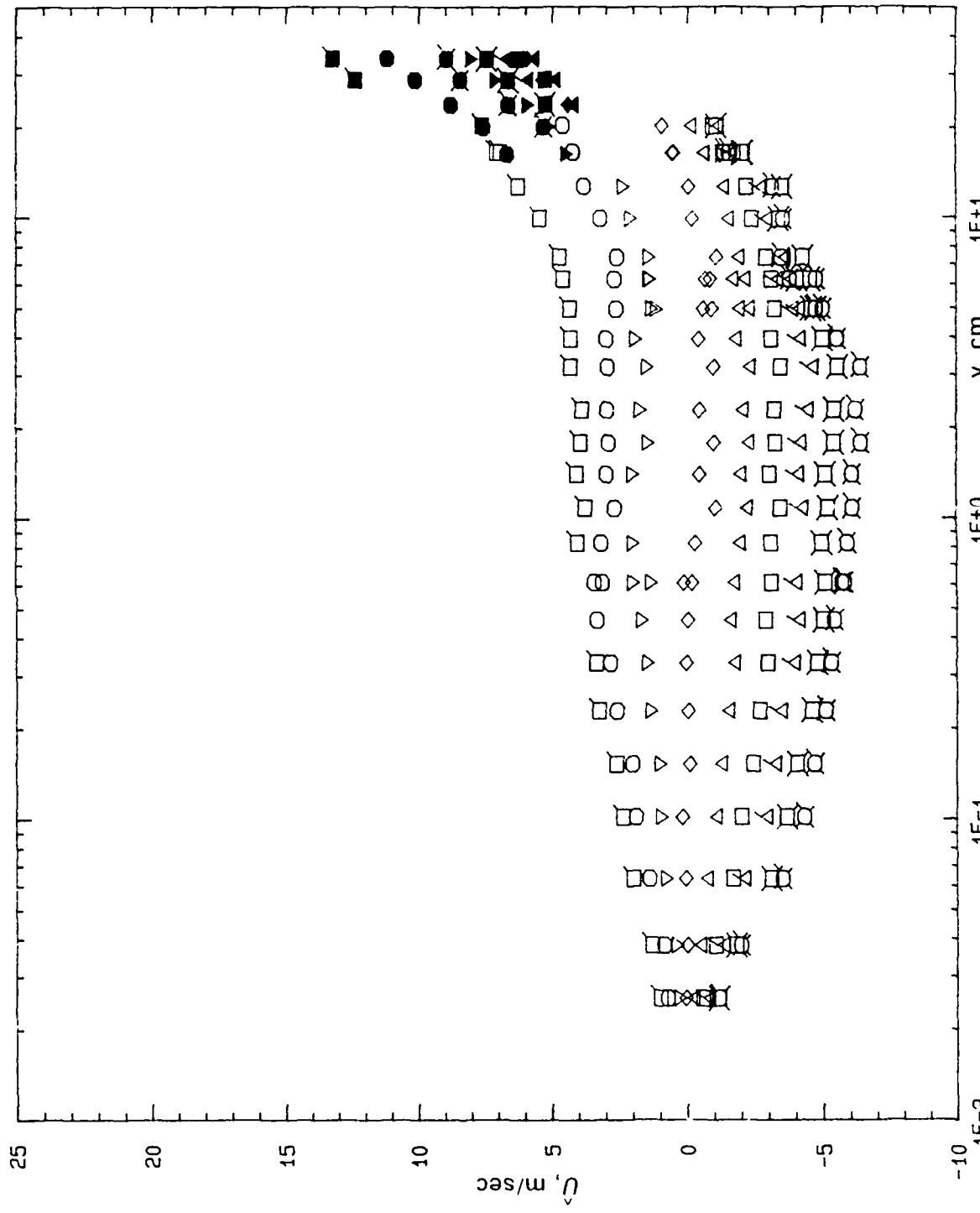


Figure 35a. Ensemble-averaged velocity profiles, \hat{U} at at $X = 3.51$ m,
 $k = 0.61$ flow for $30^\circ \leq \omega t \leq 90^\circ$ ($\square = 15^\circ$; $\triangle = 30^\circ$;
 $\diamond = 45^\circ$;
 $\nabla = 60^\circ$; $\circ = 75^\circ$; $\blacksquare = 90^\circ$; $\square = 330^\circ$; $\triangle = 345^\circ$; $\diamond = 360^\circ$)

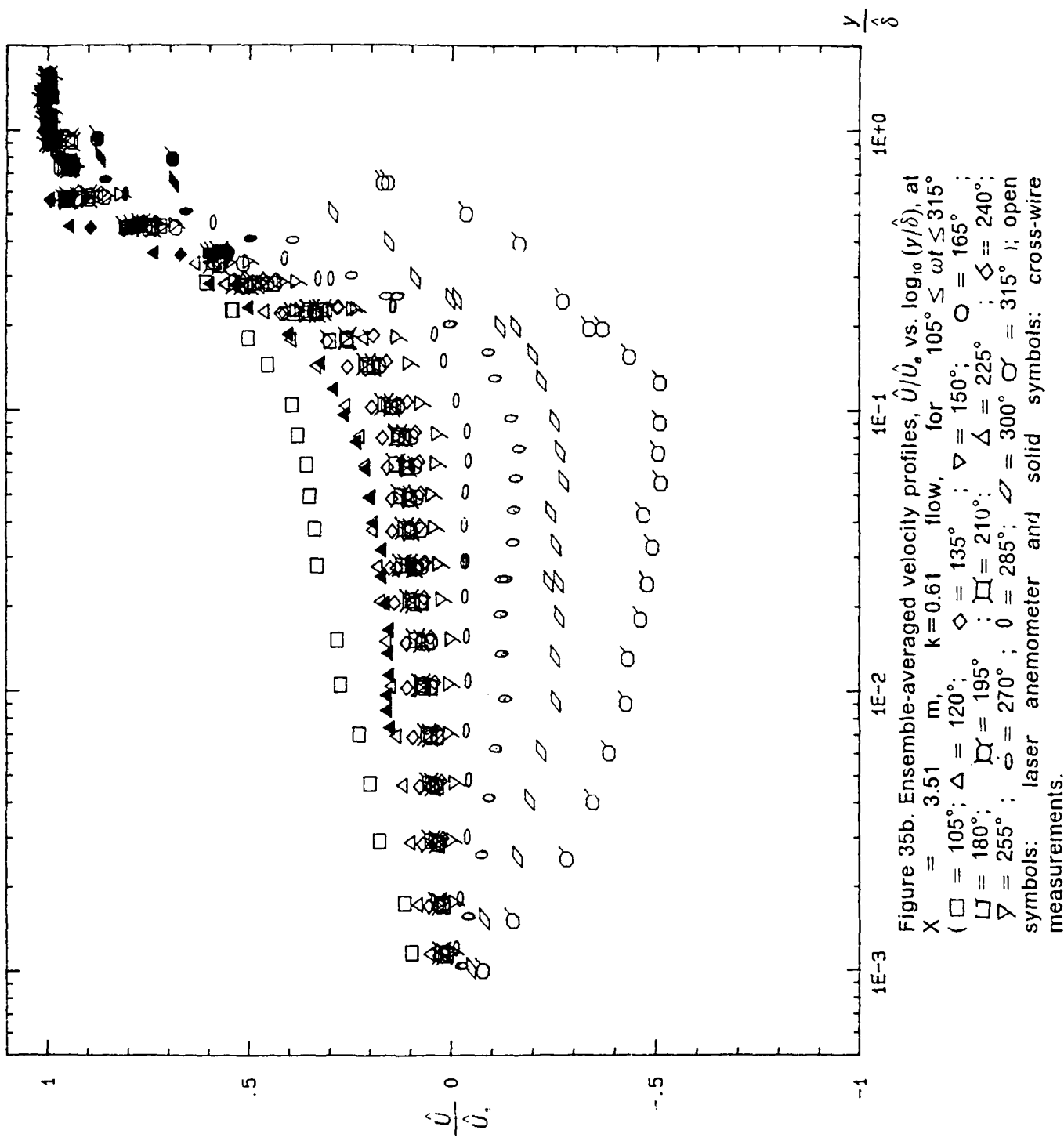


Figure 35b. Ensemble-averaged velocity profiles, \hat{U}/\hat{U}_* vs. $\log_{10}(y/\delta)$, at $X = 3.51$, $k = 0.61$ flow, for $105^\circ \leq \omega t \leq 315^\circ$

($\square = 105^\circ$; $\Delta = 120^\circ$; $\diamond = 135^\circ$; $\triangleright = 150^\circ$; $\circ = 165^\circ$;
 $\square = 180^\circ$; $\Delta = 195^\circ$; $\square = 210^\circ$; $\Delta = 225^\circ$; $\square = 240^\circ$;
 $\square = 255^\circ$; $\Delta = 270^\circ$; $\square = 285^\circ$; $\square = 300^\circ$; $\sigma = 315^\circ$); open symbols: laser anemometer and solid symbols: cross-wire measurements.

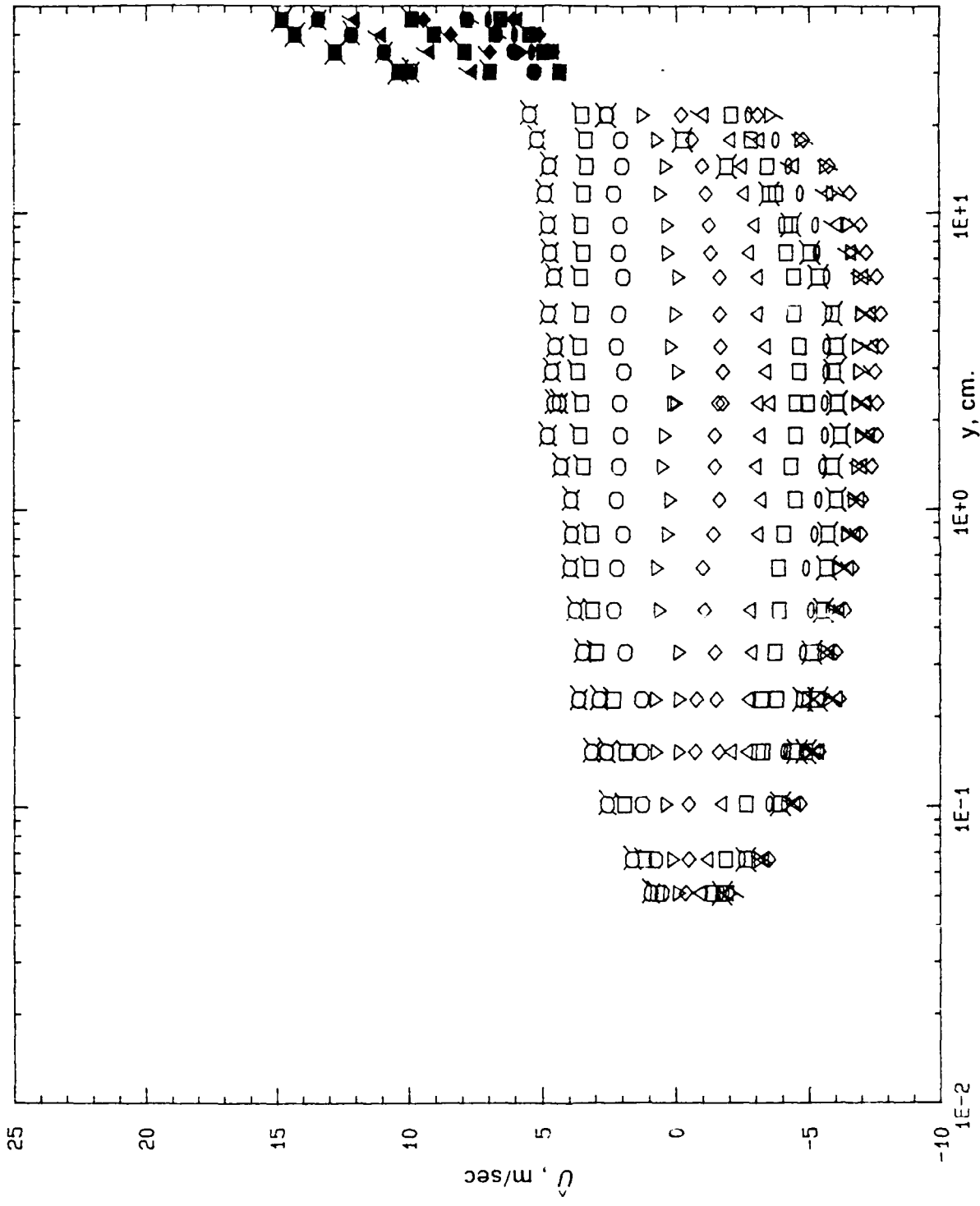


Figure 36a. Ensemble-averaged velocity profiles, \hat{U} at at $X = 4.27$ m, $k = 0.61$ flow for $300^\circ \leq \omega t \leq 105^\circ$ ($\square = 15^\circ$; $\triangle = 30^\circ$; $\diamond = 45^\circ$; $\nabla = 60^\circ$; $\circ = 75^\circ$; $\square' = 90^\circ$; $\boxtimes = 105^\circ$; $\triangle' = 300^\circ$; $\diamond' = 360^\circ$; $\nabla' = 330^\circ$; $\triangleright = 345^\circ$; $\leftarrow = 345^\circ$; open symbols: laser anenometer and solid symbols: cross-wire measurements.

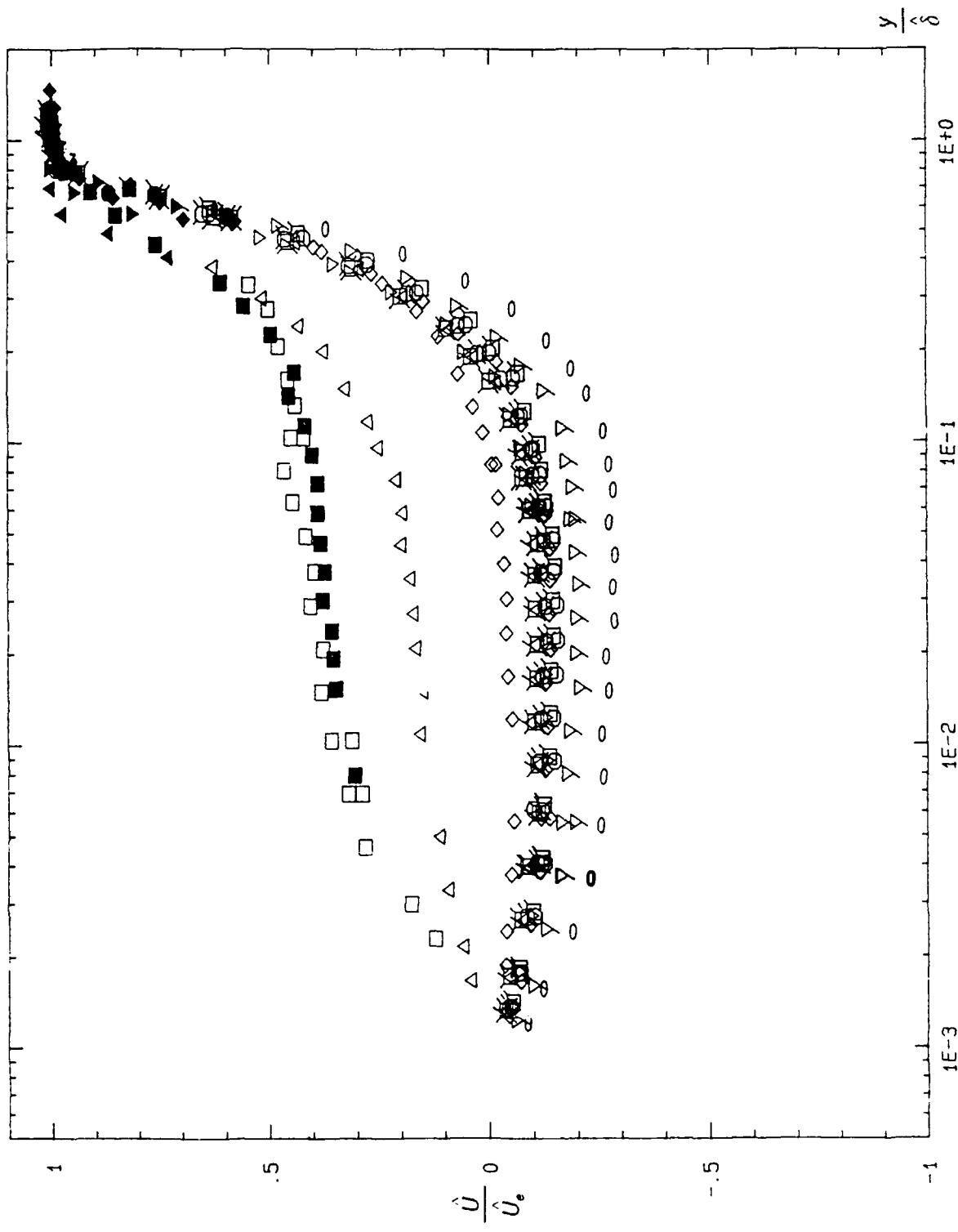


Figure 36b. Ensemble-averaged velocity profiles, \hat{U}/\hat{U}_* vs. $\log_{10}(y/\delta)$, at $X = 4.27$ m, $k = 0.61$ flow, for $120^\circ \leq \omega_f \leq 285^\circ$ (\square $\leq 285^\circ$; \triangle $= 120^\circ$; \square $= 135^\circ$; \diamond $= 150^\circ$; ∇ $= 165^\circ$; \circ $= 180^\circ$; \square $= 195^\circ$; \square $= 210^\circ$; \square $= 225^\circ$; Δ $= 240^\circ$; Δ $= 255^\circ$; \triangleright $= 270^\circ$; \circlearrowright $= 285^\circ$); open symbols: laser anemometer and solid symbols: cross-wire measurements.

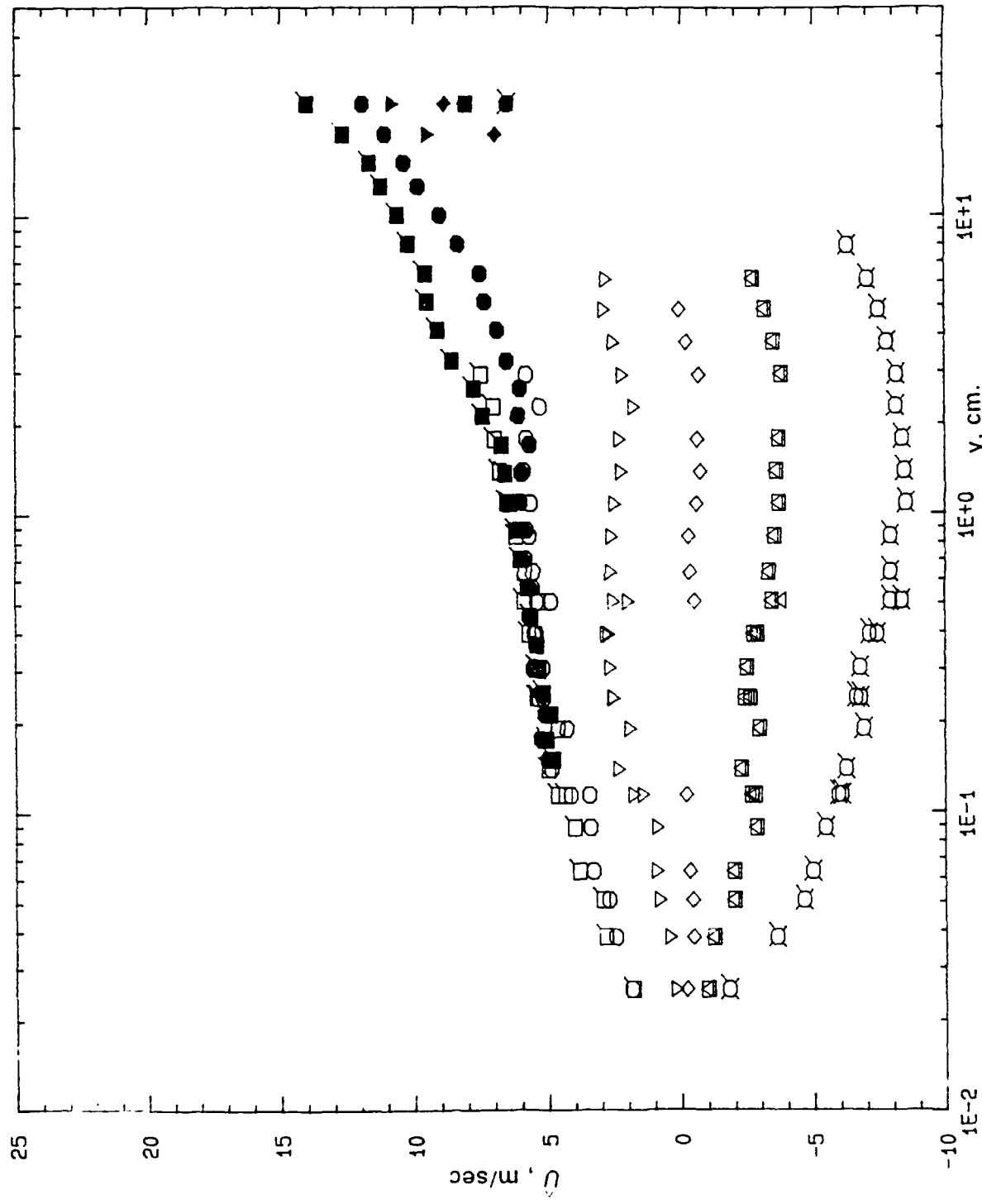


Figure 37a. Ensemble-averaged velocity profiles, \hat{U} at $X = 2.95$ m,
 $k = 1.33$ flow for $90^\circ \leq \omega_f \leq 360^\circ$ ($\square = 15^\circ$; $\triangle = 30^\circ$; $\diamond = 45^\circ$;
 $\nabla = 60^\circ$; $\circ = 75^\circ$; $\square = 90^\circ$; $\square = 360^\circ$) open symbols, laser
anemometer; solid symbols, cross-wire measurements.

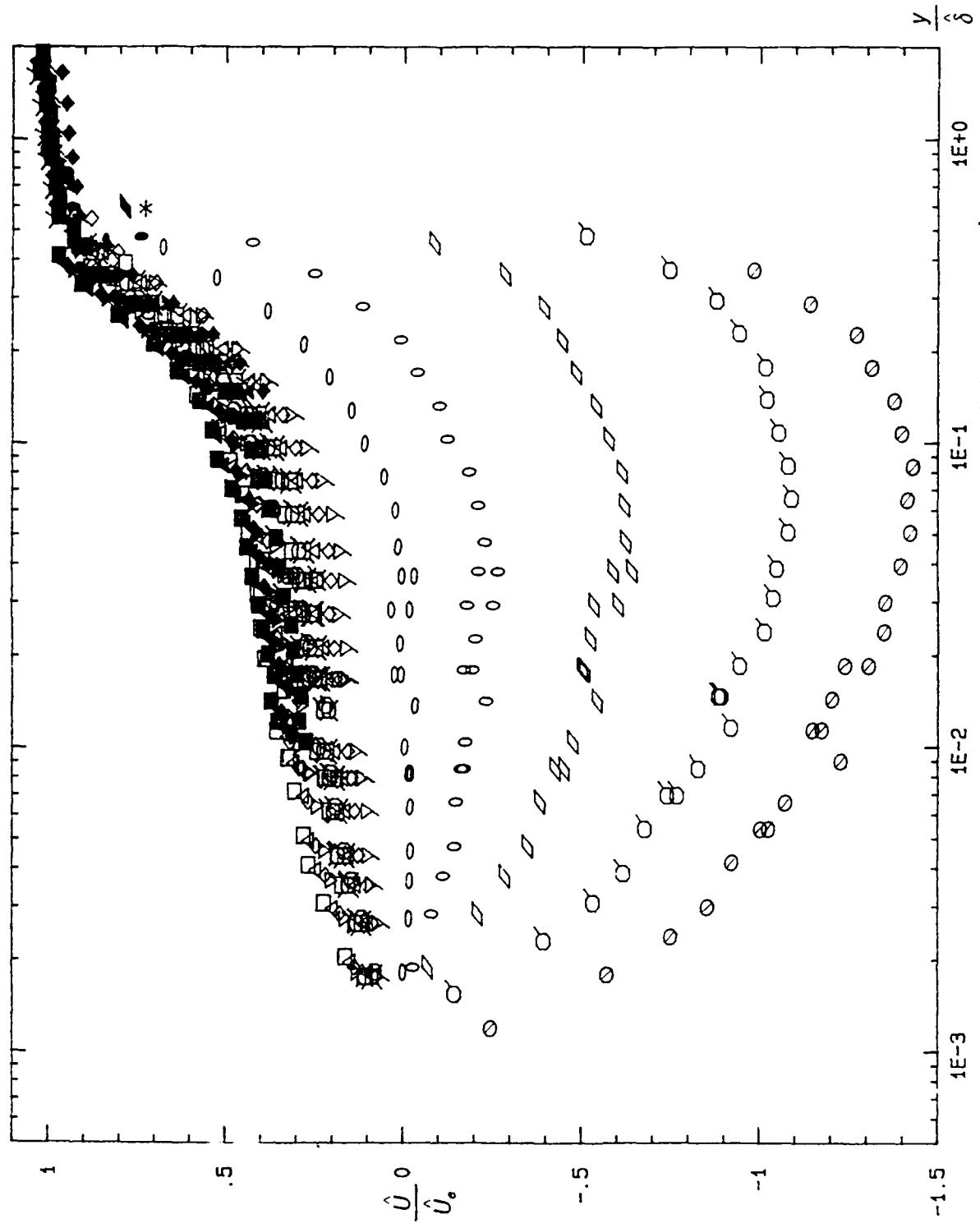


Figure 37b. Ensemble-averaged velocity profiles, \hat{U}/\hat{U}_0 vs. $\log_{10}(y/\delta)$, at $X = 2.95 \text{ m}$, $k = 1.33$ flow for $120^\circ \leq \omega t \leq 345^\circ$ ($\square = 120^\circ$; $\Delta = 135^\circ$; $\diamond = 150^\circ$; $\nabla = 165^\circ$; $\circ = 180^\circ$; $\square = 195^\circ$; $\blacktriangleright = 210^\circ$; $\blacktriangleleft = 225^\circ$; $\Delta = 240^\circ$; $\blacklozenge = 255^\circ$; $\triangleright = 270^\circ$; $\nabla = 270^\circ$; $\circ = 285^\circ$; $\circ = 300^\circ$; $\square = 315^\circ$; $\sigma = 330^\circ$; $\circledast = 345^\circ$); open symbols: laser anemometer and solid symbols: cross-wire measurements.

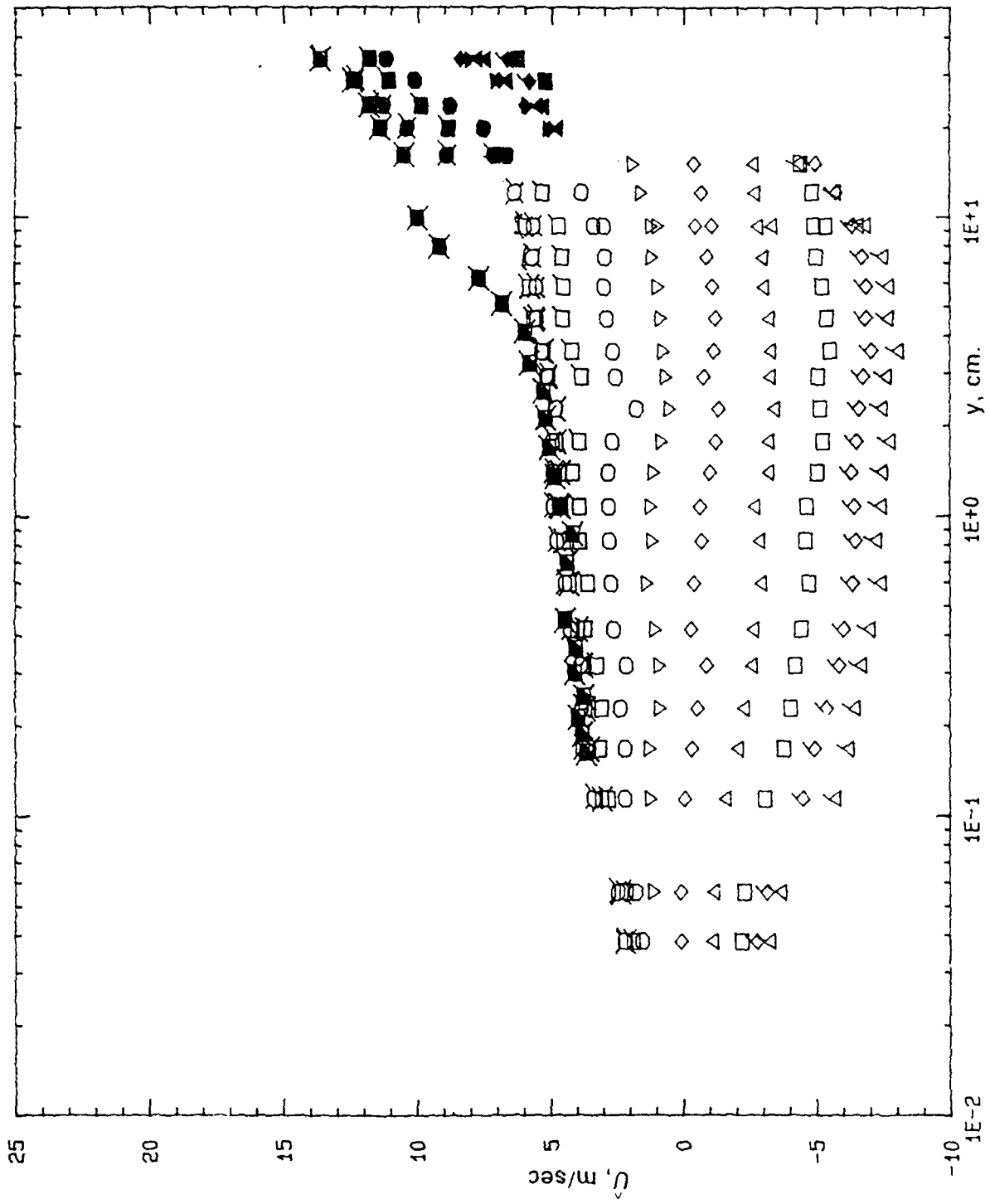


Figure 38a. Ensemble-averaged velocity profiles, \hat{U} at at $X = 3.51$ m, $K = 1.33$ flow for $345^\circ \leq \omega t \leq 120^\circ$ ($\square = 15^\circ$; $\triangle = 30^\circ$; $\diamond = 45^\circ$; $\nabla = 60^\circ$; $\circ = 75^\circ$; $\square = 90^\circ$; $\square = 105^\circ$; $\square = 120^\circ$; $\Delta = 345^\circ$; $\diamond = 360^\circ$) laser anemometer and solid symbols: cross-wire measurements.

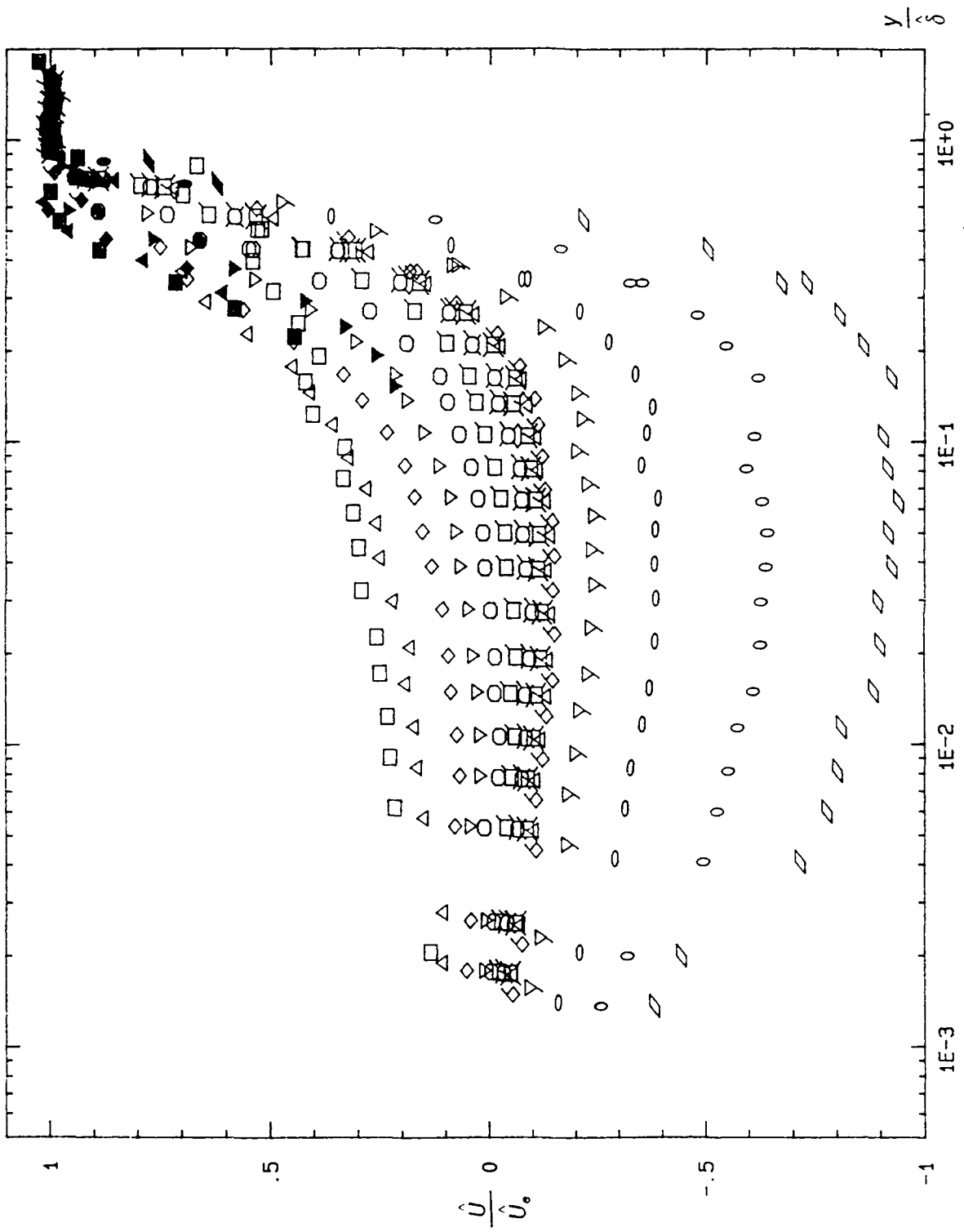


Figure 38b. Ensemble-averaged velocity profiles, \hat{U}/\hat{U}_* vs. $\log_{10}(y/\hat{\delta})$, at $X = 3.51$ m, $k = 1.33$ flow at $135^\circ \leq \omega_f \leq 330^\circ$. ($\square = 135^\circ$; $\triangle = 150^\circ$; $\diamond = 165^\circ$; $\triangleright = 180^\circ$; $\circ = 195^\circ$; $\boxtimes = 210^\circ$; $\triangleleft = 225^\circ$; $\boxdot = 240^\circ$; $\triangle = 255^\circ$; $\triangleright = 270^\circ$; $\square = 285^\circ$; $\triangleright = 300^\circ$; $\circ = 315^\circ$; $\triangleright = 330^\circ$); open symbols: laser anemometer and solid symbols: cross-wire measurements.

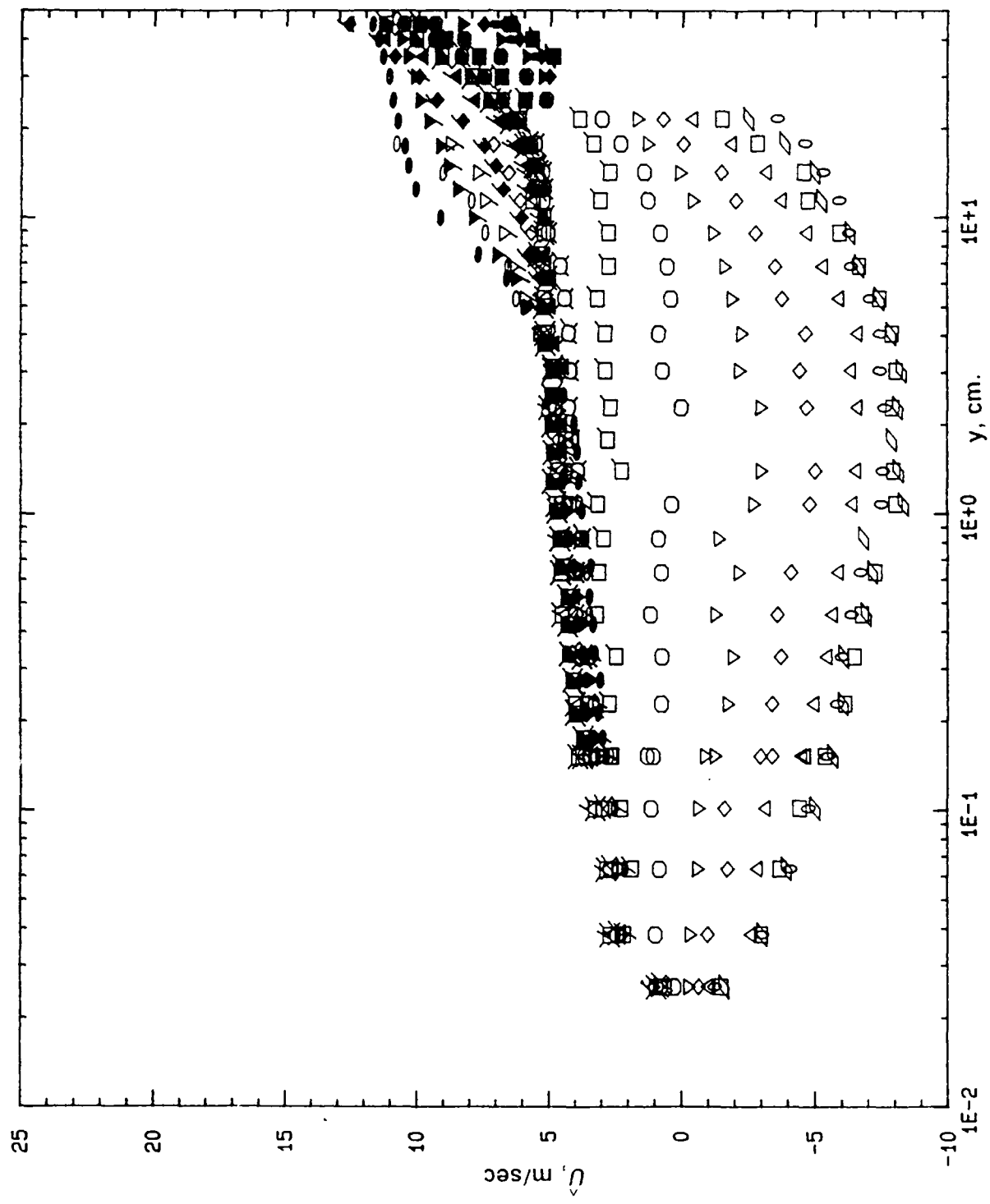


Figure 39a. Ensemble-averaged velocity profiles, \hat{U} , at $X = 4.27$ m for $k = 1.33$ flow at $345^\circ \leq \omega t \leq 180^\circ$. ($\square = 15^\circ$; $\Delta = 30^\circ$; $\diamond = 45^\circ$; $\nabla = 60^\circ$; $\circ = 75^\circ$; $\square = 90^\circ$; $\square = 105^\circ$; $\square = 120^\circ$; $\triangle = 135^\circ$; $\diamond = 150^\circ$; $\triangleright = 165^\circ$; $\circ = 180^\circ$; $\circ = 345^\circ$; $\circ = 360^\circ$); open symbols: laser anemometer and solid symbols: cross-wire measurements.

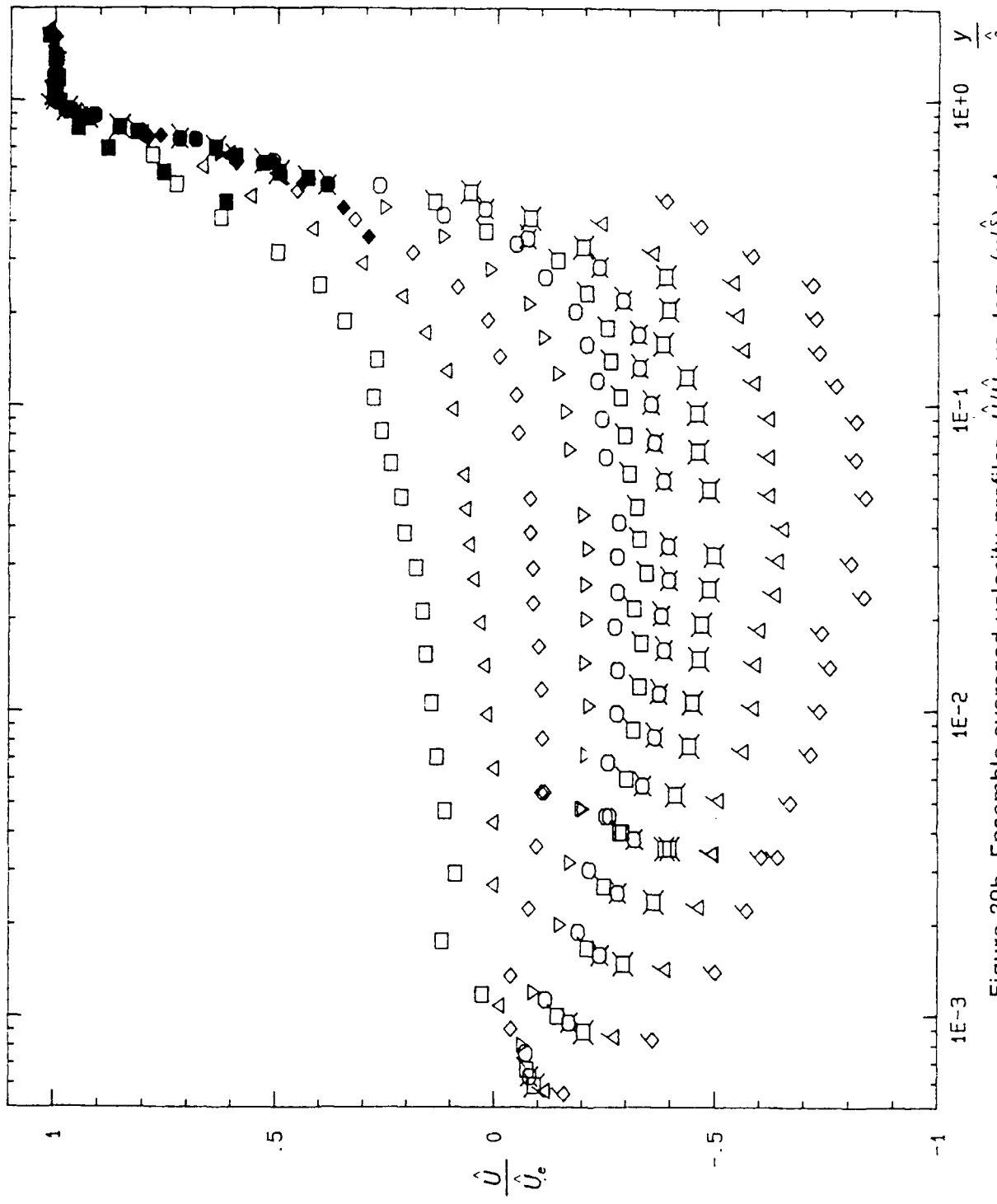


Figure 39b. Ensemble-averaged velocity profiles, \hat{U}/\hat{U}_e vs. $\log_{10}(y/\delta)$, at $X = 4.27$ m, $k = 1.33$ flow at $195^\circ \leq \omega t \leq 330^\circ$. ($\square = 195^\circ$; $\triangle = 210^\circ$; $\diamond = 225^\circ$; $\nabla = 240^\circ$; $\circ = 255^\circ$; $\square = 270^\circ$; $\square = 285^\circ$; $\square = 300^\circ$; $\triangle = 315^\circ$; $\diamond = 330^\circ$); open symbols: cross-wire measurements and solid symbols: laser anemometer

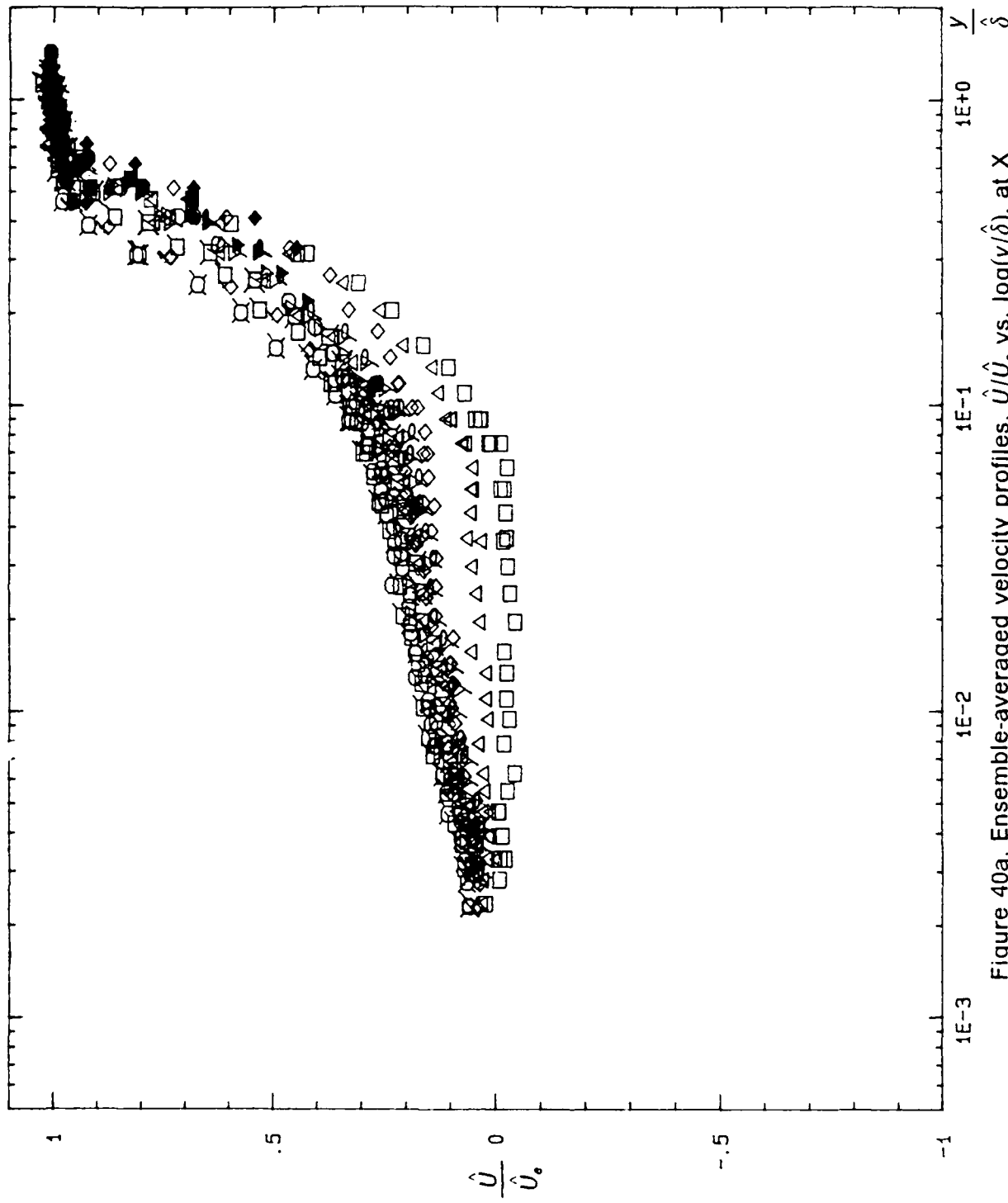


Figure 40a. Ensemble-averaged velocity profiles, \hat{U}/\hat{U}_0 vs. $\log(y/\hat{\delta})$, at $X = 3.01$ m, $k = 1.03$ flow with 'roof damper' at $15^\circ \leq \omega t \leq 180^\circ$. ($\square = 15^\circ$; $\triangle = 30^\circ$; $\diamond = 45^\circ$; $\nabla = 60^\circ$; $\circ = 75^\circ$; $\square = 90^\circ$; $\boxtimes = 105^\circ$; $\square = 120^\circ$; $\Delta = 135^\circ$; $\triangleleft = 150^\circ$; $\triangleright = 165^\circ$; $\circ = 180^\circ$); open symbols: laser anemometer and solid symbols: cross-wire measurements.

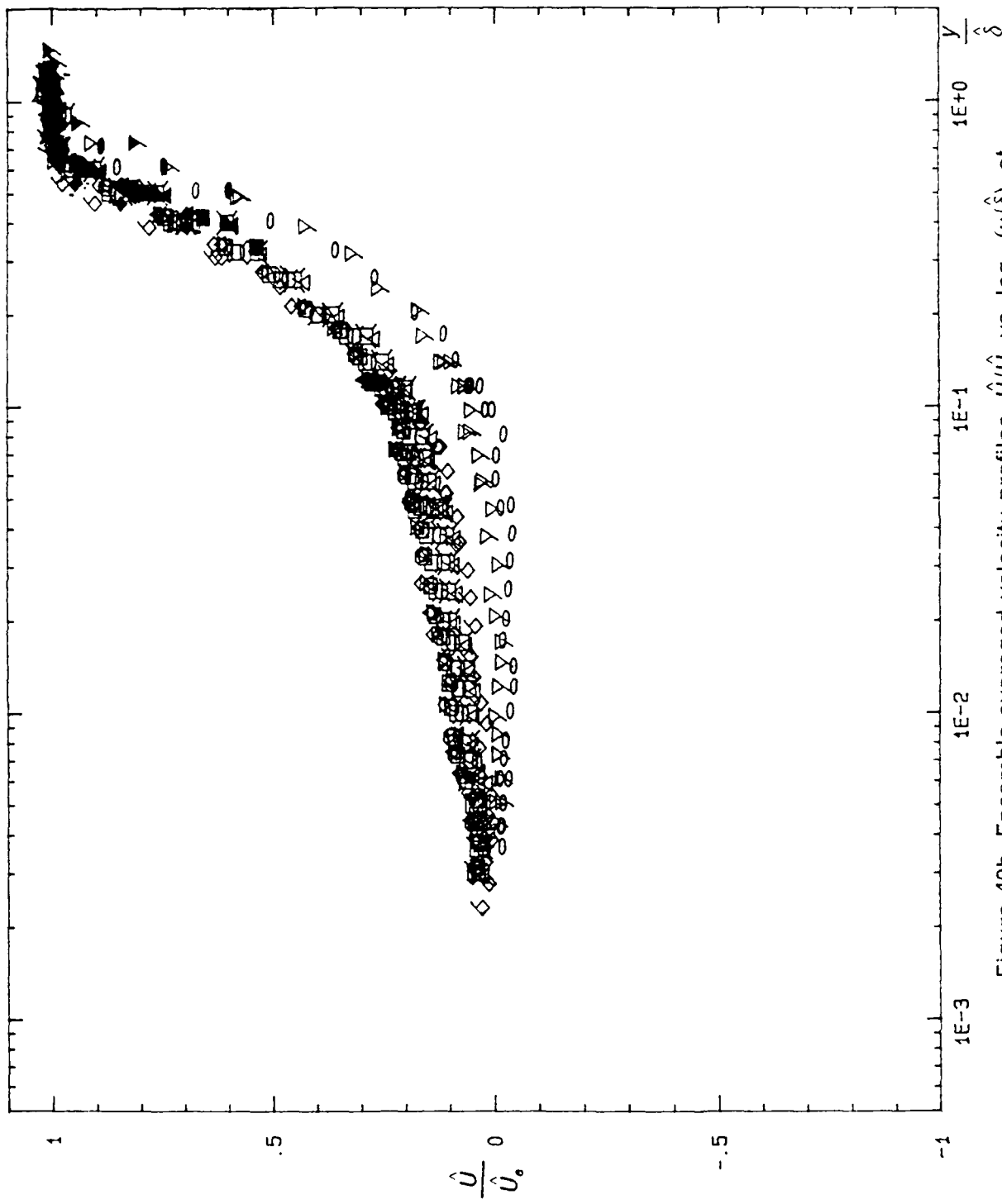


Figure 40b. Ensemble-averaged velocity profiles, \hat{U}/\hat{U}_∞ vs. $\log_{10}(y/\hat{\delta})$, at $X = 3.01$ m, $k = 1.03$ flow with 'roof damper' at $195^\circ \leq \omega t \leq 360^\circ$. ($\square = 195^\circ$; $\triangle = 210^\circ$; $\diamond = 225^\circ$; $\square = 270^\circ$; $\square = 285^\circ$; $\square = 300^\circ$; $\square = 315^\circ$; $\square = 330^\circ$; $\nabla = 345^\circ$; $\circ = 360^\circ$); open symbols: laser anemometer and solid symbols: cross-wire measurements.

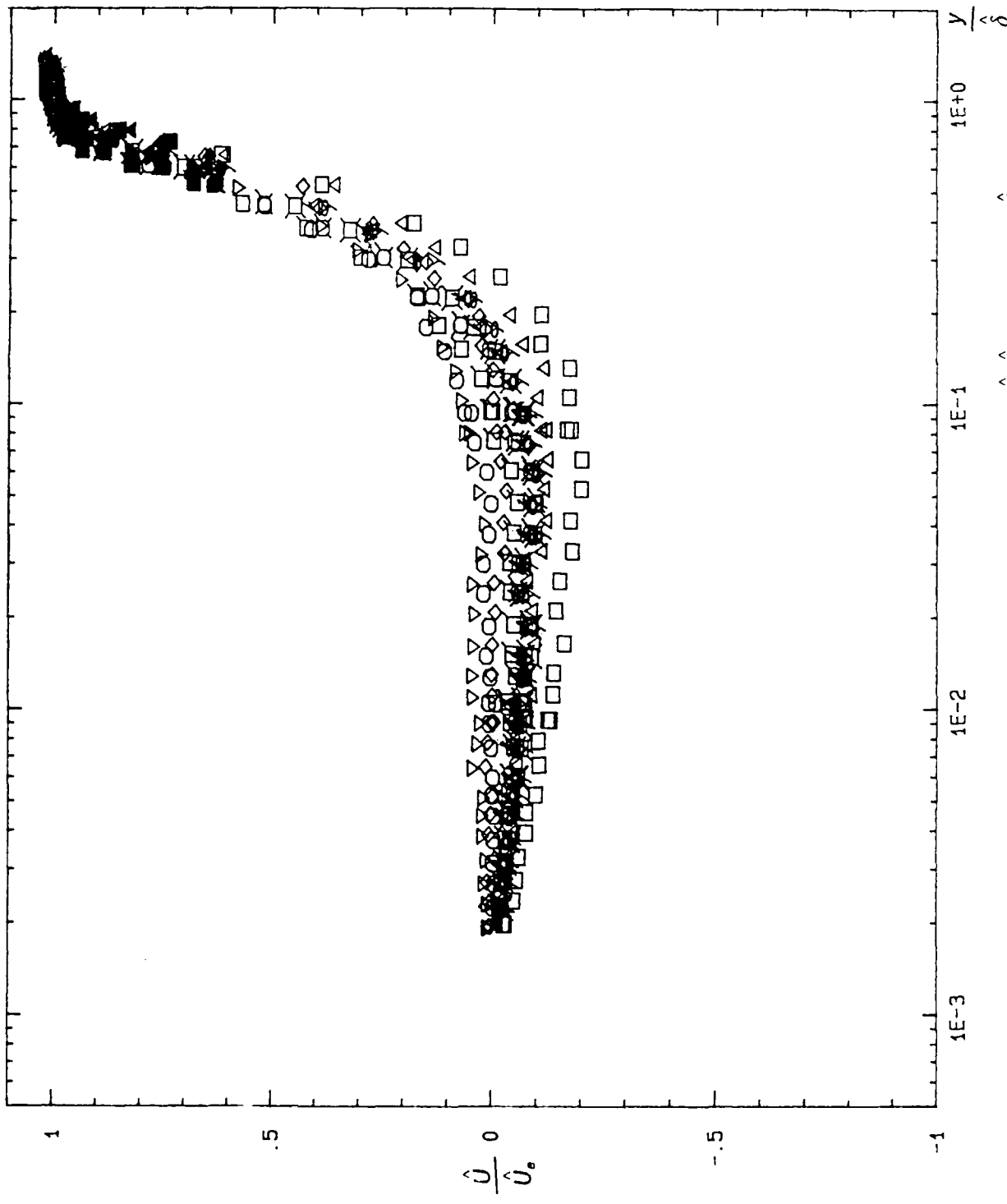


Figure 41a. Ensemble-averaged velocity profiles, \hat{U}/\hat{U}_e vs. $\log_{10}(y/\delta)$, at $X = 3.28$ m, $k = 1.03$ flow with 'roof damper' at $15^\circ \leq \omega t \leq 180^\circ$; Legend same as in figure 40a.

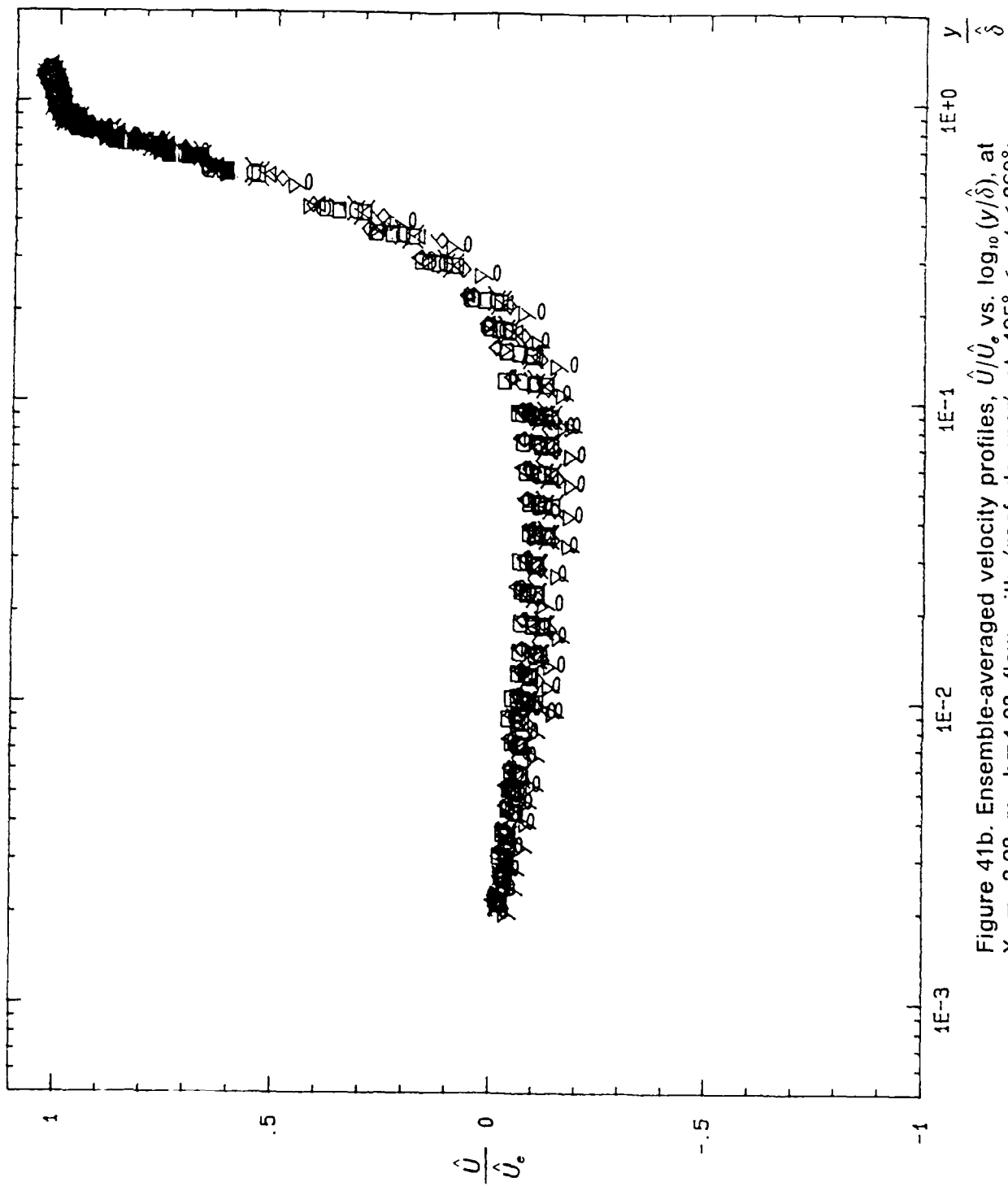


Figure 41b. Ensemble-averaged velocity profiles, \hat{U}/\hat{U}_e vs. $\log_{10}(\hat{y}/\delta)$, at $X = 3.28$ m, $k = 1.03$ flow with 'roof damper' at $195^\circ \leq \omega t \leq 360^\circ$; Legend same as in figure 40b.

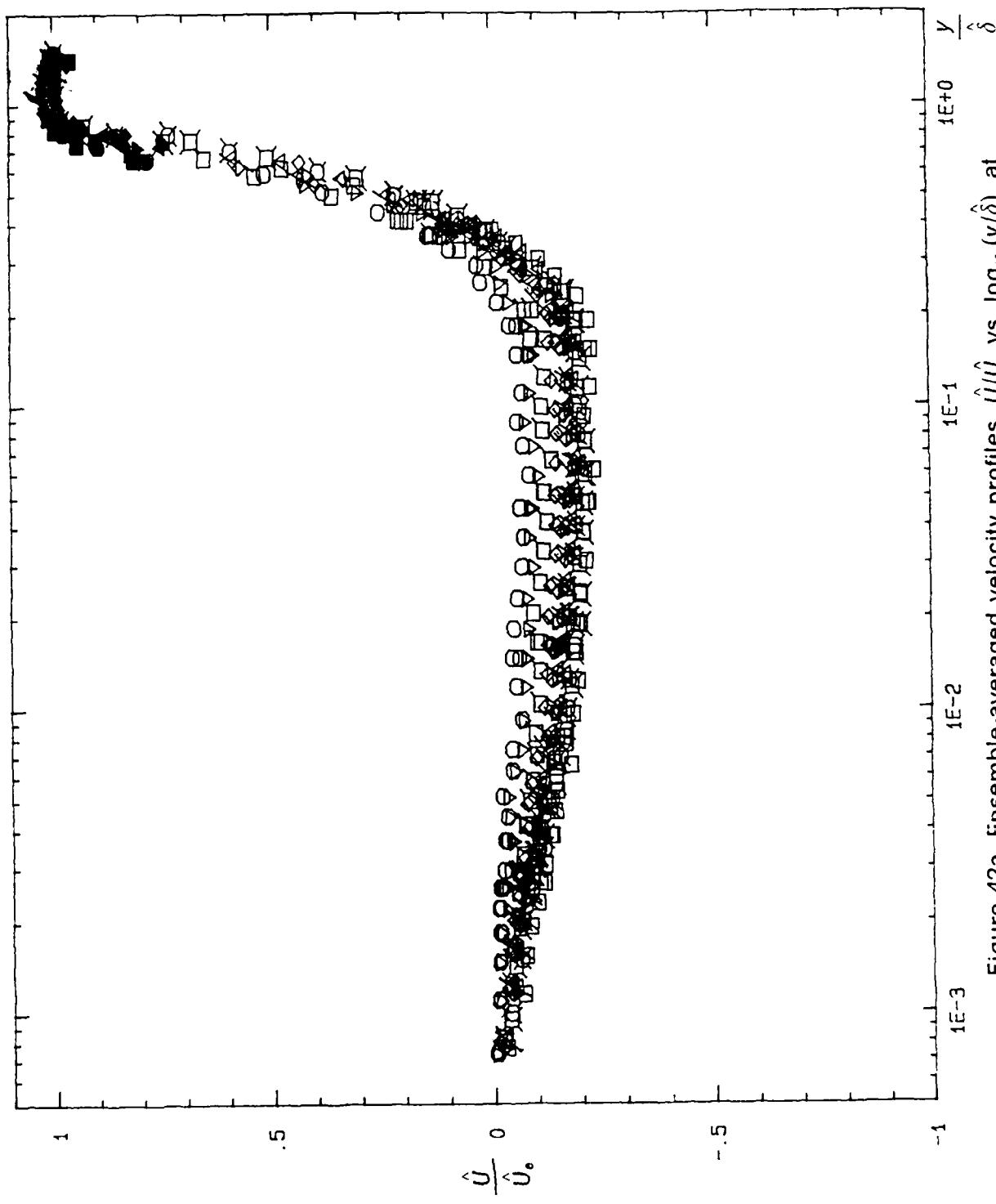


Figure 42a. Ensemble-averaged velocity profiles, \hat{U}/\hat{U}_* , vs. $\log_{10}(\hat{Y}/\hat{\delta})$, at $X = 3.59$ m, $k = 1.03$ flow with 'roof damper' at $15^\circ \leq \omega t \leq 180^\circ$; Legend same as in figure 40a.

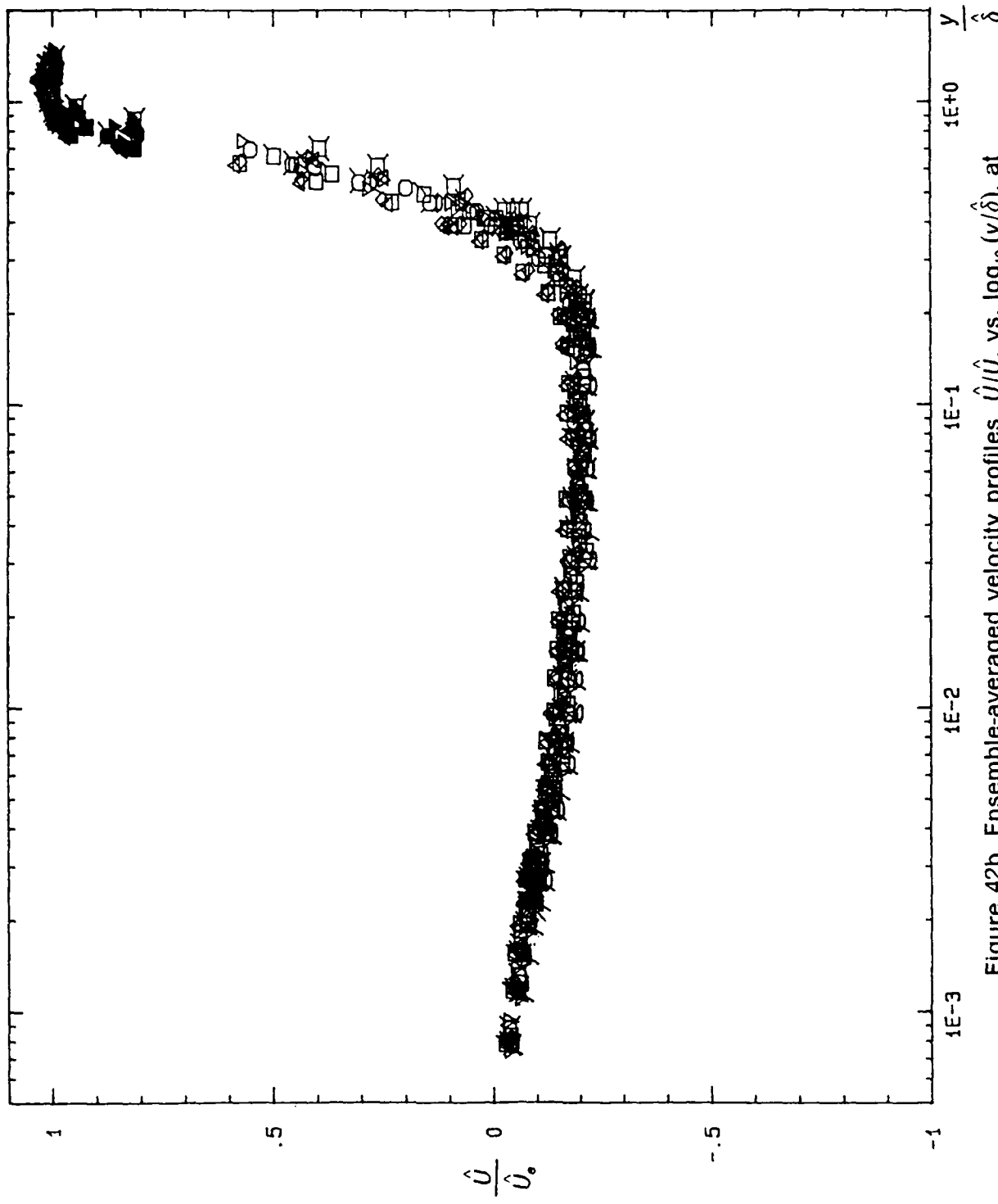


Figure 42b. Ensemble-averaged velocity profiles, \hat{U}/\hat{U}_* vs. $\log_{10}(\hat{Y}/\hat{\delta})$, at $X = 3.59$ m, $k = 1.03$ flow with 'roof damper' at $195^\circ \leq \omega t \leq 360^\circ$; Legend same as in figure 40b.

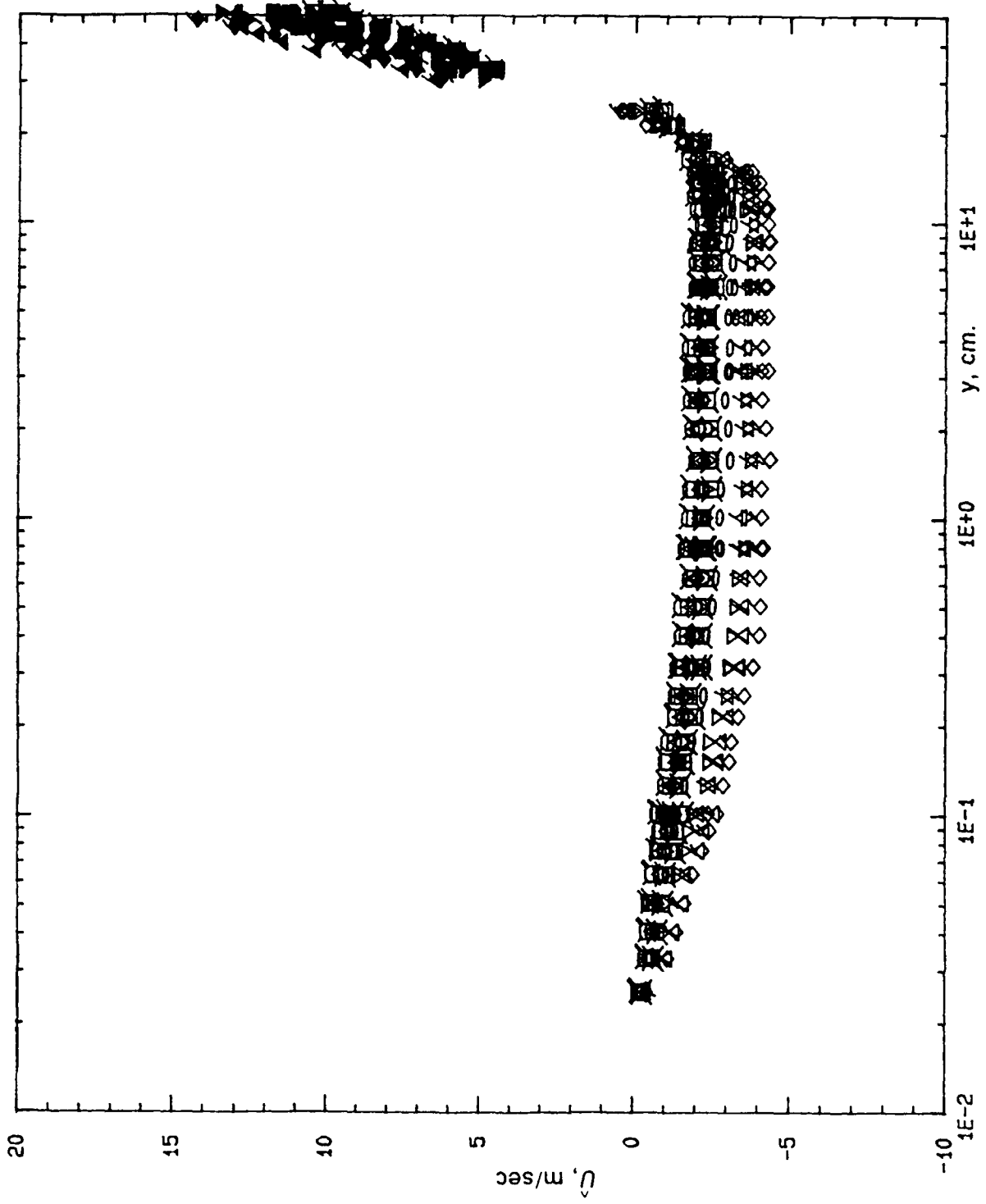


Figure 43a. Ensemble-averaged velocity profiles, \hat{U} at $X = 4.12$ m,
 $k = 1.03$ flow with 'roof damper' at $15^\circ \leq \omega t \leq 180^\circ$; Legend same as in
figure 40a.

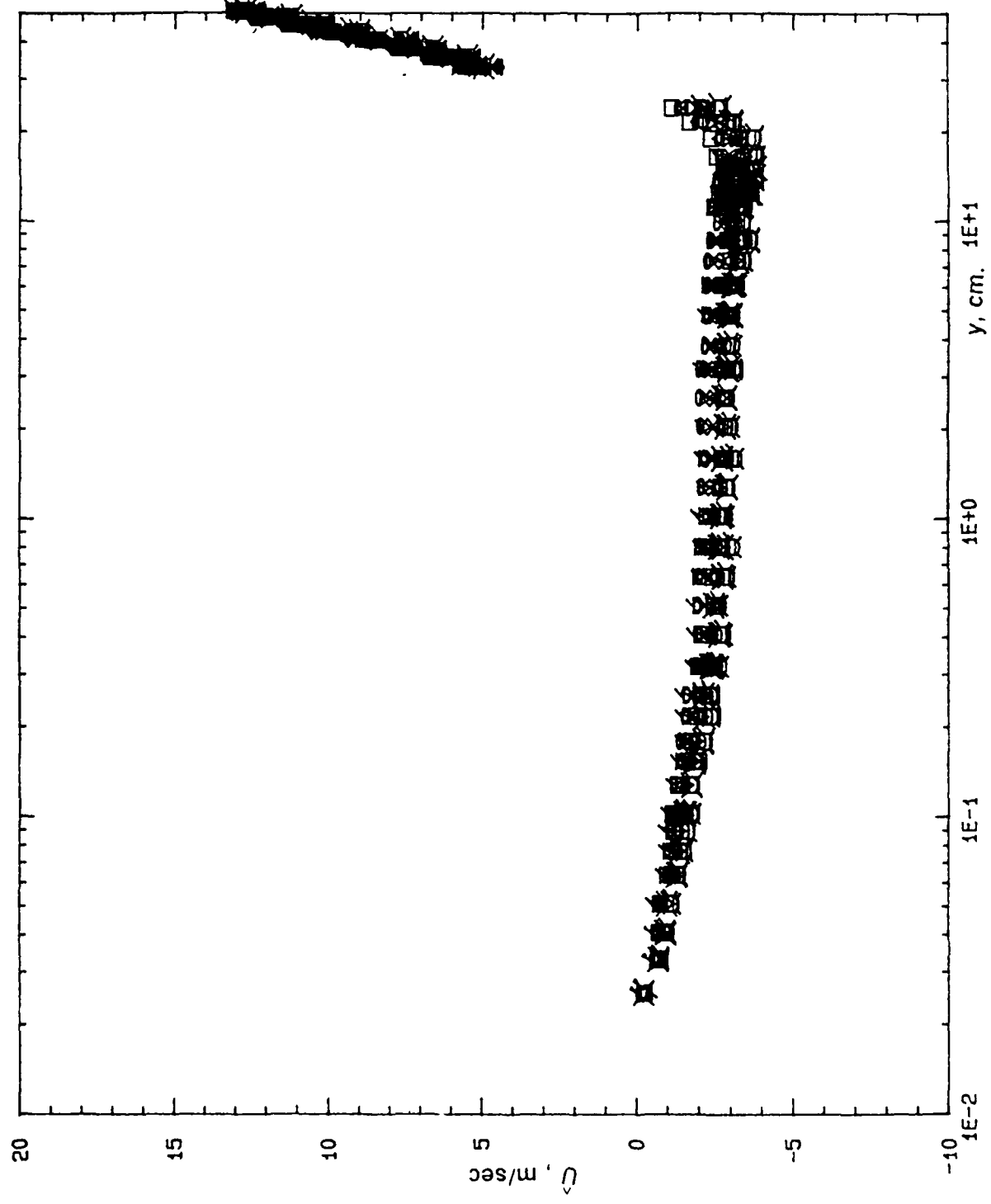


Figure 43b. Ensemble-averaged velocity profiles, \hat{U} at $X = 4.12$ m,
 $k = 1.03$ flow with 'roof damper' at $195^\circ \leq \omega t \leq 360^\circ$; Legend same as in
figure 40b.

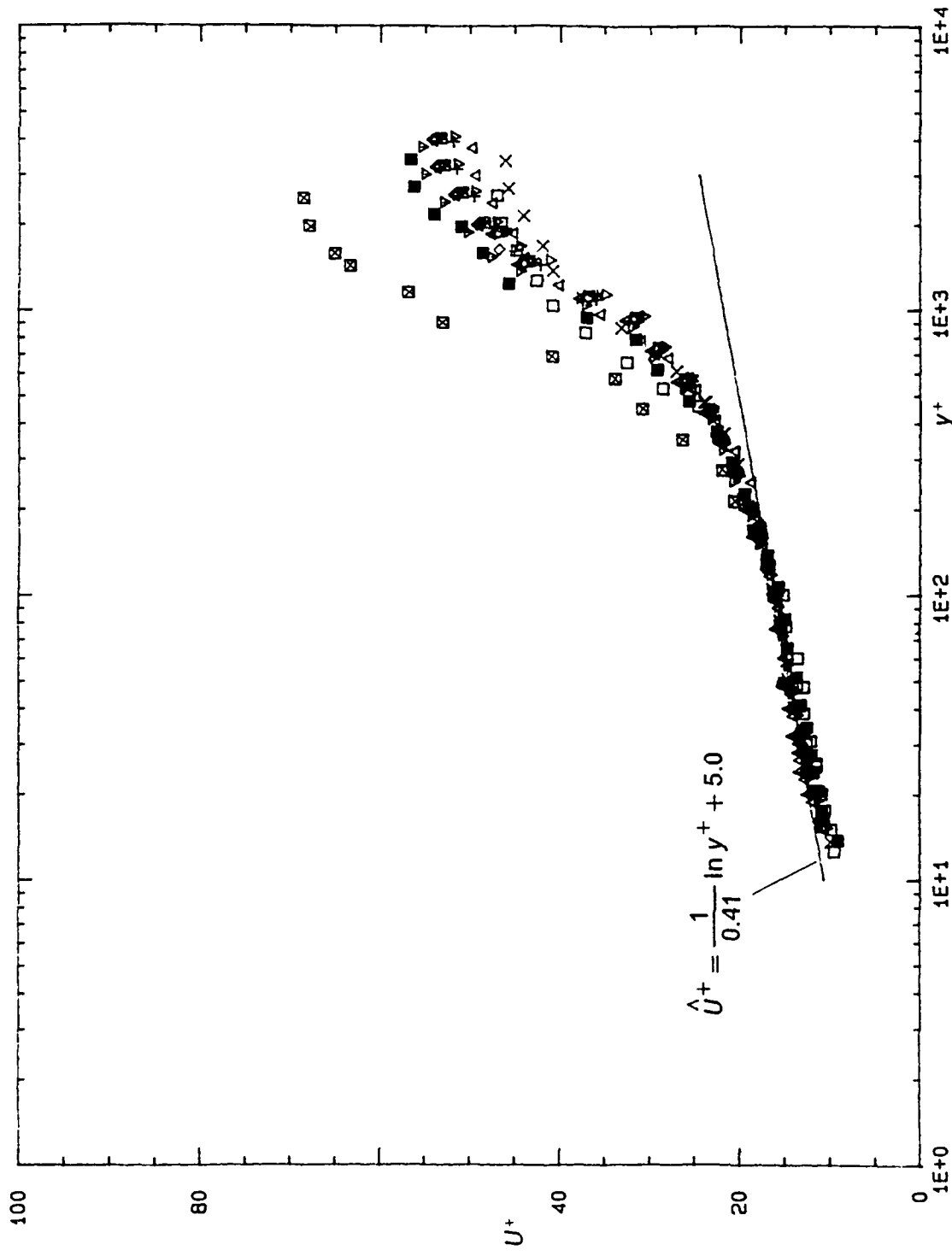


Figure 44. Ensemble-averaged law-of-the-wall velocity profiles, $\hat{U}^+ \text{ vs. } \log_{10} y^+$, $X = 2.95\text{m}$, $k = 0.61$ flow. ($\square = 90^\circ$; $\times = 105^\circ$; $\triangle = 120^\circ$; $\diamond = 135^\circ$; $*$ $= 150^\circ$; $\square = 165^\circ$; $\diamond = 180^\circ$; $* = 195^\circ$; $\square = 210^\circ$; $\triangle = 225^\circ$; $\nabla = 240^\circ$; $\triangledown = 255^\circ$; $\blacksquare = 270^\circ$). solid line given by equation 5.

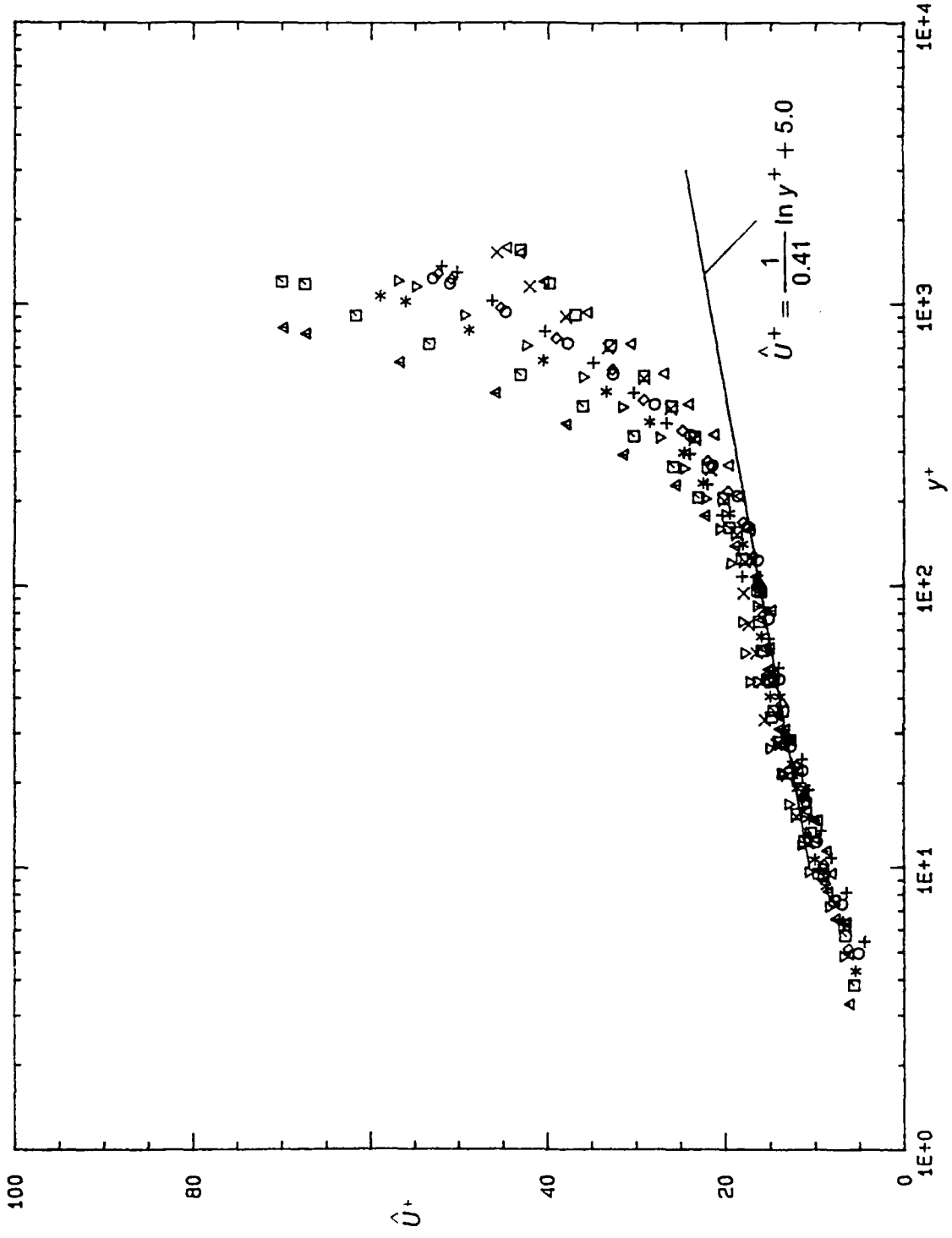


Figure 45. Ensemble-averaged law-of-the-wall velocity profiles, \hat{U}^+ vs. $\log_{10} y^+$, $X=2.95\text{m}$, $k=1.33$ flow. ($\square = 135^\circ$; $\times = 150^\circ$; $\triangle = 165^\circ$; $+ = 180^\circ$; $\nabla = 195^\circ$; $\diamond = 210^\circ$; $\circ = 225^\circ$; $*$ = 240° ; $\boxdot = 255^\circ$; $\boxtimes = 270^\circ$); Solid line given by equation 5.

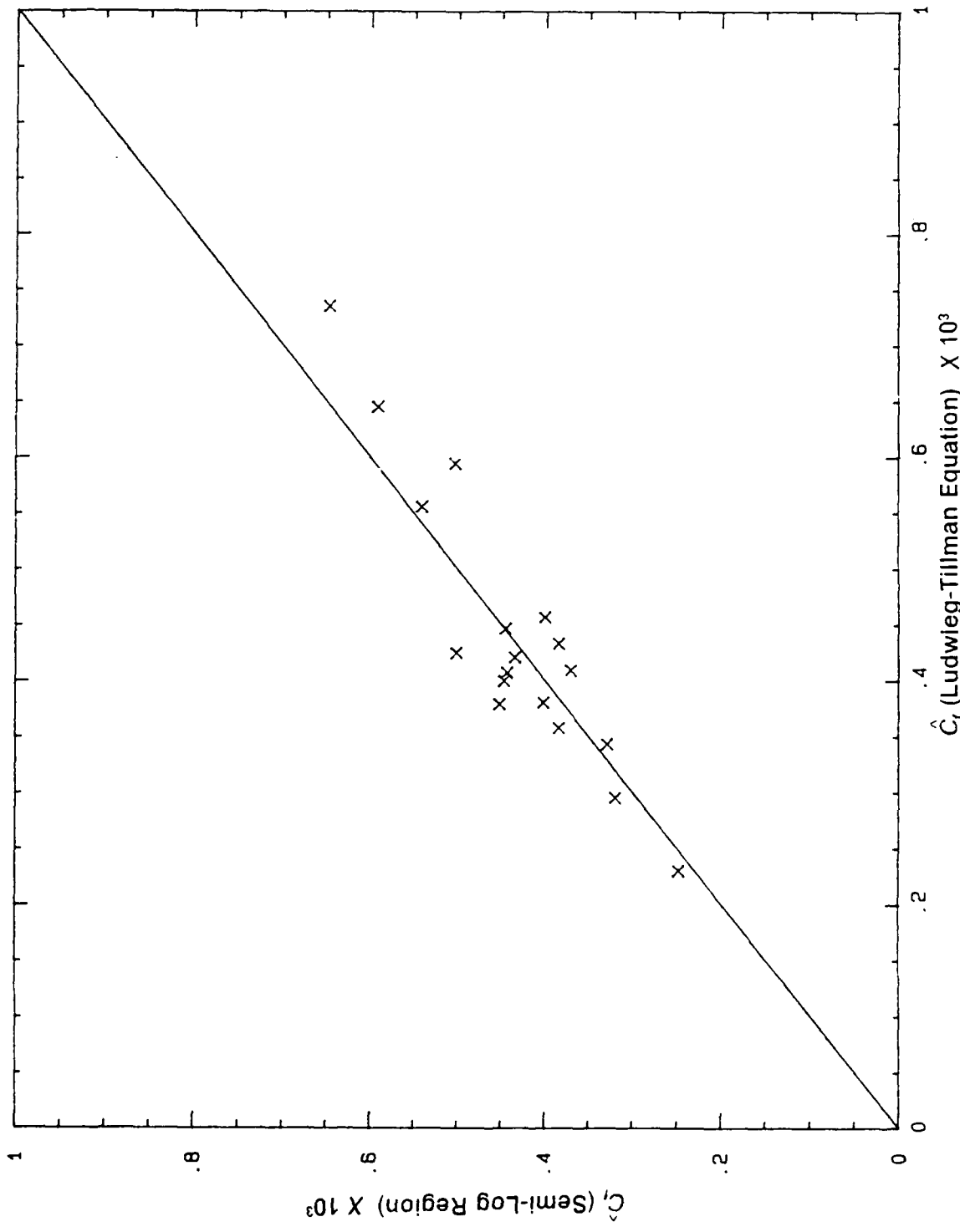


Figure 46. Correlation between \hat{C}_r obtained from semi-log region and \hat{C}_r obtained from Ludwig-Tillman equation (6) at $X = 3.28m$, $k = 1.03$ flow with 'roof damper'.

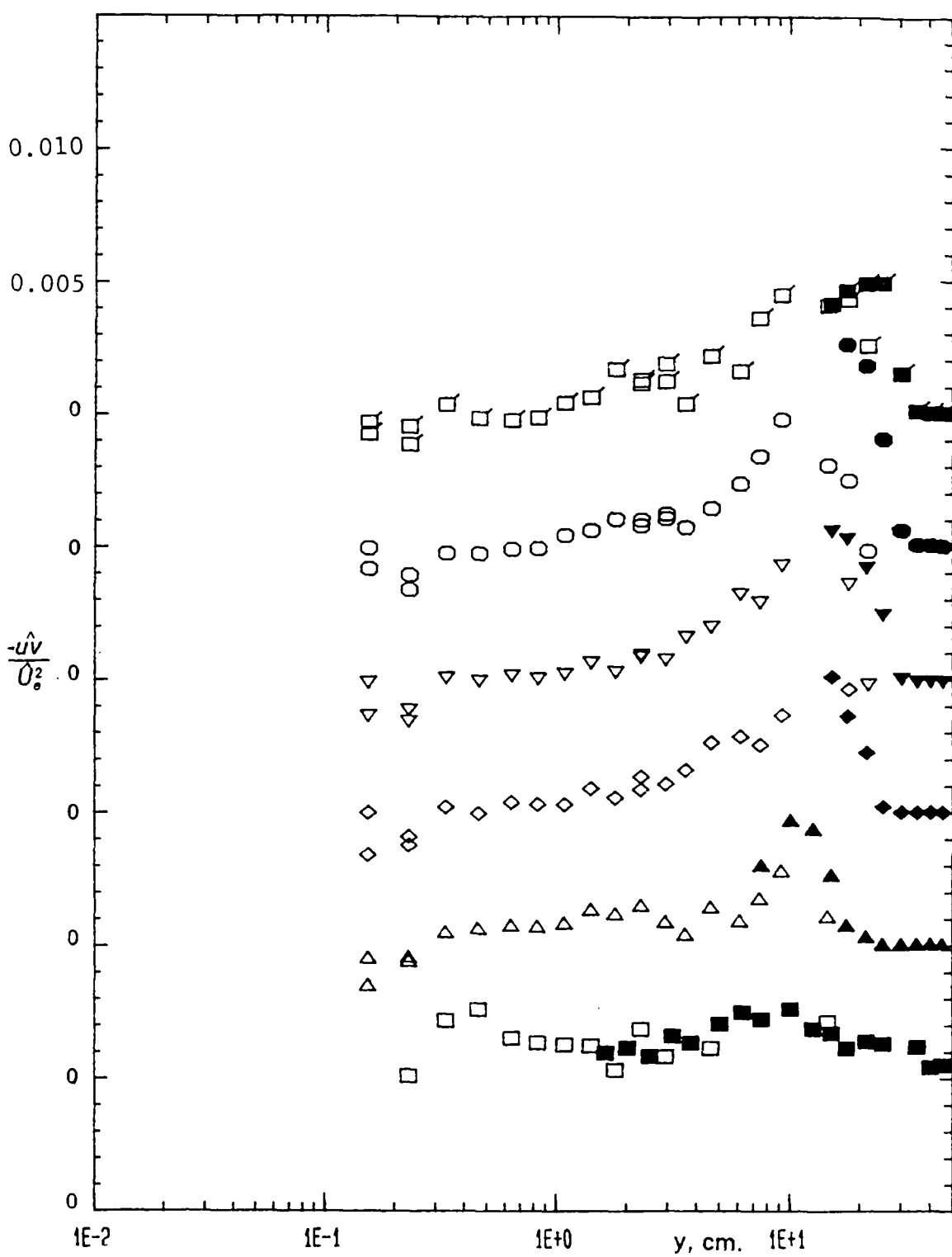


Figure 47a. Ensemble-averaged Reynolds shearing stress $-\hat{u}\hat{v}/\hat{U}_e^2$ profiles at $X = 4.27 \text{ m}$, $k = 0.61$ flow at phases $120^\circ \leq \omega t \leq 195^\circ$; ($\square = 120^\circ$; $\triangle = 135^\circ$; $\diamond = 150^\circ$; $\nabla = 165^\circ$; $\circ = 180^\circ$; $\blacksquare = 195^\circ$); open symbols, laser anemometer; solid symbols, cross-wire measurements.

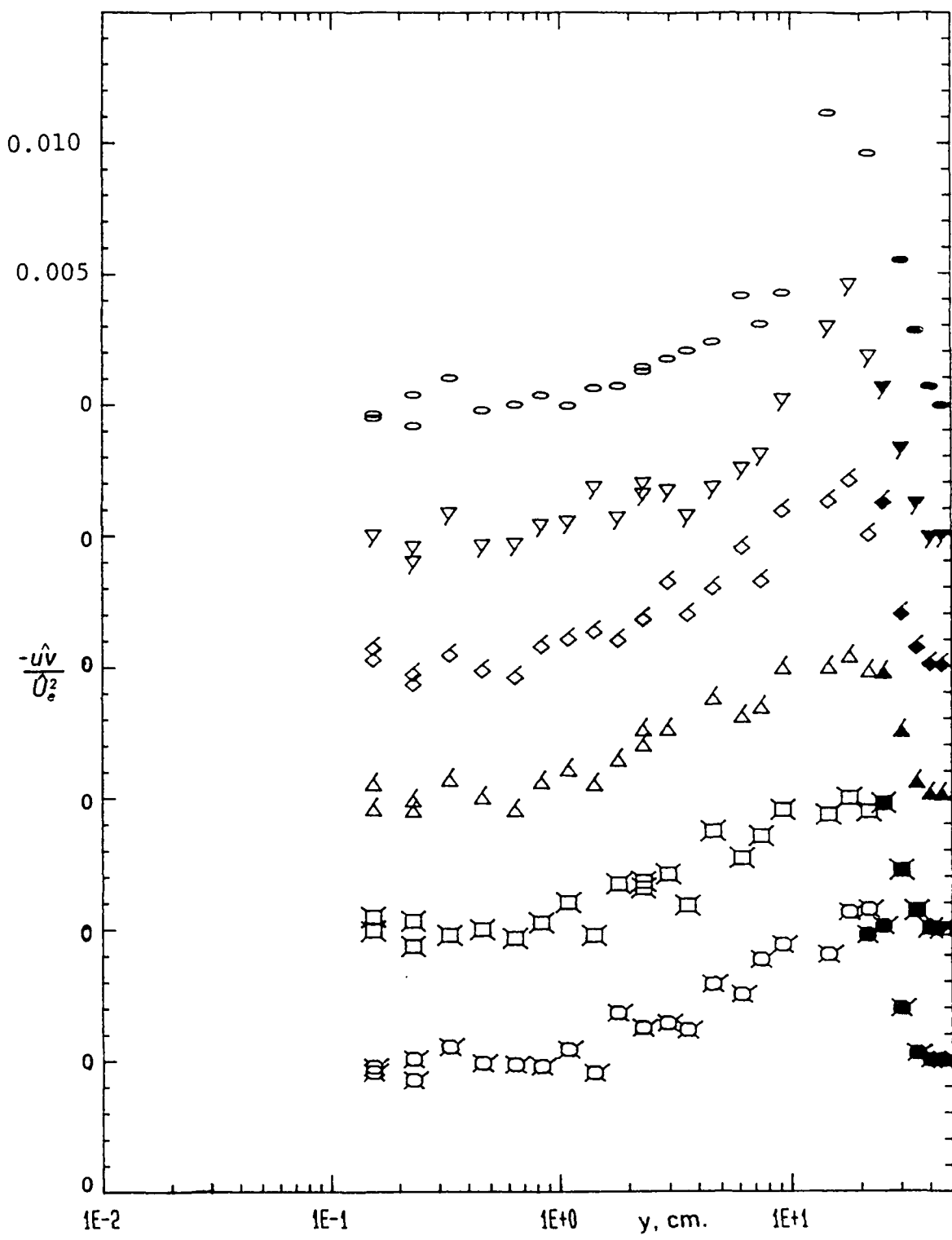


Figure 47b. Ensemble-averaged Reynolds shearing stress $-uv/\hat{U}_e^2$ profiles at $X = 4.27$ m, $k=0.61$ flow at phases $210^\circ \leq \omega t \leq 285^\circ$; ($\square = 210^\circ$; $\triangle = 225^\circ$; $\diamond = 240^\circ$; $\nabla = 255^\circ$; $\circ = 270^\circ$; $\blacksquare = 285^\circ$); open symbols, laser anemometer; solid symbols, cross-wire measurements.

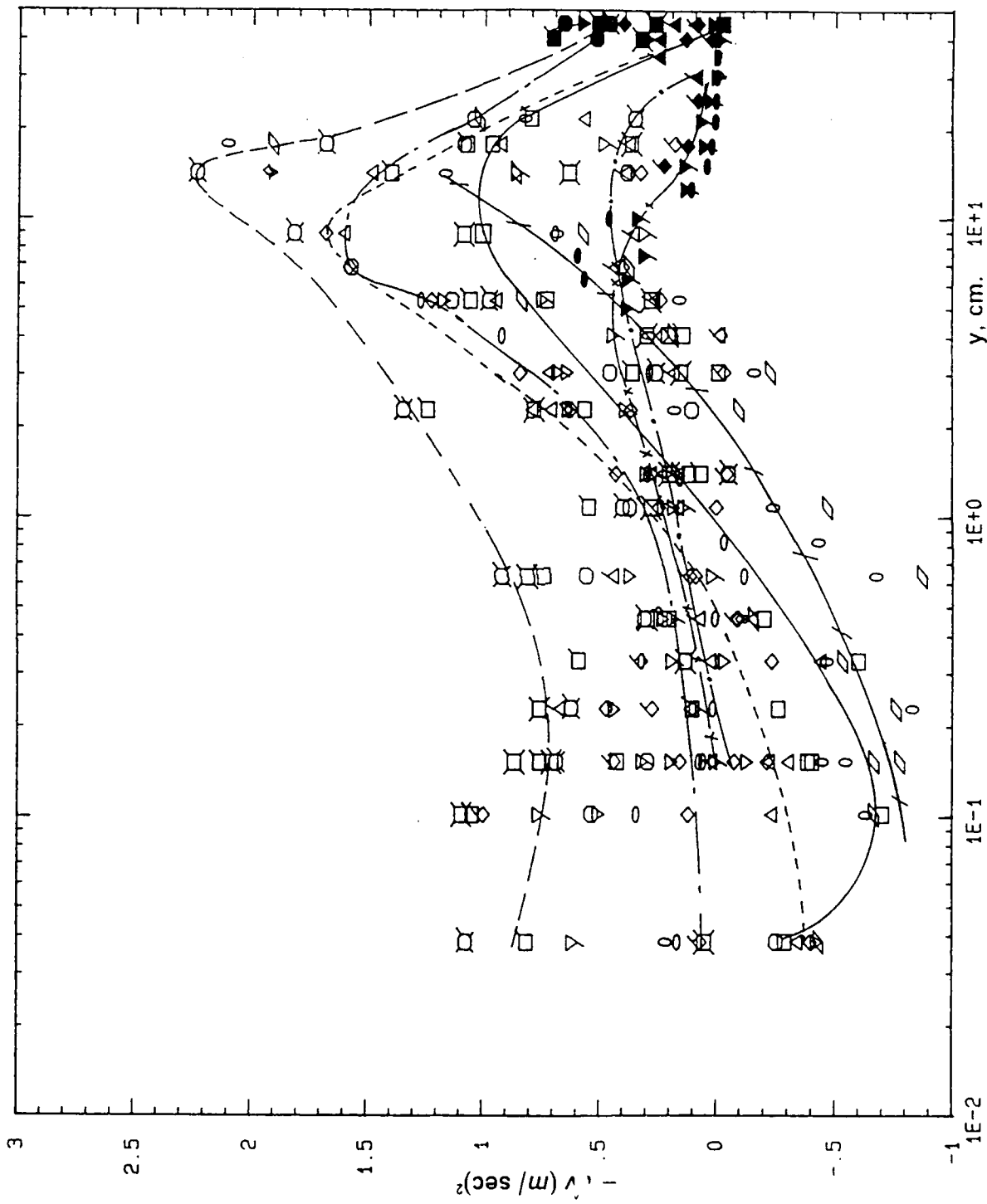


Figure 48a. Ensemble-averaged Reynolds shearing stress - $\hat{u}\hat{v}$ profiles at $X = 4.27$ m, $K = 1.33$ flow at phases $345^\circ \leq \omega t \leq 180^\circ$; Legend same as in figure 39a; Lines for visual aid only.

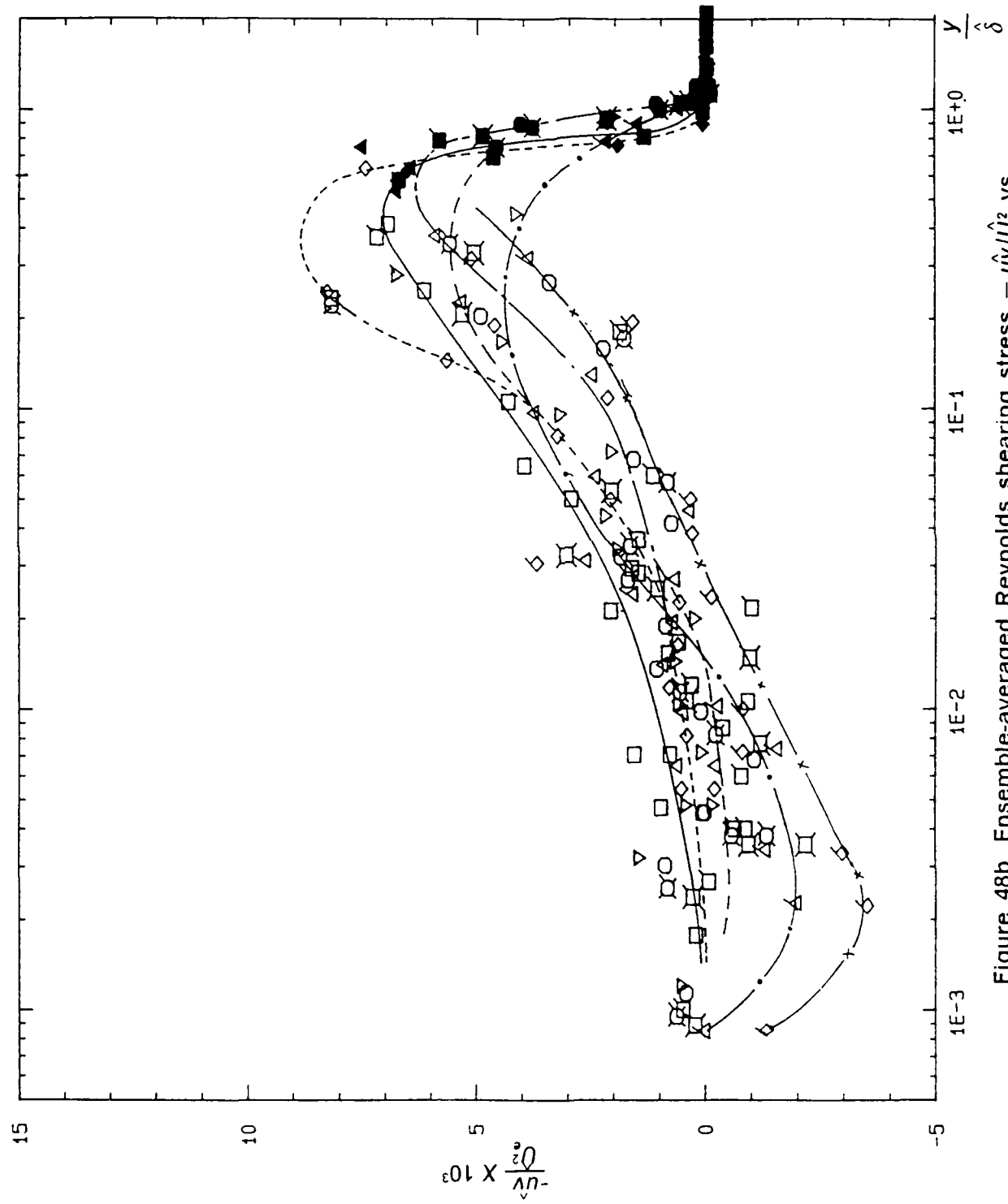


Figure 48b. Ensemble-averaged Reynolds shearing stress – $\hat{u}\hat{v}/\hat{U}_*^2$ vs. $\log_{10}(Y/\delta)$ profiles at $X = 4.27$ m, $k = 1.33$ flow at phases $195^\circ \leq \omega t \leq 330^\circ$; Legend same as in figure 39b; Lines for visual aid only.

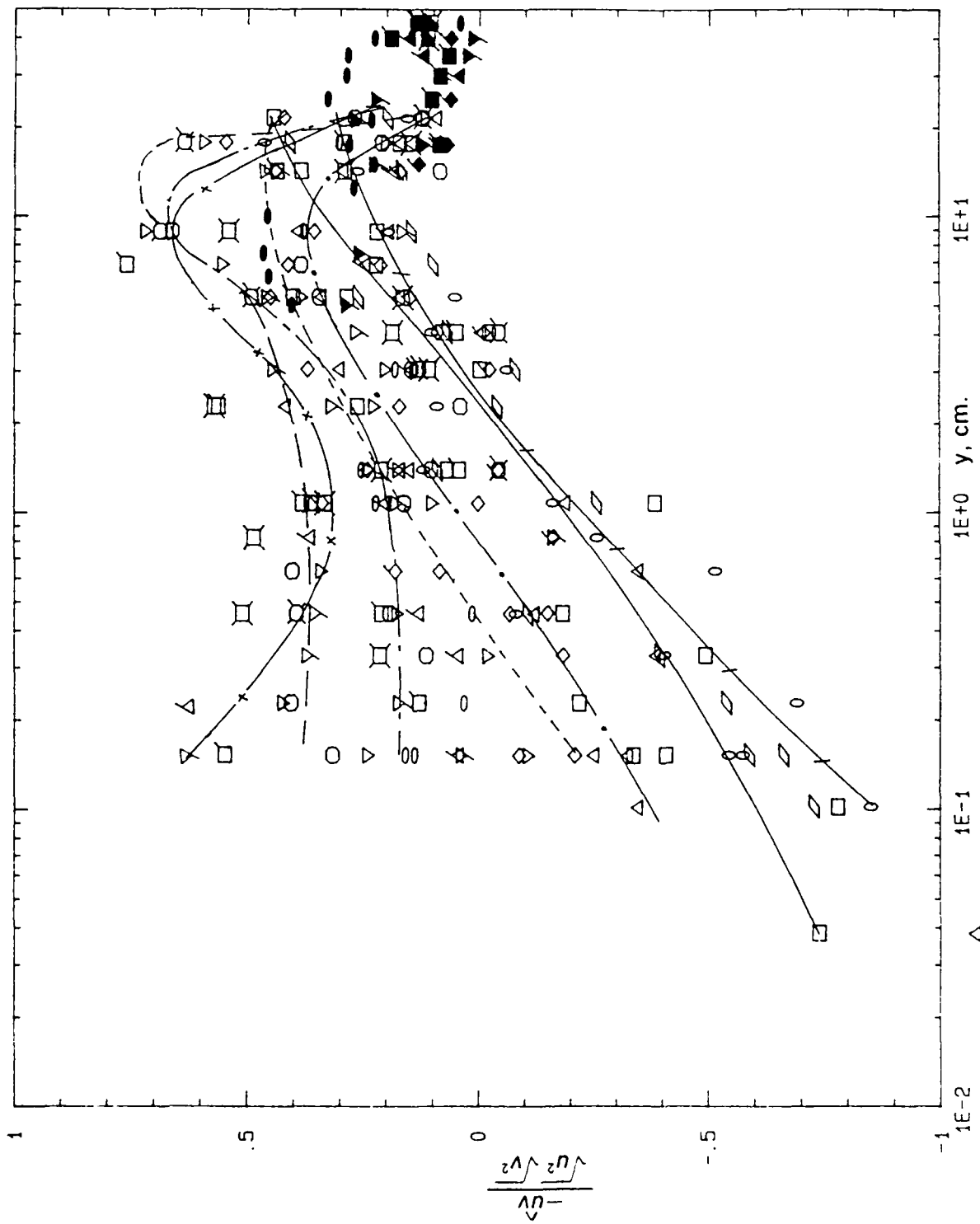


Figure 49a. Ensemble-averaged shear stress correlation profiles at $X = 4.27$ m, $k = 1.33$ flow at phases $345^\circ \leq \omega t \leq 180^\circ$; Legend same as in figure 39a; Lines for visual aid only.

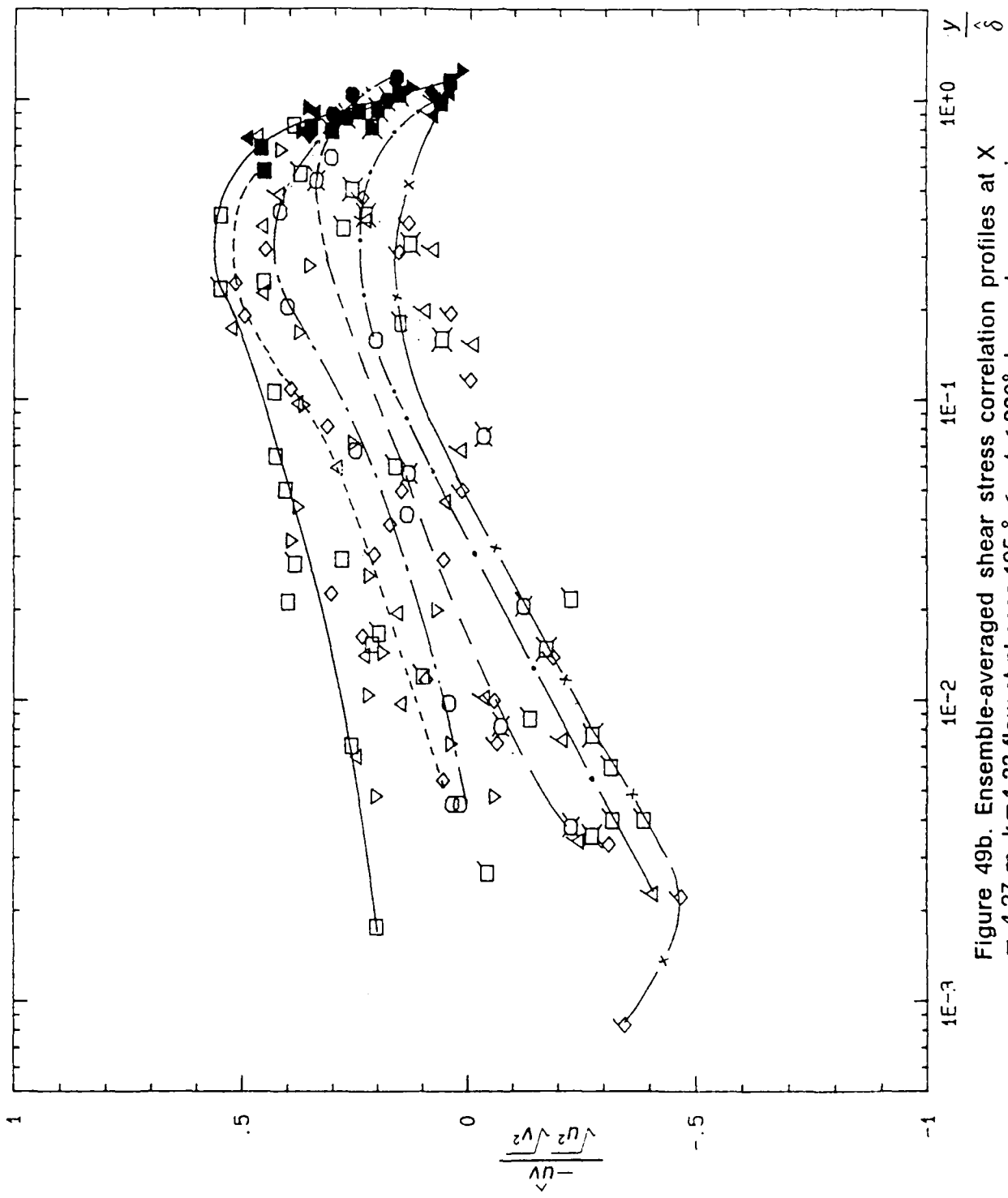


Figure 49b. Ensemble-averaged shear stress correlation profiles at $X = 4.27$ m, $k = 1.33$ flow at phases $195^\circ \leq \omega t \leq 330^\circ$; Legend same as in figure 39b; Lines for visual aid only.

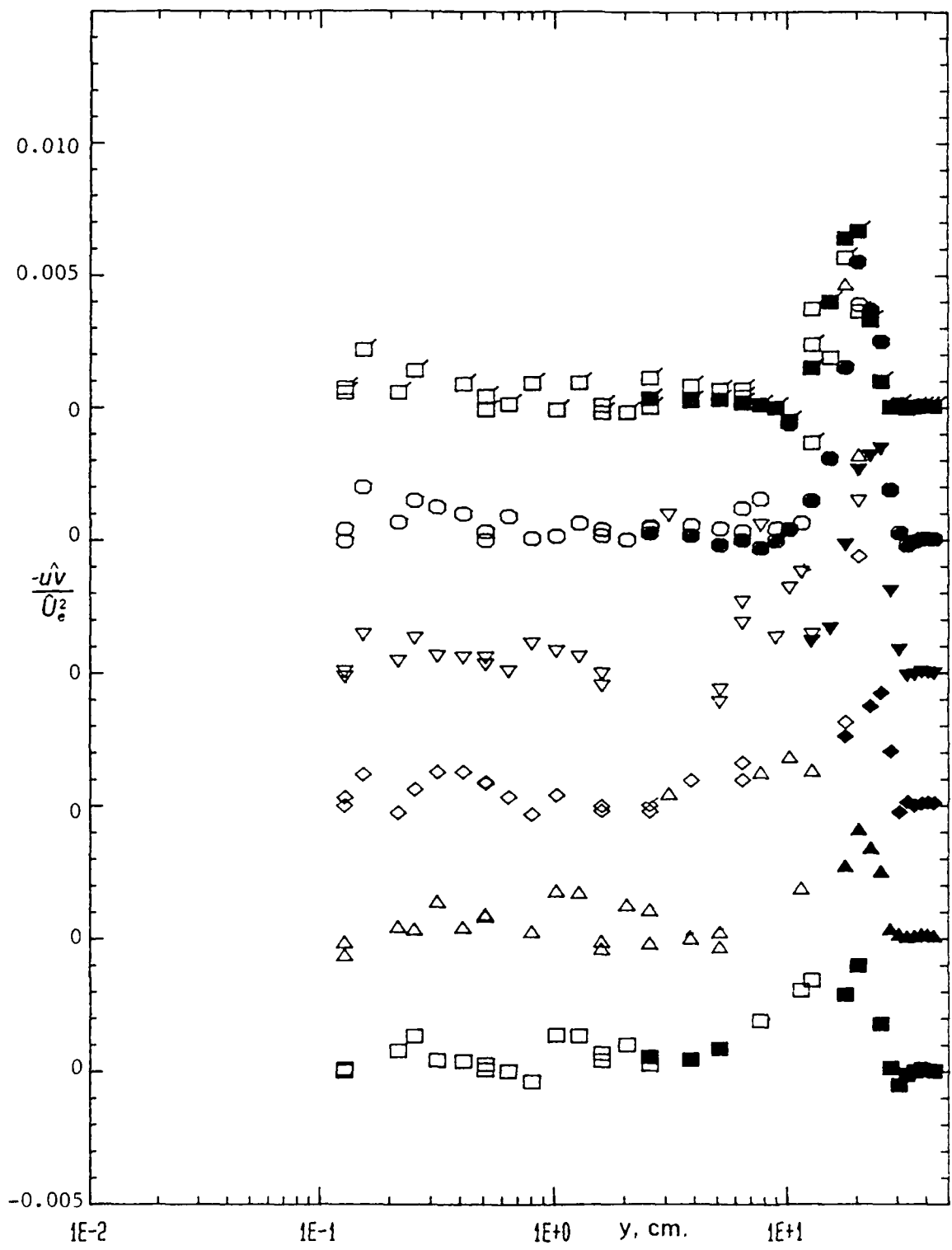


Figure 50a. Ensemble-averaged Reynolds shearing stress $-\hat{u}\hat{v}/\hat{U}_e^2$ profiles at $X = 3.59 \text{ m}$, $k = 1.03$ flow with 'roof damper' at phases $15^\circ \leq \omega t \leq 90^\circ$; Legend same as in figure 40a.

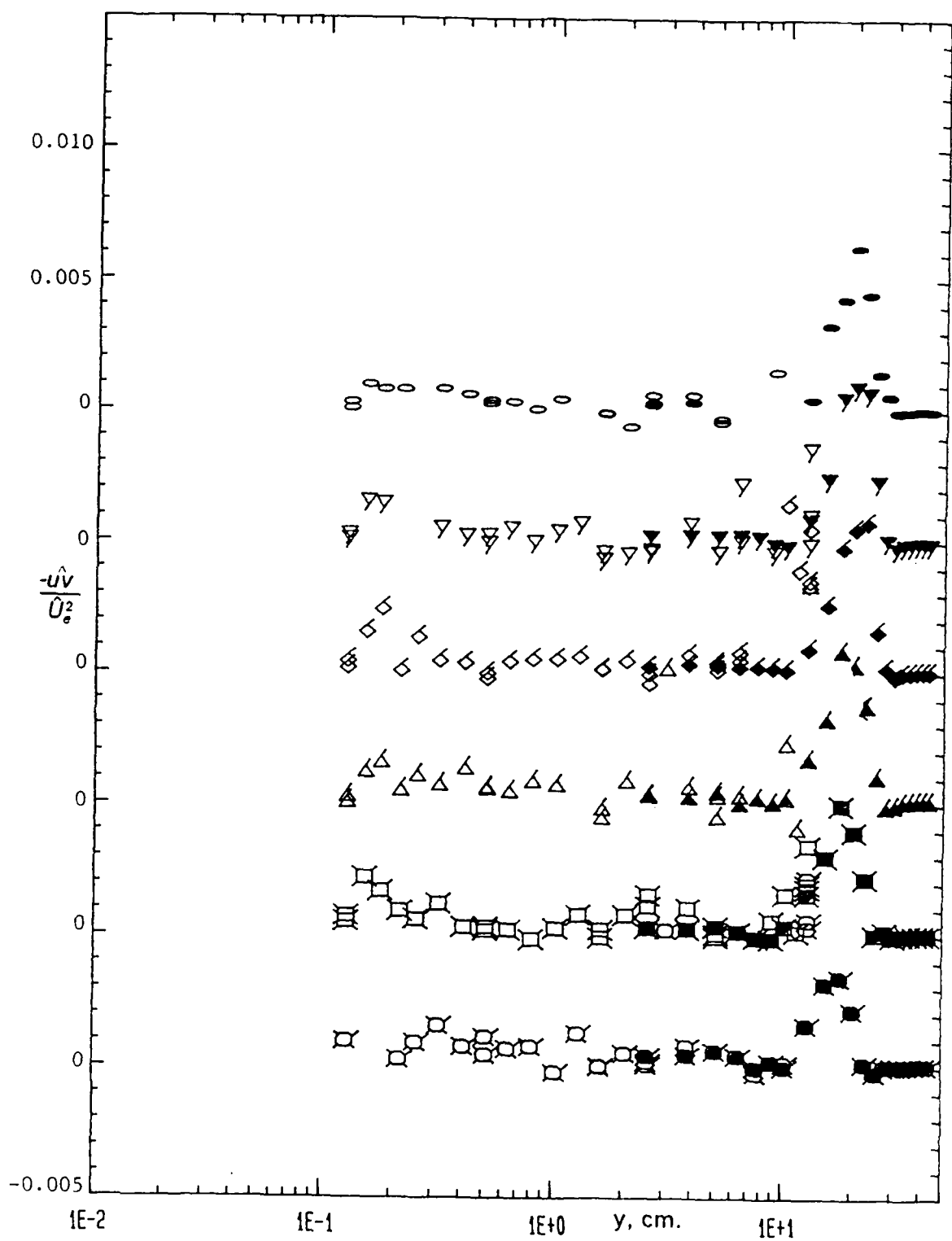


Figure 50b. Ensemble-averaged Reynolds shearing stress $-uv/U_e^2$ profiles at $X = 3.59 \text{ m}$, $k = 1.03$ flow with 'roof damper' at phases $105^\circ \leq \omega t \leq 180^\circ$; Legend same as in figure 40a.

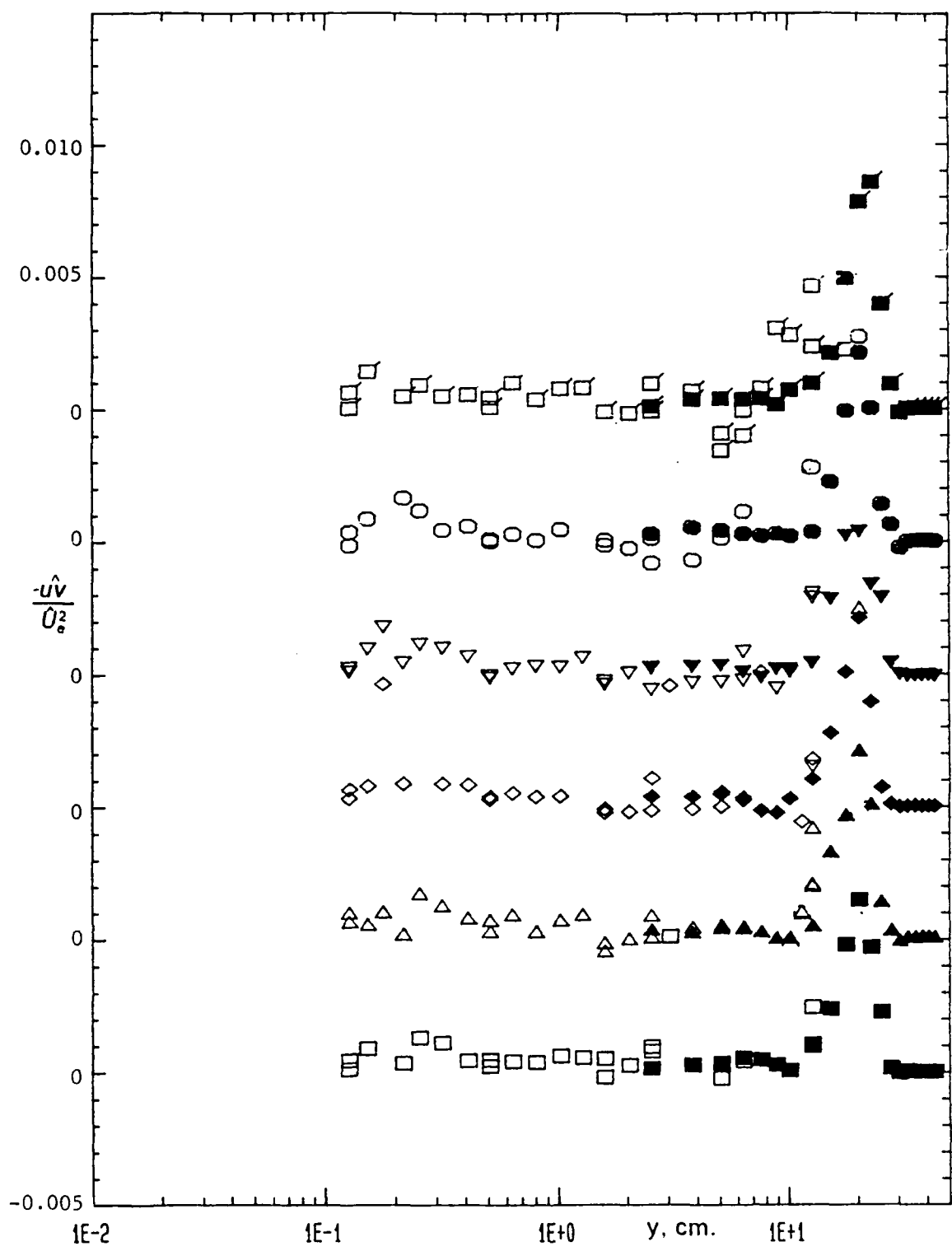


Figure 50c. Ensemble-averaged Reynolds shearing stress $-u\hat{v}/\hat{U}_s^2$ profiles at $X = 3.59$ m, $k = 1.03$ flow with 'roof damper' at phases $195^\circ \leq \omega t \leq 270^\circ$; Legend same as in figure 40a.

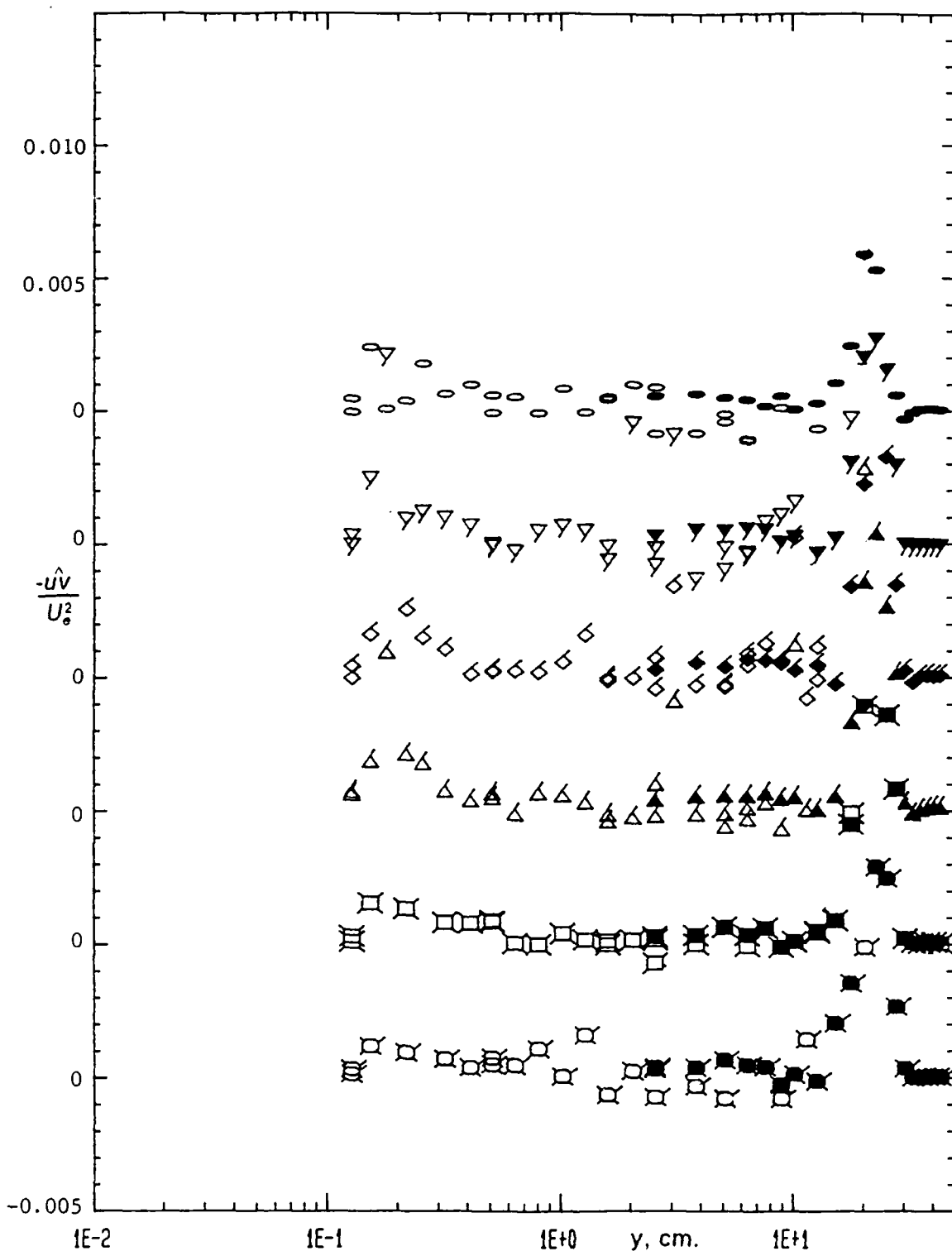


Figure 50d. Ensemble-averaged Reynolds shearing stress $-\hat{u}\hat{v}/\hat{U}_e^2$ profiles at $X = 3.59$ m, $k=1.03$ flow with 'roof damper' at phases $285^\circ \leq \omega t \leq 360^\circ$; Legend same as in figure 40a.

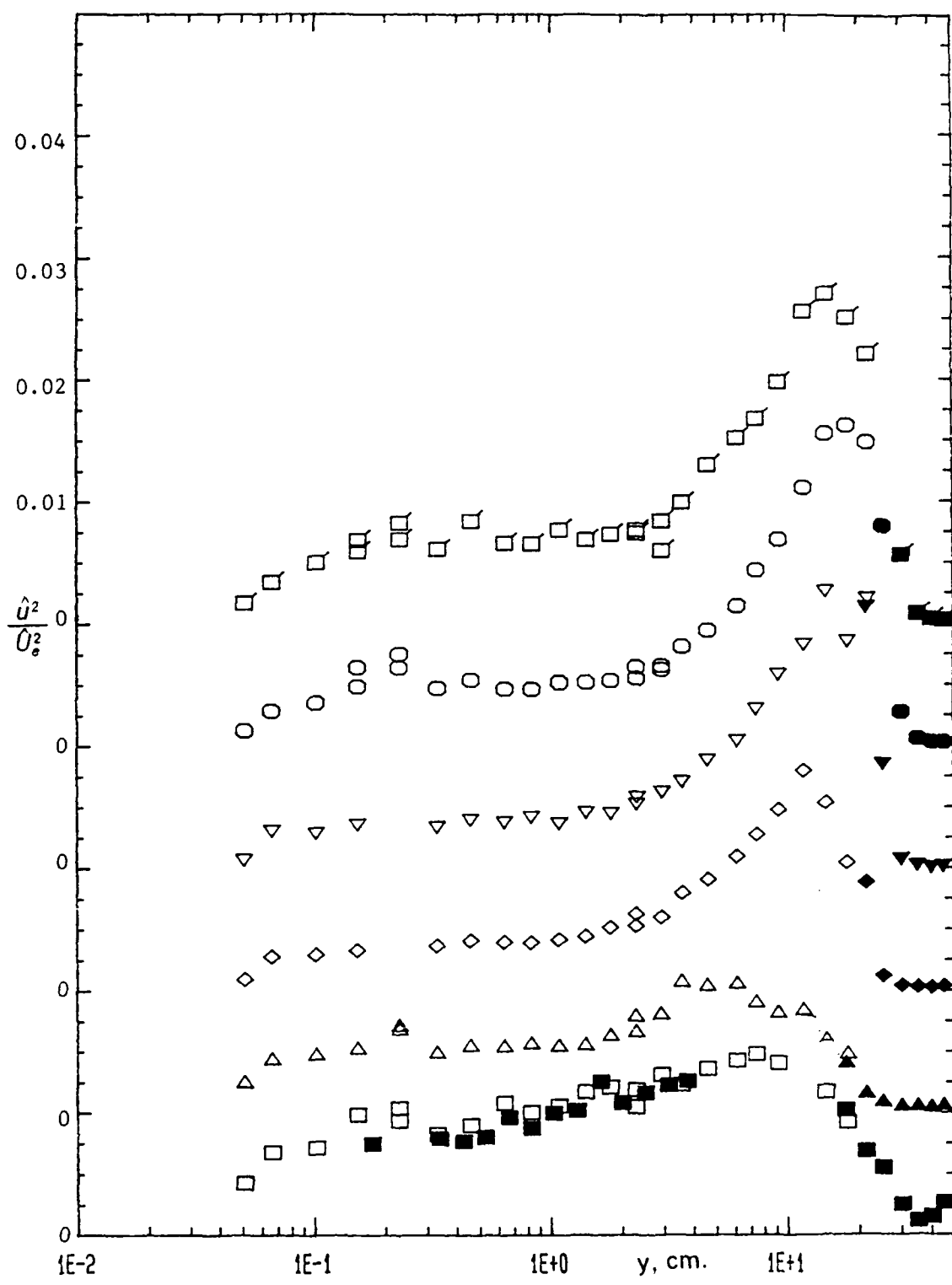


Figure 51a. Streamwise turbulence intensity \hat{u}^2/\hat{U}_e^2 profiles at $X = 4.27$ m, $k = 0.61$ flow at phases $120^\circ \leq \omega t \leq 195^\circ$; Legend same as in figure 36b.

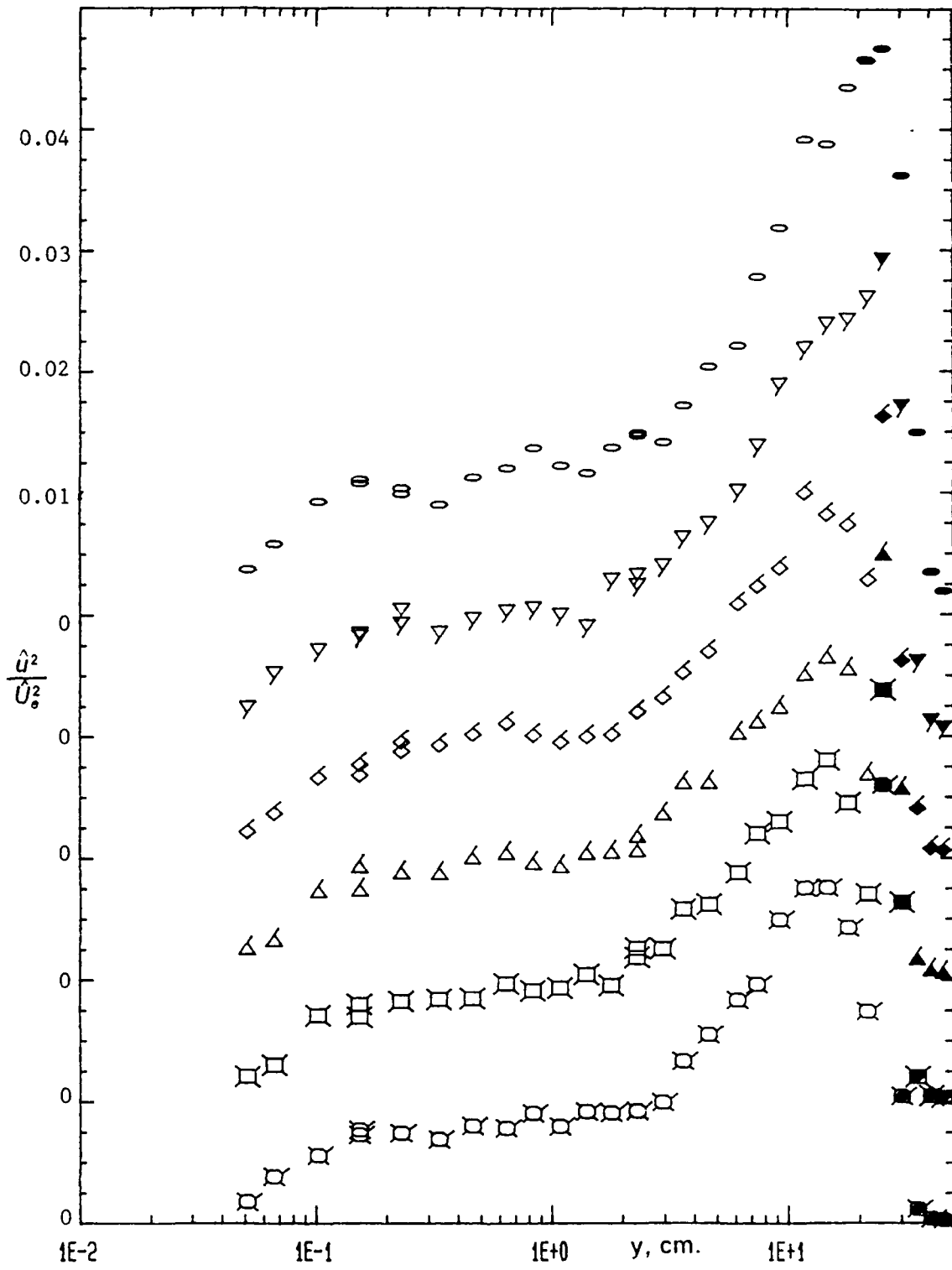


Figure 51b. Streamwise turbulence intensity \hat{u}^2/\hat{U}_e^2 profiles at $X = 4.27$ m, $k=0.61$ flow at phases $210^\circ \leq \omega t \leq 285^\circ$; Legend same as in figure 36b.

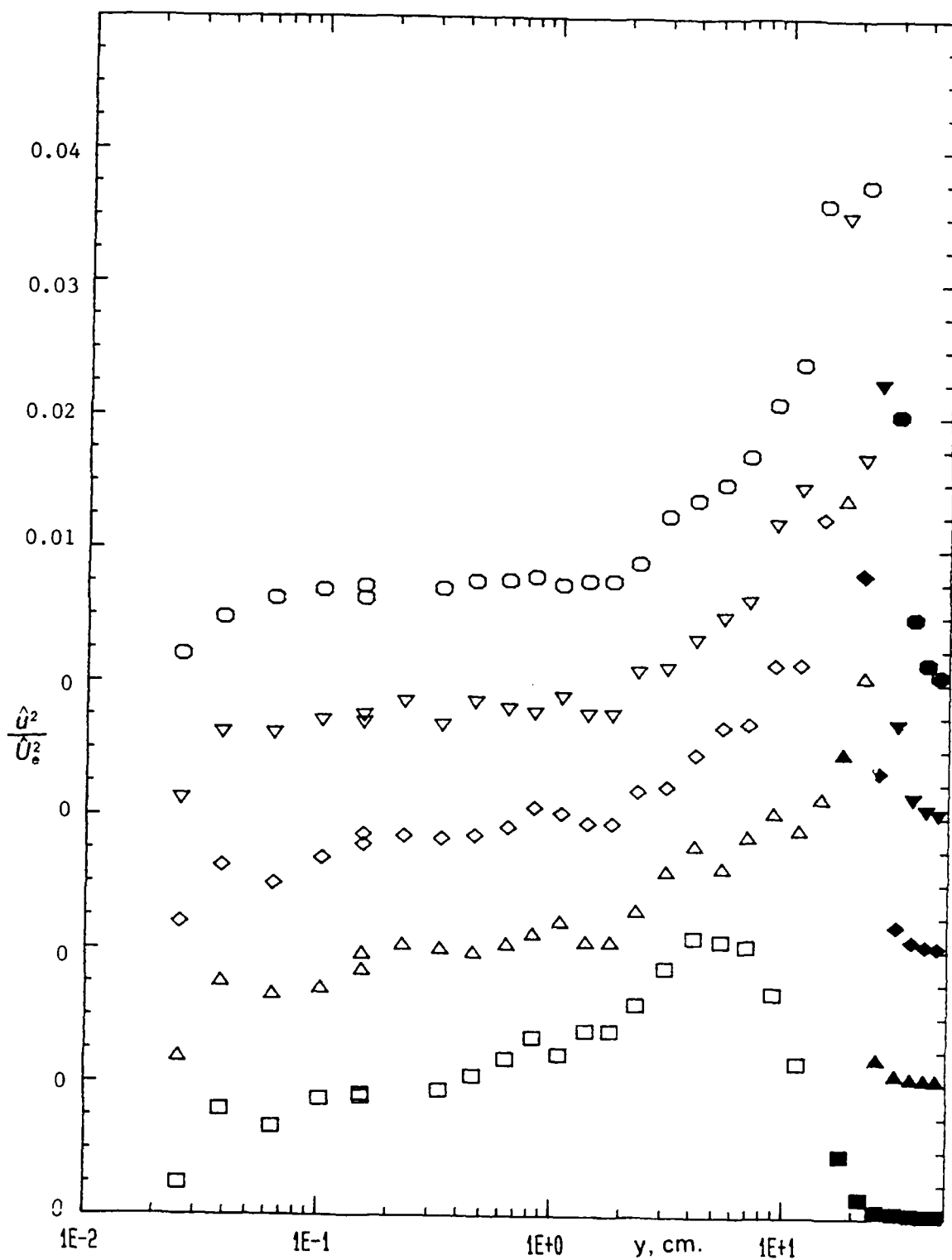


Figure 52a. Streamwise turbulence intensity \hat{u}^2 / \hat{U}_e^2 profiles at $X = 4.27$ m, $k = 1.33$ flow at phases $195^\circ \leq \omega t \leq 255^\circ$; Legend same as in figure 39b.

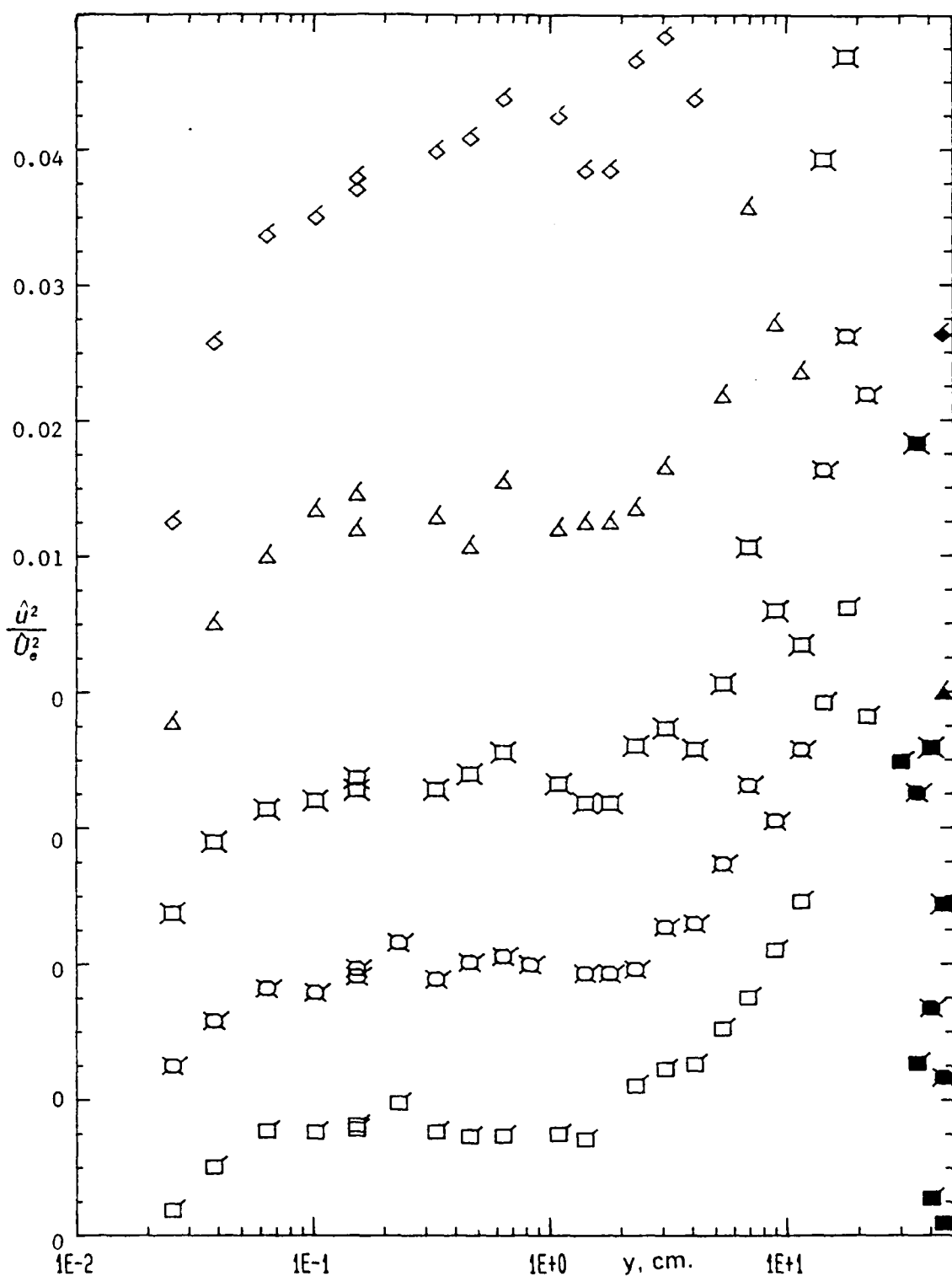


Figure 52b. Streamwise turbulence intensity \hat{u}^2/\hat{U}_s^2 profiles at $X = 4.27$ m, $k = 1.33$ flow at phases $270^\circ \leq \omega t \leq 330^\circ$; Legend same as in figure 39b.

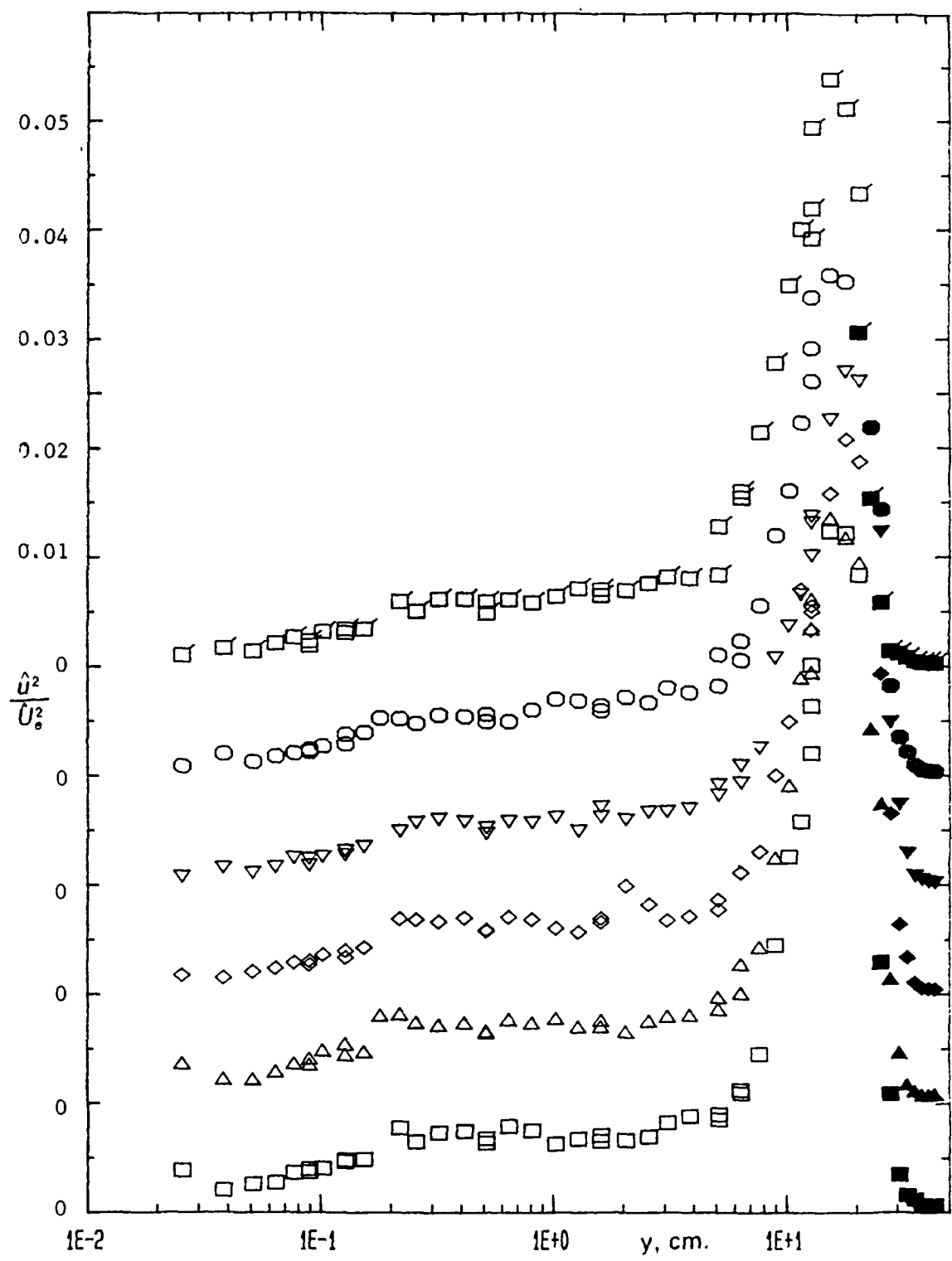


Figure 53a. Streamwise turbulence intensity \hat{U}^2 / \hat{U}_e^2 profiles at $X = 3.59$ m, $k = 1.03$ flow with 'roof damper' at phases $15^\circ \leq \omega t \leq 90^\circ$; Legend same as in figure 40a.

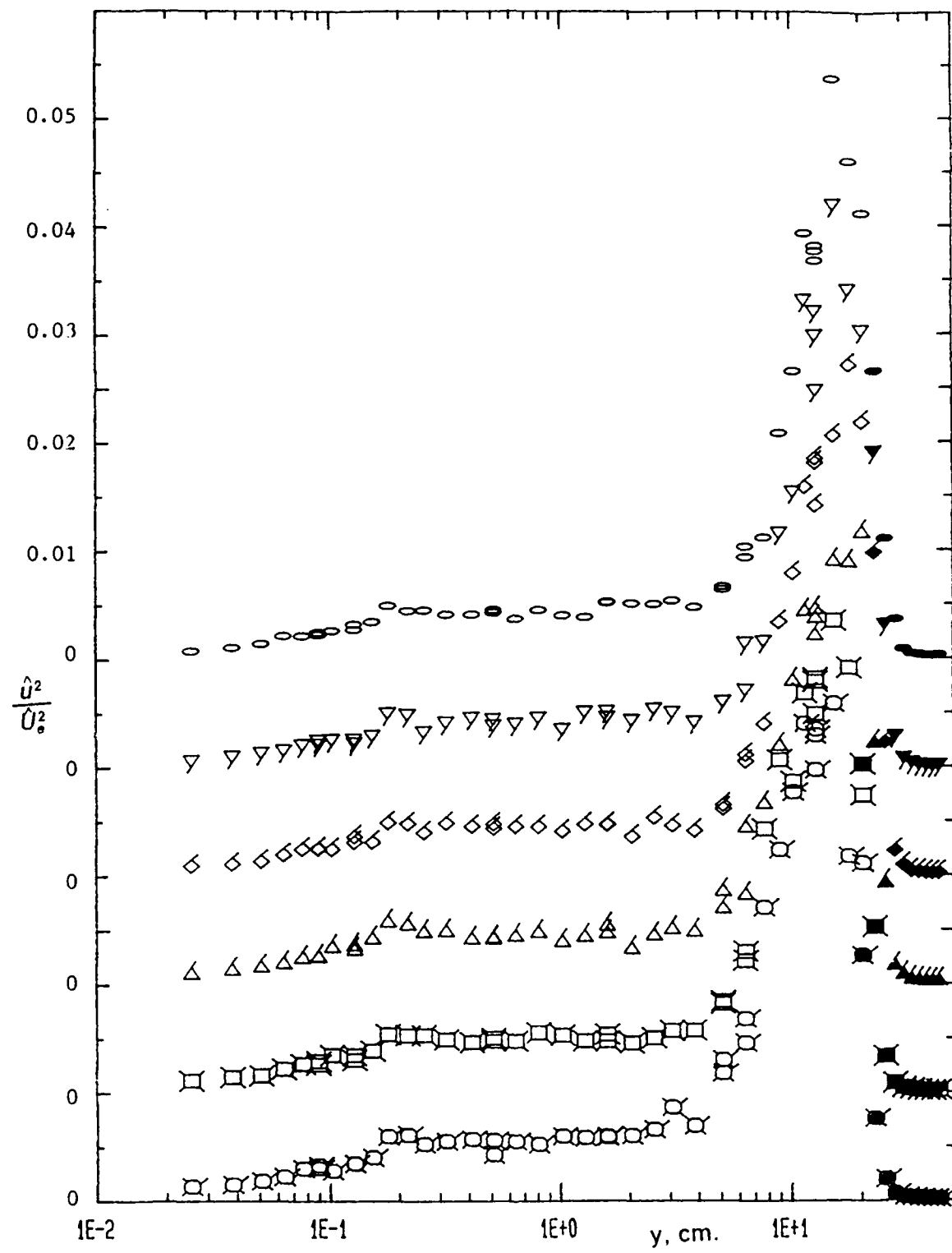


Figure 53b. Streamwise turbulence intensity \hat{u}^2 / \hat{U}_e^2 profiles at $X = 3.59$
 $m, k = 1.03$ flow with 'roof damper' at phases $105^\circ \leq \omega t \leq 180^\circ$; Legend
 same as in figure 40a.

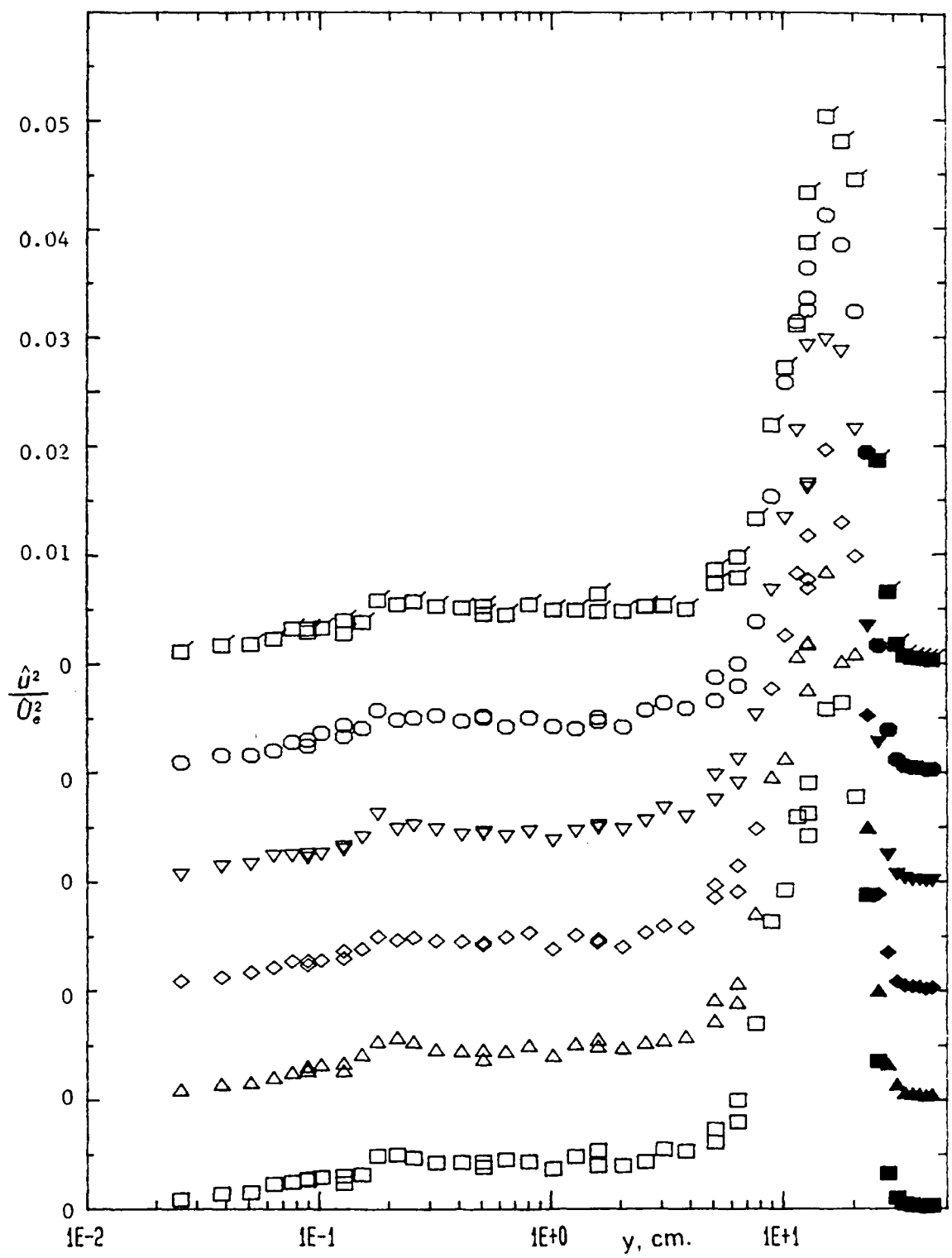


Figure 53c. Streamwise turbulence intensity \hat{U}^2 / \hat{U}_e^2 profiles at $X = 3.59$ m, $k = 1.03$ flow with 'roof damper' at phases $195^\circ \leq \omega t \leq 270^\circ$; Legend same as in figure 40b.

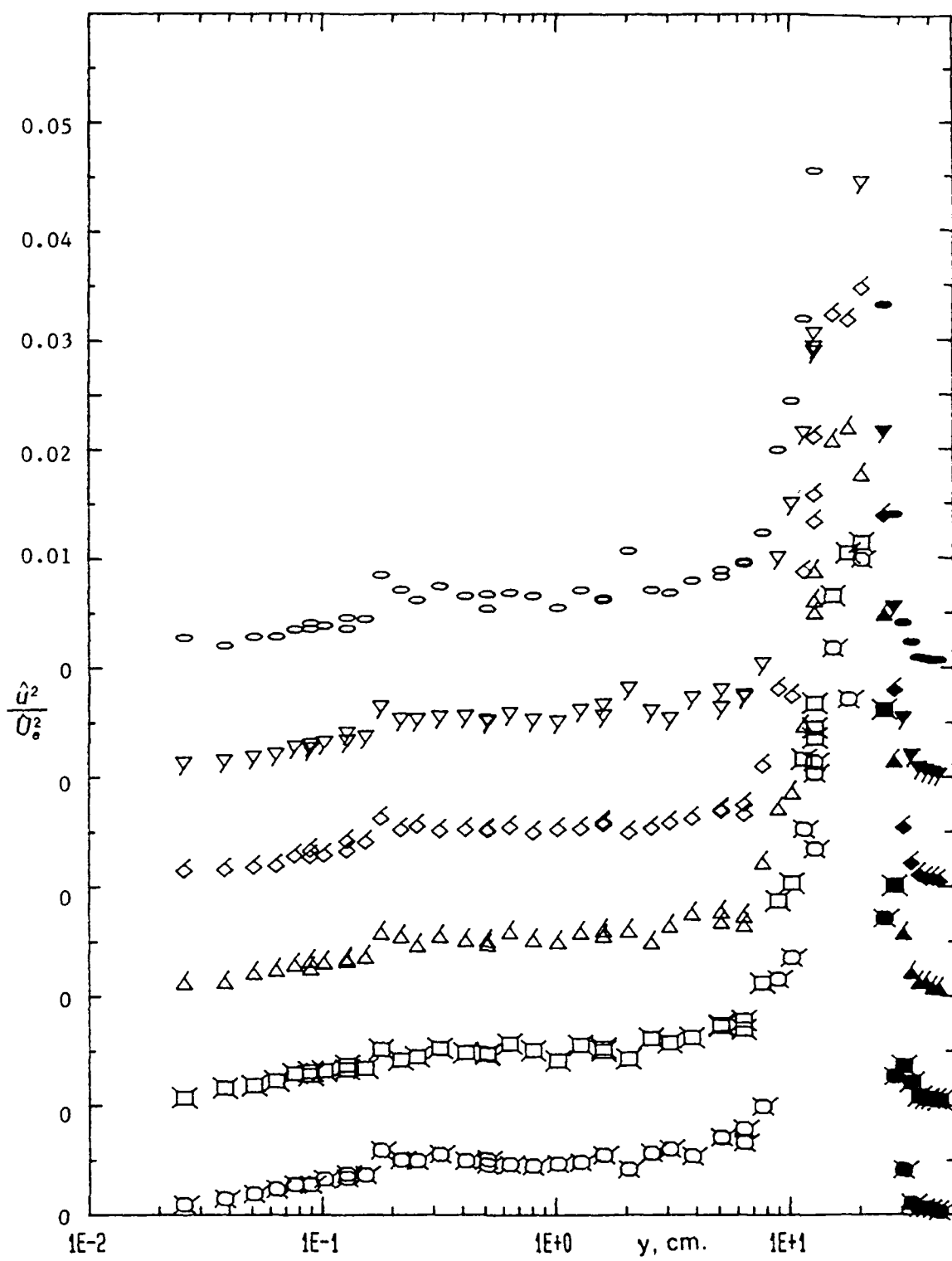


Figure 53d. Streamwise turbulence intensity \hat{u}^2/\hat{U}_e^2 profiles at $X = 3.59$ m, $k = 1.03$ flow with 'roof damper' at phases $285^\circ \leq \omega t \leq 360^\circ$; Legend same as in figure 40b.

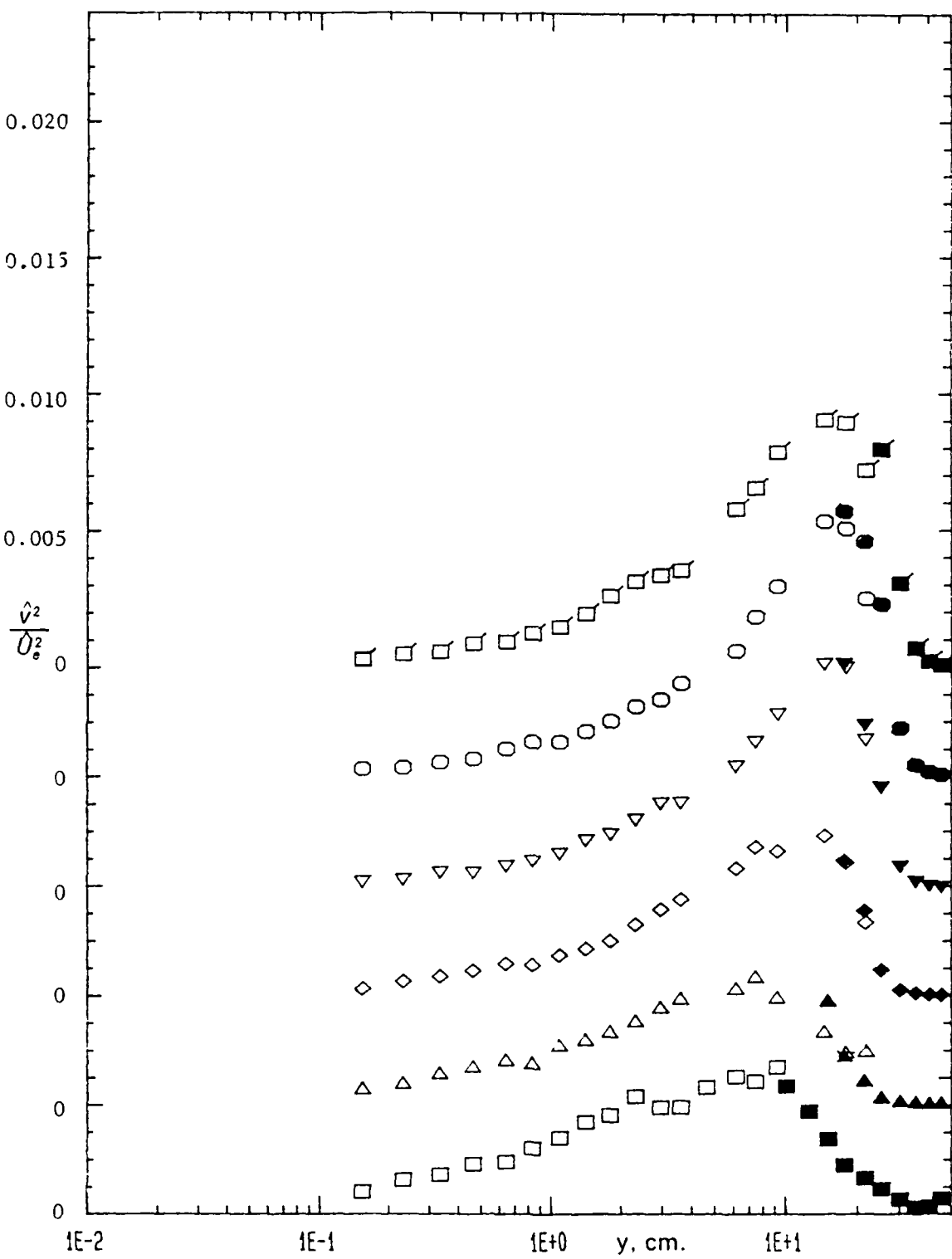


Figure 54a. Normal-to-wall turbulence intensity \hat{v}^2 / \hat{U}_e^2 profiles at $X = 4.27 \text{ m}$, $k=0.61$ flow at phases $120^\circ \leq \omega t \leq 195^\circ$; Legend same as in Figure 36b.

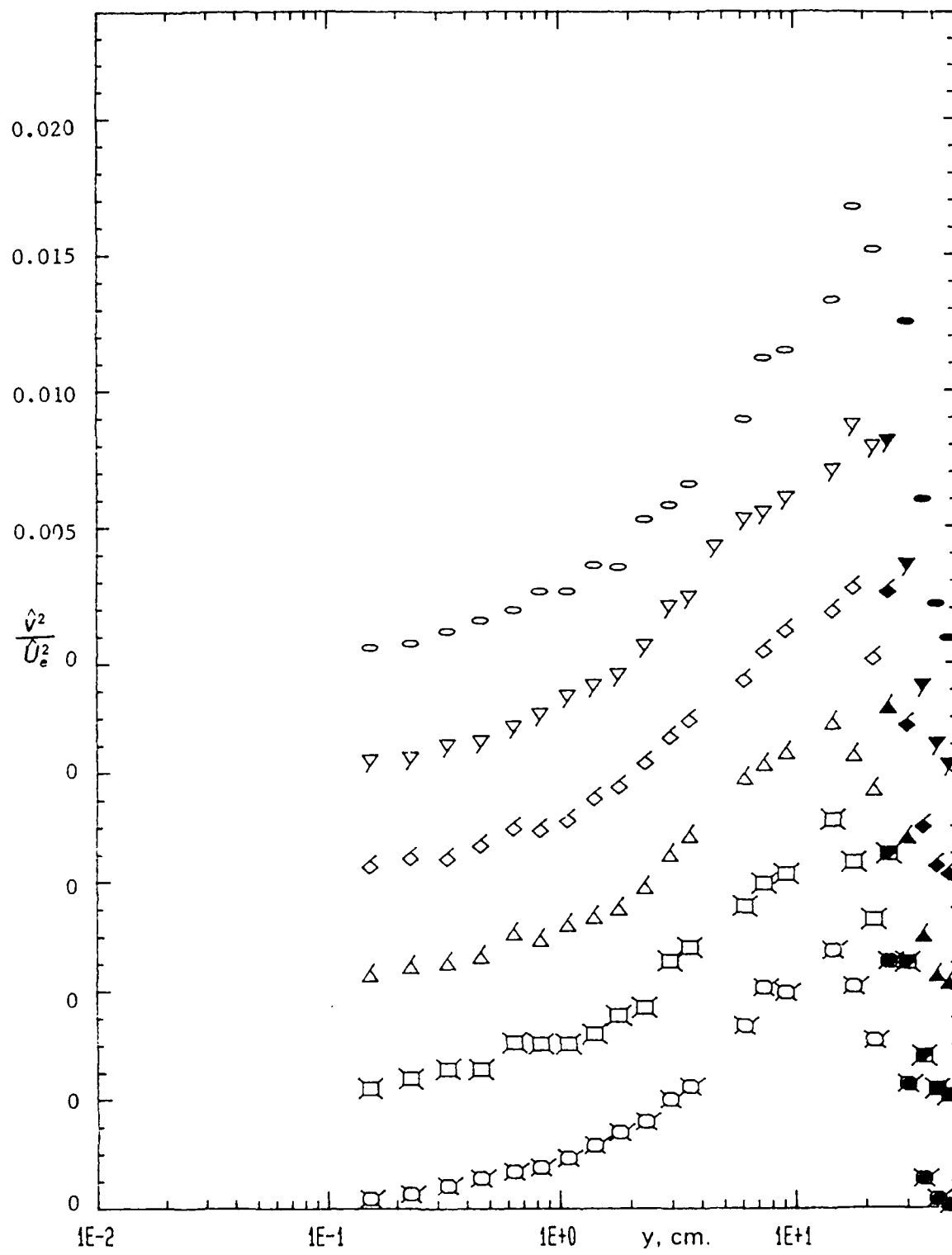


Figure 54b. Normal-to-wall turbulence intensity \hat{v}^2 / \hat{U}_e^2 profiles at $X = 4.27$ m, $k=0.61$ flow at phases $210^\circ \leq \omega t \leq 285^\circ$; Legend same as in Figure 36b.

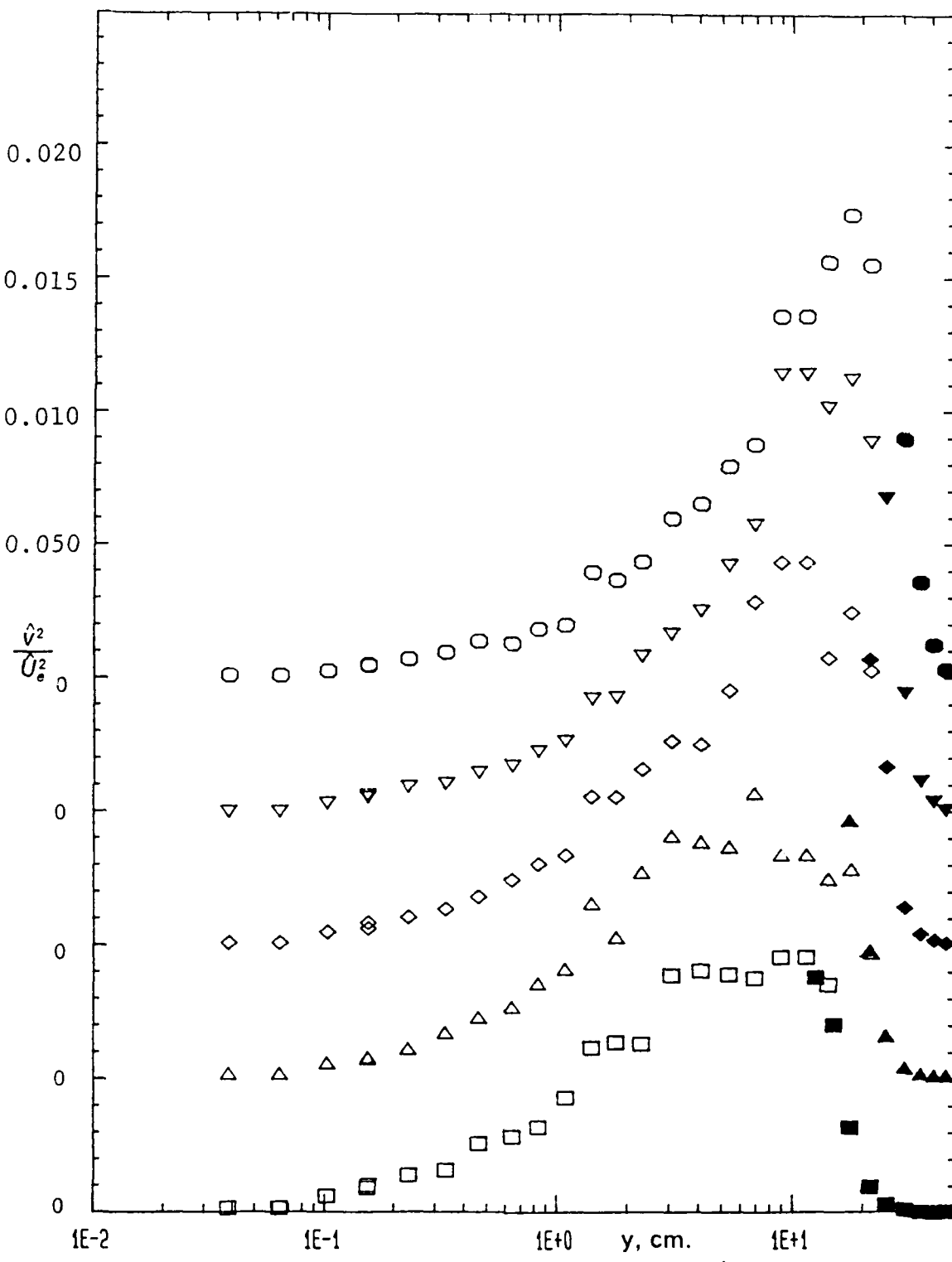


Figure 55a. Normal-to-wall turbulence intensity \hat{v}^2/\hat{U}_e^2 profiles at $X = 4.27$ m, $k = 1.33$ flow at phases $195^\circ \leq \omega t \leq 255^\circ$; Legend same as in figure 39b.

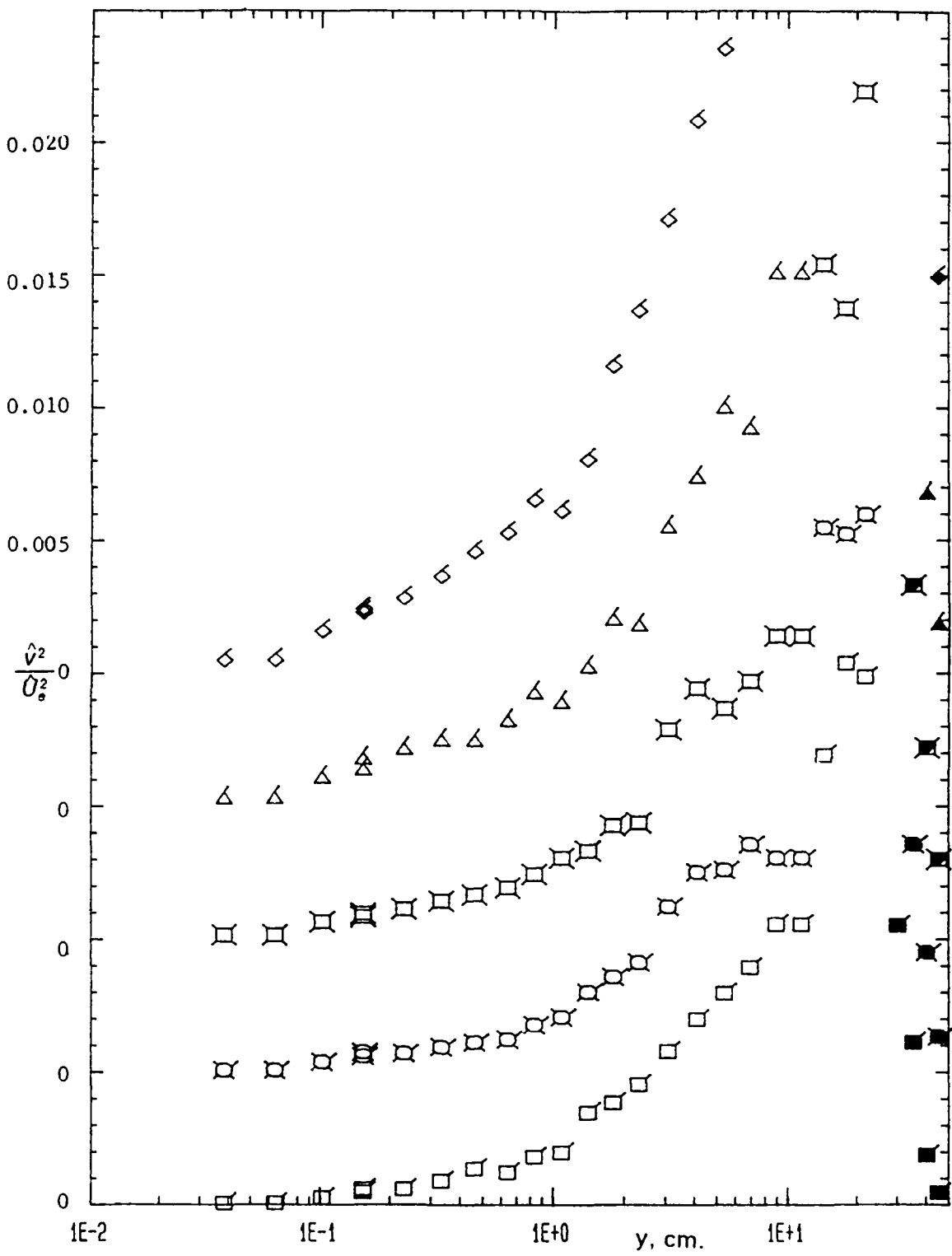


Figure 55b. Normal-to-wall turbulence intensity \hat{v}^2 / \hat{U}_e^2 profiles at $X = 4.27$ m, $k = 1.33$ flow at phases $270^\circ \leq \omega t \leq 330^\circ$; Legend same as in figure 39b.

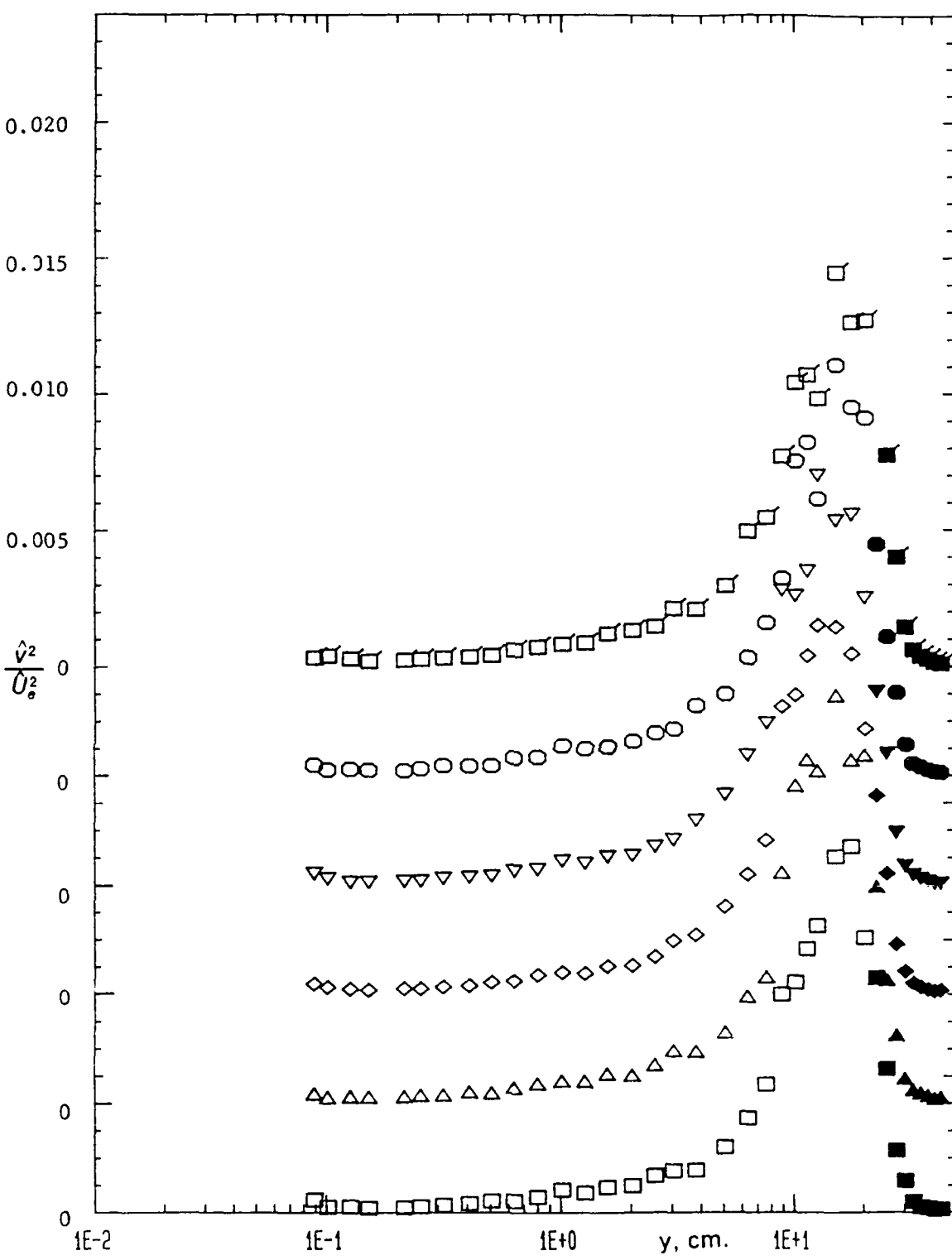


Figure 56a. Normal-to-wall turbulence intensity \hat{v}^2 / \hat{U}_e^2 profiles at $X = 3.59$ m, $k = 1.03$ flow with 'roof damper' at phases $15^\circ \leq \omega t \leq 90^\circ$; Legend same as in figure 40a.

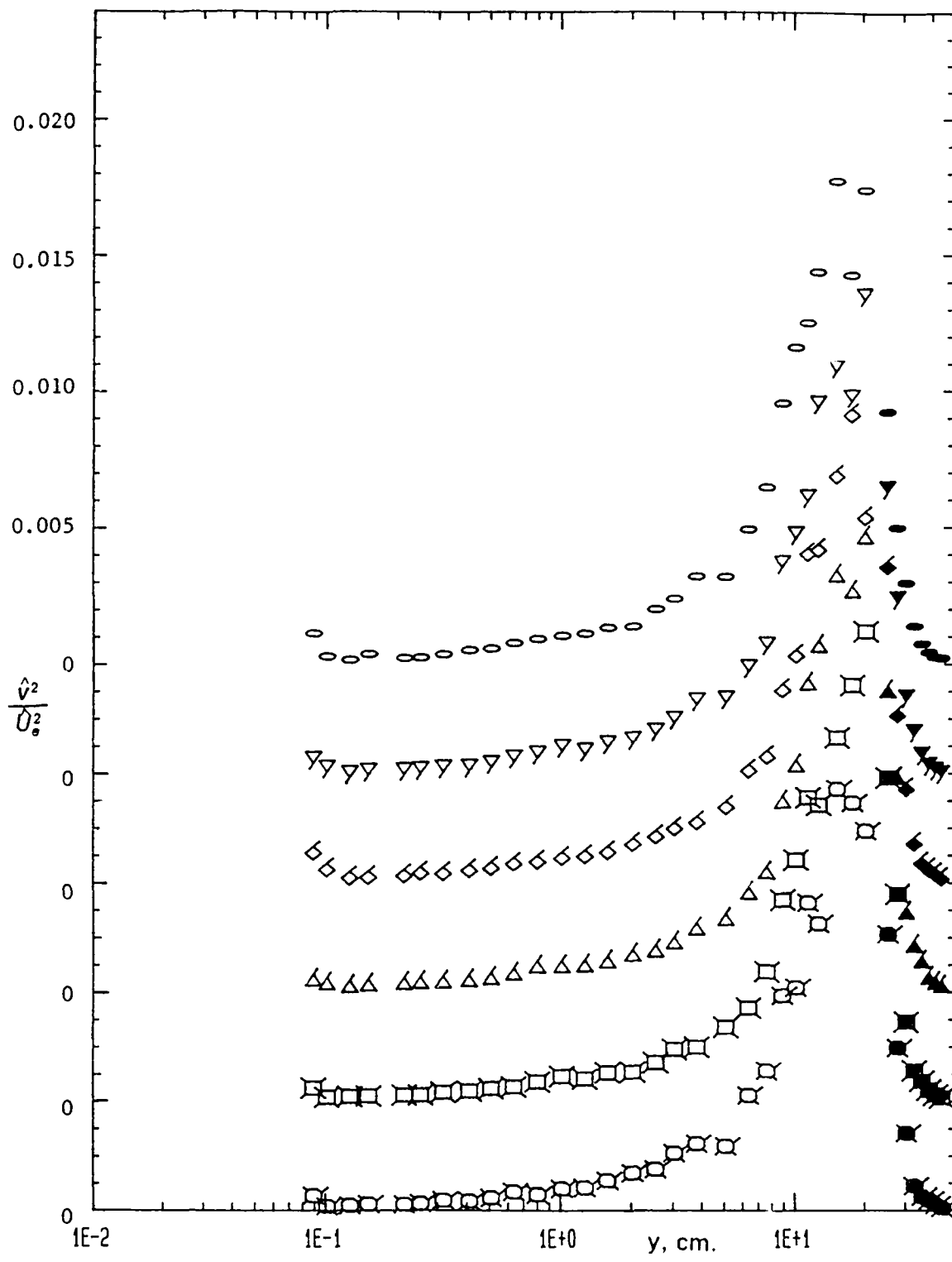


Figure 56b. Normal-to-wall turbulence intensity \hat{v}^2 / \hat{U}_e^2 profiles at $X = 3.59$ m, $k = 1.03$ flow with 'roof damper' at phases $105^\circ \leq \omega t \leq 180^\circ$; Legend same as in figure 40a.

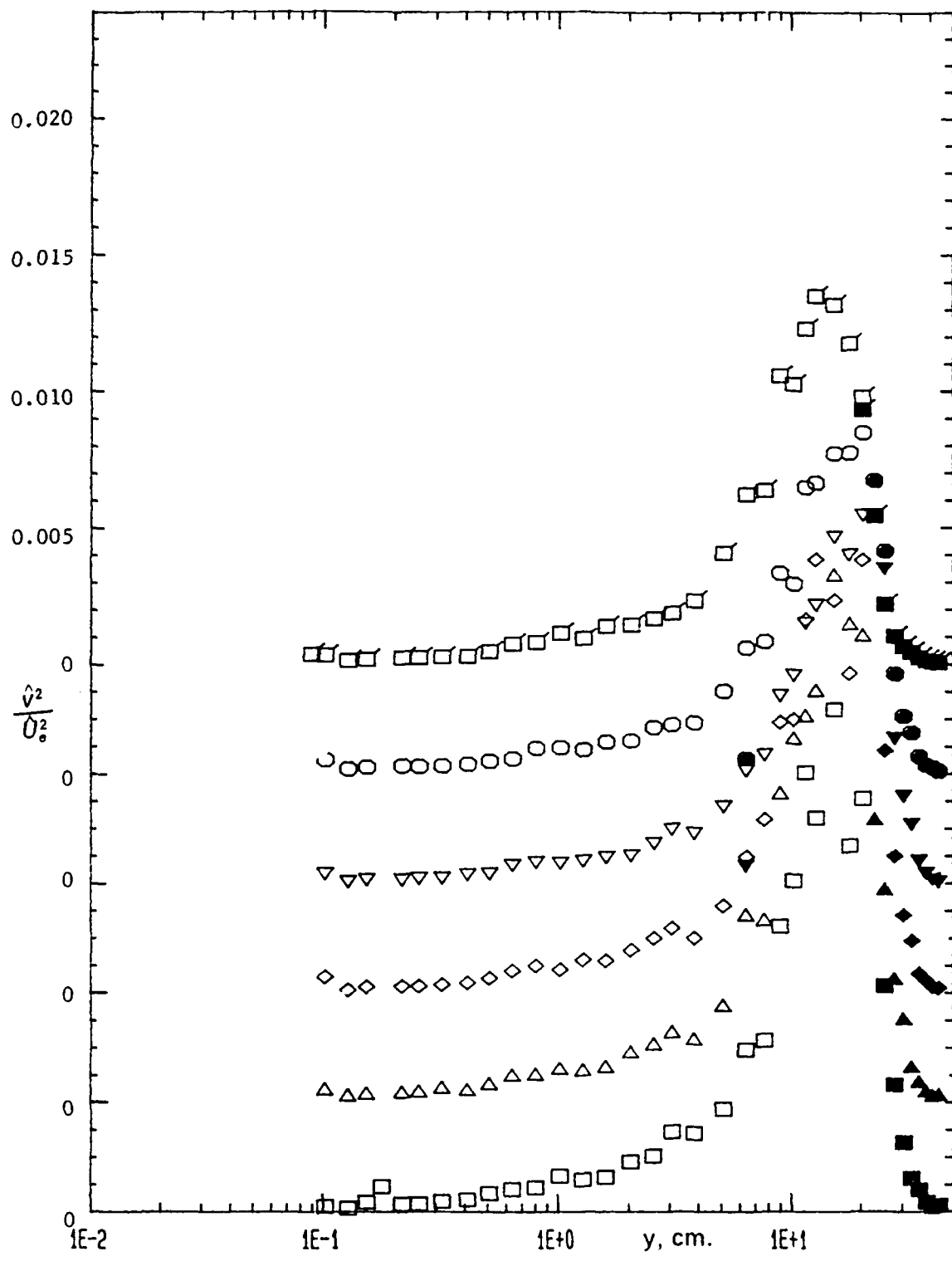


Figure 56c. Normal-to-wall turbulence intensity \hat{v}^2 / \hat{U}_e^2 profiles at $X = 3.59$
 $m, k = 1.03$ flow with 'roof damper' at phases $195^\circ \leq \omega t \leq 270^\circ$; Legend
 same as in figure 40b.

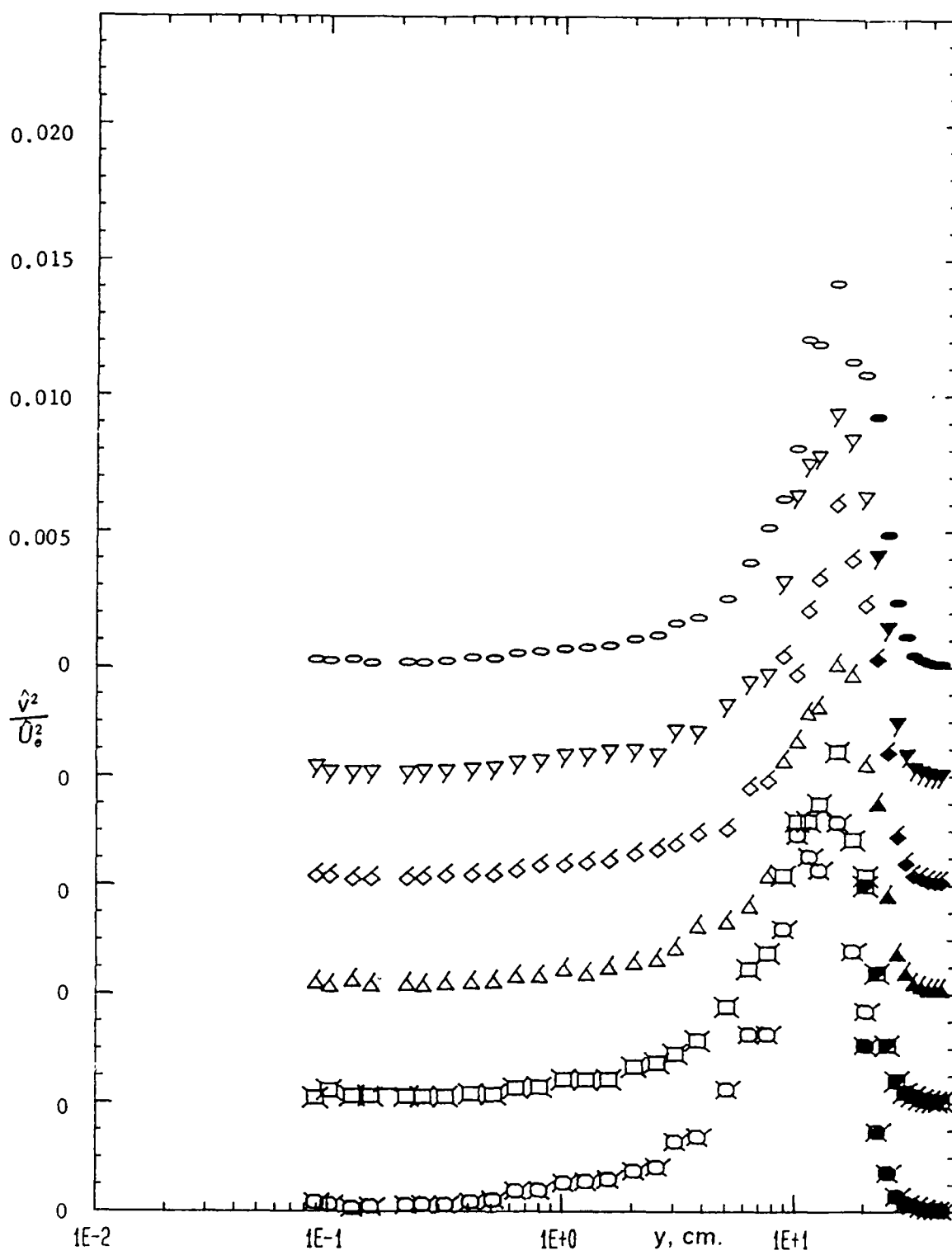


Figure 56d. Normal-to-wall turbulence intensity \hat{v}^2/\bar{U}_e^2 profiles at $X = 3.59$ m, $k = 1.03$ flow with 'roof damper' at phases $285^\circ \leq \omega t \leq 360^\circ$; Legend same as in figure 40b.

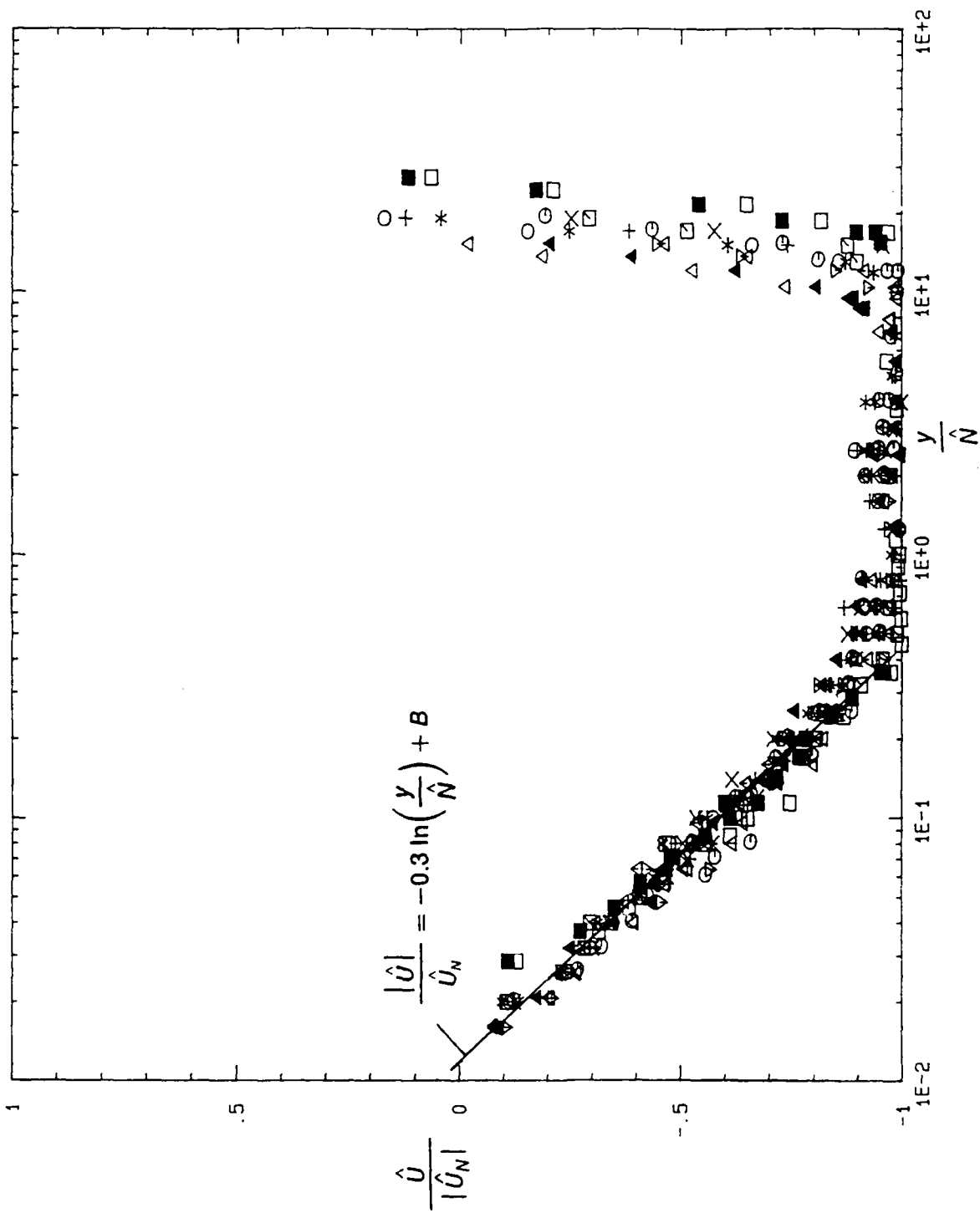


Figure 57. Normalized Backflow velocity at $X = 3.59$ m, $k = 1.03$ flow with 'roof damper'; Legend same as in figure 40a.

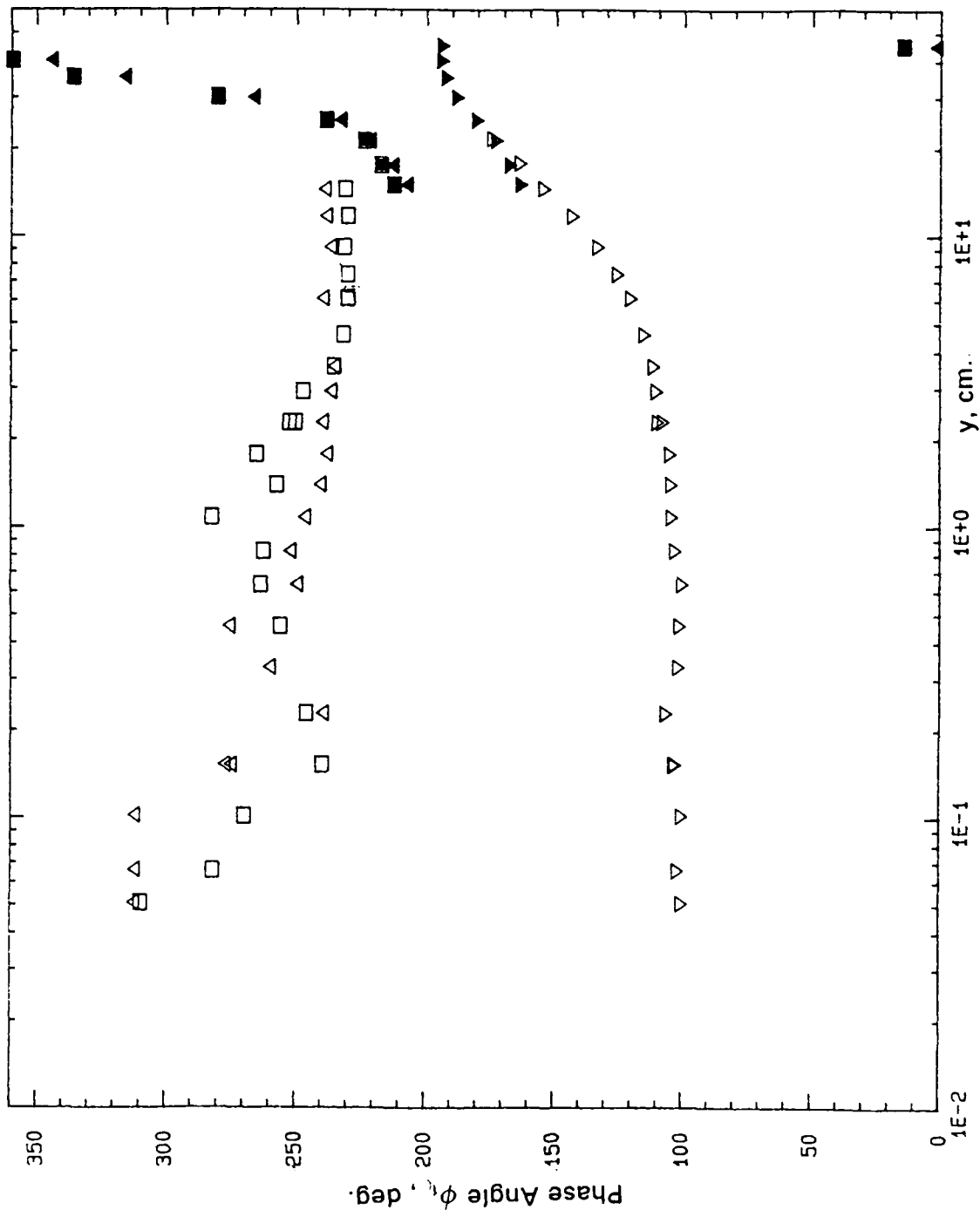


Figure 58. Variation of phase angle of first harmonics at $X = 4.27$ m,
 $k = 0.61$ flow: ($\nabla = U$; $\square = \tilde{U}^2$; $\triangle = \tilde{V}^2$); open symbols, laser
anemometer; solid symbols, cross-wire measurements.

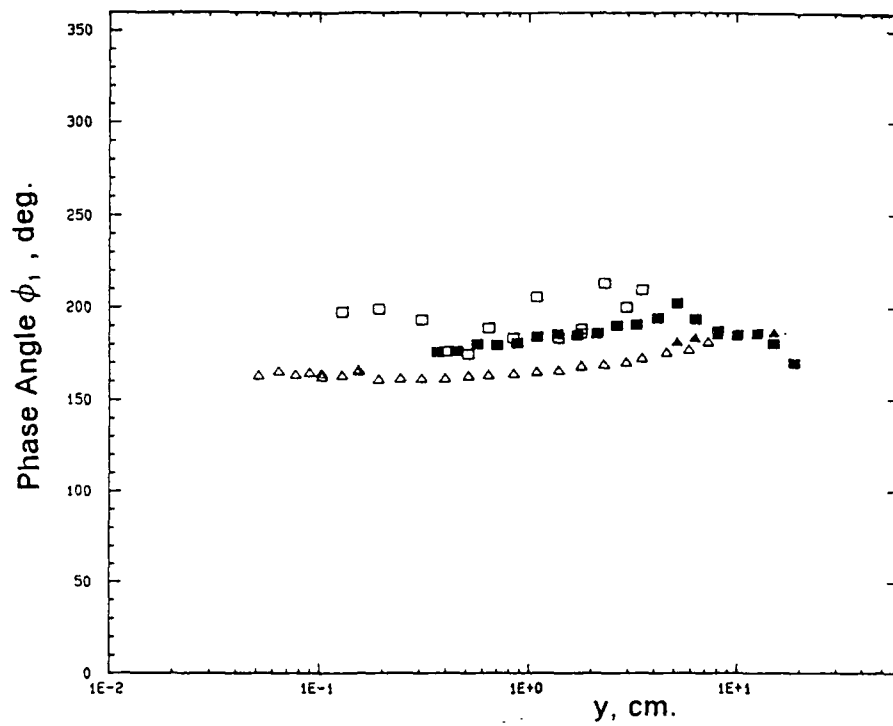


Figure 59. Variation of phase angle of first harmonics at $X=2.95$ m, $k=0.61$ flow: ($\square = U$; $\triangle = -\bar{u}v$); open symbols, laser anemometer; solid symbols, cross-wire measurements.

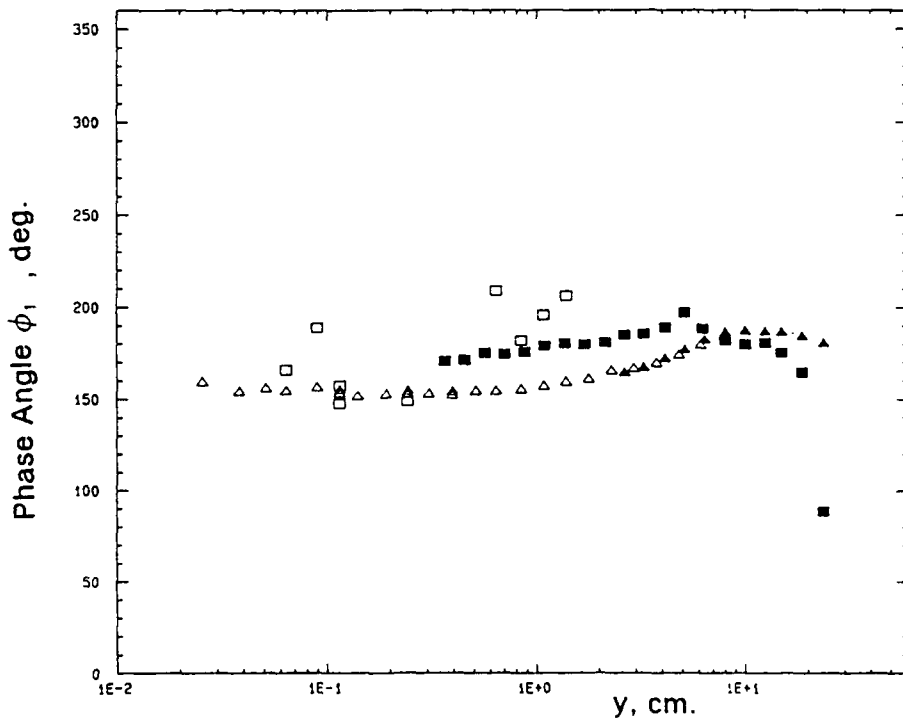


Figure 60. Variation of phase angle of first harmonics at $X=2.95$ m, $k=1.33$ flow: ($\square = U$; $\triangle = -\bar{u}v$); open symbols, laser anemometer; solid symbols, cross-wire measurements.

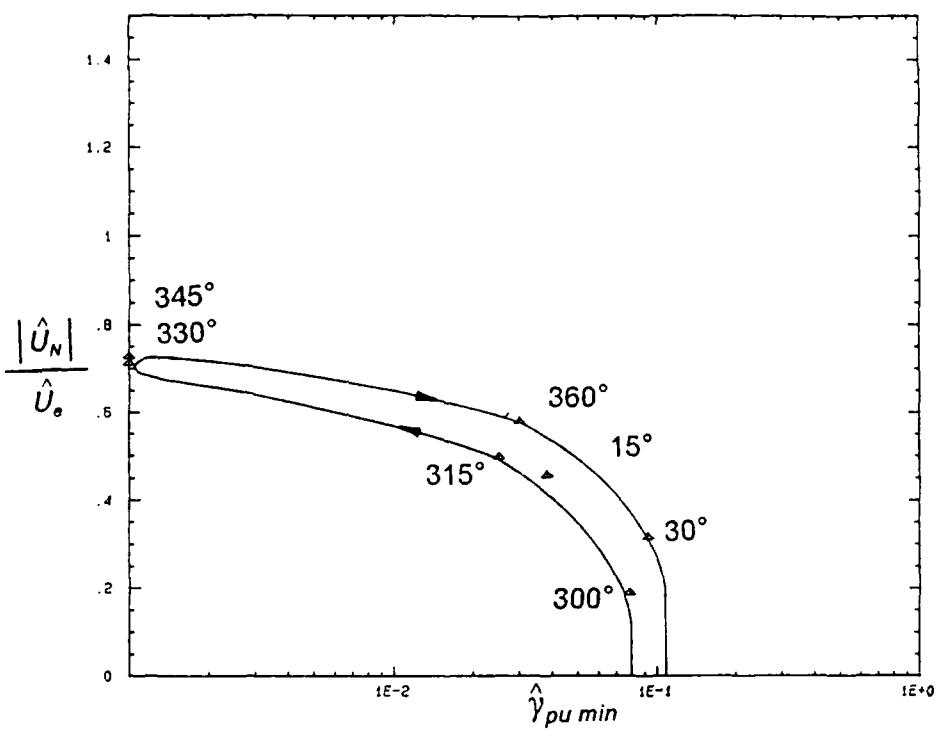


Figure 61a. $|\hat{U}_N|/\hat{U}_e$ vs. $\hat{\gamma}_{pu\ min}$ at $X = 2.95$ m, $k = 0.61$ flow.

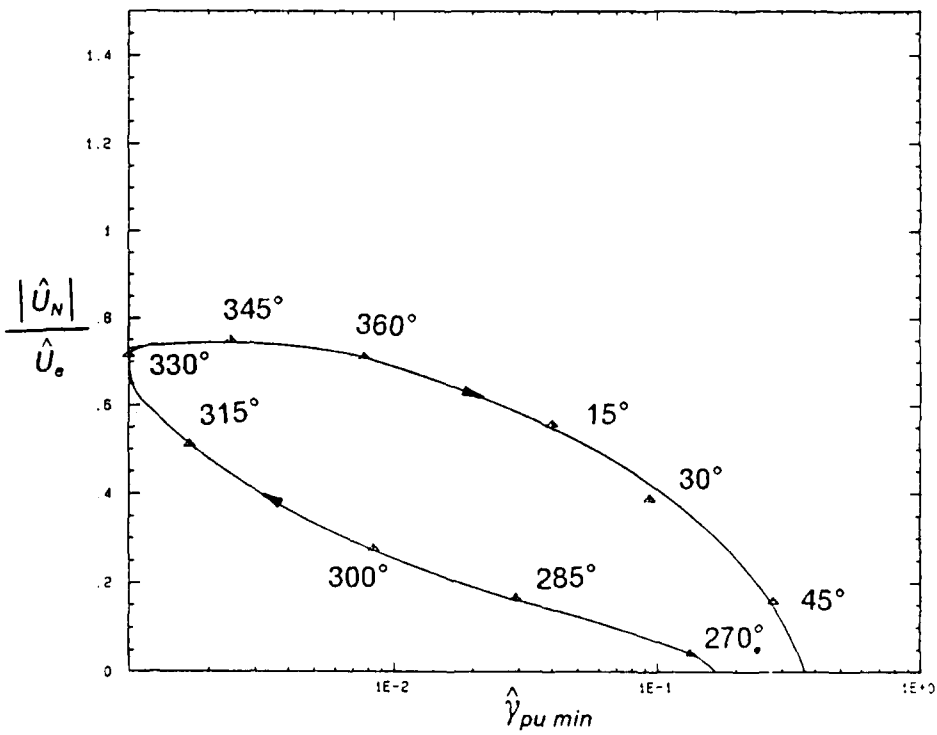


Figure 61b. $|\hat{U}_N|/\hat{U}_e$ vs. $\hat{\gamma}_{pu\ min}$ at $X = 3.51$ m, $k = 0.61$ flow.

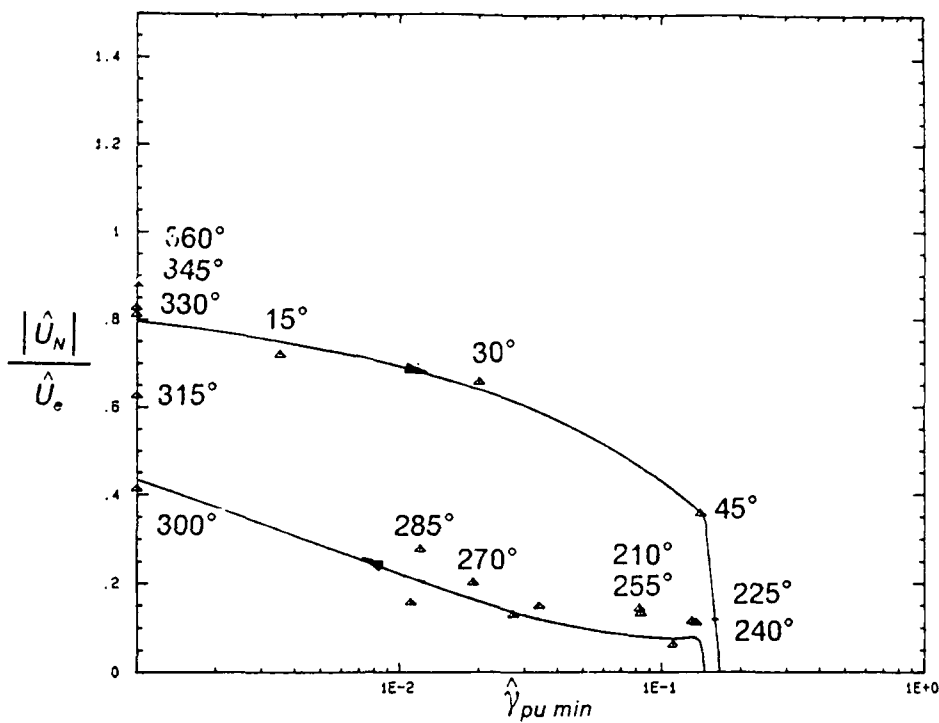


Figure 61c. $|\hat{U}_N| / \hat{U}_e$ vs. $\hat{\gamma}_{pu \text{ min}}$ at $X = 4.27$ m, $k = 0.61$ flow.

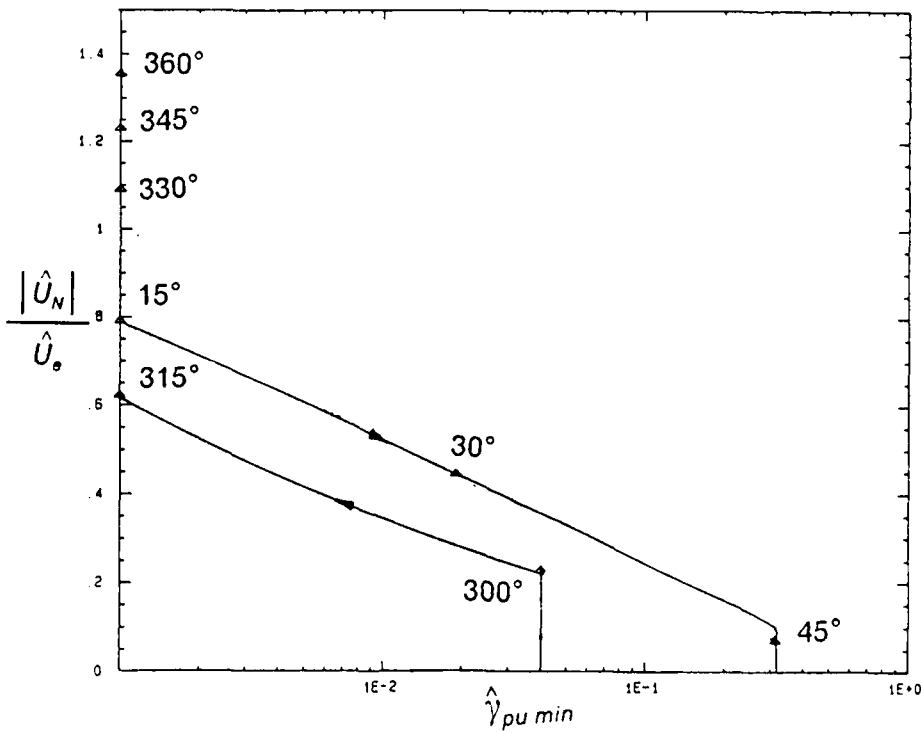


Figure 62a. $|\hat{U}_N| / \hat{U}_e$ vs. $\hat{\gamma}_{pu \text{ min}}$ at $X = 2.95$ m, $k = 1.33$ flow.

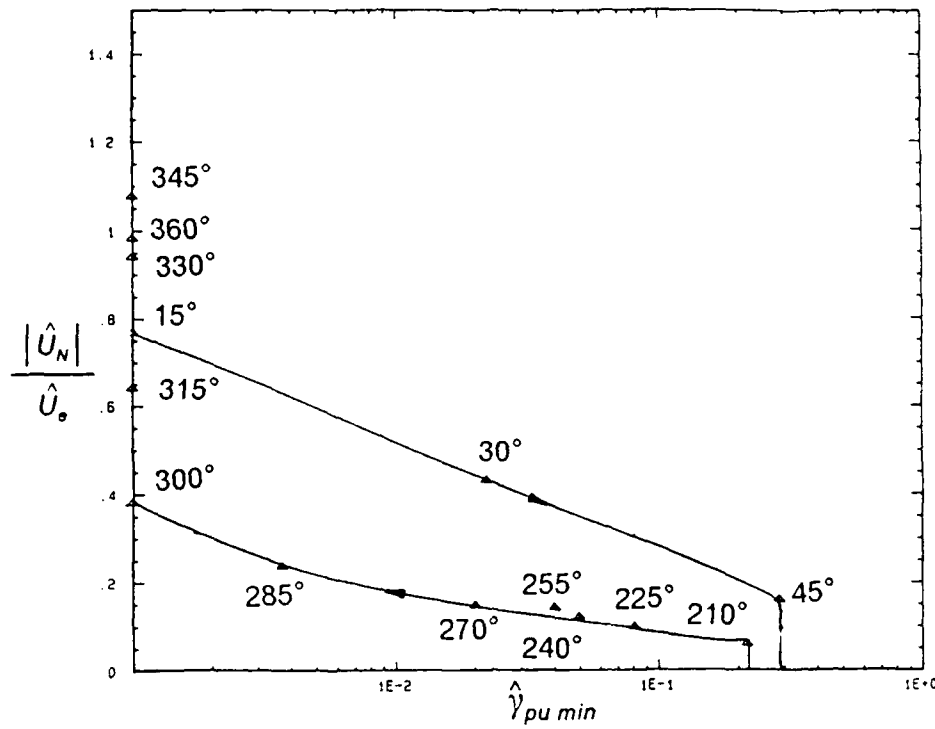


Figure 62b. $|\hat{U}_N|/\hat{U}_e$ vs. $\hat{\gamma}_{pu \min}$ at $X = 3.51$ m, $k = 1.33$ flow.

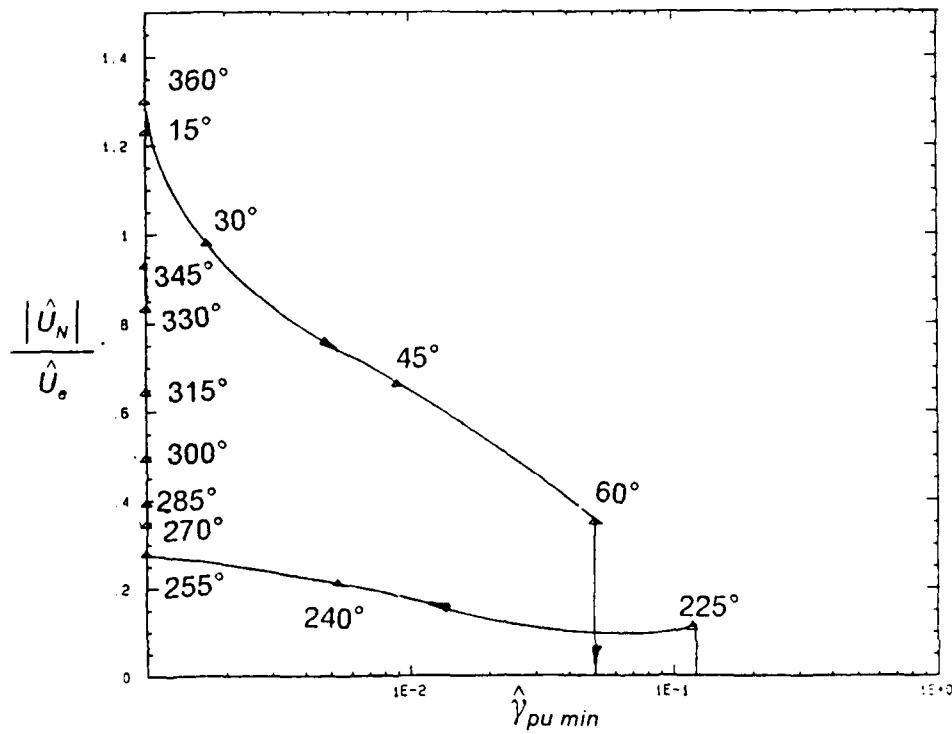


Figure 62c. $|\hat{U}_N|/\hat{U}_e$ vs. $\hat{\gamma}_{pu \min}$ at $X = 4.27$ m, $k = 1.33$ flow.

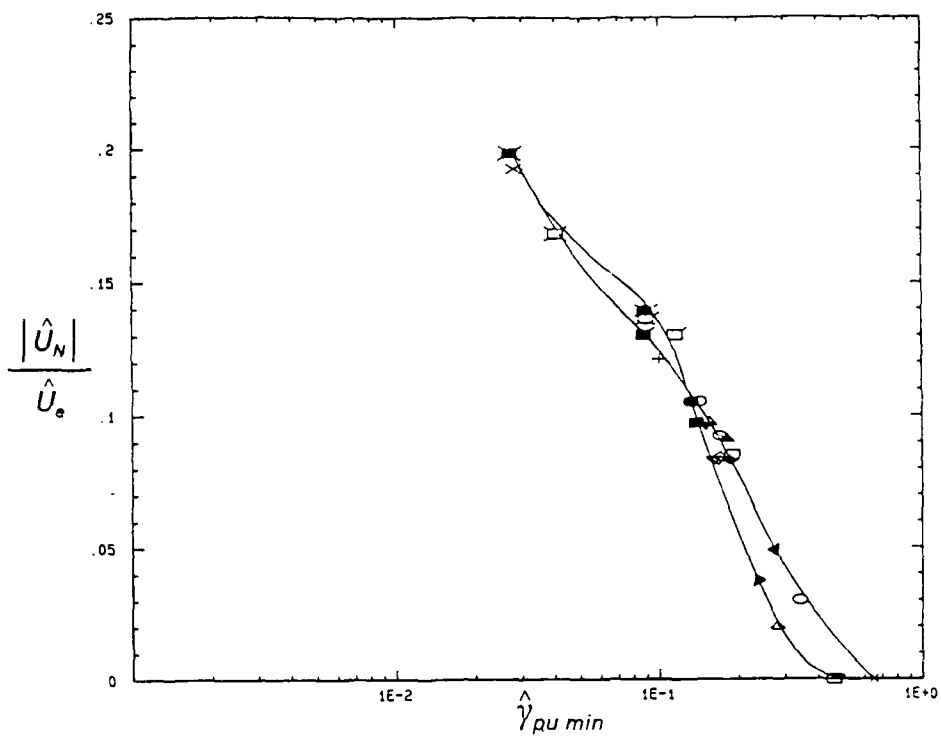


Figure 63a. $|\hat{U}_N| / \hat{U}_e$ vs. $\hat{\gamma}_{pu \min}$ at $X = 3.28$ m, $k = 1.03$ flow with 'roof damper'. ($\cdot \times = 15^\circ$; $+ = 30^\circ$; $\circ = 45^\circ$; $* = 60^\circ$; $\square = 75^\circ$; $\triangle = 90^\circ$; $\nabla = 105^\circ$; $\ominus = 120^\circ$; $\square = 135^\circ$; $\blacksquare = 150^\circ$; $\triangle = 165^\circ$; $\blacktriangle = 180^\circ$; $\diamond = 195^\circ$; $\blacklozenge = 210^\circ$; $\triangledown = 225^\circ$; $\blacktriangledown = 240^\circ$; $\circ = 255^\circ$; $\bullet = 270^\circ$; $\square = 285^\circ$; $\blacksquare = 300^\circ$; $\lozenge = 315^\circ$; $\blacksquare = 330^\circ$; $\square = 345^\circ$; $\blacksquare = 360^\circ$).

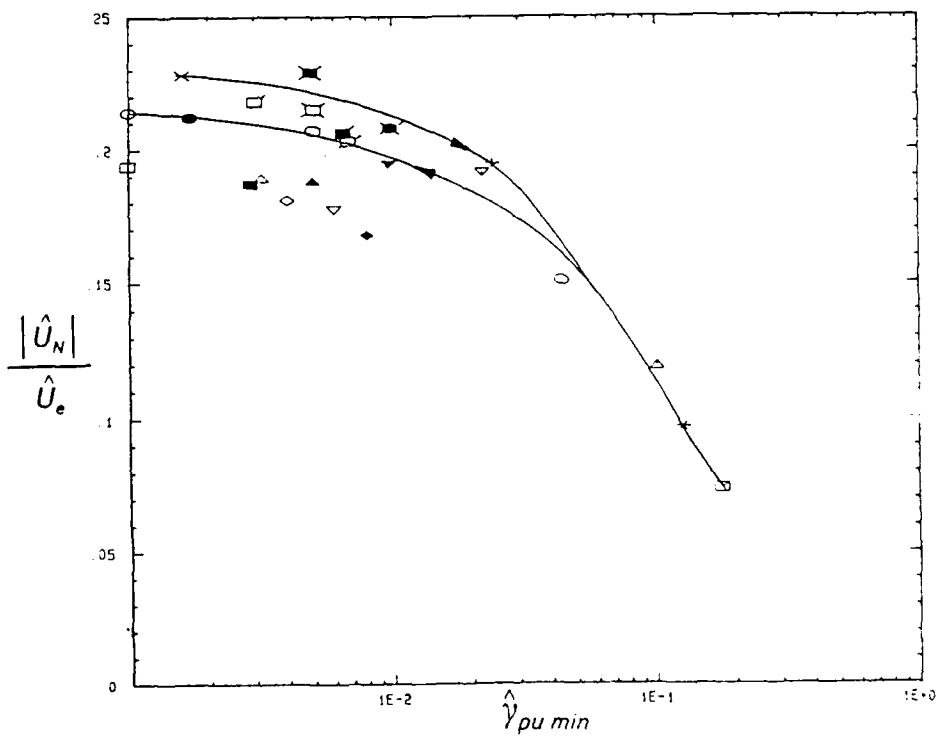


Figure 63b. $|\hat{U}_N| / \hat{U}_e$ vs. $\hat{\gamma}_{pu \min}$ at $X = 3.59$ m, $k = 1.03$ flow with 'roof damper'. Legend same as in Figure 63a.

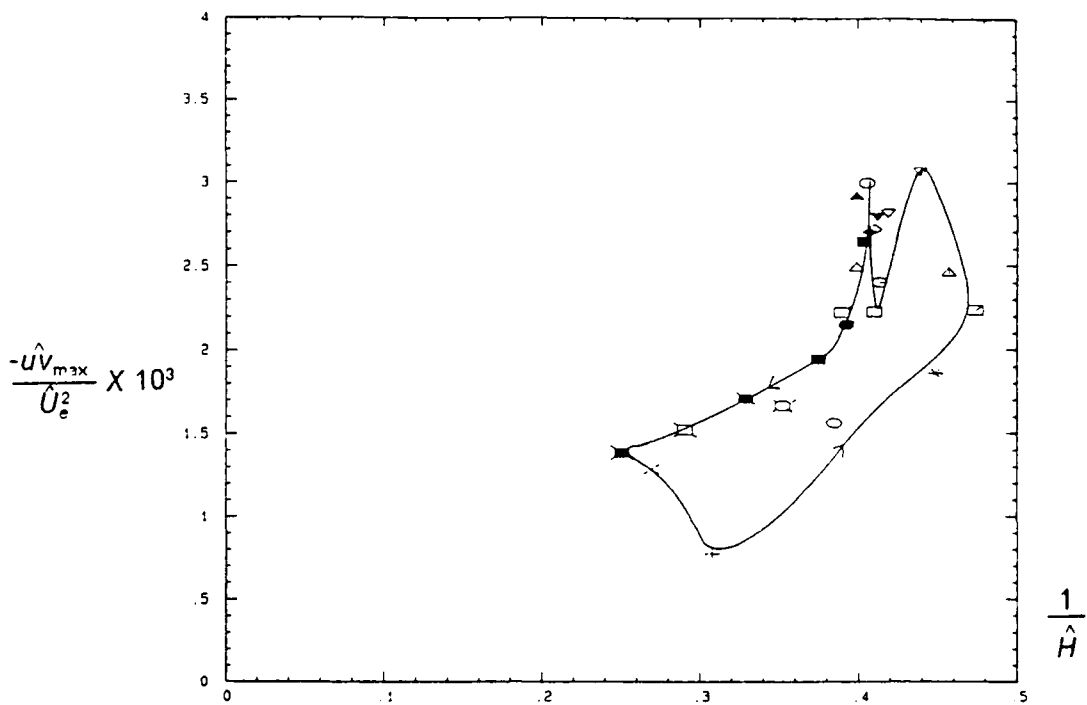


Figure 64a.— $-\hat{U}\hat{v}_{\max}/\hat{U}_e^2 \times 10^3$ vs. $1/\hat{H}$ at $X = 3.01$ m., $k = 1.03$ flow with 'roof damper'. at $X = 3.59$ m., $k = 1.03$ flow with 'roof damper'. Legend same as in Figure 63a.

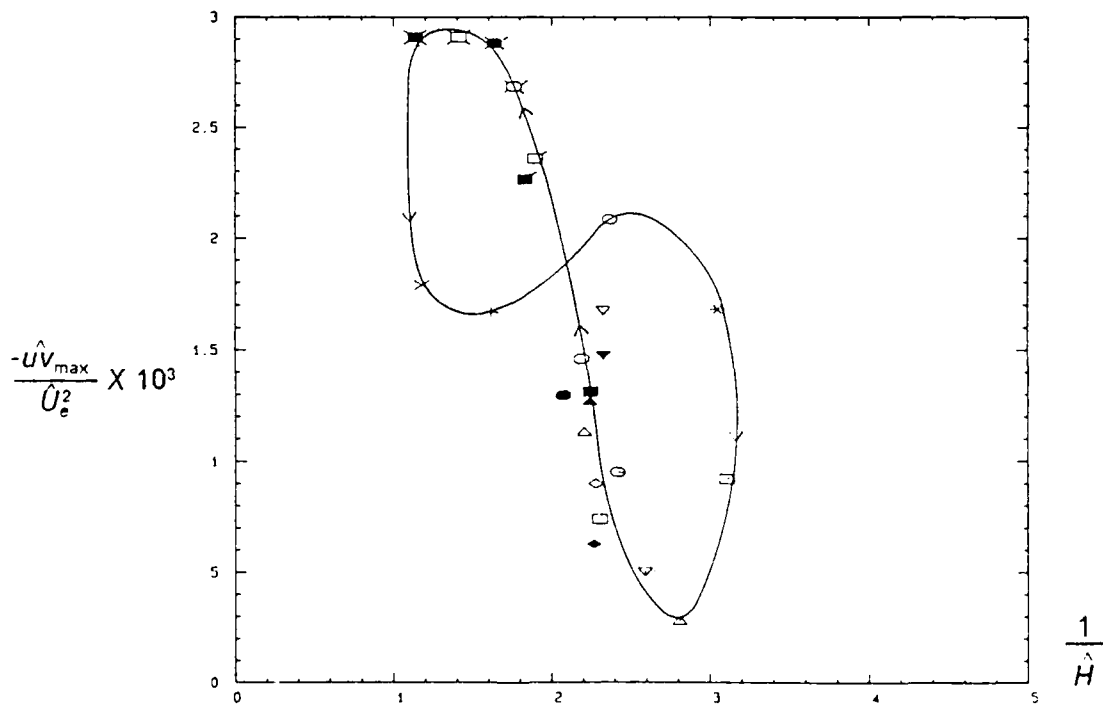


Figure 64b.— $-\hat{U}\hat{v}_{\max}/\hat{U}_e^2 \times 10^3$ vs. $1/\hat{H}$ at $X = 3.28$ m., $k = 1.03$ flow with 'roof damper'. Legend same as in figure 63a.

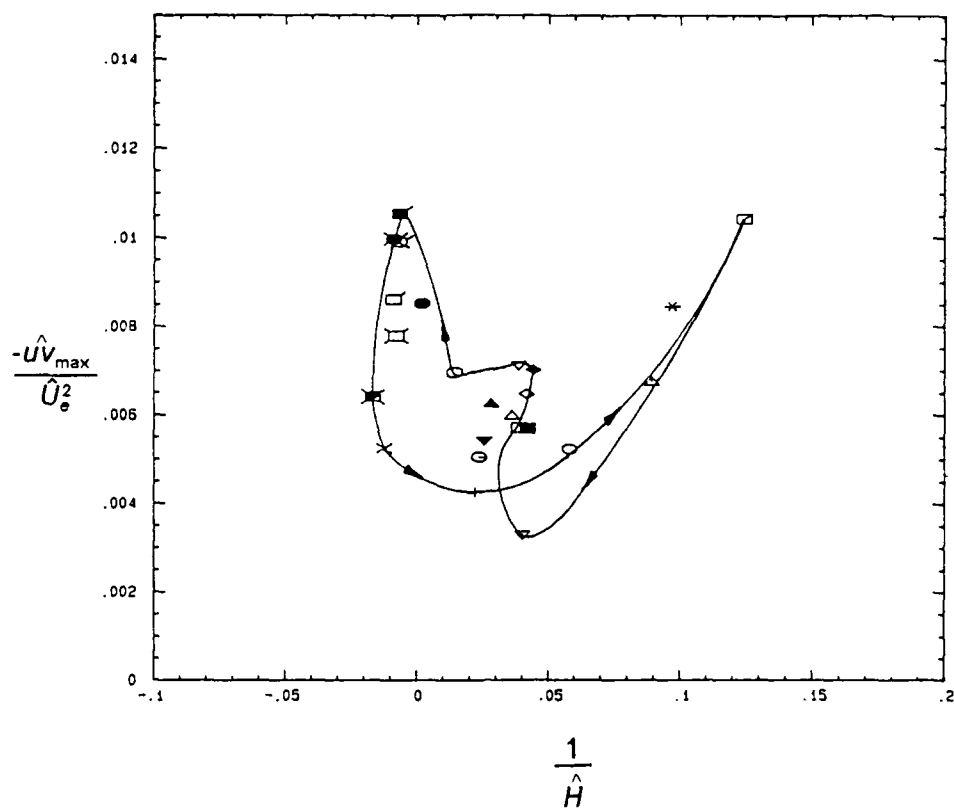


Figure 64c.— $\hat{U}\hat{V}_{\max}/\hat{U}_e^2$ vs. $1/\hat{H}$ at $X=3.59$ m., $k=1.03$ flow with 'roof damper'. Legend same as in figure 63a.

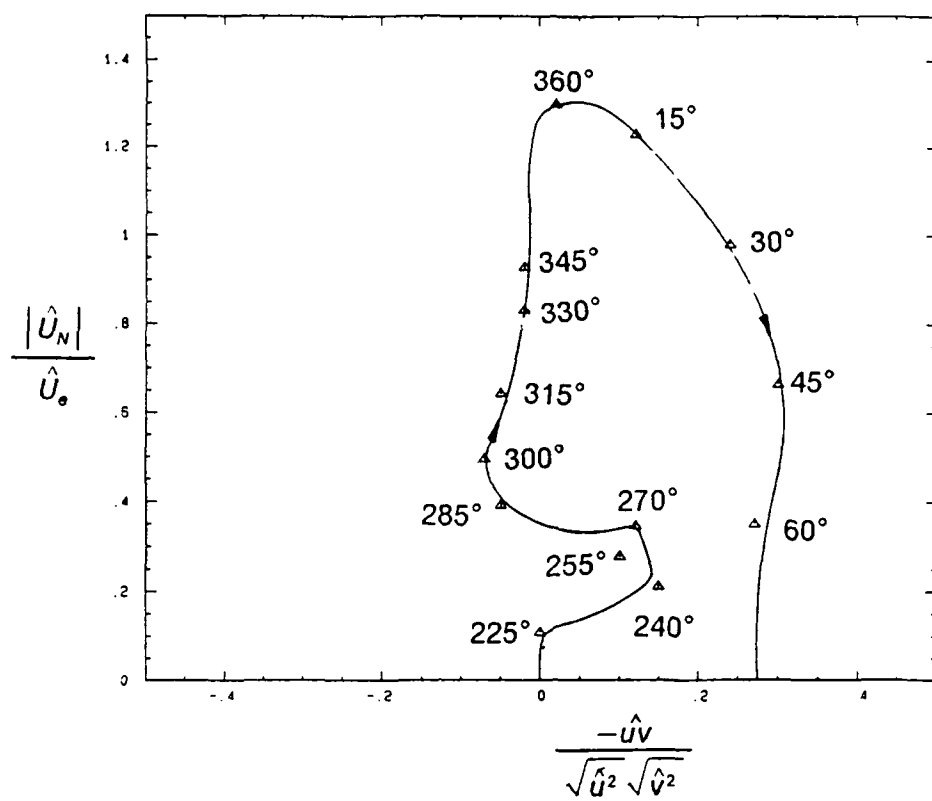


Figure 65. $|\hat{U}_N|/\hat{U}_e$ vs. $-\hat{u}\hat{v}/\sqrt{\hat{u}^2}\sqrt{\hat{v}^2}$ at $X = 4.27$ m, $k = 1.33$ flow.

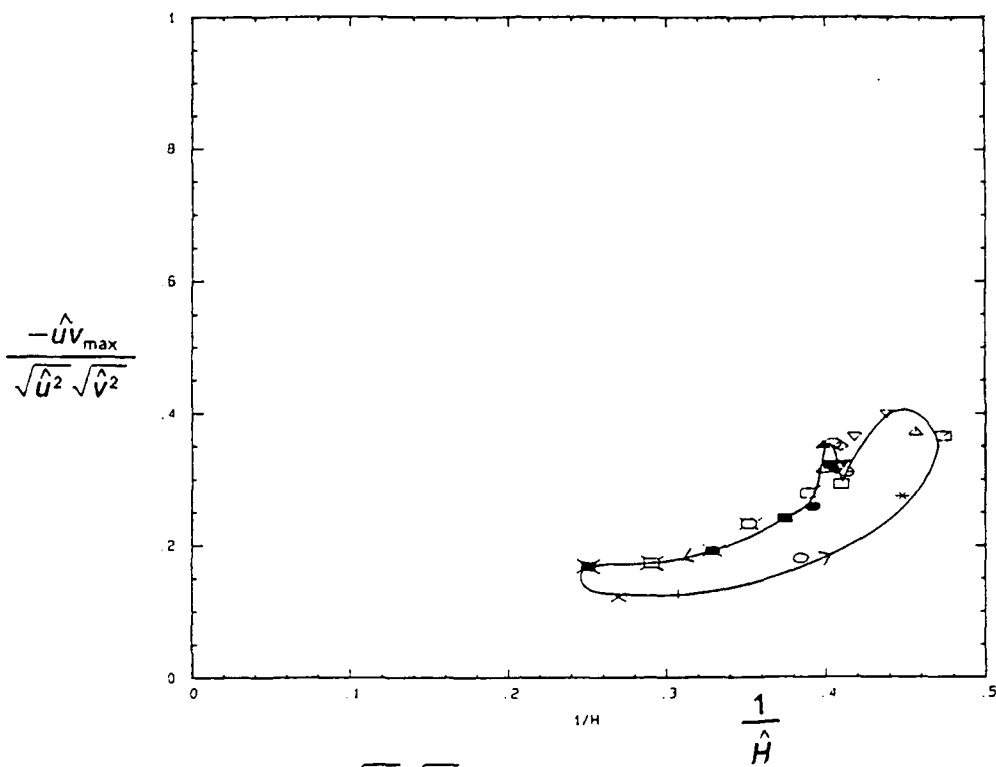


Figure 66a. $-\hat{u}\hat{v}_{\max}/\sqrt{\hat{u}^2}\sqrt{\hat{v}^2}$ vs. $1/\hat{H}$ at $X=3.01$ m., $k=1.03$ flow with 'roof damper'. Legend same as in figure 63a.

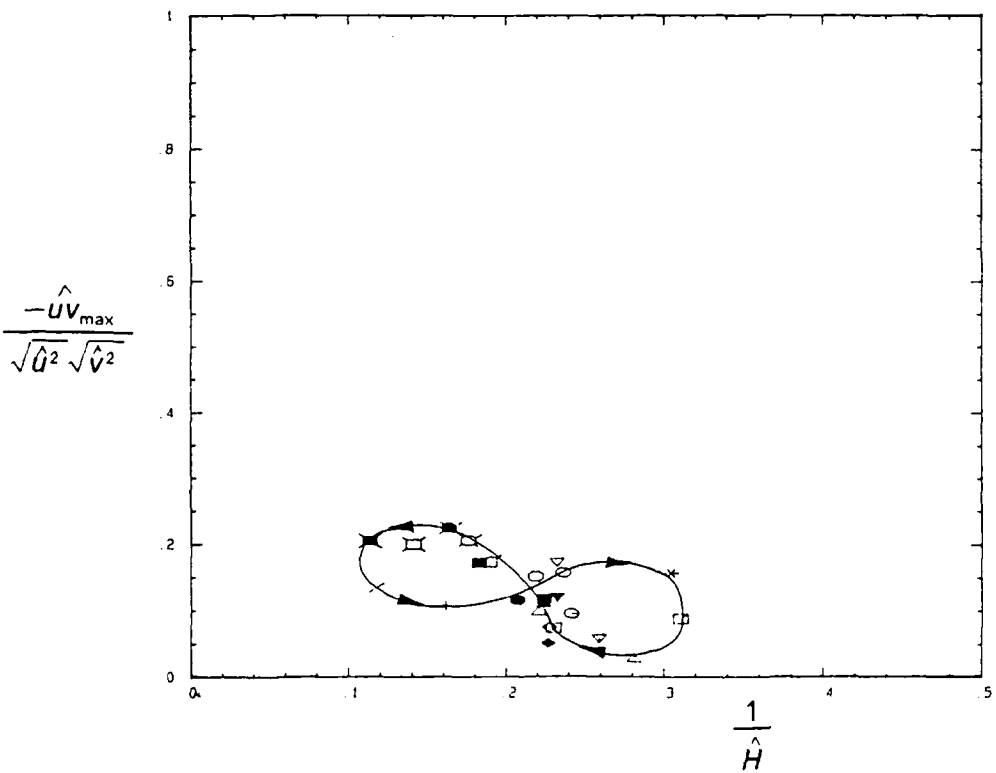


Figure 66b. $-\hat{u}\hat{v}_{\max}/\sqrt{\hat{u}^2}\sqrt{\hat{v}^2}$ vs. $1/\hat{H}$ at $X=3.28$ m., $k=1.03$ flow with 'roof damper'. Legend same as in figure 63a.

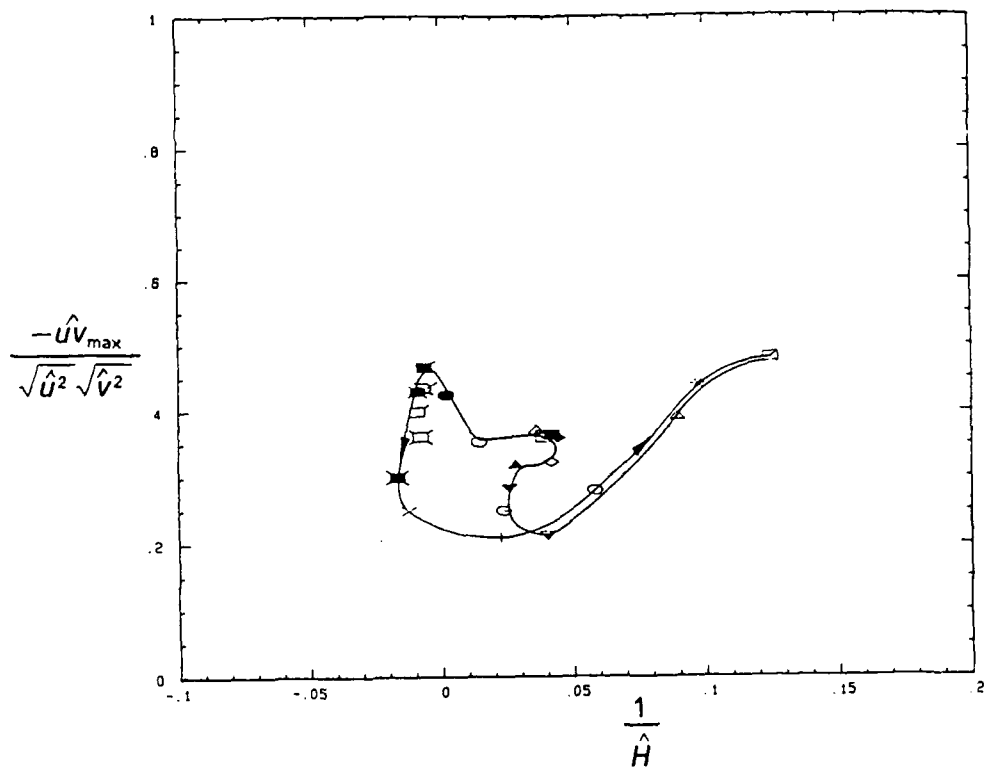


Figure 66c. $\frac{-\hat{u}\hat{v}_{\max}}{\sqrt{\hat{u}^2}\sqrt{\hat{v}^2}}$ vs. $\frac{1}{\hat{H}}$ at $X = 3.59$ m., $k = 1.03$ flow with 'roof damper'. Legend same as in figure 63a.

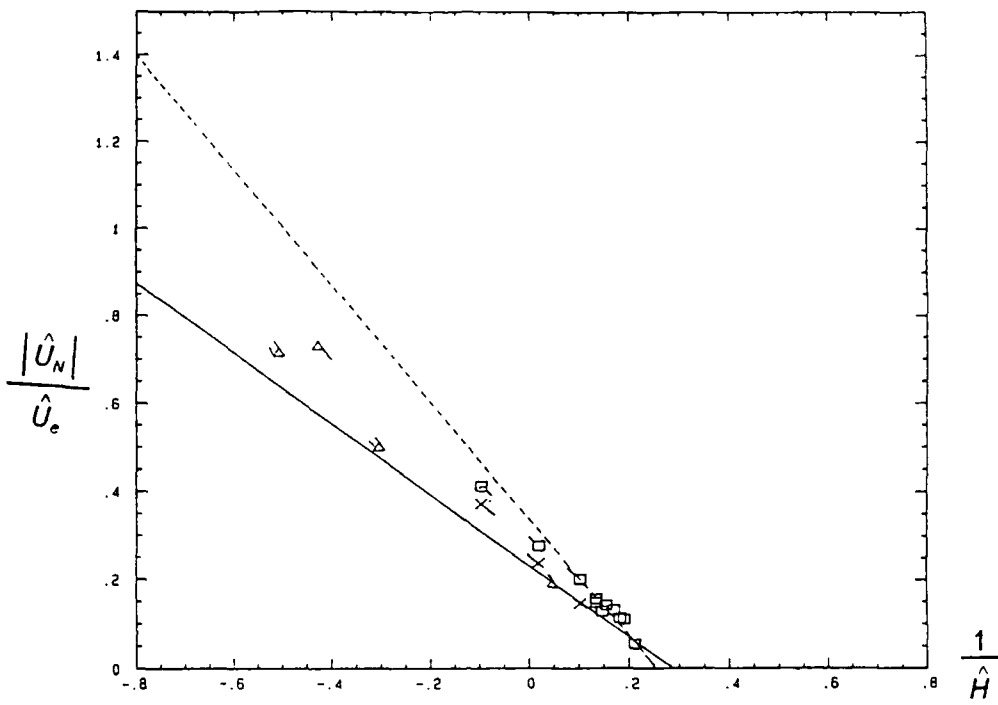


Figure 67a. $|\hat{U}_N|/\hat{U}_e$ vs. $1/\hat{H}$ for $k=0.61$ flow. solid line given by equation (11); Dashed Line given by Equation (12); Leader on symbol points in the local direction of hysteresis Loop for a given streamwise location; ($\square = 2.95m$; $\times = 3.51m$; $\Delta = 4.27m$).

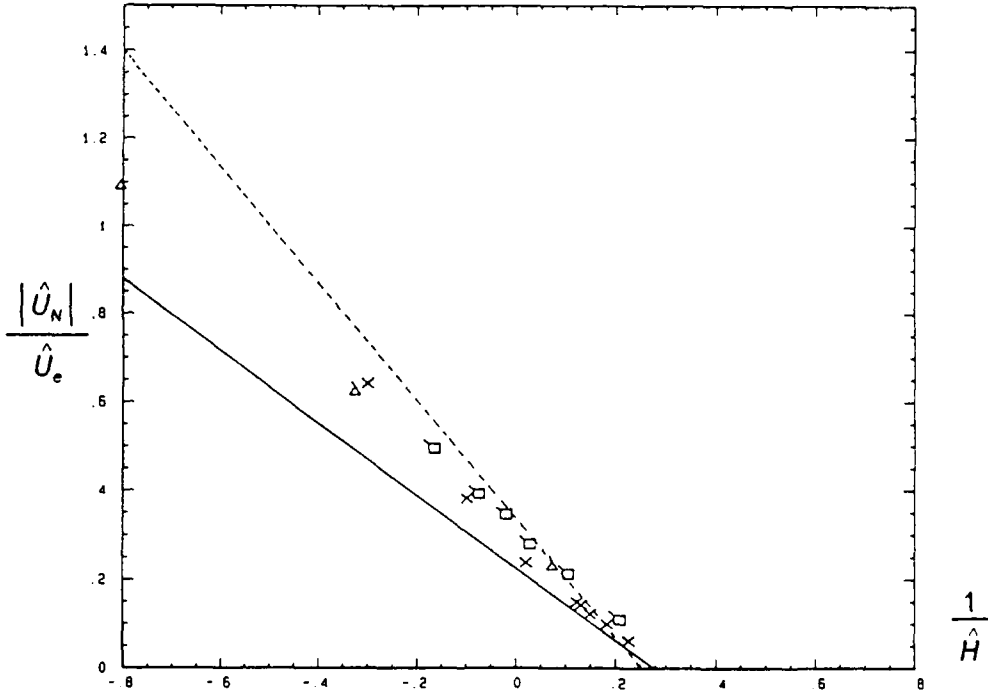


Figure 67b. $|\hat{U}_N|/\hat{U}_e$ vs. $1/\hat{H}$ for $k=1.33$ flow. solid line given by equation (11); Dashed line given by equation (12); Leader on symbol points in the local direction of hysteresis Loop for a given streamwise location. Legend same as in figure 67a.

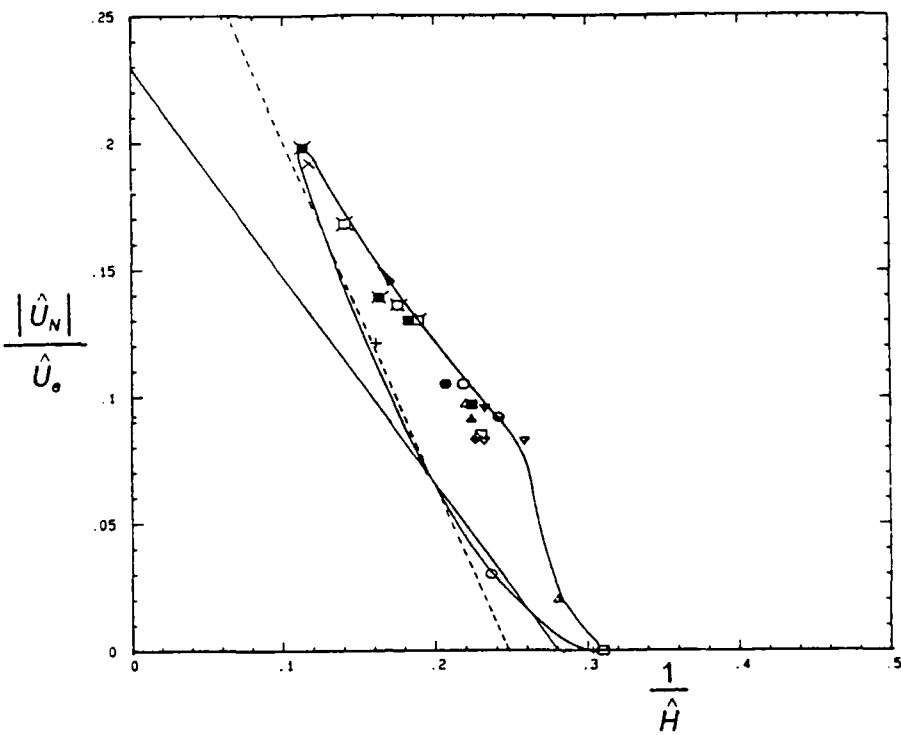


Figure 67c. $|\hat{U}_N|/\hat{U}_e$ vs. $1/\hat{H}$ at $X = 3.28$ m, $k = 1.03$ flow with 'roof damper'. solid line given by equation (11); Dashed line given by equation (12); Leader on symbol points in the local direction of hysteresis Loop for a given streamwise location; Legend same as in figure 63a.

APPENDIX A**Table 1 ($k = 0.61$ flow)**(1a) $X = 0.53$ m

ωt (deg)	\hat{U}_e (m/s)	$\hat{\delta}$ (cm)	$\hat{\theta}$ (cm)	$Re_{\hat{\theta}}$	\hat{H}	$\hat{C}_f \times 10^3$
15	4.84	0.361	0.236	722.7	1.530	5.356
30	5.06	0.312	0.209	668.9	1.494	5.203
45	6.62	0.262	0.182	764.5	1.438	5.083
60	9.65	0.204	0.144	876.9	1.417	5.085
75	13.24	0.198	0.153	1280.3	1.297	4.656
90	16.83	0.195	0.147	1567.9	1.325	4.424
105	20.50	0.199	0.155	2009.0	1.286	4.247
120	23.70	0.221	0.174	2617.0	1.269	3.863
135	25.60	0.237	0.190	3082.8	1.246	3.711
150	26.33	0.224	0.176	2926.3	1.274	3.619
165	26.75	0.238	0.186	3146.4	1.281	3.609
180	26.70	0.220	0.172	2913.2	1.279	3.624
195	26.60	0.228	0.177	2978.1	1.290	3.657
210	26.50	0.232	0.181	3034.7	1.280	3.675
225	26.24	0.225	0.175	2906.0	1.284	3.746
240	25.52	0.200	0.151	2443.3	1.322	3.798
255	23.60	0.205	0.158	2358.6	1.301	3.828
270	20.75	0.219	0.166	2185.7	1.315	3.918
285	17.50	0.237	0.178	1976.8	1.331	3.995
300	14.03	0.260	0.194	1726.9	1.336	4.121
315	9.74	0.325	0.229	1409.1	1.421	4.160
330	6.24	0.454	0.300	1184.2	1.513	4.225
345	4.62	0.539	0.346	1010.7	1.559	4.488
360	4.50	0.465	0.305	868.7	1.525	4.650

(1b) $X = 1.45$ m

ωt (deg)	\hat{U}_e (m/s)	$\hat{\delta}$ (cm)	$\hat{\theta}$ (cm)	$Re_{\hat{\theta}}$	\hat{H}	$\hat{C}_f \times 10^3$
15	6.10	0.519	0.391	1508.4	1.329	4.371
30	6.38	0.475	0.357	1441.4	1.331	4.326
45	8.18	0.351	0.270	1399.6	1.300	4.428
60	12.10	0.305	0.243	1859.3	1.255	4.271
75	16.90	0.300	0.240	2569.4	1.250	3.783
90	21.50	0.316	0.255	3465.4	1.242	3.544
105	26.15	0.334	0.270	4469.7	1.238	3.318
120	30.17	0.320	0.258	4920.6	1.240	3.243
135	32.53	0.333	0.268	5512.4	1.244	3.160
150	33.53	0.323	0.260	5519.9	1.241	3.167
165	33.96	0.308	0.248	5327.5	1.242	3.224
180	34.00	0.313	0.251	5400.0	1.246	3.174
195	33.85	0.303	0.243	5206.9	1.247	3.180
210	33.70	0.292	0.235	5007.5	1.246	3.152
225	33.40	0.293	0.235	4969.3	1.248	3.250
240	32.60	0.292	0.233	4818.2	1.251	3.252
255	30.15	0.283	0.226	4307.8	1.253	3.341
270	26.60	0.313	0.251	4223.1	1.249	3.417
285	22.60	0.343	0.273	3900.2	1.257	3.490
300	18.25	0.391	0.306	3537.0	1.278	3.478
315	13.00	0.458	0.348	2864.4	1.316	3.460
330	8.65	0.528	0.391	2139.5	1.352	3.776
345	6.51	0.566	0.415	1710.4	1.364	3.868
360	6.00	0.509	0.379	1440.8	1.343	4.261

(1c) $X = 1.83$ m

ωt (deg)	\hat{U}_e (m/s)	$\hat{\delta}$ (cm)	$\hat{\theta}$ (cm)	$Re_{\hat{\theta}}$	\hat{H}	$\hat{C}_f \times 10^3$
15	6.75	0.977	0.684	2924.4	1.428	2.925
30	6.81	1.093	0.742	3198.5	1.473	2.558
45	8.45	0.851	0.600	3210.1	1.418	2.900
60	11.95	0.669	0.477	3608.7	1.402	3.782
75	16.85	0.502	0.384	4093.1	1.308	3.281
90	21.58	0.456	0.364	4973.8	1.253	3.226
105	26.13	0.412	0.327	5405.4	1.260	3.096
120	30.20	0.415	0.316	6032.0	1.316	2.814
135	32.50	0.395	0.308	6336.6	1.283	2.908
150	33.50	0.385	0.298	6322.5	1.290	2.879
165	33.85	0.392	0.304	6522.8	1.287	2.860
180	33.90	0.391	0.304	6531.0	1.285	2.828
195	33.85	0.402	0.313	6714.4	1.284	2.790
210	33.70	0.381	0.295	6286.5	1.294	2.875
225	33.50	0.401	0.314	6664.9	1.276	2.875
240	32.70	0.413	0.323	6682.2	1.280	2.883
255	30.20	0.408	0.313	5987.0	1.304	2.905
270	26.65	0.450	0.342	5769.8	1.316	2.920
285	22.70	0.531	0.396	5689.6	1.340	2.744
300	18.78	0.659	0.461	5478.6	1.430	2.253
315	13.64	0.876	0.567	4899.5	1.544	1.792
330	9.42	1.083	0.647	3858.9	1.673	1.739
345	7.39	1.149	0.699	3270.1	1.644	2.013
360	6.86	1.080	0.687	2985.7	1.571	2.297

(1d) $X = 2.20 \text{ m}$

ωt (deg)	\hat{U}_e (m/s)	$\hat{\delta}$ (cm)	$\hat{\theta}$ (cm)	$Re_{\hat{\theta}}$	\hat{H}	$\hat{C}_f \times 10^3$
15	6.05	0.631	0.435	1664.6	1.451	3.626
30	5.80	0.535	0.368	1350.5	1.454	3.889
45	7.20	0.507	0.364	1657.4	1.395	4.008
60	11.03	0.608	0.475	3319.3	1.278	3.417
75	15.45	0.446	0.326	3186.1	1.369	3.123
90	19.90	0.419	0.307	3872.7	1.363	2.985
105	24.45	0.450	0.333	5159.0	1.350	2.805
120	28.20	0.496	0.377	6725.3	1.316	2.729
135	30.21	0.451	0.327	6259.7	1.378	2.623
150	31.20	0.434	0.318	6278.5	1.365	2.667
165	31.60	0.461	0.336	6727.3	1.371	2.654
180	31.67	0.441	0.322	6454.0	1.371	2.605
195	31.64	0.439	0.321	6428.3	1.369	2.594
210	31.50	0.431	0.317	6322.0	1.360	2.606
225	31.28	0.443	0.323	6400.5	1.370	2.650
240	30.60	0.448	0.326	6306.7	1.376	2.615
255	28.33	0.465	0.334	5998.0	1.391	2.595
270	24.92	0.492	0.350	5528.2	1.405	2.529
285	21.11	0.515	0.362	4842.6	1.421	2.635
300	17.07	0.567	0.387	4183.4	1.465	2.525
315	12.71	0.829	0.556	4475.8	1.490	2.209
330	9.09	1.189	0.758	4359.2	1.570	2.023
345	7.16	1.426	0.904	4096.0	1.578	2.040
360	6.70	1.308	0.887	3763.5	1.474	2.580

(1e) $X = 2.95$ m

ωt (deg)	\hat{U}_e (m/s)	$\hat{\delta}$ (cm)	$\hat{\theta}$ (cm)	$Re_{\hat{\theta}}$	\hat{H}	$\hat{C}_f \times 10^3$
90	14.99	2.408	1.346	12769.5	1.789	0.909
105	19.46	2.229	1.300	16032.2	1.713	0.945
120	23.33	2.321	1.318	19472.2	1.761	0.812
135	25.74	2.436	1.364	22231.0	1.786	0.744
150	26.76	2.492	1.387	23489.2	1.797	0.746
165	27.34	2.547	1.400	24207.6	1.821	0.677
180	27.34	2.517	1.384	23953.0	1.819	0.690
195	27.28	2.544	1.400	24176.5	1.817	0.709
210	27.19	2.485	1.377	23692.8	1.805	0.707
225	26.95	2.456	1.372	23380.7	1.792	0.686
240	26.26	2.542	1.372	22822.1	1.852	0.653
255	24.24	2.724	1.443	22137.5	1.888	0.624
270	21.40	3.049	1.443	19542.8	2.114	0.426
285	18.32	4.189	1.245	14429.1	3.367	0.238
300	14.90	5.957	0.278	2618.0	21.463	
315	10.65	9.687	-2.957	-19938.5	-3.276	
330	8.20	13.989	-7.117	-36943.5	-1.966	
345	7.56	17.553	-7.536	-36067.1	-2.329	

(1f) $X = 3.51 \text{ m}$

ωt (deg)	\hat{U}_e (m/s)	$\hat{\delta}$ (cm)	$\hat{\theta}$ (cm)	$Re_{\hat{\theta}}$	\hat{H}	$\hat{C}_f \times 10^3$
105	15.16	5.990	3.321	31869.7	1.804	
120	18.60	6.160	2.825	33262.1	2.181	
135	20.76	6.878	2.816	37005.0	2.443	
150	22.00	7.274	2.758	38410.4	2.638	
165	22.62	7.619	2.675	38304.7	2.848	
180	23.10	6.961	2.592	37904.3	2.686	
195	23.11	7.147	2.603	38078.7	2.746	
210	23.00	6.946	2.565	37344.2	2.708	
225	22.85	7.246	2.545	36809.1	2.847	
240	22.30	7.583	2.533	35765.9	2.993	
255	20.82	8.192	2.511	33102.3	3.262	
270	18.95	9.288	2.174	26079.3	4.273	
285	16.88	11.552	1.752	18717.5	6.595	
300	14.49	15.911	0.992	9095.7	16.047	
315	11.30	23.011	-3.366	-24079.1	-6.836	

(1g) $X = 4.27 \text{ m}$

ωt (deg)	\hat{U}_e (m/s)	$\hat{\delta}$ (cm)	$\hat{\theta}$ (cm)	$Re_{\hat{\theta}}$	\hat{H}	$\hat{C}_f \times 10^3$
120	12.70	2.104	5.465	43939.3	0.385	
135	16.20	8.370	3.264	33471.6	2.565	
150	18.50	12.857	2.710	31739.5	4.744	
165	20.22	17.105	2.498	31980.1	6.847	
180	21.10	19.526	2.625	35060.0	7.439	
195	21.60	19.778	2.651	36248.6	7.461	
210	21.90	19.484	3.307	45855.3	5.891	
225	21.80	19.542	3.707	51162.7	5.271	
240	21.25	19.877	3.607	48524.1	5.511	
255	20.00	20.640	3.185	40327.3	6.480	
270	18.40	22.788	2.320	27020.1	9.824	
285	16.66	26.330	0.479	5056.6	54.919	
300	14.82	31.818	-3.088	-28971.9	-10.304	

Table 2 (k = 1.33 flow)

(2a) X = 0.53 m

ωt (deg)	\hat{U}_e (m/s)	$\hat{\delta}$ (cm)	$\hat{\theta}$ (cm)	$Re_{\hat{\theta}}$	\hat{H}	$\hat{C}_f \times 10^3$
15	3.34	0.932	0.551	1164.6	1.692	3.970
30	4.92	0.636	0.453	1411.3	1.403	3.902
45	7.08	0.399	0.283	1270.4	1.406	4.102
60	9.80	0.210	0.163	1013.2	1.287	4.774
75	12.55	0.212	0.173	1371.5	1.227	4.761
90	15.10	0.214	0.174	1666.2	1.228	4.414
105	17.10	0.234	0.189	2043.0	1.239	4.120
120	18.60	0.221	0.179	2113.6	1.234	4.196
135	19.60	0.234	0.191	2364.2	1.227	4.158
150	20.12	0.236	0.193	2456.0	1.225	4.095
165	20.25	0.231	0.188	2411.7	1.228	4.083
180	20.21	0.246	0.201	2572.5	1.224	4.071
195	20.00	0.257	0.209	2649.9	1.230	4.037
210	19.70	0.238	0.193	2403.2	1.233	4.105
225	19.50	0.256	0.207	2557.8	1.234	4.030
240	19.10	0.251	0.203	2457.5	1.234	4.015
255	18.40	0.245	0.197	2300.2	1.243	3.984
270	17.40	0.238	0.190	2093.9	1.252	4.041
285	15.50	0.261	0.204	2005.3	1.276	4.038
300	12.45	0.312	0.238	1873.4	1.311	3.964
315	8.96	0.373	0.271	1536.7	1.377	3.924
330	8.95	0.372	0.271	1534.3	1.375	3.933
345	3.60	0.609	0.378	862.6	1.609	4.445
360	2.76	0.917	0.498	870.0	1.841	4.060

(2b) $X = 1.45 \text{ m}$

ωt (deg)	\hat{U}_e (m/s)	$\hat{\delta}$ (cm)	$\hat{\theta}$ (cm)	$Re_{\hat{\theta}}$	\hat{H}	$\hat{C}_f \times 10^3$
15	4.90	0.585	0.381	1183.0	1.534	4.007
30	5.84	0.430	0.303	1121.4	1.419	4.260
45	7.66	0.316	0.222	1074.4	1.426	5.211
60	11.05	0.283	0.198	1382.2	1.431	4.690
75	15.00	0.239	0.170	1615.9	1.407	4.134
90	18.26	0.223	0.163	1887.8	1.365	3.854
105	20.75	0.240	0.180	2365.1	1.336	3.691
120	22.48	0.242	0.180	2566.8	1.342	3.599
135	23.54	0.272	0.204	3040.1	1.334	3.479
150	24.06	0.253	0.187	2852.1	1.351	3.525
165	24.20	0.259	0.191	2932.8	1.353	3.464
180	24.06	0.266	0.197	3002.6	1.348	3.451
195	23.82	0.275	0.204	3077.7	1.345	3.412
210	23.55	0.275	0.205	3052.9	1.344	3.420
225	23.20	0.274	0.204	2994.4	1.346	3.470
240	22.74	0.271	0.201	2898.6	1.347	3.466
255	22.00	0.269	0.198	2756.4	1.361	3.480
270	20.95	0.270	0.200	2646.7	1.353	3.529
285	18.89	0.285	0.210	2514.0	1.358	3.498
300	15.42	0.314	0.229	2240.0	1.367	3.645
315	11.50	0.358	0.260	1893.8	1.377	3.807
330	8.25	0.407	0.295	1542.6	1.379	3.756
345	5.85	0.544	0.384	1423.6	1.415	4.003
360	4.80	0.593	0.404	1226.3	1.469	4.401

(2c) $X = 1.83$ m

ωt (deg)	\hat{U}_e (m/s)	$\hat{\delta}$ (cm)	$\hat{\theta}$ (cm)	$Re_{\hat{\theta}}$	\hat{H}	$\hat{C}_f \times 10^3$
15	5.65	0.870	0.555	1986.9	1.565	2.993
30	6.73	0.626	0.448	1906.7	1.399	3.245
45	8.07	0.371	0.286	1463.4	1.294	4.557
60	10.40	0.294	0.222	1463.5	1.322	4.618
75	14.60	0.397	0.300	2773.9	1.321	3.174
90	18.07	0.322	0.238	2727.6	1.351	3.184
105	20.68	0.329	0.244	3198.1	1.346	2.956
120	22.52	0.372	0.276	3934.1	1.347	2.773
135	23.71	0.363	0.270	4056.7	1.344	2.755
150	24.30	0.411	0.313	4822.0	1.312	2.939
165	24.42	0.417	0.314	4854.0	1.327	2.868
180	24.42	0.462	0.355	5482.0	1.304	2.840
195	24.18	0.447	0.335	5130.7	1.333	2.839
210	23.90	0.448	0.336	5078.3	1.336	2.854
225	23.58	0.477	0.364	5430.9	1.311	2.814
240	23.00	0.431	0.323	4696.1	1.338	2.881
255	22.36	0.442	0.330	4672.9	1.339	2.882
270	21.30	0.457	0.340	4588.7	1.343	2.917
285	19.20	0.460	0.338	4108.5	1.360	2.888
300	15.79	0.551	0.405	4052.7	1.359	2.857
315	11.95	0.616	0.427	3230.0	1.442	2.889
330	8.63	0.726	0.485	2651.2	1.496	3.003
345	6.27	0.904	0.556	2208.1	1.626	2.887
360	5.33	1.085	0.641	2162.5	1.693	2.419

(2d) $X = 2.20 \text{ m}$

ωt (deg)	\hat{U}_e (m/s)	$\hat{\delta}$ (cm)	$\hat{\theta}$ (cm)	Re_θ	\hat{H}	$\hat{C}_f \times 10^3$
15	5.32	1.647	0.884	2977.0	1.863	1.929
30	6.40	1.050	0.688	2786.5	1.527	2.937
45	8.07	0.914	0.677	3458.4	1.350	3.307
60	9.93	0.747	0.590	3708.1	1.266	3.689
75	12.90	0.722	0.543	4430.6	1.330	3.088
90	16.60	0.546	0.396	4166.0	1.377	2.777
105	19.60	0.516	0.384	4770.3	1.342	2.712
120	21.66	0.551	0.401	5491.9	1.376	2.602
135	22.90	0.539	0.389	5633.4	1.387	2.663
150	23.60	0.594	0.430	6424.9	1.382	2.598
165	23.80	0.601	0.427	6436.3	1.407	2.364
180	23.60	0.559	0.401	5997.4	1.391	2.488
195	23.44	0.646	0.455	6755.0	1.420	2.339
210	23.10	0.679	0.484	7074.4	1.404	2.348
225	22.70	0.678	0.482	6930.2	1.406	2.306
240	22.20	0.642	0.458	6438.6	1.401	2.382
255	21.50	0.670	0.479	6514.4	1.400	2.411
270	20.40	0.644	0.458	5919.1	1.404	2.461
285	18.30	0.754	0.529	6128.1	1.425	2.346
300	14.88	0.782	0.525	4947.7	1.489	2.355
315	11.10	0.867	0.557	3913.0	1.557	2.205
330	7.90	1.058	0.637	3184.7	1.662	2.195
345	5.70	1.442	0.767	2766.2	1.882	1.967
360	5.00	2.156	0.983	3112.4	2.193	1.389

(2e) $X = 2.95 \text{ m}$

ωt (deg)	\hat{U}_e (m/s)	$\hat{\delta}$ (cm)	$\hat{\theta}$ (cm)	$Re_{\hat{\theta}}$	\hat{H}	$\hat{C}_f \times 10^3$
135	17.80	2.101	1.271	14317.5	1.653	0.942
150	18.60	2.285	1.346	15848.2	1.698	0.827
165	18.70	2.333	1.294	15319.3	1.803	0.887
180	18.90	2.551	1.382	16539.2	1.845	0.636
195	18.63	2.748	1.442	17001.5	1.907	0.517
210	18.40	2.819	1.447	16855.0	1.948	0.595
225	18.11	2.977	1.491	17092.0	1.997	0.571
240	17.64	3.159	1.499	16739.4	2.108	0.453
255	17.08	3.262	1.520	16437.3	2.146	0.382
270	16.30	3.437	1.500	15476.9	2.292	0.311
285	14.65	4.576	1.308	12130.9	3.498	0.087
300	12.03	6.296	0.464	3534.6	13.565	
315	9.48	10.173	-3.316	-19901.0	-3.068	
330	7.56	18.442	-14.842	-71036.5	-1.242	
345	6.45	23.510	-26.097	-106563.1	-0.901	

(2f) $X = 3.51 \text{ m}$

ωt (deg)	\hat{U}_e (m/s)	$\hat{\delta}$ (cm)	$\hat{\theta}$ (cm)	$Re_{\hat{\theta}}$	\hat{H}	$\hat{C}_f \times 10^3$
135	13.76	4.071	1.881	16385.3	2.164	0.662
150	15.01	4.850	2.390	22713.6	2.029	0.457
165	15.79	6.401	2.788	27869.5	2.296	0.201
180	16.29	7.470	2.657	27396.6	2.812	0.104
195	16.50	8.798	2.375	24808.8	3.705	0.036
210	16.60	10.498	2.380	25016.5	4.410	0.586
225	16.80	11.585	2.118	22529.3	5.469	0.014
240	16.64	12.196	1.815	19118.2	6.720	0.088
255	16.10	12.685	1.662	16943.5	7.631	0.126
270	19.06	15.560	1.904	22968.7	8.174	0.144
285	16.97	16.194	0.333	3572.4	48.699	
300	14.50	19.475	-1.922	-17642.7	-10.133	
315	11.30	25.094	-7.552	-54021.8	-3.323	

(2g) $X = 4.27 \text{ m}$

ωt (deg)	\hat{U}_e (m/s)	$\hat{\delta}$ (cm)	$\hat{\theta}$ (cm)	$Re_{\hat{\theta}}$	\hat{H}	$\hat{C}_f \times 10^3$
165	10.12	5.721	3.540	22678.4	1.616	
180	10.95	5.186	2.875	19932.1	1.804	
195	11.91	7.487	3.360	25332.6	2.228	
210	12.92	11.052	3.674	30052.3	3.008	
225	13.88	15.744	3.273	28756.3	4.811	
240	14.60	20.079	2.119	19582.3	9.477	
255	15.00	23.954	0.661	6277.7	36.235	
270	15.17	26.957	-0.529	-5079.3	-50.968	
285	14.50	29.730	-2.201	-20206.4	-13.506	
300	12.84	34.817	-5.775	-46945.0	-6.029	

Table 3 ($k = 1.03$ flow with 'roof damper')(3a) $X = 1.63$ m

ωt (deg)	\hat{U}_e (m/s)	$\hat{\delta}$ (cm)	$\hat{\theta}$ (cm)	Re_{θ}	\hat{H}	$\hat{C}_f \times 10^3$
15	16.85	0.279	0.235	2504.4	1.190	
30	17.41	0.260	0.221	2435.3	1.175	
45	19.02	0.240	0.206	2485.3	1.163	3.454
60	21.05	0.235	0.202	2688.9	1.163	3.384
75	22.27	0.238	0.203	2862.8	1.173	3.351
90	22.68	0.249	0.211	3033.4	1.177	3.340
105	22.85	0.258	0.219	3160.9	1.181	3.336
120	23.03	0.263	0.222	3237.0	1.184	3.332
135	23.10	0.268	0.226	3304.4	1.186	3.328
150	23.02	0.272	0.229	3331.3	1.188	3.330
165	22.96	0.271	0.229	3321.6	1.186	3.329
180	22.94	0.262	0.221	3211.8	1.185	3.332
195	22.96	0.259	0.219	3184.9	1.180	3.326
210	22.94	0.252	0.214	3105.8	1.178	3.326
225	22.89	0.251	0.214	3094.9	1.177	3.330
240	22.80	0.250	0.212	3053.2	1.181	3.339
255	22.68	0.249	0.210	3017.5	1.184	3.343
270	22.45	0.241	0.202	2876.1	1.190	3.365
285	22.25	0.252	0.212	2990.1	1.188	3.363
300	21.90	0.257	0.217	3006.5	1.187	3.372
315	21.40	0.266	0.224	3038.6	1.188	3.382
330	20.47	0.273	0.229	2966.3	1.191	3.411
345	19.01	0.286	0.239	2875.2	1.198	3.456
360	17.49	0.294	0.245	2714.4	1.197	

(3b) $X = 3.01$ m

ωt (deg)	\hat{U}_e (m/s)	$\hat{\delta}$ (cm)	$\hat{\theta}$ (cm)	$Re_{\hat{\theta}}$	\hat{H}	$\hat{C}_f \times 10^3$
15	12.05	5.748	1.547	11804.5	3.714	
30	12.30	5.404	1.661	12933.8	3.254	
45	13.20	4.373	1.678	14022.5	2.606	
60	14.30	3.249	1.456	13184.7	2.231	0.503
75	15.10	2.695	1.279	12224.7	2.108	0.648
90	15.50	2.672	1.217	11942.4	2.195	0.592
105	15.70	2.837	1.242	12340.0	2.285	0.541
120	15.90	3.045	1.258	12659.4	2.421	0.445
135	16.00	3.210	1.313	13300.8	2.444	0.501
150	16.00	3.326	1.341	13586.6	2.480	0.447
165	16.00	3.386	1.349	13662.2	2.510	0.402
180	16.00	3.466	1.381	13991.8	2.509	0.452
195	16.00	3.410	1.398	14159.2	2.440	0.435
210	16.00	3.303	1.340	13574.5	2.464	0.371
225	16.00	3.285	1.375	13925.0	2.390	0.400
240	15.90	3.282	1.352	13608.6	2.428	0.384
255	15.80	3.371	1.366	13668.3	2.467	0.444
270	15.70	3.491	1.369	13607.8	2.550	0.384
285	15.50	3.622	1.407	13803.4	2.575	0.329
300	15.28	3.813	1.428	13814.0	2.670	0.320
315	14.90	3.872	1.362	12847.5	2.843	0.248
330	14.30	4.125	1.356	12274.7	3.043	
345	13.33	4.499	1.305	11016.8	3.446	
360	12.30	5.106	1.279	9955.9	3.993	

(3c) $X = 3.28 \text{ m}$

ωt (deg)	\hat{U}_e (m/s)	$\hat{\delta}$ (cm)	$\hat{\theta}$ (cm)	$Re_{\hat{\theta}}$	\hat{H}	$\hat{C}_f \times 10^3$
15	12.29	12.452	1.467	11415.4	8.487	
30	12.53	12.179	1.967	15603.7	6.191	
45	13.30	11.245	2.654	22347.1	4.237	
60	14.01	9.621	2.935	26030.0	3.278	
75	14.36	8.159	2.537	23061.0	3.216	
90	14.77	7.863	2.207	20633.4	3.563	
105	15.26	8.472	2.191	21170.1	3.866	
120	15.70	9.172	2.216	22027.6	4.138	
135	15.92	9.617	2.214	22317.9	4.343	
150	15.90	9.689	2.173	21870.1	4.459	
165	15.90	9.769	2.152	21658.1	4.540	
180	15.90	9.775	2.186	22001.0	4.472	
195	15.91	9.763	2.223	22389.5	4.392	
210	15.88	9.618	2.183	21943.9	4.406	
225	15.80	9.547	2.220	22208.8	4.300	
240	15.78	9.679	2.251	22482.4	4.301	
255	15.70	9.780	2.140	21270.0	4.570	
270	15.59	10.206	2.111	20838.1	4.834	
285	15.41	10.608	2.010	19606.8	5.278	
300	15.24	10.855	1.983	19133.5	5.473	
315	14.95	11.120	1.954	18492.4	5.691	
330	14.43	11.396	1.863	17014.6	6.118	
345	13.60	11.697	1.648	14187.9	7.098	
360	12.70	12.222	1.386	11142.5	8.819	

(3d) $X = 3.59 \text{ m}$

ωt (deg)	\hat{U}_e (m/s)	$\hat{\delta}$ (cm)	$\hat{\theta}$ (cm)	$Re_{\hat{\theta}}$	\hat{H}	$\hat{C}_f \times 10^3$
15	12.27	22.531	-0.279	-2166.4	-80.787	
30	12.38	21.842	0.487	3817.2	44.846	
45	12.90	22.021	1.281	10463.4	17.187	
60	13.37	21.673	2.103	17802.2	10.305	
75	13.11	19.791	2.462	20434.7	8.038	
90	13.14	18.082	1.615	13438.5	11.193	
105	13.88	17.970	0.719	6320.4	24.983	
120	14.87	19.105	0.450	4236.3	42.455	
135	15.41	20.228	0.782	7626.9	25.874	
150	15.37	20.646	0.868	8445.4	23.787	
165	15.34	20.607	0.741	7198.1	27.802	
180	15.43	20.360	0.573	5595.6	35.544	
195	15.50	20.493	0.855	8392.2	23.961	
210	15.43	20.231	0.894	8732.5	22.631	
225	15.30	20.208	0.778	7540.2	25.958	
240	15.20	20.382	0.520	5000.6	39.221	
255	15.05	20.975	0.296	2816.1	70.966	
270	14.85	21.902	0.037	351.1	586.413	
285	14.64	22.742	-0.207	-1921.3	-109.705	
300	14.58	23.532	-0.154	-1419.1	-153.057	
315	14.36	23.545	-0.162	-1472.5	-145.366	
330	14.03	23.515	-0.212	-1880.6	-111.056	
345	13.55	23.279	-0.183	-1572.4	-126.999	
360	12.77	23.134	-0.388	-3137.8	-59.604	

APPENDIX BDATA ORGANIZATION

Sets of the ensemble-averaged velocity and turbulence quantities data have been stored on diskettes and are available to interested users. These data are stored on 5.25 inch high capacity floppy diskettes, which can be used with IBM/AT with high capacity drive or compatable machines. High capacity diskettes were chosen to minimize the number of diskettes. These data may become available also on 60 mbyte streaming tape.

Diskette numbers 1 to 7 contain data for $k = 0.61$ and 1.33 flows and 8 to 12 contain data for $k = 1.03$ flow with "roof damper"; as shown in the following table.

Diskette number	Shearwise location (m)	Flow Code	Data type	Total number of data files
1	0.53	1	$\hat{U}, \hat{u}^2, \hat{v}^2, -\hat{uv}$	192
2	1.45	2	"	"
3	1.83	3	"	"
4	2.20	4	"	"
5	2.95	5	"	"
6	3.51	6	"	"
7	4.27	7	"	"
8	1.63	1	$k = 1.03$ with "roof damper"	96
9	3.01	2	"	"
10	3.28	3	"	"
11	3.59	4	"	"
12	4.12	5	"	"

Data file designation

(i) First letter represents the flow.

L = Low frequency flow ($f = 0.596$ Hz, $k = 0.61$)

H = High frequency flow ($f = 0.954$ Hz, $k = 1.33$)

R = flow with "roof damper" ($f = 0.954$ Hz, $k = 1.03$)

- (ii) Second letter represents the streamwise distance (see the table).
- (iii) Third letter (or third and fourth) letter identify the type of data.

U = ensembled-averaged velocity

\hat{U}^2 = ensembled-averaged \hat{u}^2

\hat{V}^2 = ensembled-averaged \hat{v}^2

$\hat{U}\hat{V}$ = ensembled-averaged $\hat{-uv}$

- (iv) Phase angle is represented by last two (or three, as the case may be) digits.

Example: Data file H1U-180 represents ensemble-averaged velocity data for $k = 1.33$ flow at $X = 0.53$ m, and at a phase angle of 180 degrees.

Data file organization

All data files contain laser and valid X-wire data except for R1($k = 1.03$ flow with "roof damper" at $X = 1.63$ m), where only X-wire data were taken. First line of the data files contain streamwise location (X in inches), phase angle (ωt), number of bins (24), number of laser points (NL), number of X-wire points (NL) and a dummy number. Next, NL line contains laser data with each line containing four entries, i.e., distance from wall in inches (y), U (or \hat{u}^2 , \hat{v}^2 , $\hat{-uv}$), uncertainty (ΔU or $\hat{\Delta u}^2$, $\hat{\Delta v}^2$, $\hat{\Delta -uv}$) and a flag (0, for laser data). X-wire data entries contain y , U (or \hat{u}^2 , \hat{v}^2 , $\hat{-uv}$) and a flag (1, for X-wire data).

A program to read the data files, READ is available on each diskette, READ plots the laser (small circle) and X-wire (larger circle) on a semi-log plot on the screen. X-axis of the plot is the distance from the wall on a semi-log scale (3.6 cycle, 0.01 cm to 60 cm) and Y-axis is the quantity, i.e., \hat{U} , \hat{u}^2 , \hat{v}^2 , or $\hat{-uv}$. Vertical scale is scaled between minimum and maximum value of the data but user can alter the scale by selecting option 2. User

can also print the numerical values of laser and X-wire data on the screen by selecting option 3 or 4.

END

DATE

FILMED

DTIC

JULY 88